# SIMULATING HYGROMORPHIC TIMBER CURVATURE

A Computational Framework for Passive Bilayer Deformation with Reversible Locking Mechanisms

MSc Graduation Thesis


Sinan Wehrli 6309801
MSc Architecture, Urbanism, and Building Sciences
Master Track Building Technology

First Mentor Gabriele Mirra
Second Mentor Stijn Brancart


June 2026

# SIMULATING HYGROMORPHIC TIMBER CURVATURE

A Computational Framework for Passive Bilayer Deformation with Reversible Locking Mechanisms

**Sinan Wehrli**
6309801

**Mentors**
Dr. Gabriele Mirra
Computational Design

Dr. Stijn Brancart
Structural Design

**Delft University of Technology (TU Delft)**
Faculty of Architecture and the Built Environment

**Msc Architecture, Urbanism and Building Sciences**
Track - Building Technology

# ABSTRACT

The tendency for timber to expand and contract in response to changes in moisture content is largely regarded as a limitation that can lead to splintering, warping, and cracking in built elements. More recently, however, research has explored the applicability of timber's transformative behaviour in dynamic sectors of construction, with a large focus turning towards deployable structure. By employing laminated bilayer configurations, timber deformation can be controlled to exhibit both monoclastic (uni-directional) and anticlastic curvature (involving opposing curvature signs across two principal directions) under fluctuations in relative humidity. To accurately simulate these deformations across multiple panels and configurations, this study investigates the development of computational workflows for simulating hygromorphic bilayer behaviour based on material properties, bilayer dimensions, and environmental conditions.

For deriving monoclastic geometries, an adapted version of Timoshenko's bi-metal bending formula was implemented to calculate two-dimensional curvature. The resulting data was integrated into a particle-spring computational model capable of computing deformation behaviour across varied fibre orientations. To assess consistency and reliability, simulated curvatures for 90° and 45° fibre orientations were re-evaluated against Timoshenko calculations for total bilayer thicknesses of 2.5 mm, 3.5 mm, 4.5 mm, 5 mm, 7 mm, and 9 mm, presenting an overall predictive accuracy of approximately 90%.

The development of anticlastic simulations required empirical data derived from 18 physical bilayer samples. Oak was selected as the active layer, and spruce as the passive layer, to investigate nine separate bilayer configurations with controlled dimensions of 160 mm × 160 mm. Three total bilayer thicknesses of 6 mm, 8 mm, and 10 mm were tested alongside active-to-passive layer ratios of 1:1, 2:1, and 3:1. Samples were stabilised at 55% relative humidity, within a temperature range of 24-27, before being laminated and then conditioned at a 95% relative humidity to induce hygromorphic deformation. Curvature in both principal directions was derived through geometric analysis of 3D scans from each sample, allowing scaling relationships between arc length and bilayer thickness to be established and integrated into a second computational workflow. Comparative analysis between physical samples and digital simulations demonstrated that the proposed framework could successfully approximate anticlastic deformation behaviours and reproduce multi-directional curvature with opposing signs.

Alongside the computational investigations, the kinematic potential of curve-line elements as a reversible locking mechanism were explored. Given the degree of variation in hygromorphic curvature, activation for a range of arc amplitudes was considered through physical polypropylene samples. For strip sizes of 100mm x 40mm (length x width), arcs with amplitudes of 2.5mm, 5mm, 7.5mm, 10mm, 12.5mm, 15mm, 17.5mm, and 20mm were mechanically deformed to assess behaviour. The final prototype assessed reversible locking for a monoclastic strip with an integrated system of adjacent alternating curve-line panels. Through activation and collision method interaction, overlapping elements are tensioned together with an adapted "Z-hook" pin. The final model demonstrated structural integrity, and resisted re-flattening over an extended period of 24 hours within a controlled, indoor environment. While large-scale deployable structures were not developed within this research, the findings establish a foundational computational and kinematic framework for the future upscaling of hygromorphic bilayers into adaptive free-form shell structures.

# ACKNOWLEDGMENTS

In achieving my master's thesis at the Faculty of Architecture and the Built Environment at TU Delft I would like to express my gratitude to all the people, both near and 14, 215km away, for guiding, supporting and inspiring me throughout this entire process. From stepping into a research topic that was completely unfamiliar to me, to learning how to spell the word hygromorphic properly, my mentors, family, and friends have all helped me bridge my interest in computational design and timber construction into a truly engaging research project.

First and foremost, I would like to express my gratitude to my mentors Gabriele Mirra and Stijn Brancart, for their truly incredible support.

To Gabriele; you have always presented a genuine interest and motivation in my project throughout these last 8 months that has helped inspire me continuously in my research. Especially in moments where I have felt untethered and lost in the direction of my progress, you have always been present and solution-oriented in guiding me on the next step. I am very grateful for your willingness to offer up your time so often to help me. I never felt disregarded in this process, and I thank you for taking all my thoughts, questions and confusions seriously.

To Stijn; your advice has been deeply necessary in all my moments of uncertainty and miss-direction. From helping me to understand and re-frame my scope, to providing guidance on how to solve conceptual blocks, your outlook has been a steady constant in this journey. Your questions and ideas have made me reflect critically on my process, and have always strengthened my project.

Across academia and research, I would like to thank Sofia Brenes for offering up her time in guiding me through the 3D scanning process at the DINED research lab, and for being so readily available last-minute when I was rushing to collect final sample data. I would like to thank the team at the wood workshop for graciously supporting me in cutting down, trimming, and thinning all my timber samples.

I would also like to thank Laura Kiesewetter, primary author to one of the more critical papers in my research field, for her advice and insight over email correspondence.

Finally, I would like to thank the decidedly enormous emotional support group that was my friends and family from the Netherlands, to Italy, and across the globe to Australia, for their never-ending support and love.

To my parents; who have both sat through hundreds of intensely confusing and distantly unhinged rants on bendy timber to validate, critique, and/or nod approvingly on my progress. Words carry meaning but I still find it difficult to express how infinitely grateful I am to have had both your support throughout this entire thesis. I have, and always will, feel your love even 14,000 km across oceans

To my twin brother, Tiziano Wehrli; I will remain in perpetual shock and disbelief at your enduring commitment to pursue a PhD. But in saying that, I am eternally grateful for all your advice and critical insight. I wish you all the greatest success and achievements, you are deserving of it all.

To one of my closest friends, Isabella Harrison; on all the midnight calls you've been patient and loving enough to accept. You've built me up bigger every time, and I could not have overcome all these challenges without you.

To my roommates, Artemisia Goldsmith Ganzerlli, and Sinja Reichenbecher; who have sat through (almost) every single night of dinner and heated discussions on timber, water, and how the two interact. It has been deeply comforting to have been surrounded by people persevering through the same challenges as me.

And a final thank you to my laptop (and the replacement model I had to buy) for suffering through all my Google tabs, Illustrator and Photoshop files, and the solitary 400MB InDesign file that crashed my OneDrive. It appears we both got through this degree together.

# TABLE OF CONTENTS


**ABSTRACT** 3

**ACKNOWLEDGMENTS** 4

**1 INTRODUCTION** 8

1.1 Background 9
*1.1.1 Deployable structures 9*
*1.1.2 Hygromorphic Actuation 10*

1.2 Problem Statement 11

1.3 Relevance 13
*1.3.1 Scientific relevance 13*
*1.3.2 Societal relevance 13*

1.4 Objectives and Boundary Conditions 14
*1.4.1 General objectives 14*
*1.4.2 Sub-objectives 14*
*1.4.3 Boundary conditions 14*

1.5 Research Questions 15
*1.5.1 Main research question 15*
*1.5.2 Sub-questions 15*
*1.5.3 Background questions 15*

1.6 Scope 15

**2 METHODOLOGY** 16

2.1 Methodology 17
*2.1.1 Literature Review 17*
*2.1.2 Constructing the Computational Tool 18*
*2.1.3 Physical prototyping of a reversible locking system 18*
*2.1.4 Thesis Schedule 19*

**3 LITERATURE REVIEW** 22

3.1 Designing with timber 23
*3.1.1 Deployable structures 23*
*3.1.2 Material properties of timber 24*

3.2 Structures of hygromorphic panels 34
*3.2.1 Classification based on geometric form 34*
*3.2.2 Structural stiffness and load distribution across Gaussian Curvatures 35*

3.3 Simulating bilayer bending 37
3.3.1 Mathematical prediction 37
3.3.2 Computational simulation 38

3.4 Reversible locking system for passive curvature 40
3.4.1 Curve-line folding 40
3.4.2 Compliant kinetic mechanisms 41

**4 SIMULATING MONOCLASTIC CURVATURE** 42

4.1 Introduction 43

4.2 Constructing a tool for predicting bilayer bending 44
*4.2.1 Defining the workflow parameters 44*
*4.2.2 Computational frameworks from literature 44*
*4.2.3 The foundational framework: space frame lattice 46*
*4.2.4 Timoshenko's formula for predicting bilayer curvature 49*
*4.2.5 Validating the Grasshopper script 51*
*4.2.6 Final simulation goals 53*

**4.3 Multi-element assemblage** 55
*4.3.1 Principal curvature lines to inform fibre orientation* 55
*4.3.2 Simulation for synclastic curvature* 55
*4.3.3 Reflection on multi-element simulations* 56

**4.4 Flowchart of simulative tool for monoclastic curvature** 58

**5 SIMULATING ANTICLASTIC CURVATURE** 60

**5.1 Predicting anticlastic curvature** 61
*5.1.1 Introducing multi-directional orthogonal expansion* 62
*5.1.2 Rebuilding the space frame* 62

**5.2 Developing the bilayer samples** 66
*5.2.1 Equipment and materials* 66
*5.2.2 Cutting the timber* 68
*5.2.3 Conditioning the individual timber layers* 69
*5.2.4 Laminating the panels* 72
*5.2.5 Raising the moisture content of the bilayers* 74

**5.3 Informing the anticlastic simulative tool** 75
*5.3.1 Deriving curvature from samples* 75
*5.3.2 Informing the computational tool* 77

**5.4 Flowchart of simulative tool for anticlastic curvature** 80

**6 REVERSIBLE LOCKING SYSTEM** 82

**6.1 Introduction** 83

**6.2 Early-stage exploration** 84
*6.2.1 Behaviour of curve-line elements for varied degrees of curvature* 84
*6.2.2 Curvature locking through alternating curve-line action* 85

**6.3 Designing a reversible locking system** 91
*6.3.1 Material selection* 91
*6.3.2 Detailing of curve-line elements with polypropylene* 92
*6.3.3 Digital fabrication and construction of a reversible locking system* 93

**7 SCALING-UP FOR REAL-WORLD APPLICATION** 100

**7.1 Construction process** 101

**8 DISCUSSION AND CONCLUSION** 104

**8.1 Introduction** 105

**8.2 Discussion of main findings** 106
*8.2.1 Simulating hygromorphic deformation* 106
*8.2.2 Anticlastic curvature* 106
*8.2.3 Reversible locking* 108
*8.2.4 Further research suggestions* 108

**8.3 Conclusions** 110
*8.3.1 Sub-research questions* 110
*8.3.2 Implications and recommendations* 112
*8.3.3 Reflection on considerations and limitations* 113

**9 LITERATURE AND FIGURE REFERENCES** 116

LITERATURE 117

FIGURES 123

**10 APPENDIX** 130

# INTRODUCTION 001



***figure 1:*** *The Urbach Tower at Stuttgart [view from base] (source: ICD University of Stuttgart, 2019)*

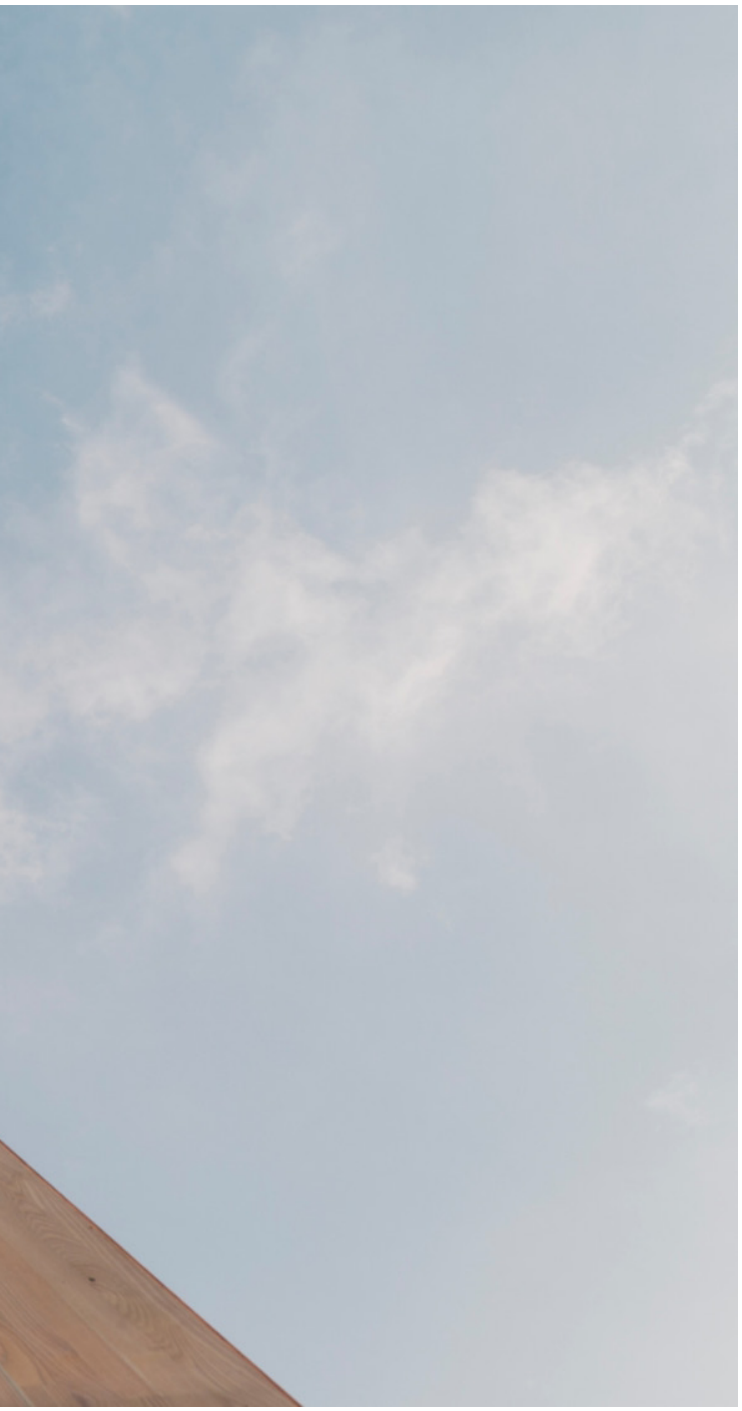

## 1.1 Background

This research investigates how the hygromorphic shape-changing properties of timber can be computationally simulated for the prediction of uni-directional and multi-directional curvature. Alongside the development of predictive computational workflows, the study also explores the kinematic mechanisms of a reversible locking mechanism capable of integrating with hygromorphic deformation and stabilising curved geometries. Although the research does not explore the construction of a fully deployable structure, both the simulation tools and locking system present foundational contributions for supporting the design of free-form deployable shell systems composed of interconnected hygromorphic panels.

### 1.1.1 Deployable structures

The term deployable structure is assigned to a structural system, that is defined by a specific characteristic; its ability to transform from a small, compact configuration, into an enlarged open form through activation by an external or passive mechanical force (Hanaor & Levy, 2001; Fenci & Currie, 2017).

While small-scale examples of man-made deployable structures such as umbrellas, collapsible chairs, and hand-held fans are quite commonly recognised (Doroftei & Doroftei, 2014), and have existed for centuries, the last few decades have seen a rise and development in new systems of much more complex deployable structures.

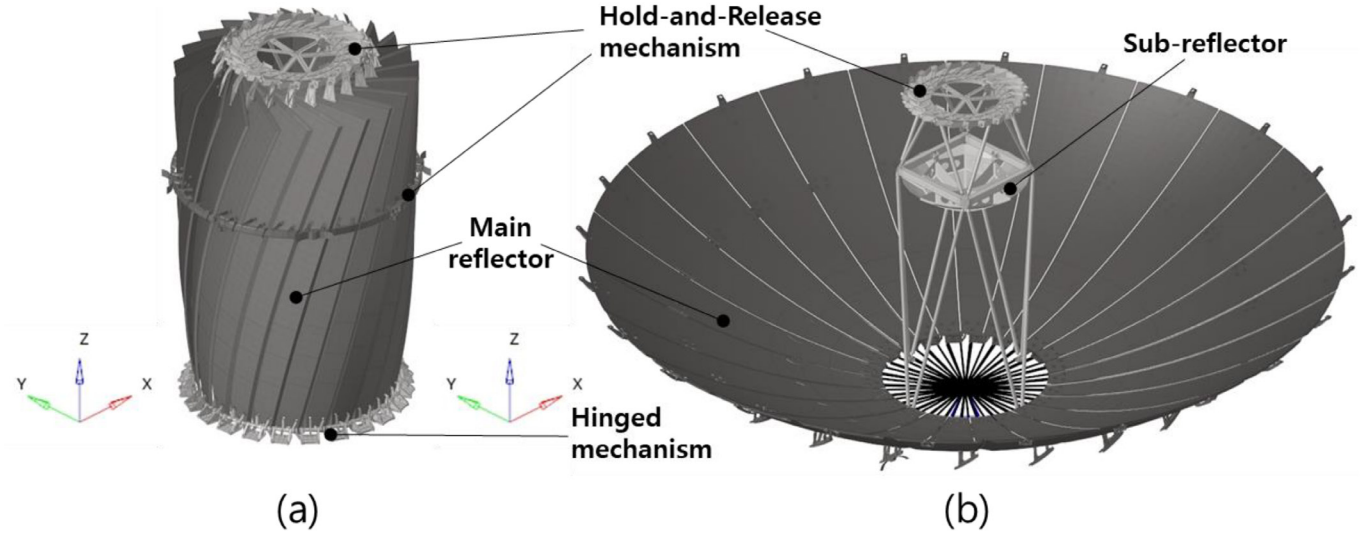


***figure 2:*** *Deployable reflector antenna (source: Kim et al., 2024)*

These advancements have occurred predominantly within the field of spatial engineering, and include systems for antennas, reflectors, and solar arrays (Fenci & Currie, 2017), which all require much more precise engineering and resilient designs for transport and ease-of-activation in outer space (see figure 2).

Building on these novel developments, it was no surprise that the fields of civil engineering and architecture soon saw rise in more advanced transformable structures at larger scales (Doroftei & Doroftei, 2014; Fenci & Currie, 2017). These more modern systems allowed for large-span shelters that were constructed from numerous elemental parts, and could remain fully openable (Wood et al., 2023). Prior to this, configurations such as tents, yurts, and other temporary small-scale shelters had been the predominant examples of deployable structures in numerous ancient cultures (Doroftei & Doroftei, 2014).

The term "deployable structure" encompasses a considerably large range of different structural configurations (see appendix). In the context of hygromorphic bilayers, the most relevant system is a fully demountable structure comprised of smart-materials (the bilayers), that can be stored as separate components and assembled on-site (Hanaor & Levy, 2001).

Throughout this paper, the general term, "demountable structure", will still be used primarily when referring to potential systems of design with hygromorphic bilayers. The background serves more to clarify the scope of the paper, rather than to limit the definition of the structure.

### 1.1.2 Hygromorphic Actuation

Processes of transformable and reversible deployment do not exist exclusively as man-made inventions and technologies. Many man-made deployable systems require mechanical force from human labourers or participants, kinetic energy in the form of air or water, or electrical energy to achieve full activation. Conversely, when we observe the natural world, it becomes apparent that transformable elements can be found across a range of scales and species, including within the leaves of plants, wings of insects, extensible worms, and even in the movable structure of the human body (Doroftei & Doroftei, 2014).

When addressing this behaviour in immobile, non-cognitive organisms, such as plants, their motions and deformations can be distinguished between active and passive systems (Zhan et al., 2023). Active systems involve living cells that trigger motion by moving ions or altering the permeability of membranes (Burgert & Fratzl, 2009). Alternatively, passive systems can function on dead tissue, and follow pre-determined motions in response to environmental stimuli, including light, gravity, temperature, and humidity (Yao & Ishii, 2019; Burgert & Fratzl, 2009). One such transformation is the anisotropic swelling and shrinking of wood due to changes in the ambient humidity

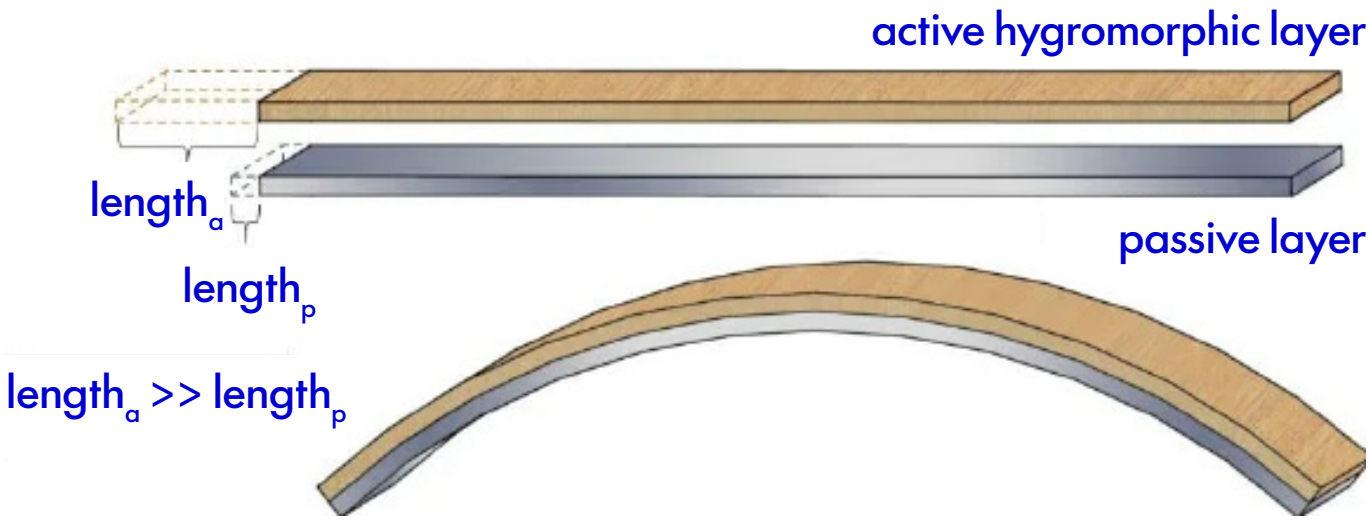


***figure 3:*** *Bilayer diagram demonstrating hygromorphic bending (source: Holstov et al., 2015)*

of the surrounding environment; referred to as hygromorphic deformation (Yao & Ishii, 2019; Xhexhi & Aliaj, 2025; Thybring et al., 2022; Wood et al., 2023).

In recent years, this moisture-induced transformation has gained particular interest in subfields of material science for the development of "self-shaping wood" (Yao & Ishii, 2019). When manufactured as a bilayer-laminate in a cross-ply board configuration, the swelling in one layer will be restricted by the second orthogonal layer, causing the board to deform into a curved surface, as can be seen in figure 3 (Peng et al., 2023; Rüggeberg & Burgert, 2015; Grönquist et al., 2020; Wood et al., 2023). This effectively emulates deployment from a flat two-dimensional (2D) sheet to a curved, three-dimensional (3D) shelter, demonstrating the potential for research on hygromorphic actuation as a system for deployable structures (Grönquist et al., 2020; Abdelmohsen et al., 2019; Wood et al., 2023; Wood et al., 2018; Wood et al., 2016).

## 1.2 Problem statement

The construction of modern, large-span deployable structures has become increasingly prevalent, often taking the form of systems that are pulled or lifted into shape, or of pre-curved, modular elements (Wood et al., 2023). While these geometries are highly efficient once realised, offering lightweight, material-efficient, and structurally resilient solutions across a range of applications (Doroftei & Doroftei, 2014; Bechert et al., 2025), their design and construction processes remain complex. Challenges include the need for highly precise three-dimensional components for assembly and activation, labour-intensive and material-heavy formwork, extensive bracing systems to achieve curvature, and additional layers for enclosure (Wood et al., 2020; Wood et al., 2023).

In response to these challenges, hygromorphic timber bilayers have emerged as a promising material system that is capable of generating curvature passively, rather than relying on external mechanical actuation. Exploiting timber's natural responsiveness to changes in relative humidity, allows hygromorphic systems to function as passive "zero-energy" actuators that transform autonomously from flat states into curved configurations (Wood et al., 2016; Wood et al., 2018).

Despite this potential, current research on hygromorphic systems remains limited in both application and predictive capability. Existing studies primarily focus on adaptive facade systems and curved wall elements, with little exploration into their use in deployable structural systems (Reichert et al., 2015; Wood et al., 2016; Wood et al., 2020).

Addressing this gap requires the development of accessible computational workflows that are capable of simulating hygromorphic deformation across a broader range of curvature behaviours. These computational tools have becomes increasingly more important, as they allow

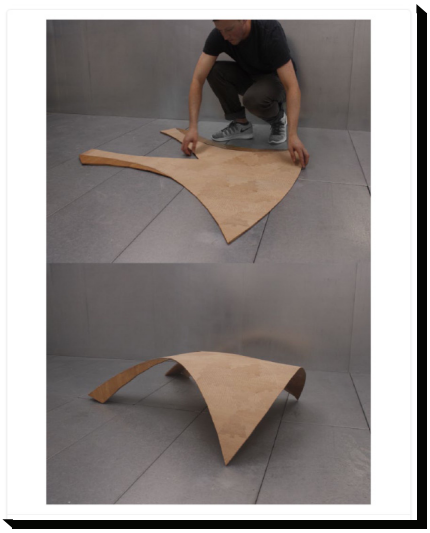

***figure 4:*** *Material computation—4D timber construction (source: Wood et al., 2016)*

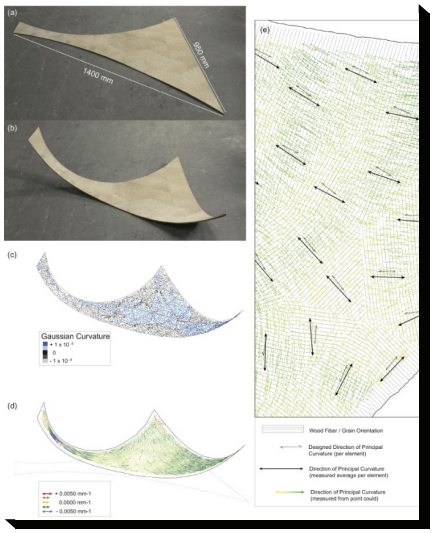


***figure 5:*** *Hygroscopically actuated wood elements for weather responsive and self-forming building parts (source: Wood et al., 2018)*

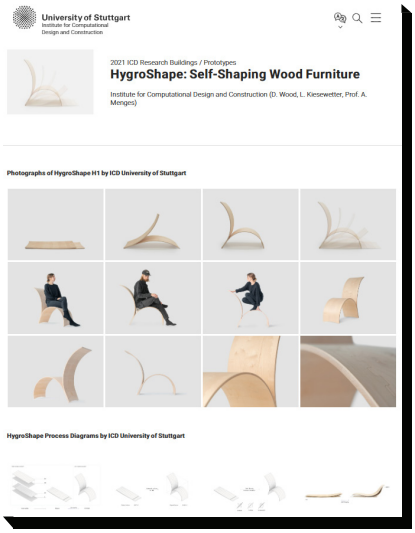


***figure 6:*** *HygroShape: Programming Flat-pack, Self-shaping Wood Furniture (source: Kiesewetter et al., 2025)*

designers to simulate material behaviour without relying solely on iterative physical prototyping which can be extremely time-consuming and costly. Although computational tools have been proposed in research (see figure 4-6), the methodology behind their development has been insufficiently documented or is presented as inaccessible, limiting their reproducibility. They also focus solely on monoclastic curvature, where bending occurs uni-directionally along a single axis, while anticlastic deformation, involving simultaneous opposing curvatures, remains under-explored. This limitation restricts the ability to computationally investigate more complex free-form shell geometries that could emerge from interconnected hygromorphic systems.

In parallel to the development of predictive simulation tools, there is also limited research into reversible locking systems that are capable of stabilising deployed hygromorphic shells without permanently restricting their movement. Currently, built applications commonly rely on a third restraining layer (see figure 7 & 8), or an external bracing system to maintain curvature (Wood et al., 2020; Wood et al., 2023; Bechert et al., 2025). While effective, these approaches reduce reversibility and undermine the advantages associated with flat-pack transport and autonomous deployment.

Ultimately, this paper focuses on the design and validation of computational workflows for predicting both monoclastic

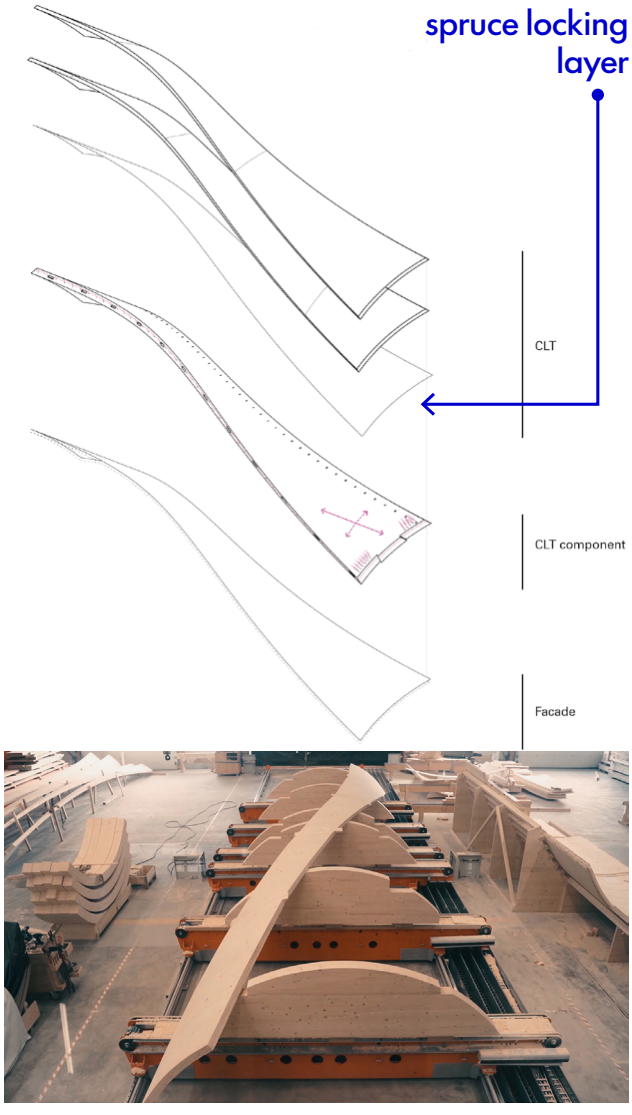


***figure 7 & 8:*** *Stability of bilayers is achieved by press laminating an additional elastically bent spruce locking layer (source: ICD University of Stuttgart, 2019)*

and anticlastic hygromorphic curvature (see figure 9), alongside the exploratory development of a reversible locking mechanism. These research gaps are necessary topics to address in order to accommodate the future development of deployable structures, which serves as the broader architectural context of the research.

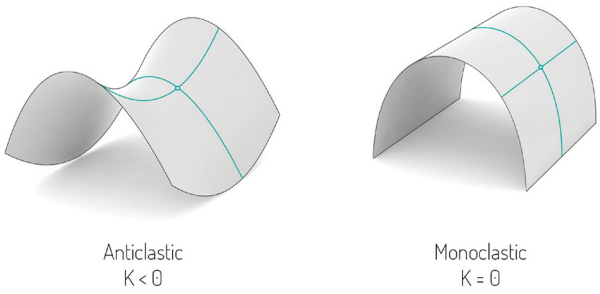


***figure 9:*** *Anticlastic and monoclastic curvature (source: Naboni et al., 2018)*

## 1.3 Relevance

The goal of constructing deployable structures from hygromorphic panels that can serve as practical shelters at a human-scale still demands a greater understanding on how bilayers deform across different timber species, fibre orientations, and dimensions, as well as their structural integrity, adaptability, and construction.

The current academic scope for achieving this final goal is considerably vast, and far too demanding for the timeline of this paper. Therefore, in order to support research and provide a positive contribution to existing knowledge gaps, this paper will focus specifically on developing and improving predictive computational tools, while validating a reversible locking system for actuating bilayers. Both aspects of the research are foundational to broadening the potential designs and applications for future-case large-scale deployable structures.

### 1.3.1 Scientific relevance

From a scientific perspective, this thesis contributes to research at the intersection of computational design and timber engineering. The research carried out presents simulative computational tools for monoclastic and anticlastic curvature in bilayers across varied fibre orientations, timber species, and bilayer thicknesses, while also validating the design of a reversible self-locking system that activates through induced curvature in bilayers. Validation will be achieved by testing physical samples, while the integration of humidity input, material behaviour, and geometric transformation will inform the physics-based digital modeling.

This cross-disciplinary approach demonstrates how material research can contribute to digital workflows to support the development of new design precedents for real-world applications.

### 1.3.2 Societal relevance

Beyond its technical and scientific contributions, this research carries implications for the construction sector, short-term events and gatherings, and humanitarian sectors.

Hygromorphic behaviour is often treated as a material phenomenon that impedes on the applicability of timber in construction. By leveraging passive environmental actuation, the deployment process is less dependent on fuel, electricity, machinery, or human labour, making the design more accessible and lowering the threshold for construction participation. This shift toward material-driven behaviour, rather than energy-intensive mechanical shaping, can help promote a more sustainable production process by minimizing waste and industrial over-processing.

Furthermore, deployable systems are effective for pavilions, exhibitions, outdoor events or festivals, and emergency scenarios, as their modularity can accommodate efficient transport, quick and simple assembly, and demountability for re-use.

## 1.4 Objectives and boundary conditions

### 1.4.1 General objectives

Existing research has demonstrated the use of computational tools to predict uni-directional curvature, but lacks the procedural transparency needed to recreate, build, and further develop these tools. In order to achieve more complex, large-scale deployable structures, such tools are essential for quickly designing, validating, and exploring a range of options without the need to produce numerous physical samples, which can be extremely time-consuming.

Consequently, one of the main objectives of this paper is to develop and validate a simulative computational tool for monoclastic curvature, while also expanding on the precedents identified in the literature to develop a simulative model for anticlastic curvature, which will be validated through physical testing.

While it is necessary to construct computational tools that consider the necessary bilayer dimensions and fibre orientations for larger, interconnected deployable systems, there is a lack of research focusing on the behaviour of self-locking systems that activate as bilayers transition from a flat state to curved elements. The second objective of this paper is to design a system that can passively activate without external human intervention, and prevent the deployed structure from re-flattening as the relative humidity of its outdoor environment fluctuates. Physical prototypes of the self-locking elements will be used to replicate the activation process and verify the design's applicability.

### 1.4.2 Sub-objectives

- Integrating the influence of longitudinal, radial and tangential swelling in timber to inform the computational workflow.
- Integrating the influence of varied panel thickness to inform the degree of curvature for the computational workflow.
- Ensuring transformability of the perpendicular fibre orientations of the passive and active layers in the computational model.
- Physical prototyping to explore the kinematic mechanism of locking elements.
- Assess the structural integrity of the locking system to resist flattening.

### 1.4.3 Boundary conditions

This paper will focus on evaluating design feasibility through digital simulations, material samples, and physical models.

For the predictive tools, generated geometries will be compared to mathematical formulas derived from literature to determine accuracy, as well as the curvature analysis of physical prototypes. Material testing will be limited to small, thin timber layers (less than 10mm thick, with length x width less than 200mm x 200mm) rather than the construction of large-scale panels for human shelters which is beyond the scope of this research.

The timber species selected for the tests is dependent on how accessible and costly certain types of hardwoods and softwoods are. Final materials acquired were sourced near the university, in Delft, the Netherlands, at a local wood shop and include oak as the hardwood, and spruce as the softwood.

The locking elements will be designed with polypropylene, presenting an ideal material for early kinematic exploration. Given the time-consuming process required for drying, conditioning, laminating and deforming the bilayers, physical testing of the locking behaviour will use alternative materials that emulate the curving process more quickly.

## 1.5 Research questions

### 1.5.1 Main research question

***How can a computational design workflow be developed for simulating hygromorphic bilayer deformation to support the design of deployable free-form structures?***

### 1.5.2 Sub-questions

**To what extent can the computational workflow be adapted to generate different target geometries?**

**How can material data be effectively integrated in a digital simulation of hygromorphic behaviour?**

**To what extent can be varied bilayer configurations generate anticlastic curvature behaviour?**

**How can hygromorphic deformation facilitate the kinematic activation of an integrated locking system?**

**How can a joinery system be designed to achieve both structural equilibrium and reversibility for curved forms?**

### 1.5.3 Background questions

In order to develop a strong foundation of understanding for the scope of the main research question, several background questions were outlined. These guided the direction of literature research, and provided an overview on the process of working with timber and deployable structures:

1. What triggers hygromorphic deformation in timber?
2. How does the cellular structure of timber react to moisture absorption?
3. Why are bilayers commonly implemented when working with hygromorphic deformations?
4. How and why do different species of timber influence the final degree of curvature?
5. What are the different types of curvature that can be achieved with a single bilayer?
6. By what process is anticlastic curvature generated over monoclastic curvature
7. What are different types of computational software that can assist in achieving curvature predictions?
8. What are different kinematic systems that can achieve activation through curvature deformation?
9. What types of locking systems accommodate reversibility?

## 1.6 Scope

This thesis project combines elements of architecture, computational design, and material research to form a hybrid research framework. The main focus is on developing and improving simulative tools for hygromorphic curvature.

While this paper touches briefly upon topics of manufacturability, long-term durability, environmental performance, and on-site construction logistics, these areas fall outside the scope of the project. This is largely due to the time constraints for the thesis, which has been deliberately limited to digital and physical testing of proof-of-concept geometries and self-locking mechanisms; excluding long-term performance, compliance, and large-scale architectural application.

# METHODOLOGY 002

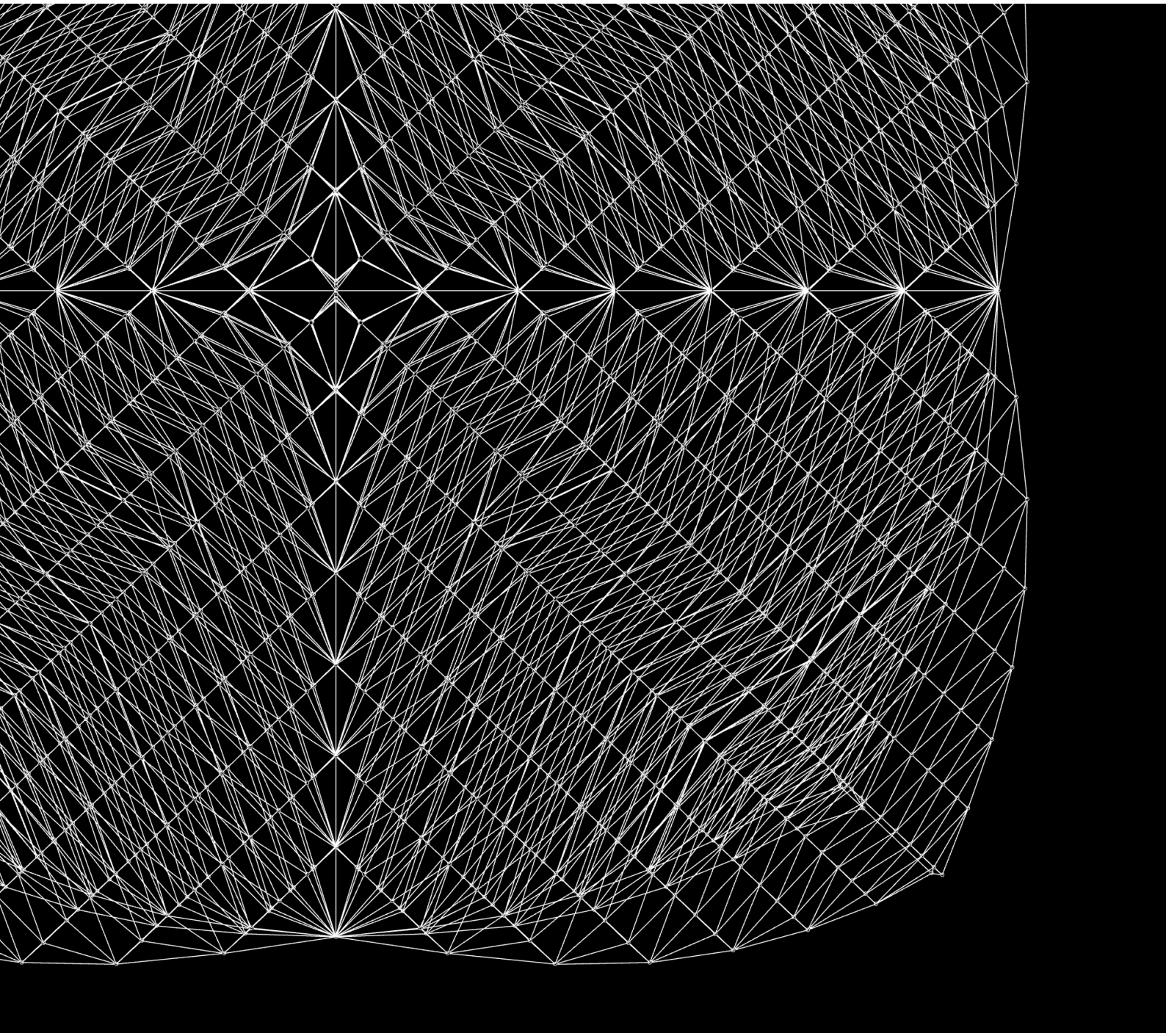

***figure 10:*** *Top-view of bilayer curvature for four inter-locked panels (source: own work)*

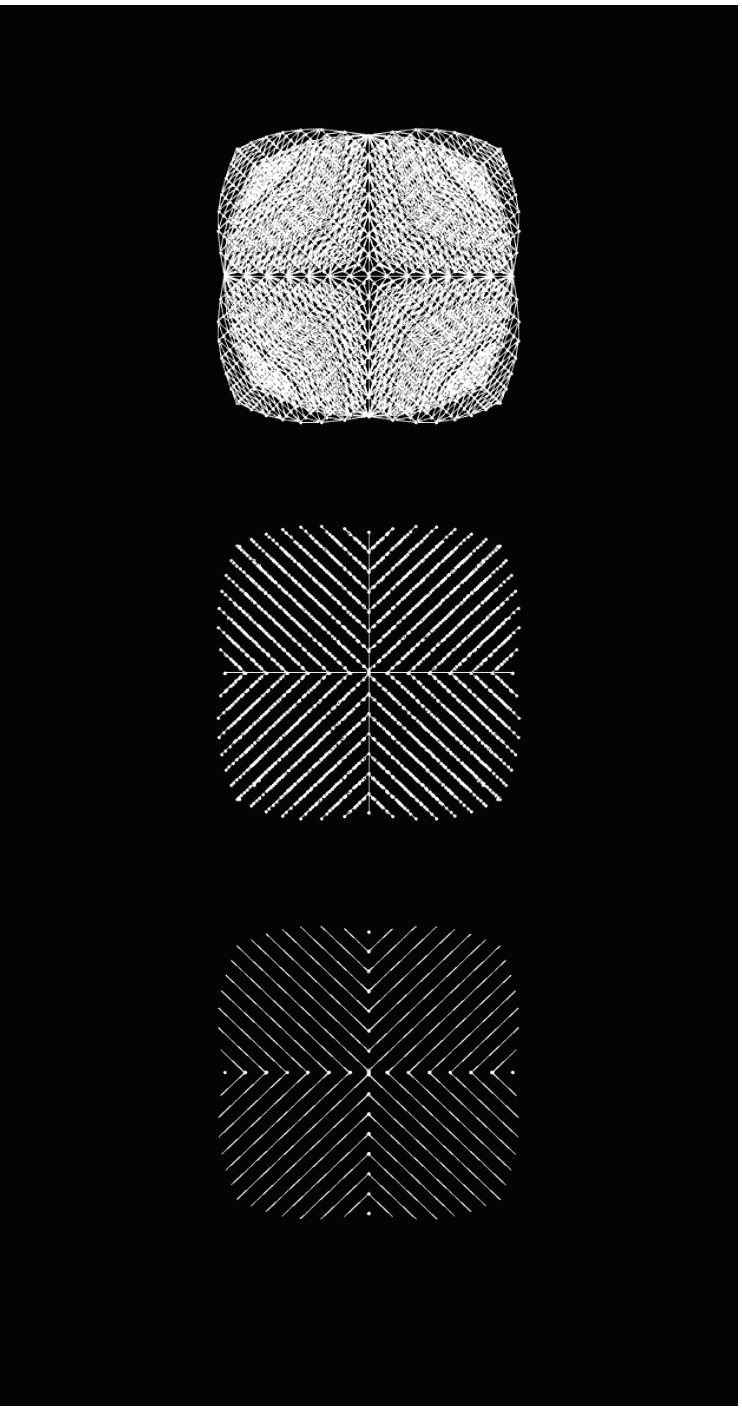

## 2.1 Methodology

Within this chapter, the methodology for research and the process of validating the topic are outlined, demonstrating how the different phases inform each other. To achieve the final research outcome, this study transitions through three parts - one of which is expanded into two components – including analysis on the current literature of the topic, development of the computational design tools, the design of the self-locking system, and the design exploration of potential future structures.

### 2.1.1 Literature review

To understand the topic, determine research gaps, and develop an informed solution, an extensive literature review was carried out not only at the beginning but also continuously throughout the thesis timeline in order to re-inform, direct and solve issues.

To guide the research, it was centred around three main topics: the construction and effects of hygromorphic bilayers, computational and mathematical tools for predicting curvature, and different systems of self-locking mechanisms.

**Construction and effects of hygromorphic bilayers**

This component of the research focused on the methods for constructing a bilayer, how their production can allow us to control the direction and type of curvature (as either monoclastic or anticlastic curvature), how the dimensions and thickness of a panel influence the degree of

curvature, and how panelised bilayers can be interlocked to form larger structures. This will also allow for verification on the viability of the research topic.

**Computational and mathematical tools for predicting curvature**

The intention behind the computational tool was to build a replicable predictive tool for future research to build upon to allow for future upscaling of more complex deployable forms.

The tool was developed as a simulative system based on existing understanding of hygromorphic behaviour. The research was focused on uncovering different modeling or mathematical formulae that could accurately emulate the deformations of hygromorphic bilayers.

**Systems of self-locking mechanisms**

To ensure the deployable structure remains upright once the panels have activated and deformed, a system to lock the entire structure into its final form needs to be developed.

The intention is for this system to be integrated with the panels – rather than being external – and therefore the research focuses on gathering precedents for other built-in locking mechanisms.

## 2.1.2 Constructing the computational tools

Building on the research from the literature review, this part of the project explores the development of the computational design tool.

Rhinoceros3D is the primary software employed and allows geometries to be modeled and viusalised in a digital space, while Grasshopper serves as a visual programming language that assists in constructing the geometries and ensuring they can be adapted or changed easily. A plethora of plugins can be integrated with Grasshopper to expand the capabilities of the software and create more dynamic forms.

Kangaroo Physics - a Grasshopper plugin - allows for the simulation of deployment under real-world conditions, while Karamab3D - a secondary plugin - is used to determine the structural forces and stresses within the deployed structure, Python code is used to discretise the 2D flat-pack form of the undeployed structure into individual bilayer panels.

Validation of the tool is carried out through comparison of the digital simulations of curved elements against physical material research on the behaviour of bilayer panels. The results inform the success of the tool; proposing a precedent for designs at a larger scale and more advanced manufacturing.

## 2.1.3 Physical prototyping of a reversible locking system

In order to assess the validity of a locking system that can activate effectively with hygromorphic deformation - and achieve a stable state when deployed - physical modeling is employed. The main focus is on determining the kinematic feasibility for a conceptual reversible system through exploration of different prototypes.

Due to the extensive amount of time required to construct a hygromorphic bilayer, activation is explored through pseudo-systems that can achieve curvature through heat-bending, and mechanical deformations instead.

## 2.1.4 Thesis schedule - Post A1

***figure 11:*** *Thesis timeline developed for A1 (source: own work)*

## 2.1.4 Thesis schedule - Post A2

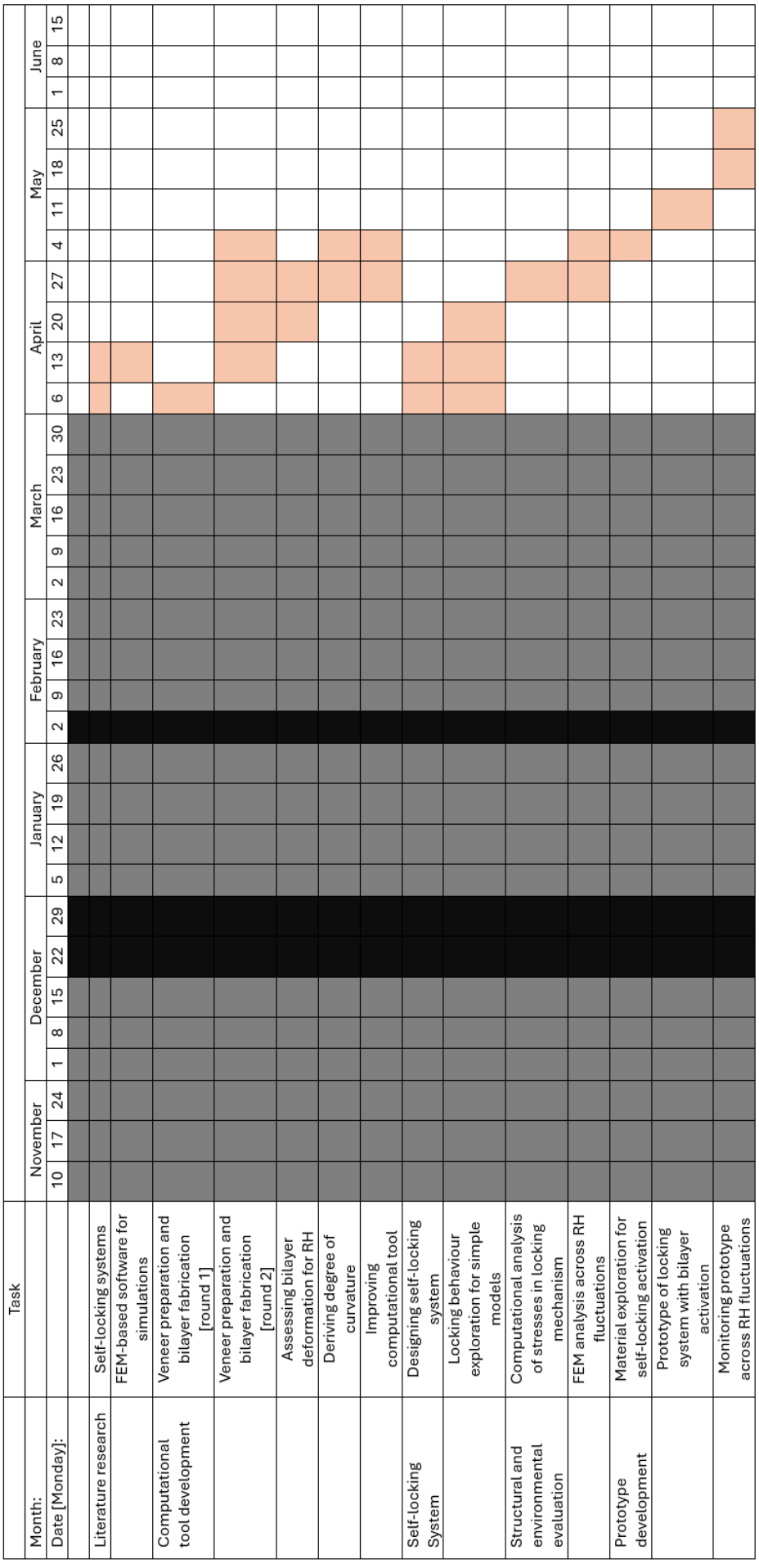


***figure 12:*** *Re-construction of thesis timeline at A2 (source: own work)*

***figure 13:*** *Deconstructed top-view of different elements for bilayer curvature simulations (source: own work)*

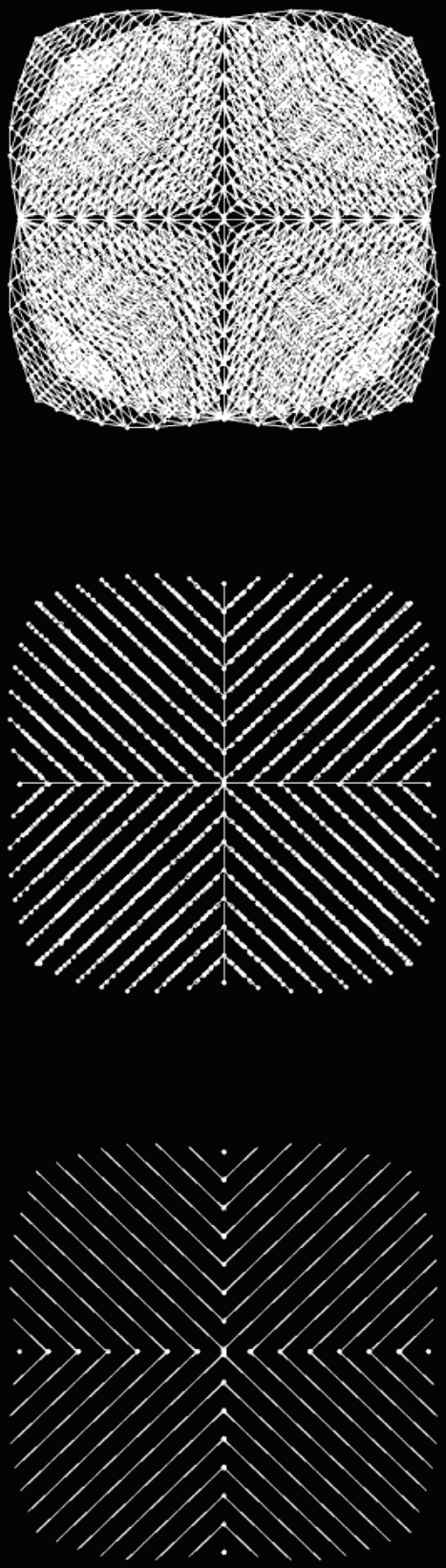

# LITERATURE REVIEW

# 003



***figure 14:*** *Manufacturing of hygromorphic bilayer wall elements (source: ICD University of Stuttgart, 2019)*



## 3.1 Designing with timber

### 3.1.1 Deployable structures

While the primary outcome of this paper is not the design and validation of a large-scale deployable structure, hygromorphic bilayers still remain relevant as a future application to these systems. The computational workflows are therefore developed to support this intention, positioning the research in a broader context. They provide a means for predicting curvature behaviour and determining the required dimensions, thicknesses, and fibre orientations necessary to potentially design free-form, deployable shell geometries.

This core intention is rationalised by the intensive material use and complexity of modern deployable systems, which rely on a vast number of elements and unsustainable materials such as glass, steel, and aluminium (Hanaor & Levy, 2001). Existing deployable systems encompass a broad range of mechanisms, with some of the more significant categories including lattice bar structures, foldable plate systems, tensegrity frameworks, membrance structures, and smart-material systems (Averseng & Dubé, 2012; Doroftei & Doroftei, 2014; Fenci & Currie, 2017; Hanaor & Levy, 2001). These typologies rely on principles of kinematic activation, material deformation, and structural equilibrium to achieve reversible deployment across varying scales, and are explored in greater detail in appendix 1 (A.1).

The behaviour of hygromorphic bilayers falls into the category of smart-materials, as they leverage passive material behaviour to deploy, rather than relying on mechanical joints, motorised activation, or manual

labour. Given that curvature is generated independently by the bilayer as the timber absorbs or releases moisture (Wood et al., 2018), additional elements or labourers are not required to expand the structure and curve it into a final form. For conventional deployable materials, like glass, steel or aluminium, achieving this same curvature as a kit-of-parts demands forced manual deformation. This process requires far greater energy than the production and passive curving of timber (Shames et al., 2011; see figure 15), presenting a significant environmental advantage for maintaining lower embodied energy.

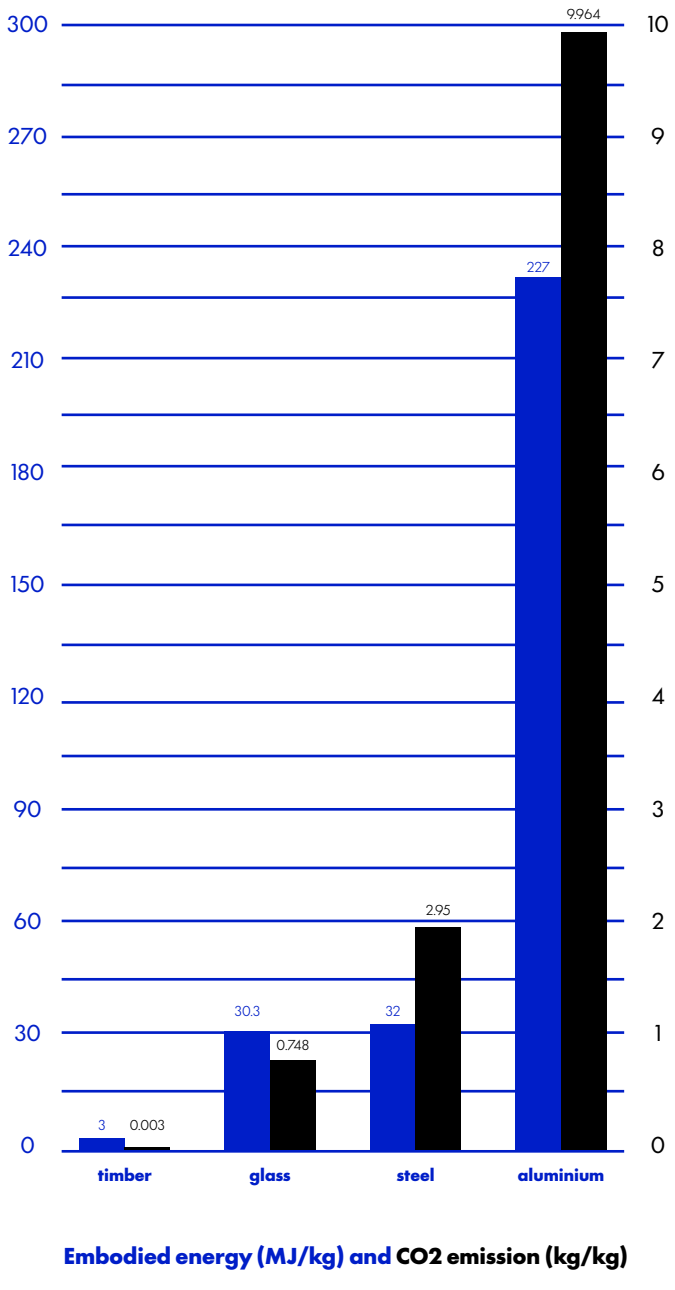


***figure 15:*** *Embodied energy and CO2 emission comparison table (source: adapted from Shames et al., 2011)*

## 3.1.2 Material properties of timber

As a hygroscopic material, timber is able to passively exchange moisture with its environment in response to fluctuations in relative humidity. The intake of moisture triggers dimensional expansion within the wood's cellular structure, inducing a state of flexibility and greater transformative potential. For centuries, this characteristic has been adopted for practical applications in traditional craft and manufacturing, most notably in shipbuilding, passive joinery, and furniture design (Salzberger, 2024). However, while the practical application of wood behaviour is rooted in ancient tradition, a researched understanding on how the structural composition of timber supports this behaviour has only emerged recently. This first chapter will elaborate on the cellular structure of timber, how it achieves water absorption and storage, the measurement of moisture content, and the anisotropic properties of timber that influence its expansion.

### The cellular structure of timber

As is the case for many other bio-materials, wood can attract water molecules from the surrounding environment and absorb them within its material structure. This process is facilitated by the microscopic composition of cellulose, hemicellulose, and lignin in different patterns along the cell walls of the timber (Zhan et al., 2023). The hierarchical composition of these three biopolymers also helps support the structural integrity of the cell wall, and directly affects the degree and direction of hygroexpansion (referring to the dimensional expansion or contraction of a material as it absorbs or releases moisture).

Cellulose is a linear polysaccharide (a type of complex carbohydrate), comprised of 3000 or more glucose units, assembled into an orderly structure of long chains, which are bundled to form microfibrils (microscopically narrow thread-like strands). These microfibrils serve as the primary structural support in tissues and cells, providing tensile strength to the cell wall and playing a key role in tissue homeostasis.

Lignin is a polymer which constitutes one-fourth to one-third of the total dry weight of trees, and binds the cellulose fibres to provide rigidity, and a resistance to

degradation.

Finally, hemicellulose is a softer biopolymer that surrounds and interacts with the cellulose microfibrils, serving as a matrix that binds and spaces them. This contributes to the flexibility of the timber's microstructure, and its capability to transfer loads (Zhang et al., 2022).

Plant cell walls are assembled by the cellulose, hemicellulose and lignin across different cell wall patterns, where the most critical aspect of each biopolymer, in relation to its impact on the hygroexpansion of timber, is its degree of structural stiffness. The cellulose fibrils are embedded in a softer matrix of hemicellulose and lignin across multiple secondary wall layers (see figure 16), where cellulose exhibits a degree of stiffness of approximately 134 gigapascals (GPa), while the lignin and hemicellulose are considerably more compliant at 2 GPa and 0.02 GPa, respectively (Zhan et al., 2023).

The considerable difference stiffness results in a composite structure where high-stiffness cellulose microfibrils are embedded within a "softer" lignin and hemicellulose matrix that is organized across the multiple layers of the secondary cell walls. (Zhan et al., 2023).

Ultimately, at the microscopic scale, each individual cell wall functions as a complex and sophisticated composite, where the mechanical properties of the cellulose, hemicellulose, and lignin all exhibit varied degrees of stiffness. Given that the cellulose microfibrils act as the primary structural reinforcement, they exhibit a very high degree of stiffness approximating 135 gigapascals (GPa), whereas in contrast, the surrounding matrix of hemicellulose and lignin is significantly more compliant. The lignin exhibits an approximate stiffness of 2GPa, while the hemicellulose exhibits a much lower value of around 20 megapascals (MPa) (Zhan et al., 2023). Understanding this interaction is critical, as the swelling of the softer matrix against the stiff microfibrillar skeleton ultimately drives the hygroscopic shape-changing behaviours observed in hygromorphic materials.

**Water absorption and storage**

In wood, water can be present in two primary forms depending on its location within the hierarchical macrostructure. This is either as "bound water" within the cell walls, or as "free water" contained in the macro-voids of the

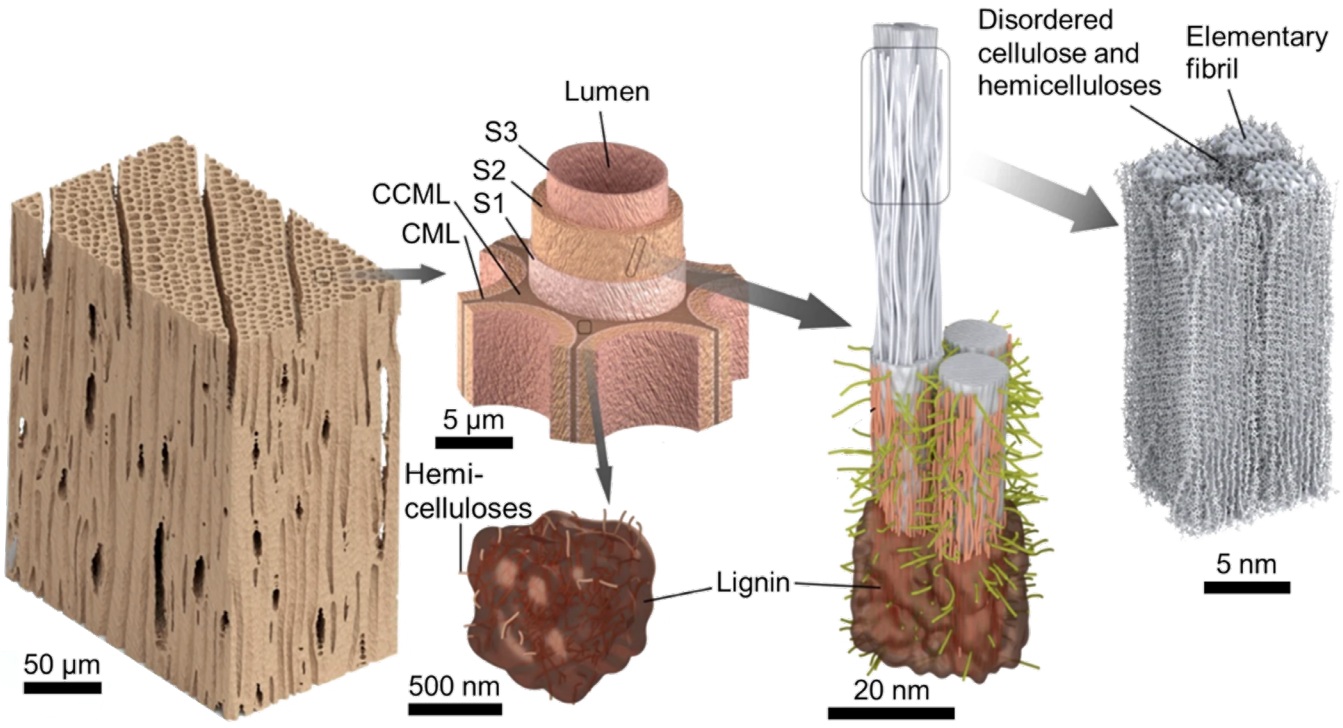


***figure 16:*** *Cellular breakdown of softwood, where the secondary cell walls (S1, S2, and S3) are nanofibre reinforced composites of cellulose fibrils embedded in an organized matrix of amorphous hemicellulose and lignin. (source: Jakes et al., 2020)*

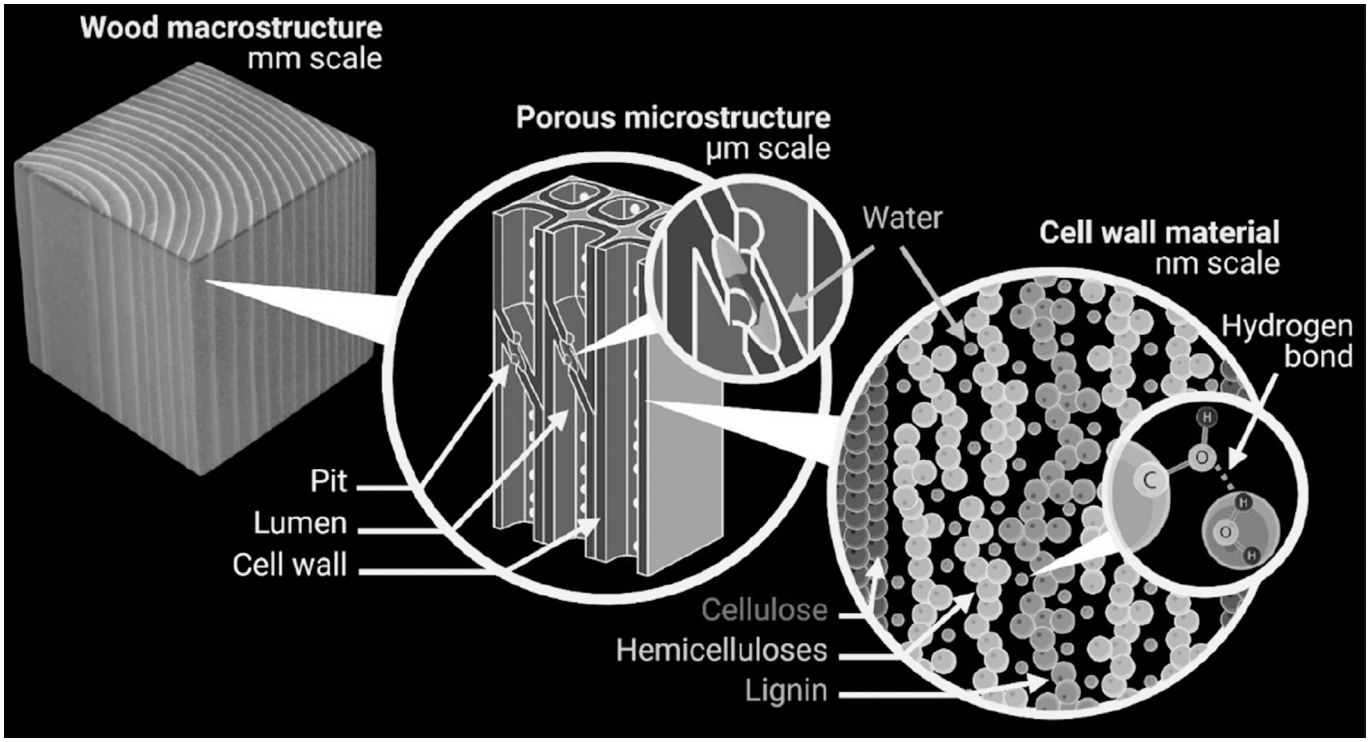


***figure 17:*** *Water present across different locations in wood, including bound water in the cell wall, and free water found in lumina and pits. (source: Thybring et al., 2022)*

lumen – which refers to the void spaces located in the interior of wood cells, between the cell walls (see figure 17).

The process of absorbing bound water directly into the cell wall matrix is attributed to the hydroxyl groups of the cell wall polymers (the cellulose, hemicellulose, and lignin), which capture water molecules through hydrogen bonding and store them within extremely small nano-pores.

As the cell walls are composed of microscopic fibrils and amorphous regions (as a result of the soft matrix), bound water below the fibre saturation point will occupy nano-pores and inter-fibrillar spaces to a range below the fibre saturation point of around 27-30%. The process of hydrogen bonding between the hydroxyl groups and the absorbed water causes the cell walls to swell as it becomes hydrated. (Reichert et al., 2015).

At any point below the fibre saturation point, which typically occurs within a timber moisture content range of 27-30% moisture content with a relative humidity of around 95-98%, the absorbed water will be stored as bound water and occupies nano-pores within the inter-fibrillar spaces of the compliant hemicellulose-lignin matrix. This process of moisture uptake and storage is achieved through hydrogen bonding between the hydroxyl groups of the cell wall polymers (the cellulose, hemicellulose, and lignin) and the incoming water molecules. Cellulose and hemicellulose have a higher content of hydroxyl groups than lignin, but interactions occur most readily with the hemicellulose hydroxyls, rather than the cellulose. This is due to the crystalline form of the cellulose microfibrils which make it impenetrable to water. (Stagno et al., 2022).

As these water molecules are drawn into the nano-pores between cellulose chains, they exert an internal swelling pressure that results in a molecular displacement, forcing the microfibrils further apart. The result is a macroscopic volumetric expansion and dimensional transformation that is characteristic of hydrated timber (Reichert et al., 2015).

Beyond the fibre saturation point, the maximum amount of bound water has been absorbed. Any additional water will be stored as free water in the macroscopic cavities of the wood, including the cell lumina, pits, and vessels. This is generally referred to as the over-hygroscopic range and relates to the relative humidity of the surrounding climate.

Across the full range of relative humidity values (0-100%), the hygroscopic range extends from 0% to approximately 95-98% relative humidity. Within this range, water is stored primarily within the wood cell walls, whereas

in the over-hygroscopic range – extending from around 95-98% to 100% for full saturation – the additional water is stored as free water (Thybring et al., 2022).

This differentiation is important as it reflects a change in the dominant sorption mechanisms (see next section) of the timber, how the water is stored, and how that influences the microstructure. When compared to bound water, free water has only a minor influence on the overall structure of the timber as it doesn't deform the cell walls, and instead remains bound to the cavities and voids through surface tension (Reichert et al., 2015).

**Moisture content**

The dynamic between water absorption, storage, and desorption are reflected in sorption isotherms, which graph the equilibrium moisture content (EMC) of wood as an interlinked function of the surrounding relative humidity. This represents the fundamental framework for understanding the behaviour of moisture exchange between wood and its environment.

The moisture content of wood is defined as the percentage between the mass of water and the mass of oven-dry solid wood material, completely devoid of any water content (see figure 18). While more specifically the

$$w = \frac{m_{wet} - m_{dry}}{m_{dry}} \times 100$$

***figure 18:*** *Moisture content ratio where,* ***w*** *is the moisture content,* ***m****wet is the mass of the wood before drying, and* ***m****dry is the mass of oven-dried wood material (source: own work)*

EMC is the moisture level of the timber when it is perfectly balanced with the surrounding climate; neither gaining nor losing moisture over time (Thybring et al., 2022).

The isotherms are non-linear graphs, and their results are species-dependent, reflecting the differences in wood density, anatomical structure, and chemical composition. As stated earlier, timber experiences a hygroscopic range and an over-hygroscopic range, which also impact the dominant sorption mechanisms and result in a varied logarithmic graph.

Water sorption and capillary movement is differentiated between softwoods and hardwoods due to their anatomical structure (Xhexhi & Aliaj, 2025). Softwoods, such as fir and pine, have larger lumens, thus enabling more rapid water sorption and movement through capillary action but with a reduced capability to wick water through their cell walls. Conversely, hardwoods like beech and oak, have a denser cellular structure, resulting in a slower initial uptake of water (due to the dense structure of the cell wall) but a larger capacity to wick water through the hydrogen bonding of hemicellulose hydroxyls (Stagno et al., 2022).

One of the added complexities to the content of water within the cellular structure of timber is that the state of moisture within the cell walls is path-dependent. This means that the moisture content being in equilibrium with a specific relative humidity depends not just upon the level of relative humidity, but also on whether the wood approached equilibrium by desorption or absorption (Thybring et al., 2022). This path dependence is termed "sorption hysteresis", and a long-standing explanation for this behaviour relates to the availability of sorption sites for water, and how it varies between dry wood and wet wood. As wood dries, the cellular structure shrinks and the hydroxyl groups in the hemicellulose are freed from the water, causing them to re-attach to each other and therefore reducing the number of sorption sites.

Conversely, during the water sorption process - as wood re-wets itself - the number hydroxyl groups available are fewer than when compared to timber that has already absorbed moisture and has expanded (due to hemicellulose being attached to each other). As the moisture content increases, more energy is required to swell the structure of the cell walls and force pairs of hydroxyl groups to split to allow for more sorption sites for the water to bond to (Patera et al., 2016).

Given this behaviour, this paper only explores bilayer curvature for absorption and ignores the behaviour for desorption. These discrepancies are noted in sorption isotherms, which display a slightly varied logarithmic graph

to differentiate the higher moisture content during desorption versus a lower moisture content during absorption at the equivalent relative humidity (see figure 19).

Temperature also plays a significant role in the plotting of sorption isotherms, as it impacts the thermodynamic equilibrium between the water vapour in the air and the water held by the wood. A 2016 research paper (Simón et al., 2016) found that for sorption isotherms plotted at different temperature for the same wood species, the EMC decreased as the temperature increased for a constant relative humidity. This indicates that wood holds less moisture at higher temperatures when under the same humidity conditions. An explanation to this behaviour is that higher temperatures reduce the tendency for water molecules to bind to sorption sites in the cell wall polymers as they are too energetic, thus reducing moisture uptake.

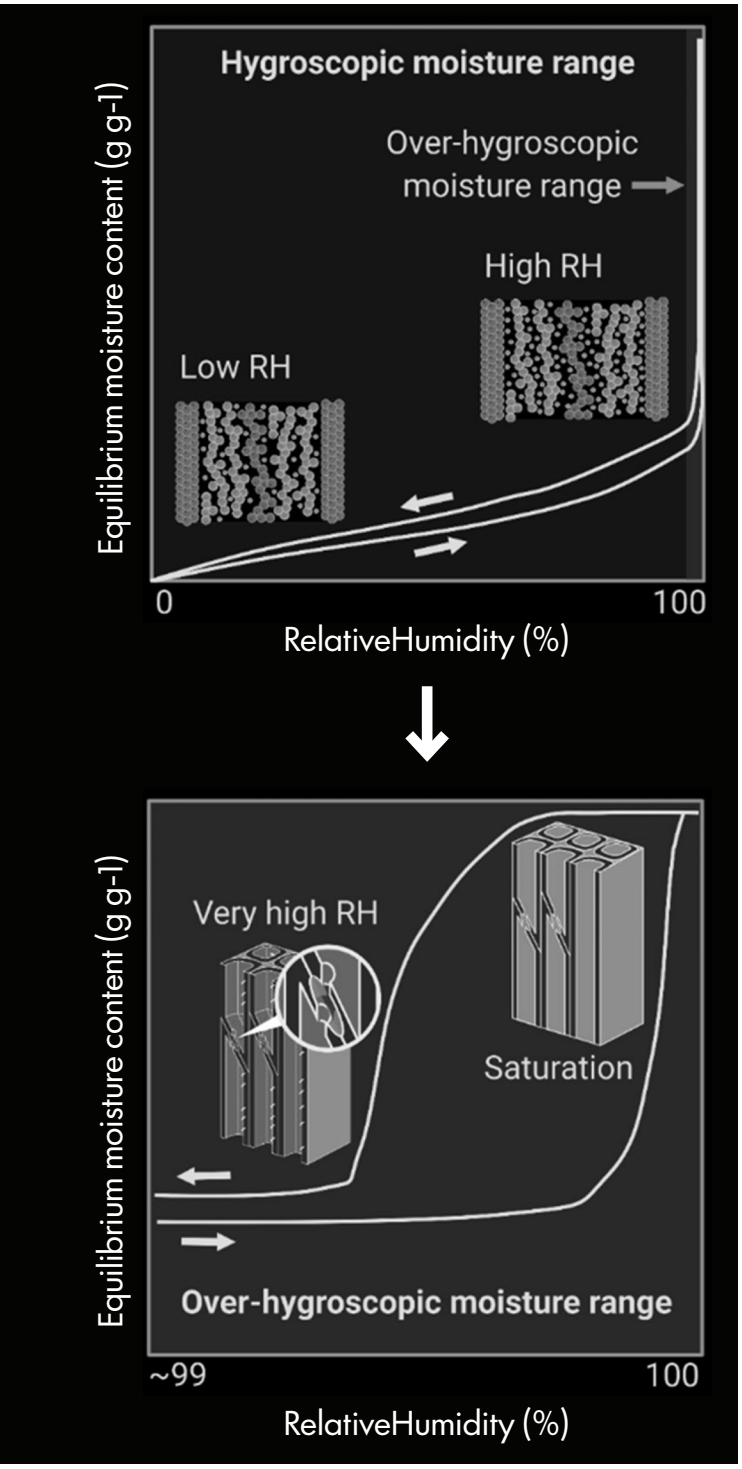


***figure 19:*** *Schematic of sorption isotherms for absorption (diagonal up arrow) and desorption (diagonal down arrow), with a zoom of the over-hygroscopic moisture range (bottom diagram). Vertical difference between the two graphs indicates the sorption hysteresis (source: Thybring et al. 2022)*

**Hygroexpansion of timber**

As an over-arching term, anisotropic materials exhibit different mechanical properties depending on the direction of the forces or stresses applied to them. When timber absorbs water, its volume increases and the cell wall is expanded as the hydroxyl groups bond with the water; commonly referred to as swelling. Conversely, as the water evaporates, the wood's dimensions and volume will decrease through a process of shrinkage.

For timber, the processes of swelling and shrinking are not proportional in all directions. When subjected to hygroexpansion, the deformation of timber varies specifically along three mutually perpendicular planes, meaning that timber exhibits orthotropic properties (a sub-category of anisotropy). These orientations refer to the longitudinal, radial and tangential directions, and they relate to the timber's fibre orientation and the position of its growth rings (Thybring et al., 2022).

Longitudinal expansion, which occurs parallel to the wood fibres, is the smallest deformation and typically exhibits linear swelling ranging from about 0.1-0.3%. This occurs as the rigid cellulose microfibrils – that dominate the tensile behaviour of timber – are oriented along the longitudinal axis, resulting in high levels of stiffness and strongly constrained dimensional change (Avramidis, 2004).

Alternatively, when timber experiences radial expansion, occurring from the centre of the log (the pith) to the outer bark, and tangential expansion, which is exhibited along the curvature of the growth rings, the degree of swelling or shrinkage is much larger. In these directions, hygroexpansion is governed by the expansion of the cell walls – which results

in an increased distance perpendicular to the cellulose microfibrils, as water molecules cannot penetrate them. This indicates that transverse expansion is not governed by the microfibrils and is therefore not constrained by them in the same way longitudinal expansion is constrained (Thybring et al., 2022).

When compared, the tangential expansion generally displays the greatest degree of expansion – within a range of around 6-12% – while radial expansion exhibits a swelling range of 3-6% (both still considerably greater than longitudinal expansion) (Avramidis, 2004) (see figure 20). It is still not clearly understood what causes the discrepancy between the two transverse directions.

As a consequence of the timber's orthotropic expansion and the differing degrees of deformation in each direction, the original location that a timber plank was cut from - in relation to the log - heavily influences the final form and direction of deformation as the plank absorbs or release moisture (Avramidis, 2004) (see figure 21). Even independent planks that remain unlaminated can experience cupping, twisting, and bowing across their length if they are dried unevenly.

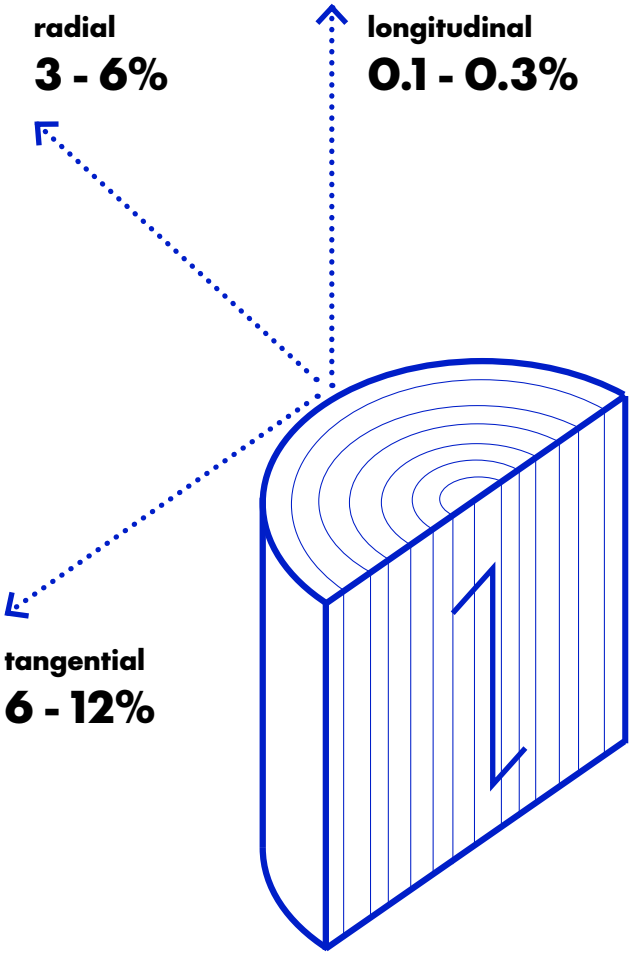


***figure 20:*** *Diagram indicating direction and degree of expansion in the longitudinal, radial, and tangential directions (source: own work)*

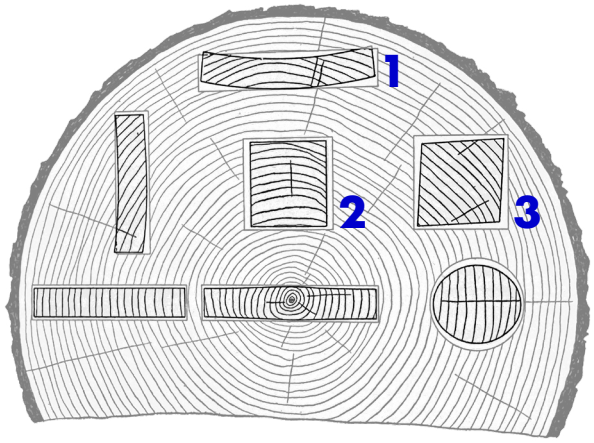


***figure 21:*** *Plank deformations relative to their position on the log. (1) cupping, (2) cross grain shrinkage, (3) diamonding, (4) cylindrical shrinkage (source: Rowell, 2012)*

## 3.2.2 Hygromorphic bilayers

The study and optimisation of hygromorphic bilayers has grown rapidly in recent years, with research ranging across fields like wood science, material mechanics, and computational modelling. These engineered composite systems exploit the inherent moisture-driven swelling and shrinkage of timber to produce predictable and reversible shape changes in response to fluctuations in relative humidity.

This mechanism relies on the differential hygroexpansion between two bonded wood layers, where one layer primarily drives the expansion or shrinking - referred to as the "active" layer - and the other restricts the movement - referred to as the "passive" layer. This imbalance induces bending, twisting, or other curvatures, enabling autonomous movement without the need for external energy or mechanical actuators.

### Species selection for panels

When selecting wood types, it is important to make a distinction between hardwoods and softwoods as

their dissimilar cellular compositions significantly impact the moisture-induced deformation of a panel, and the interaction between the two bonded layers.

Hardwoods, originating from flowering plants, are highly porous when compared to softwoods, allowing water to infiltrate more readily into the cell walls. They also have a higher hemicellulose content, and therefore their cell walls can reach greater hydration through the binding of water molecules to the hemicellulose hydroxyls, resulting in substantial swelling (Stagno et al., 2022). This makes hardwoods particularly suitable as the active layer, where greater expansion or contraction is desired.

In comparison, softwoods mostly originate from conifers and contain tracheids – elongated, tube-like cell voids that function for water transport and structural support – rather than open pores. While this provides adequate structural stiffness, it results in a lower density of cellular wall structure for hydroxyl bonding and expansion, leading softwoods to exhibit a smaller tendency to swell when absorbing water. This makes them very effective as the passive layer (see figure 22), providing restraint and stability to the bilayer to induce curved deformation (Abdelmohsen et al., 2019).

**Moisture conditioning of wood boards**

The core principle of hygromorphic design relies on the bonding of two wood layers with distinctly different expansion coefficients. While this is achieved by pairing hardwoods and softwoods, actively encoding the bilayer's moisture-driven motion requires precisely setting the moisture content of each layer prior to lamination. This bonding process effectively seals the humidity differential between the layers, helping to program the eventual deformation of the overall system (El-Dabaa & Abdelmohsen, 2023).

Depending on the desired relative humidity for actuation, the timber panels are first conditioned through drying or humidification to a carefully controlled moisture content level that reflects the humidity range in which the bilayer is intended to operate.

In humid, tropical regions, the relative humidity will naturally be higher, generally ranging from around 70% to 90%, while in very dry regions, the relative humidity usually remains below 40%. The conditioning process is typically done in climate-controlled chambers, with the active layer reaching a moisture content level that will respond strongly to humidity changes later. The passive layer is also conditioned,

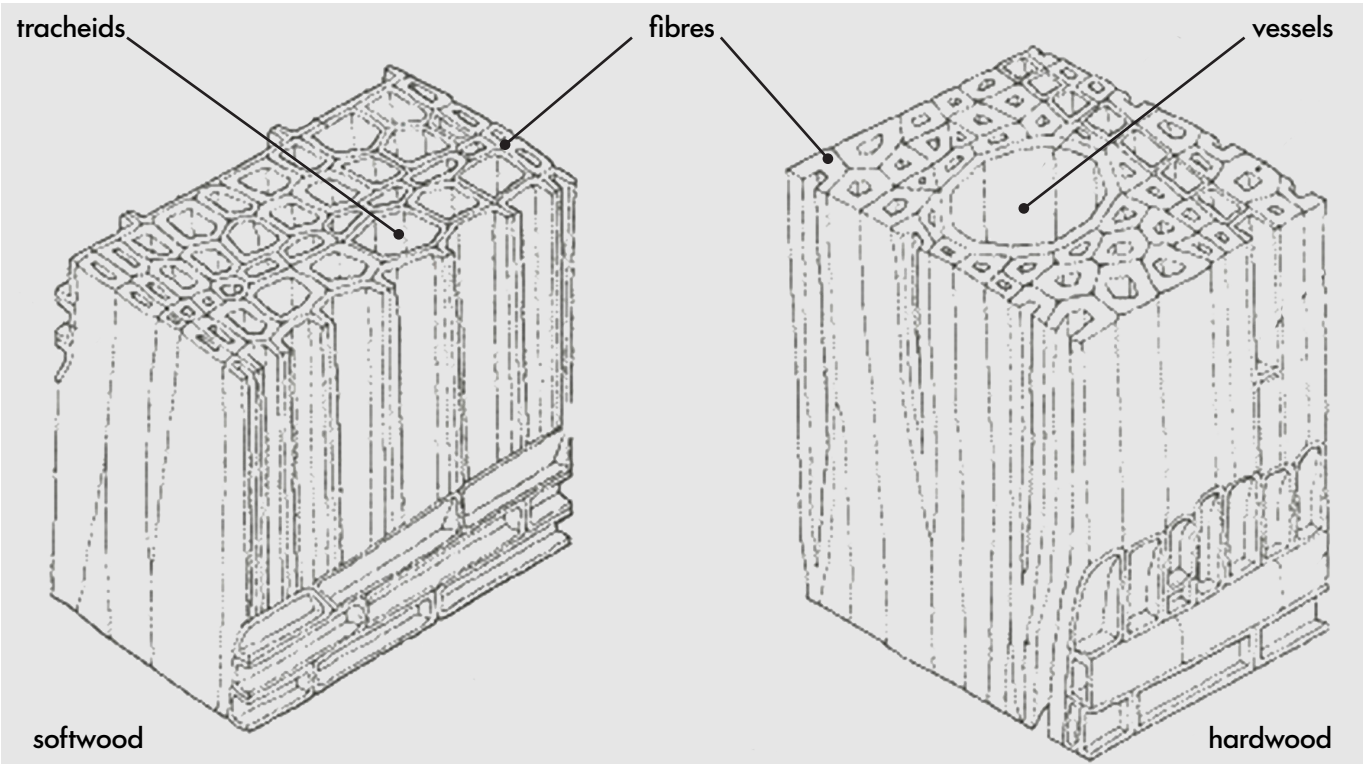


***figure 22:*** *Diagram representing the differences in microscopic structure between softwoods and hardwoods (source: Ibitolu, 2018)*

but to a lesser extent; resulting in smaller, more stable swelling or shrinking. Once the two layers are laminated, the moisture imbalance is locked into the composite (Kiesewetter et al., 2025).

Conditioning the panels to the desired initial moisture content is critical for their performance in different climates: for drier environments, if both layers are overly dry at the time of bonding, subsequent moisture-deformations may be too small to generate the desired curvature. Alternatively, in more humid climates, overly saturated panels will lead to a reduced quantity of moisture-uptake, leading to diminished swelling. Therefore, moisture conditioning must consider the desired humidity for activation, to ensure bilayers achieve significant swelling or shrinkage (Wood et al., 2020; Kiesewetter et al., 2025).

**Cutting of lumbar**

In earlier sections it was discussed that the direction of the wood's grain and the layering of growth rings influenced the degree deformation across three mutually perpendicular directions; the longitudinal, radial and tangential orientations. As a result, given that orthotropic swelling is locked into the timber's very anatomy, different cutting methods will result in planks that exhibit very different curvatures and deformations.

As a general rule, wood first begins to shrink along the outer surface (closest to the bark), with the inner parts shrinking later (Swedish Wood, n.d.). In veneer and board production, quarter-cutting results in a log being cut to quarters and planks sliced at a perpendicular angle to the growth rings (see figure 23). In this form, the tangential length of the board's section is shorter while the radial length is longer, resulting in reduced hygroscopic deformation.

For plain-cut veneers, the log is sliced in half and cuts are carried out parallel to the initial division (see figure 23). This exposes the boards to a greater tangential length, and narrower radial length – especially for boards cut from the outermost edges – resulting in larger moisture-induced swelling and shrinkage, often leading to bending or cupping.

Rotary-cut veneers follow the circumferential path of the log, maximising the tangential orientation (see figure 23). Naturally, this usually results in the greatest degree of hygroexpansion with the most pronounced shape-change

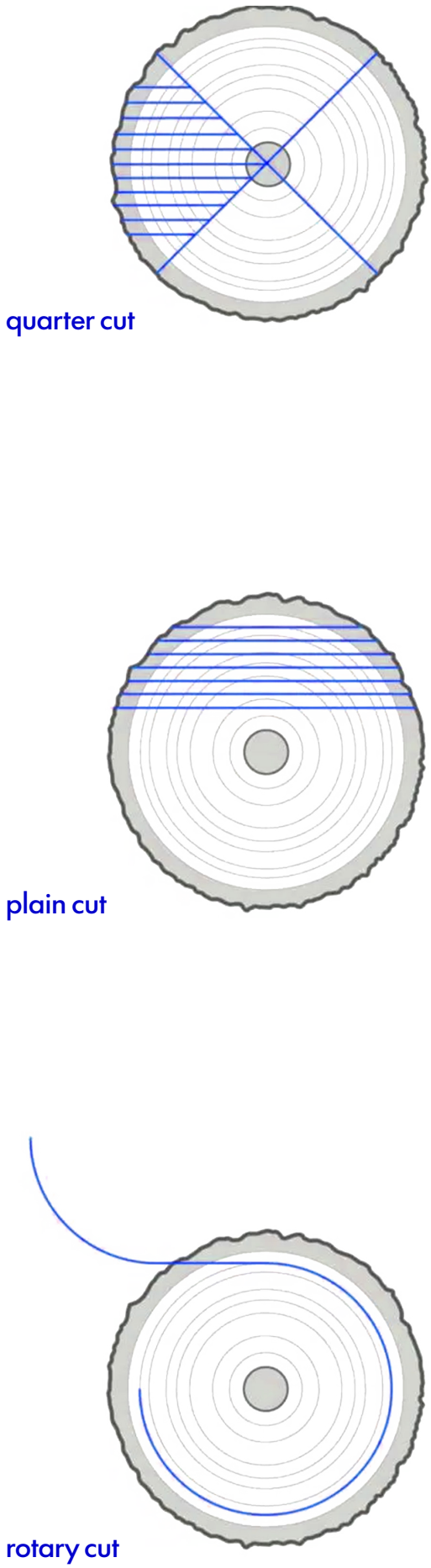


***figure 23:*** *Diagrammatic representation of different timber cuts for planks (source: Todd, 2018)*

(El-Dabaa & Abdelmohsen, 2023).

Although the different timber cuts are useful to determine which planks will achieve the greatest deformations, linking grain orientation to the radial and tangential angles, rather than through visual assessment, helps to define the orientation of fibres in a plank more clearly. The angle is derived between the grain and the short axis of a sample; for example, in a rectangular sample, fibres at 0° are parallel to the short axis, while fibres at 90° are parallel to the long axis. Fibres at 45° represent the diagonal of the sample.

Numerous research papers found that samples with 0° grain orientation had the fastest response speed associated with the highest curvature, followed by samples with 45° grain orientation, and finally samples with 90° grain orientation (El-Dabaa & Abdelmohsen, 2023; Abdelmohsen et al., 2019).

## Constructing bilayer panels

Hygromorphic bilayers are composed of two wood layers with contrasting hygroscopic responses, arranged as an active layer and a passive layer, to purposefully generate curving deformations as a result of the imbalance in their swelling and shrinking coefficients.

The active layer is usually made from a specific wood specie or following a specific cut that allows for a high degree of hygroscopic swelling – often being a hardwood such as beech or maple, or a softwood veneer oriented tangentially (although this is used less commonly). This ensures the active layer will absorb or release moisture more readily and exhibit significant dimensional change perpendicular to the fibre direction. Alternatively, the passive later is selected for its comparatively lower degree of moisture deformation, resulting in greater dimensional restraint. Softwoods, such as spruce, fir or pine, are commonly used for this layer (Abdelmohsen et al., 2019).

When positioning the two layers, it is important to ensure there is a differential grain orientation between them (see figure 24). The active layer should be oriented so that maximum swelling or shrinkage occurs along the axis where curvature is desired, while the passive layer must be oriented with its grain direction at an orthogonal (90 degree) angle to the active layer so as to resist the expansion (Peng et al., 2023; Reichert et al., 2015). This arrangement ensures that when changes in humidity trigger swelling or shrinking, the active layer undergoes significant hygroexpansion, while the passive layer exhibits minimal deformation along that same axis, leading to an imbalance in strain that is necessary for bending.

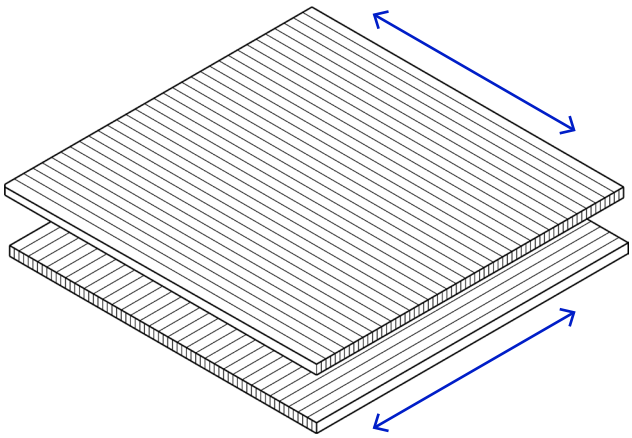

***figure 24:*** *Orthogonal fibre orientations for a hygromorphic bilayer (source: own work)*

As a comparison, if we consider two layers that are oriented in the same fibre direction, their degree of expansion would be much more uniform – even for the different expansion coefficients of hardwood versus softwood – leading to parallel deformation and little, to almost no, curvature.

## Adhesives

Adhesive wood bonding is used widely in the production of engineered wood composites and wood products such as furniture, flooring, and glue-laminated timber (GLT). It is crucial that the adhesive bonding ensures the transfer of stress from one layer to the next, and maintains its bonding strength over an extended period of time.

Wood moisture content is a critical factor in the physical processes and chemical reactions of adhesives as they cure and bind adherents. Moisture content directly affects how the adhesives penetrate into the wood's cellular structure and how it cures, therefore influencing the strength of the wood bond. A high content of moisture in wood causes cavities to be filled in the cell walls which reduces the adhesive penetration, or it can lower the viscosity of the adhesive, leading to excessive penetration and increased

curing time, which makes the bond strength weaker. For an adhesive to set properly, the solvent needs to flow away from the adhesive and into the adjoining cell walls of the timber adherent, where it will set and cure into the cellular structure. As a result, most bonding processes require the wood to be at a certain moisture content level.

A 2024 research paper by Tran et al. assessed structural adhesives such as melamine-urea-formaldehyde (MUF) and one-component polyurethane (1C PUR), which are commonly used to bond wood products. The setting reactions of formaldehyde-based adhesives, involve polycondensation reactions (a process by which small molecules link together to form polymer chains while releasing byproducts) that release water. As a result, chemical reactions can be slowed down by the presence of excessive moisture in the wood. In addition, the availability of water during the curing process influences the mobility of polymer chains, which can modify the product distribution of the formaldehyde-based adhesive (Tran et al., 2024). In the context of isocyanate-based adhesives, such as 1C PUR, their curing process requires a minimum amount of water to activate. The isocyanate needs to react to water in the wood, making it more tolerant to timber with higher moisture content than water-based adhesives. Water borne adhesives that cure through chemical reactions without heat are sensitive to rapid water loss, such as when applied to very dry timber, and therefore perform best on wood with a moisture content of 8–12% (Tran et al., 2024). As a result, for the purpose of this research, it would be more effective to use isocyanate-based adhesives in the material testing of bilayers.

**Lamination process**

The lamination process for the bilayers is important for locking the moisture imbalance into the composite. Once the two layers have been conditioned to the desired moisture content level and aligned orthogonally, a layer of water-tolerant structural adhesive is applied between the two layers.

They are then stacked and pressed together, either under light mechanical pressure or in a hot-press, depending on the type of adhesive being used, which ensures penetration of the adhesive through the wood's surface (Peng et al., 2023). This process can take several minutes for hot press or several hours in the case of cold press (Herzog et al., 2021).

## 3.2 Structures of hygromorphic panels

Following the review on different systems and mechanisms of activation, hygromorphic panels fall most closely within the category of smart-material deployable structures, given that their transformation is governed by the inherent cellular structure of the panels, rather than through mechanical joints or external actuation.

As the design of hygromorphic bilayer panels induces continuous bending, their final deployed configurations – when reaching the desired moisture content – results in curved geometry, rather than planar or faceted forms. The differential swelling between the two layers drives the panel towards a state of minimum elastic energy, manifesting as monoclastic or anticlastic curvatures. The third most common form of curvature is synclastic, which can only be achieved with multiple bilayers joined together (Wood et al., 2018).

These curved forms are differentiated by the measure of their Gaussian curvature, K, calculated as the product of the shell's curvature along two primary, orthogonal axes (commonly referred to as principal curvature) (Wood et al., 2018). This governs the shape-finding, design, and structural performance of deployed hygromorphic systems.

### 3.2.1 Classification based on geometric form

In differential geometry, the principal curvatures represent the minimum and maximum values of curvature at a specific point on a shell's surface. The orientation of these curvatures are termed the principal direction, and they are mathematically represented by orthogonal unit vectors called principal vectors (see figure 25).

To determine the values for principal curvatures, a central point on the surface of a shell is selected, and the normal planes generated from that point are used to cut the surface in two perpendicular directions. The curvature of the resulting sections is assigned a sign based on the curve's orientation relative to the surface normal vector: positive for curves concave to the normal, and negative for those convex to it, with a value of zero denoting a straight line. The final Gaussian curvature (K) is derived as the scalar product of these two principal curvature values (Neugebauer et al., 2018).

It is important to note that the actual numerical value of K isn't the most critical element, but rather the sign of the result. Where K is greater than 0 (positive for $K > 0$), the surface is bending with the same sign in both principal directions, resulting in synclastic curvature, and characterised

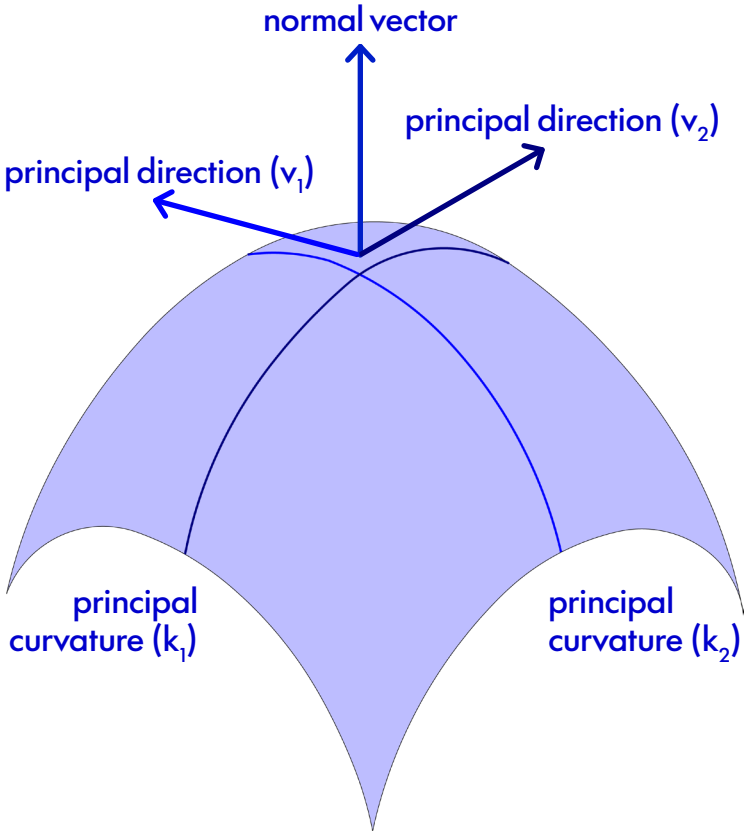


***figure 25:*** *Illustration of principal directions and curvatures on a synclastic shell (source: own work)*

by a dome-like geometry (see figure 26).

Where K is less than 0 (K < 0), the surface is curving in opposite perpendicular directions. This represents anticlastic curvature, resulting in a saddle-like shape (see figure 34).

If K is equal to zero (K = 0), then the surface is exhibiting negligible curvature in one of the perpendicular directions (resulting in a flat line). This is referred to as monoclastic curvature (or single curvature), and is associated with semicylindrical forms (see figure 26) (Vekariya & Makwana, 2021).

### 3.2.2 Structural stiffness and load distribution across Gaussian Curvatures

The Gaussian curvature of a surface alters its structural capabilities and the way it distributes applied loads; a principal that is central to shell theory and validated across mathematical studies (Qatu et al., 2010). The three-dimensional equations of elasticity linked to shell theory are very complicated when written for curvilinear co-ordinates and given that their specification expands into a mathematical research degree – which is beyond the scope of this research paper – the following section follows a more simplified explanation on the effect of loads.

Monoclastic shells, with zero Gaussian curvature, exhibit mechanical behaviour similar to a plate with a singular principal curvature. In these systems, the load-path distribution is constrained primarily along the axis of curvature, thereby inhibiting the potential for bidirectional in-plane force transfer. As a result, they generally deform more under transverse loads, as their mechanical response is dominated by bending moments, leading to greater stresses in specific areas of the structure. This also results in a lower degree of stiffness when compared to other Gaussian curvatures with non-zero curvature. Doubly-curved shells (synclastic or anticlastic) leverage multi-directional curvature to facilitate more efficient membrane-stress distribution through in-plane tension and compression. This increases global stiffness, and reduces the displacement of the shell under equivalent loading (Mahmood & Khalil, 2023).

In the case of synclastic curvature – such as domes – both principal curvatures possess the same sign, creating a biaxial compression field. This geometric configuration facilitates a more uniform distribution of internal stresses by engaging both principal directions as primary load paths. As a result, the structural performance is significantly enhanced; empirical studies indicate that doubly-curved morphologies exhibit superior critical cracking loads and higher post-cracking stiffness in reinforced shells compared to their monoclastic counterparts (Lee, 2024).

For anticlastic curvature, including saddle surfaces with opposing signs for principal curvatures, a couple system

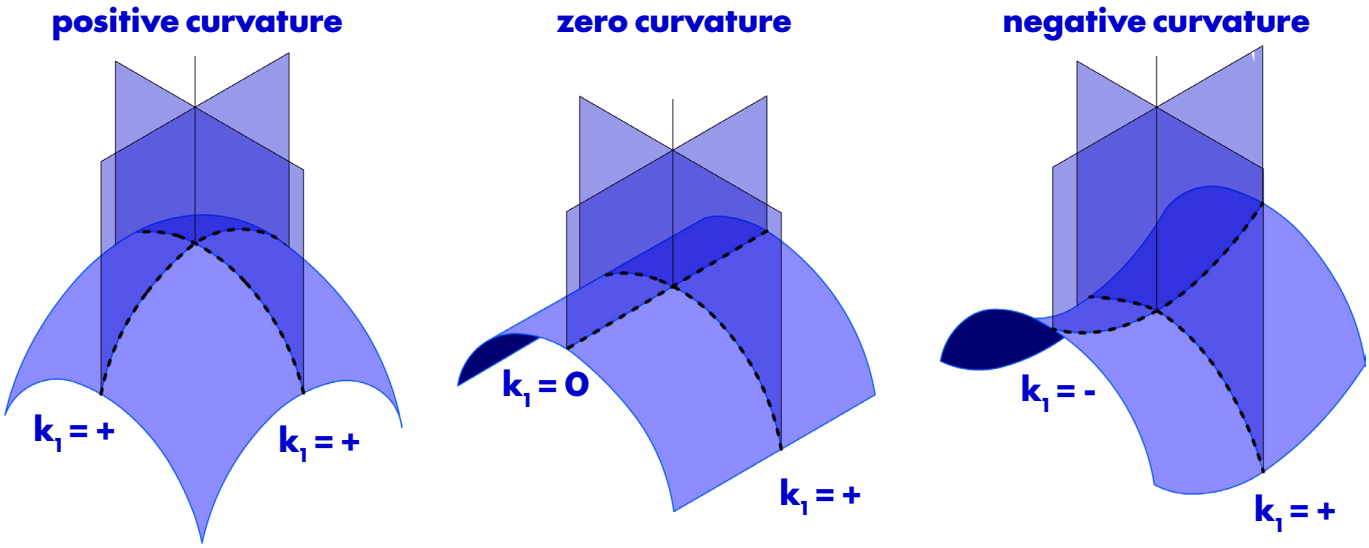


***figure 26:*** *Illustration of different Gaussian curvatures: synclastic, monoclastic, and anticlastic from left to right (source: adapted from Seehanam, 2023)*

of tensile and compressive stresses are generated which enhance structural stiffness and load distribution. The structural integrity of anticlastic shells is more resilient than synclastic as the geometry channels forces through membrane action that resists deformations and distributes stress more easily across the surface (Lee, 2024).

These distinctions are important in architecture as they demonstrate how doubly-curved shells achieve greater stiffness and more efficient load distribution than single-curved shells, with the latter necessitating greater cross-sectional thickness or additional reinforcements to mitigate bending-induced stresses. Although ultimately, despite this distinction, both double and single curvature systems are utilised extensively in contemporary practice, balanced by the trade-offs between form-found structural optimisation and fabrication feasibility.

## 3.3 Simulating bilayer bending

### 3.3.1 Mathematical prediction

In recent empirical research, the most reliable method for predicting the curvature of hygromorphic bilayers is through the adaption of Timoshenko's mathematical formula for bimetallic bending (Wood et al., 2018; Kiesewetter et al., 2025; Zhan et al., 2023; see figure 27). This was originally an analytical approach developed for temperature-driven expansion between two metals with different heat expansion coefficients to determine their degree of curvature as bending occurred. Preceding research on self-shaping wood has adapted and rigorously tested the formula for its validity (Wood et al., 2018; Kiesewetter et al., 2025; Wood et al., 2016).

In the context of moisture-responsive bilayers, the variables for thermal expansion coefficients are exchanged for the swelling coefficients (or more accurately; the coefficient of moisture expansion), which are determined through laboratory settings by measuring the dimensional change in wood samples as a function of their change in moisture content. The moisture content differences between the active and passive layers are applied to the formula, rather than temperature differences (Wood et al., 2018).

Figure 28 presents the adapted Timoshenko formula for timber bilayer bending, where the physical properties considered in the formula are **E**, denoting the Young's Modulus of the two layers, and **a** which denotes the respective differential swelling coefficients; both values of which can be taken from literature or online directories

$$\frac{1}{\rho} = \frac{(\alpha_2 - \alpha_1)(t - t_0)}{\frac{h}{2} + \frac{2(E_1 I_1 + E_2 I_2)}{h}\left(\frac{1}{E_1 a_1} + \frac{1}{E_2 a_2}\right)}$$

$$\frac{a_1}{a_2} = m, \quad \frac{E_1}{E_2} = n,$$

where,

| | | |
|---|---|---|
| [alpha]1 & [alpha]2 | = | coefficients of expansion |
| t & t0 | = | initial and final heating range |
| E1 & E2 | = | moduli of elasticity |
| I1 & I2 | = | second moment of area |
| h | = | overall thickness of the strip |
| a1 & a2 | = | individual metal thicknesses |

***figure 27:*** *Timoshenko's bi-metal formula (source: Timoshenko, 1925)*

$$\frac{1}{\rho} = \frac{6(1+m)^2}{\left(3(1+m)^2 + (1+mn)\left(m^2 + \frac{1}{mn}\right)\right)} \frac{(\alpha_2 - \alpha_1)(c - c_0)}{h}$$

$$= k\frac{\Delta\alpha\Delta c}{h}, \quad m = \frac{h_1}{h_2}, \quad n = \frac{E_1}{E_2}$$

where,

| | | | | | |
|---|---|---|---|---|---|
| p | = | final curvature | E1 & E2 | = | moduli of elasticity |
| [alpha]1 & [alpha]2 | = | differential swelling coefficients | h | = | overall thickness of the strip |
| c0 & c | = | initial & final moisture content | h1 & h2 | = | individual layer thicknesses |

***figure 28:*** *Timoshenko's adapted formula for hygromorphic curvature (source: Kiesewetter et al., 2025)*

like Granta EduPack. The variable **h**, denotes the total thickness of the bilayer configuration (where **h1** and **h2** are the thickness of the individual active and passive layers), while the moisture content is denoted by **c0** at the point of fabrication, and **c** for the final curved state (Kiesewetter et al., 2025).

### 3.3.2 Computational simulation

While the Timoshenko formula is effective for presenting curvature across a range of different timber species and layer thicknesses, it is limited for the design and visualisation of dynamic geometries with different fibre orientations.

To supplement the formula, GH and Rhinoceros 3D can be employed for dynamic and transformative three-dimensional modeling. As a visual coding program, GH offers numerous components that can be interconnected across a wide range of configurations to build up a near-infinite degree of forms and shapes (Rutten, 2026; see figure 29). This allows a bilayer to be modeled in numerous

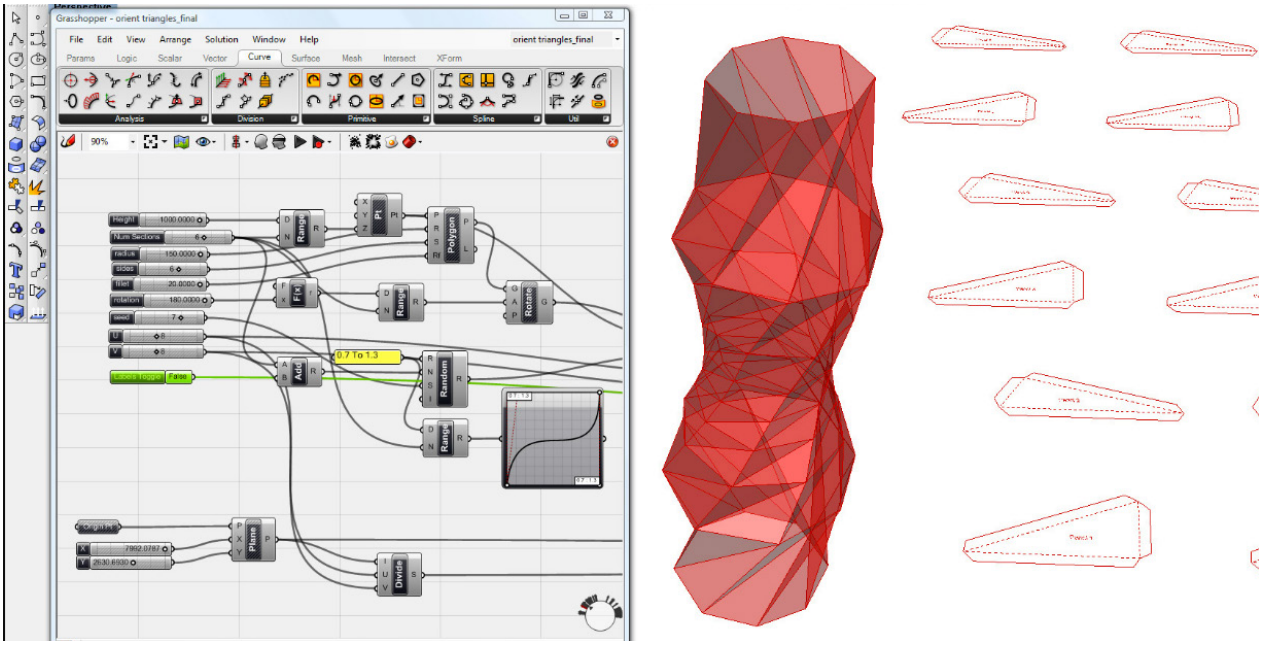


***figure 29:*** *Grasshopper 3D interface with scripting components for parametric modeling (source: Shapeways, 2017)*

different ways, including as rectangular prisms, mesh surfaces, or interconnected system of lines and nodes, which can be re-modeled smoothly with sliders to alter the width, length and height. This level of dynamic modeling is necessary to accommodate the shape-changes that inevitably occur during the curvature simulations.

In constructing the goals for the simulative tool, a key necessity was the inclusion of material data to enable the prediction of curvature across a range of different timber species and dimensions. Within GH, the plugin Kangaroo Physics is an effective tool that allows material data to be encoded into the script to inform the final simulation (Piker, 2017).

Information such as the Young's Modulus and the second moment of inertia for different types of timber help to determine the axial strength and bending strength of the polylines in the digital model (which are representative denominations for the structure of an actual bilayer). As Kangaroo solves for equilibrium, rather than prescribing to a fixed form, it enables the geometry to emerge from the encoded material logic; making it possible to simulate how variations in layer thickness can influence the final curvature.

## 3.4 Reversible locking system for passive curvature

As has been explored in the literature, the timber bilayers will lose or gain moisture as they seek to achieve equilibrium with the surrounding environment. This leads to a natural tendency for the curvature to reverse - and the bilayers to re-flatten - as the relative humidity of the surrounding environment fluctuates.

In certain applications, this behaviour can be desirable, such as in passively responsive external shading systems that adapt to changes in solar intensity throughout the day (Zhan et al., 2023; Cheng et al., 2024). However, for deployable structures intended to function as temporary shelters, it is necessary for the system to maintain its deployed from over an extended period of time and resist the shape changes triggered by fluctuations in relative humidity. The challenge, therefore, lies in developing an integrated locking system that is not only reversible - allowing the structure to be retracted for transport or storage - but also capable of responding passively to the changing geometry of the bilayer.

A very simple, yet highly responsive solution is the implementation of curve-line folding elements, which transition from a flat state into a stable, elevated position as the bilayer begins to curve.

### 3.4.1 Curve-line folding

Origami is a popular Japanese art form based around the concept of folding paper along a pattern of straight lines - without stretching or tearing - to construct complex 3D shapes. A variation on the art form involves the folding of paper along a curved line, rather than straight, in a technique commonly referred to as curve-line folding (Vergauwen et al., 2017; see figure 30). 3D forms are generated when either opposing face along the crease is

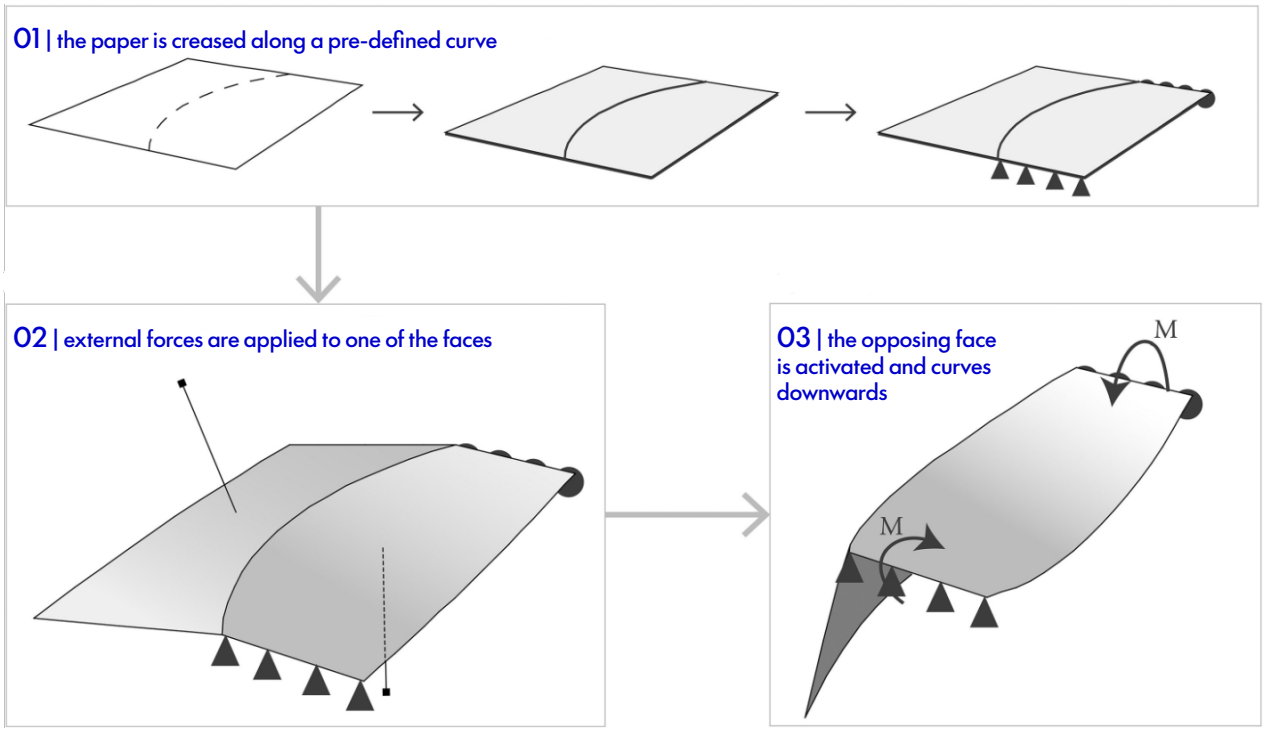


***figure 30:*** *Step-by-step process of curve-line folding deformation (source: Vergauwen et al., 2017)*

mechanically curved into an arc that approximates the shape of the crease. This external force triggers the opposite face to deform along the crease towards the face being acted upon.

Although numerous small-scale models explore the potential of curve-line folding to create visually fascinating 3D shapes, applications extending to contemporary design or in architecture are quite limited due to the complexity of the concept (Vergauwen et al., 2017). Additionally, designing curve-line folding elements for buildings or sculptures will result in static 3D objects that cannot return to their initial flat state. This is due to the plastic deformation at the crease being permanent, unless one of the curved faces is acted upon by a mechanical motion that reverses the curvature of the curve-line element.

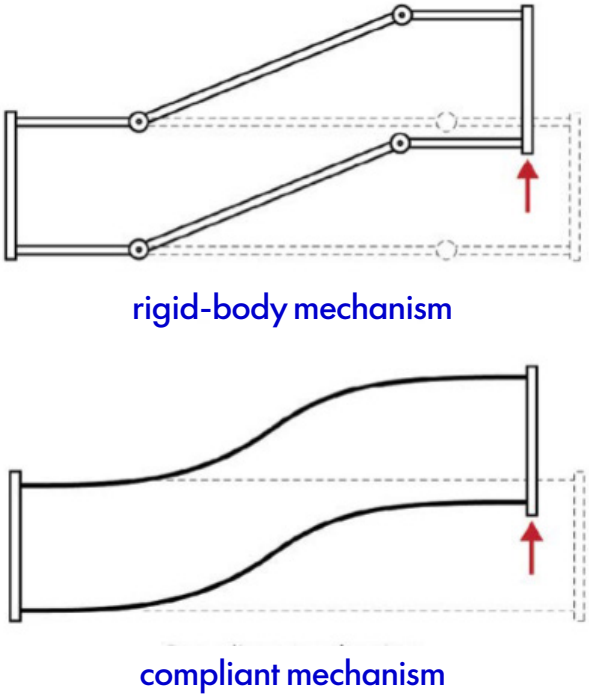


***figure 31:*** *Comparison between rigid-bod and compliant mechanisms (source: Körner et al., 2016)*

## 3.4.2 Compliant kinetic mechanisms

In contrast to conventional rigid-body mechanisms, compliant mechanisms achieve flexibility through the controlled elastic deformation of flexible elements, where only one part of the member exhibits locally defined stiffness (see figure 31). A noticeable advantage of this system is not only the reduction in the number of parts required for deformation, but also the minimization of wear and tear, unlike classical joints that depend on lubrication and regular maintenance (Körner et al., 2016).

A historic example of a compliant kinetic mechanism is the bow, although in modern-day they are generally found at smaller scales, such as in the use of medical devices, or in the packaging industry as snap-locks for plastic containers. Applications at a larger scale are not so common, especially for architecture or building construction (Howell et al., 2013).

To achieve movement in kinetic systems, it is necessary for actuators to transform energy into motion. Hygromorphic bilayers present a passive form of actuation, whereby they transform mechanical energy from moisture-induced swelling or shrinkage into a curving motion (Körner et al., 2016). The entire process of curve-line activation is centred around compliant kinetic systems that achieve their motion from constrained elastic deformation of structural parts (Vergauwen et al., 2017). This presents hygromorphic curvature as a very effective system for triggering curve-line activation as it behaves under the same kinematic mechanisms. As a bilayer panels bends into an arc through differential strain, the curvature that is produced will slowly begin to match the curvature of the curve-line crease. Since curve-line folding relies on this exact curvature from one of the faces to induce angular rotation in the adjacent face, the bilayer deformation works to passively activate the folding behaviour.

However, designing with curve-line activation is still considerably complex due to the interdependency of geometry, forces, and material properties, especially when working with fold lines with multiple degrees of curvature, for example in the case of an annulus with multiple concentric circular fold lines, where little is still known about their activation logic (DeSimone & Teresi, 2025). Conversely, the geometric logic of folding along a single curve is mathematically and practically well understood. To achieve an integrated locking system that is not overtly complex, this paper focuses on the kinematic process of activation for curve-line elements with a single curve of activation.

# SIMULATING MONOCLASTIC CURVATURE

# 004

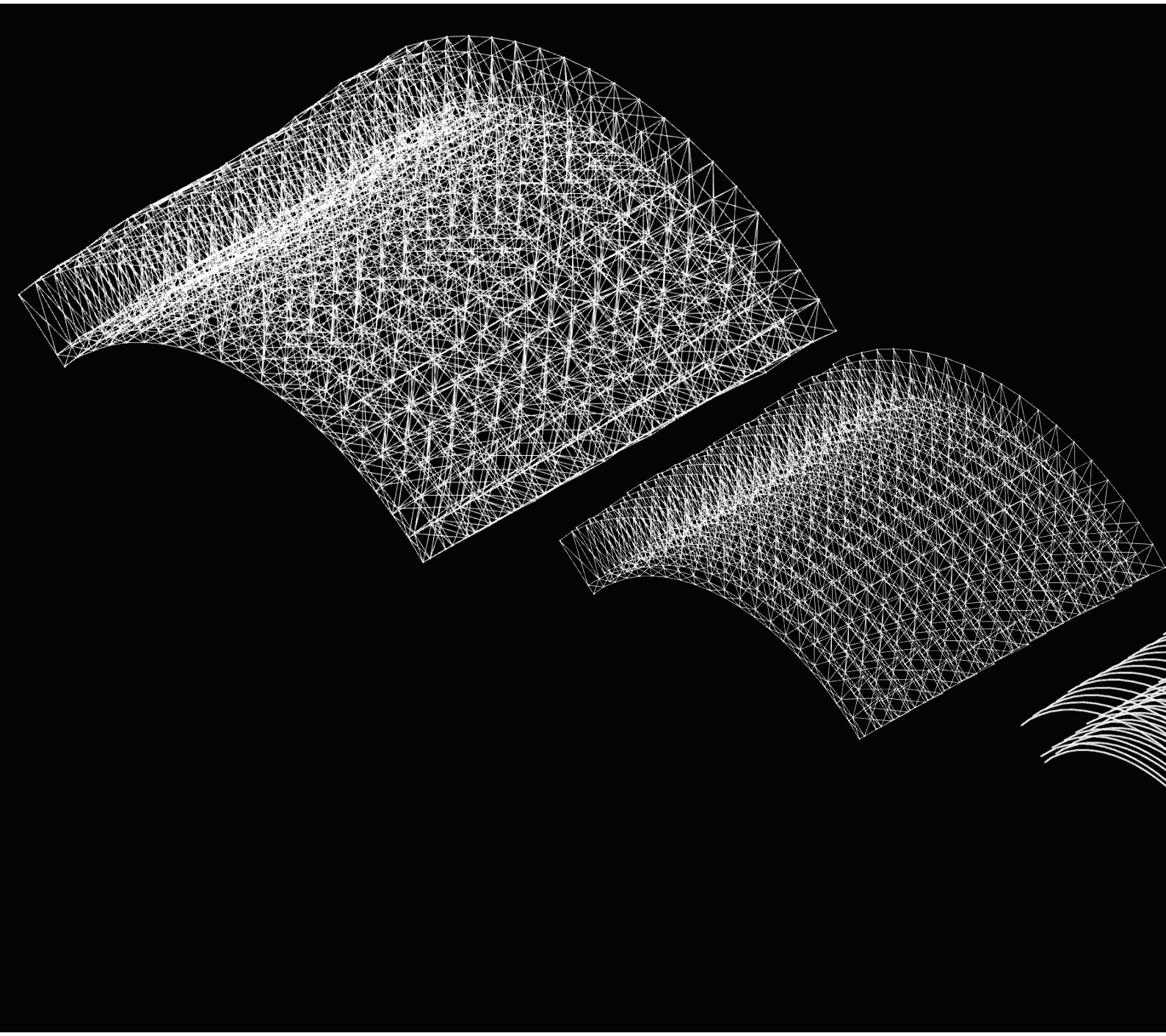

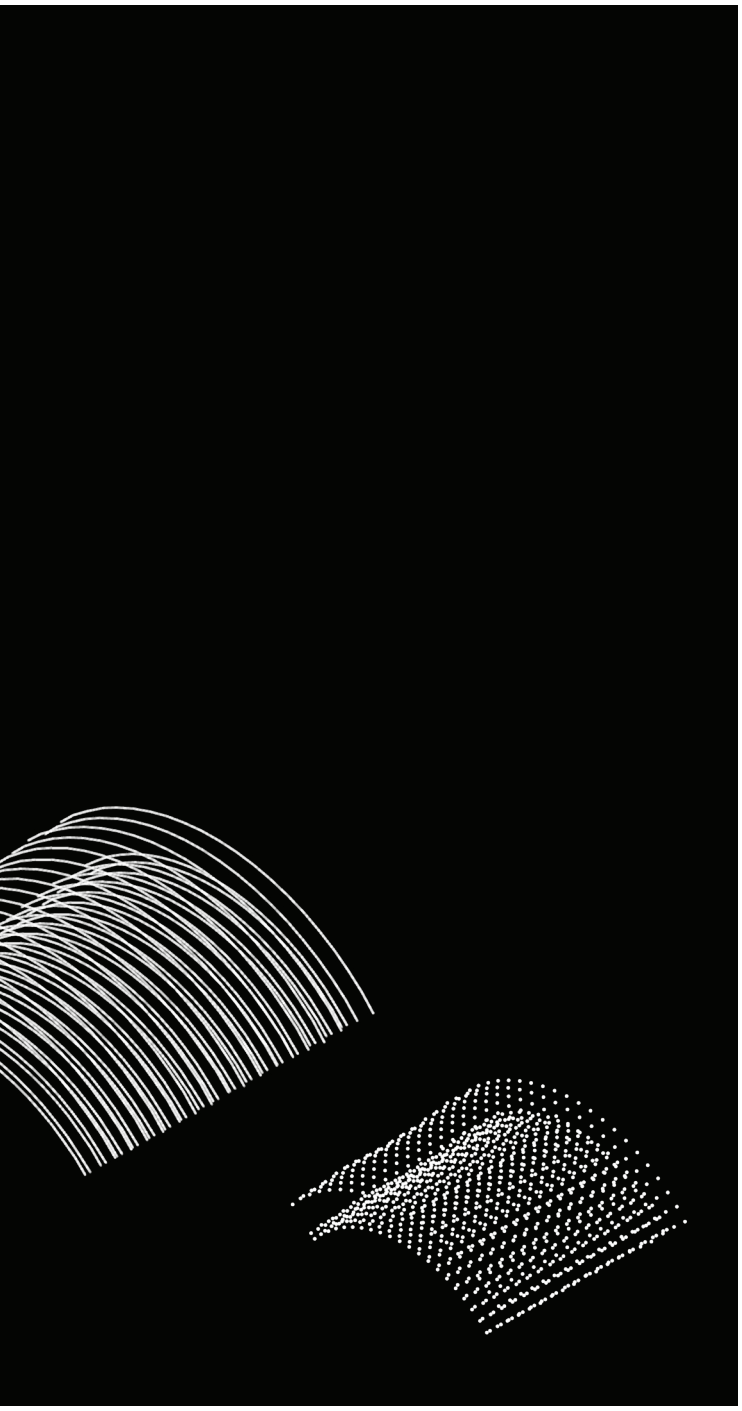

## 4.1 Introduction

The field of responsive architecture in the context of hygromorphic timber bilayers is relatively new, and results in a severe lack of empirical research. While there have been several research papers that focused on small-scale bilayer strips for adaptive solar shading, this thesis is focused more specifically on research centering around deployable structures; covered most notably in three recent studies. Each of these three papers has presented research that aligns most closely with the current state-of-the-art in computational predicting, pre-programming, manufacturing, and deploying of self-shaping hygromorphic structures (Wood et al., 2016; Wood et al., 2018; Kiesewetter et al., 2025).

In their paper "Material computation—4D timber construction: Towards building-scale hygroscopic actuated, self-constructing timber surfaces", Wood et al. (2016) presented techniques and technologies that allowed for the upscaling of bilayer elements into more complex building surfaces.

Building on the 2016 paper, Wood et al. (2018) presented "Hygroscopically actuated wood elements for weather responsive and self-forming building parts – Facilitating upscaling and complex shape changes" to outline manufacturing principles for employing a range of shape changing patterns to achieve uni- and bi-directional surface curvature.

Most recently, Kiesewetter et al. (2025) employed bilayers for furniture design, demonstrating real-world applications at a small-scale to help validate the plausibility of construction with hygromorphic bilayers. Their paper

"HygroShape: Programming Flat-pack, Self-shaping Wood Furniture" takes advantage of the constant indoor humidity levels to pre-program bilayer elements that activate at indoor humidity levels, and drive the assembly of furniture from flat-packed states into complex 3D geometries. Their paper presents a computational tool for predicting uni-directional curvature, and validates it with physical products.

The objective of this paper is to build on the computational tools presented in each of the papers, while addressing the lack of locking elements that limit their application in outdoor environments, where fluctuations in relative humidity pose a risk to undesirable re-flattening.

## 4.2 Constructing a tool for predicting bilayer bending

One of the most critical aspects of this thesis is being able to accurately predict, model, and simulate the deformations carried out by the hygromorphic bilayers. This section outlines the methodology for designing a bilayer system that emulates the deployed form of a shell structure, including material characterisation, curvature prediction, fibre orientation, and the iterative design process.

### 4.2.1 Defining the workflow parameters

To achieve a workflow that was well-informed and addressed the most important aspects of the design process, a set of goals were outlined to provide a basis on the parameters that should inform the final script ( see figure 32, on next page), including;

- (1) Visualising both layers as a singular, integrated system.
  *[Each layer need to not only inform the overall deformation independently, but also integrate effectively with each other to avoid unreliable results]*
- (2) Material property parameters to allow for adaption across different timber species.
  *[The rigidity of different timber species needs to be encoded into the simulated geometry to ensure real-world accuracy]*
- (3) Prediction with Timoshenko equation.
  *[The degree of curvature calculated from the adapted Timoshenko formula must support the validity of the script]*
- (4) Curvature flow mapped for different geometries.
  *[For any deployed structure, the direction of principal curvature from each support to the others needs to be mapped to inform fibre orientation]*
- (5) Simulation of bilayer deformations informed by fibre orientation.
  *[Fibre direction on the active layer should dominate the deformations for the shape-prediction, while also allowing for variability in their orientation]*
- (6) Discretisation of generated geometry to determine bilayer dimensions.
  *[Once deployed, the shell surface needs to be discretised into uniform panels - where possible - to inform the dimensions of the bilayers]*

### 4.2.2 Computational frameworks from literature

The three most relevant papers mentioned in the introduction of this paper all incorporate a computational workflow to help support the manufacturing process of bilayers for specific deformations.

This is important for saving time and resources in determining which timber species, humidity ranges, fibre orientations, and bilayer sizes should be employed for the final system.

Unfortunately, a significant limitation in current literature is the lack of procedural transparency. While the papers identify the software they use, they frequently withhold the specific methodologies required to replicate the predictive computational models, offering only broad overviews of the process carried out.

As a result, the absence of detailed methodologies in the literature meant that a predictive framework had to be developed independently. The workflow was built from first principles found in the literature, and expanded sequentially

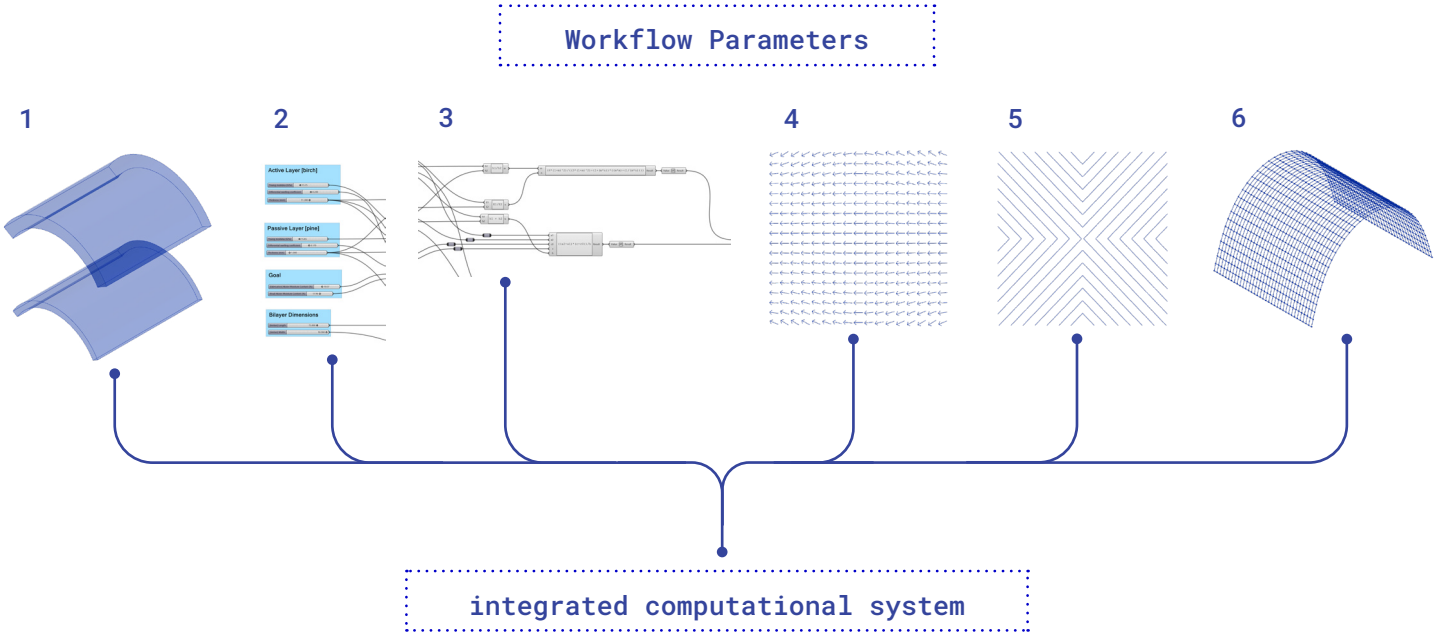


***figure 32:*** *Diagrammatic representation of the parameter goals for computational workflow (source: own work)*

through an iterative scripting process to ensure the final script addressed the necessary parameters.

### Research-informed scaling ratio

In their paper, Kiesewetter et al. (2025) provide a more elaborated description of their computational workflow, compared to the other papers. They highlight the inclusion of a scale factor between the width of the active layer and the width of the passive layer that is derived "... from curvature predictions computed with the Timoshenko formula, and back-calculated using trigonometry" (Kiesewetter et al., 2025, see figure 33A & B). The transformed positions of the vertices of the layers - following the scaling - serve as the goal objects for the shape matching, and allow the curved geometry of the shell to be reconstructed (see figure xx).

A notable drawback is that this scaling process relies on a native Grasshopper component, which only accommodates two-dimensional scaling parallel to the direction of the box's edges. This severely limits the workflow's applicability for geometries with more than one curvature direction; such as synclastic or anticlastic forms.

Despite this, the foundational logic wherein the

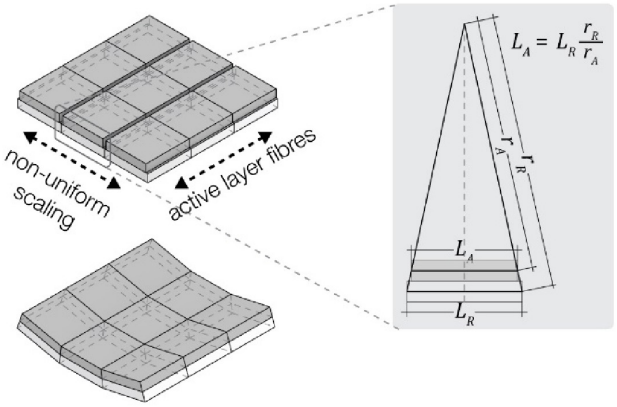


***figure 33A:*** *Width scale factor between the active and passive layers, based on the Timoshenko formula (source: Kiesewetter et al., 2025)*

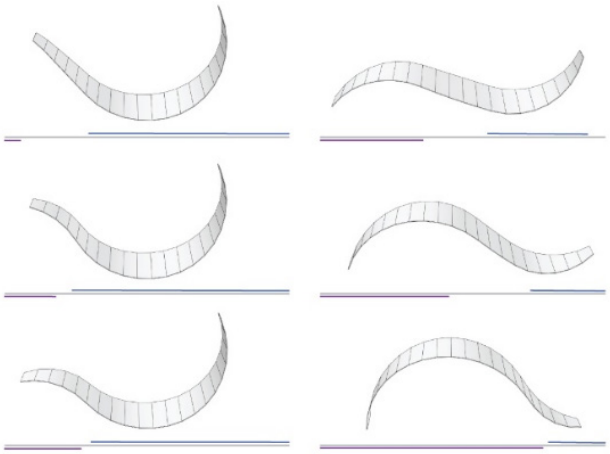

***figure 33B:*** *Furniture design variations based on varied scale factors (source: Kiesewetter et al., 2025)*

scale factor between the active layer and the passive layer is derived from Timoshenko calculations served as a sound starting point for the workflow developed in this paper.

### 4.2.3 The foundational framework: space frame lattice

#### Application of scaling ratio within space frame curvature

Rather than relying on a native Grasshopper component with limited capabilities, the scaling ratio was initially explored through the design of a simple, single-layer space frame whose transformation into a curved shell is driven by the kinematic constraints between the two layers.

By anchoring the base springs of the grid, and introducing selective linear expansion along the primary x-axis of the upper surface, a dimensional mismatch is created between the two structural planes. Where the upper grid will increase in scale uni-directionally, while the lower grid remains static (see figure 34)

Since the transverse y-axis and the vertical connectors maintain a constant length, the system cannot accommodate the longitudinal extension within a planar,

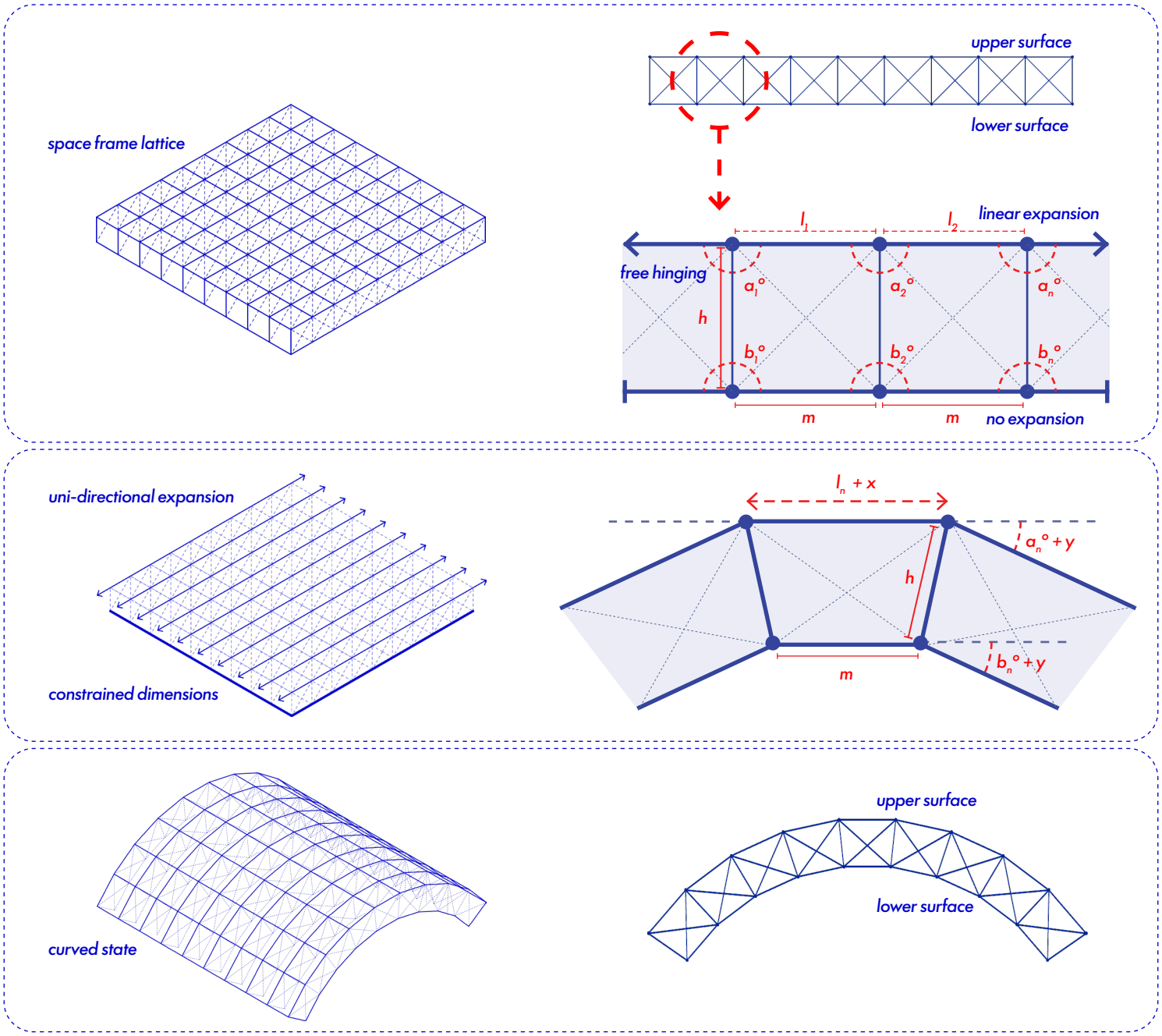


***figure 34:*** *curve-forming of space frame through linear expansion of top grid (source: own work)*

two-dimensional state. To resolve this internal strain, the structure undergoes a uniform hinging of the joints along the base grid, translating the horizontal elongation into a uniform radial displacement to display curvature.

This process demonstrates how a controlled, non-uniform growth within a rigid lattice can be leveraged to achieve predictable, large-scale curvature from simple rectilinear components.

### Introducing fibre orientation

When constructing a bilayer, the fibre direction does not necessarily need to remain parallel to the edges of the material. During fabrication, any rectangular configuration for a bilayer can be cut from a timber plank at non-orthogonal angles, providing a wider range of options for directional expansion (see figure 35).

To replicate this flexibility within the computational workflow, and support the design of more complex free-form structures, a rotational parameter was introduced to pivot the orthogonal grid of the space frame along the horizontal axis. As the grid rotated, the extents of each row were recalculated to ensure that the geometry remained constrained within the boundaries of the bilayer.

Within Grasshopper, early iterations relied on the native "Contour" component which generates a series of parallel planar slices through a 2D surface mesh or 3D solid. However, in later stages of development, where predicting anticlastic curvature became necessary, the component proved insufficient, as it limited the simulation of curvature across two opposing directions. It became necessary to manually script the rotational parameters and organise boundary conditions to re-define the grid extents. These developments and their implementation will be discussed in greater detail in the following chapters.

Once incorporated into the workflow, the "Contour" component could easily accommodate the rotation of grid lines, allowing the space frame to be continuously re-constructed to the desired fibre orientation. See appendix 4 (A.4) for different fibre orientation explorations.

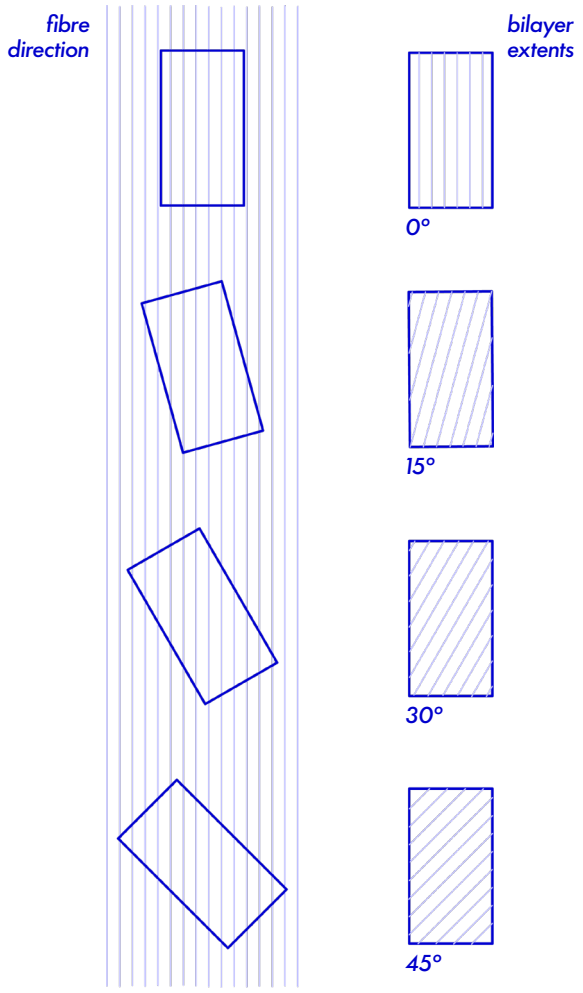


***figure 35:*** *How varied cuts of timber can achieve different fibre orientations for identical bilayer dimensions (source: own work)*

### Reconstructing the space frame

While the initial computational script successfully managed a standard orthogonal space frame, the inclusion of an adaptable fibre orientation significantly increased the system's complexity. Whenever the direction of expansion was no longer aligned with the primary edges of the rectangular grid (see figure 36), the shape-finding process became more nuanced and introduced greater structural

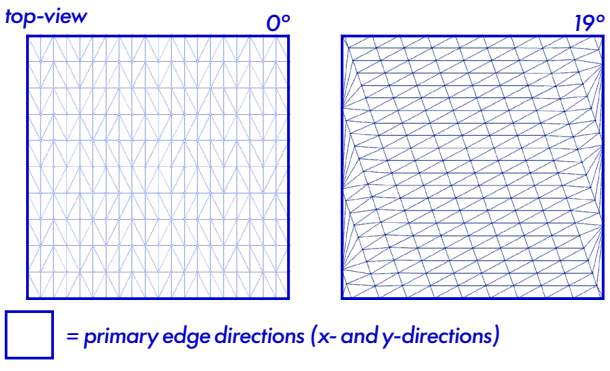


***figure 36:*** *Varied space frame structures for 0° fibre rotation and 19° fibre rotation (source: own work)*

instability.

This misalignment introduced torsional forces and asymmetrical stresses along the axis of expansion, shifting the system from a predictable 2D curve into a complex 3D deformation (see figure 37).

To address this, the structural parameters of the digital model had to be expanded and re-calibrated. It was necessary to achieve a balance between accommodating the elasticity of the horizontal members to achieve their intended expansion, and the axial stiffness of the remaining structural elements - the vertical struts and diagonal bracing - to prevent the system from losing its structural integrity.

Managing these competing constraints meant that any slight over-calculation in the force components would override the rigidity of the connectors, leading to a breakdown in the space frame's structure. Or, alternatively, a lack of expansion in the horizontal components would lead to a lack of curvature.

Ultimately, achieving a stable, constrained state for the space frame proved to be a significant challenge. As the structure deformed into its target curvature, it frequently suffered from vertical instability. Rather than maintaining a uniform thickness, the system exhibited a tendency to "narrow" or "pinch" at the boundaries as the vertical members suffered from excessive angling, as demonstrated in figure 38 below.

This localized collapse at the edges indicated that the internal bracing was insufficient to counteract the lateral

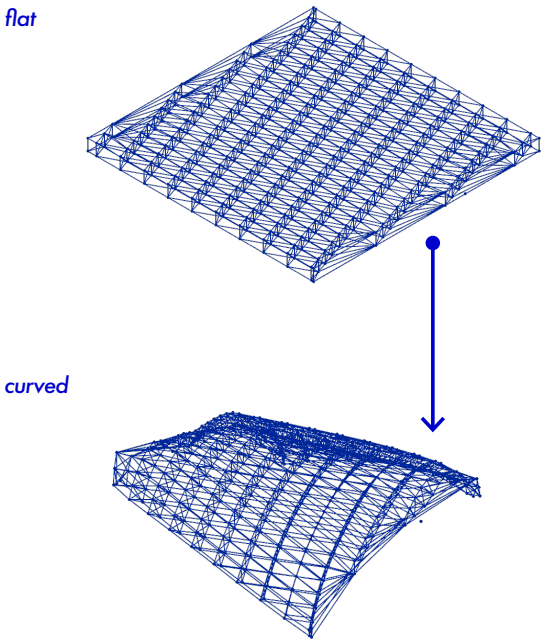


**figure 37:** *Simulated bending for a grid with 19° fibre rotation (source: own work)*

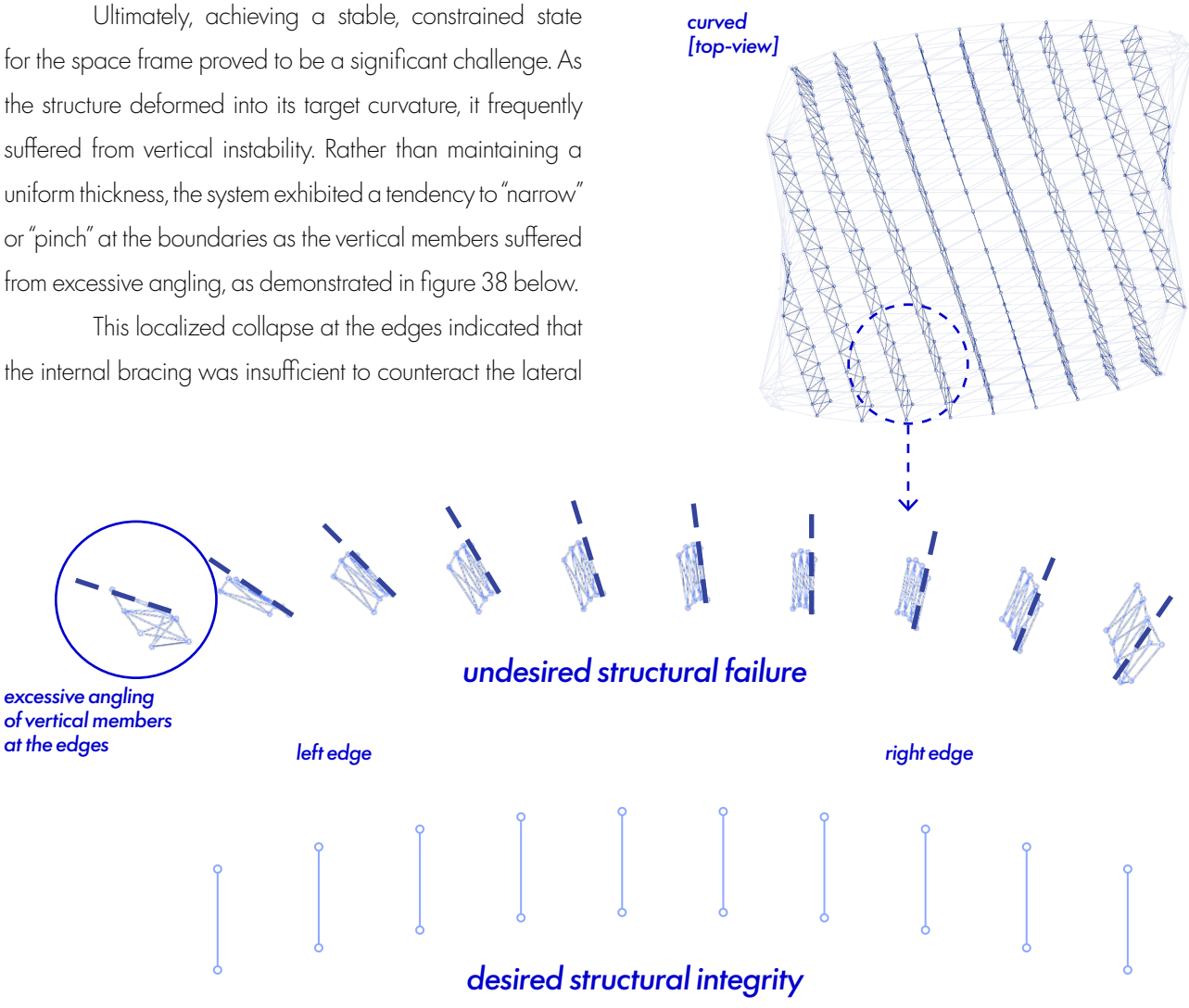


**figure 38:** *Unwanted slanting of vertical members as compared to desired member behaviour (source: own work)*

forces generated by the off-axis expansion, resulting in a structural failure where the shell would fold in on itself rather than holding its intended arched profile.

### Mitigating torsional rotation for non-orthogonal expansion

Continued exploration of the form-finding methods identified planar constraints as an effective strategy for mitigating unwanted torsional rotation within the structure.

In this approach, specific groups of points within the space frame are constrained to predefined geometric planes, establishing rigid two-dimensional boundaries for their movement. By limiting displacement to these planar regions, the system prevents lateral deviation and uncontrolled twisting, while still allowing deformation along the intended axis of expansion. This constraint-based logic enables greater geometric stability and more predictable curvature behaviour during the simulation process.

The robustness of this workflow was validated through a series of simulations with varied off-axis fibre orientations, including 10°, 20°, 30°, and 45° degree rotations. As can be seen in figure 39 on the right, when viewed from above, the grid lines - along which the space frame is expanding - successfully do not exhibit any lateral, out-of-plane bending.

This final iteration demonstrated a high degree of precision, yielding negligible torsional bending along the expansion axis for all tested fibre orientations, and that planar anchoring is a key requirement for stabilizing the form-finding.

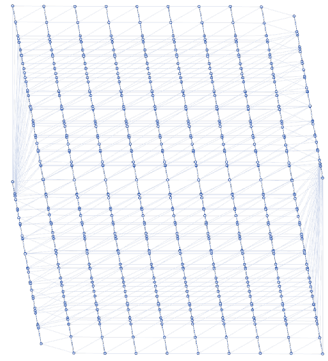

*10° fibre orientation*

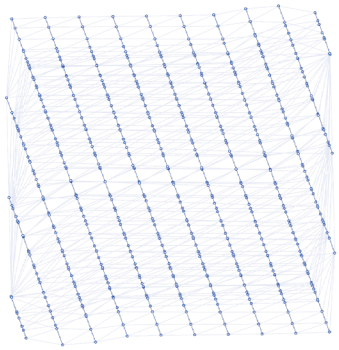

*20° fibre orientation*

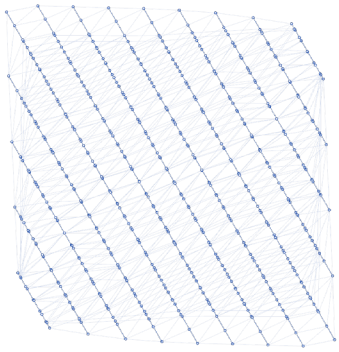

*30° fibre orientation*

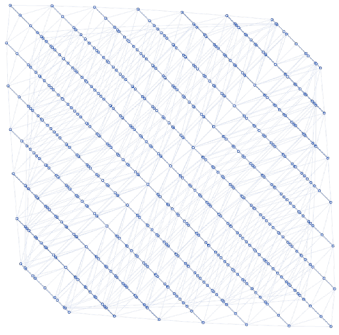

*45° fibre orientation*

***figure 39:*** *Verifying structural integrity for varied fibre orientations (source: own work)*

## 4.2.4 Timoshenko's formula for predicting bilayer curvature

### Visual modelling of Timoshenko formula

Incorporating mathematical formulae into Grasshopper is very straightforward as there are numerous native components for mathematics, as well as an "Expression" component for writing up more complex, or extended formula.

The equation is governed by a series of dynamic parameters controlled via number sliders. These inputs allow

for real-time adjustments to the structural and hygroscopic properties of the timber bilayer including;

- Young's Modulus (GPa)
- Differential swelling coefficients
- Thickness (mm) of the active and passive layers (as separate number sliders)
- Water moisture content (%) at the point of fabrication, and for the final goal

Once the curvature (1/p) was solved for the desired timber species and bilayer thickness, the value was re-calculated to determine the radius (r), and used to build a



***figure 40:*** *Bilayer curvature for the simplified Timoshenko formula, with separated active and passive layers (source: own work)*

simple visual geometry of the curvature (see figure 40). This geometry provides a visual guide to compare the simulated deformation of the lattice against the expected curvature from the formula for the selected timber species and bilayer thickness.

**Informing the curvature of the space frame**

To transition from arbitrary geometric deformation to a material-specific simulation, it was necessary for the script to incorporate the curvature results from Timoshenko's adapted formula. This analytical model serves as the mathematical foundation predicting the steady-state curvature of timber elements subjected to moisture-induced strain.

Although the formula accurately determines the resulting curvature, it does not account for the rate of expansion of the bilayer itself. To address this limitation, the calculated curvature was used to define the neutral axis located at the interface between the active and passive layers, establishing a geometric baseline from which the deformation behaviour could be simulated. The conversion from curvature to expansion was then achieved through a geometric offset operation.

By offsetting the neutral axis curve to the specific thickness of the active and passive layers, the relative arc lengths of the top and bottom surfaces could be calculated. The ratio of these two lengths against the original length of the timber member yields a scaling factor (see figure 41) that represents the precise degree of expansion, or contraction, required to achieve the material-driven curvature predicted by the Timoshenko formula.

The scale factor was subsequently applied to the springs between the points defining the space frame. These

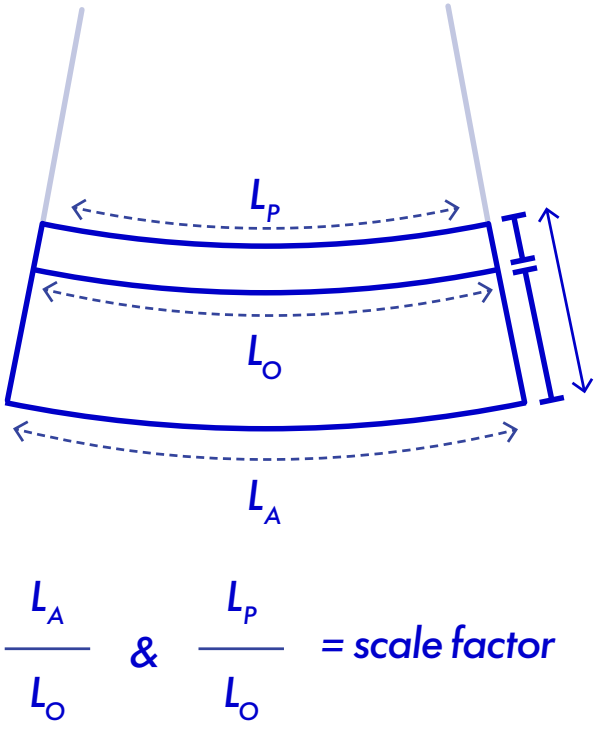


***figure 41:*** *Scale factor based on offsetting Timoshenko curvature (source: own work)*

connections govern the target distances between adjacent points as the system seeks equilibrium when simulated. By modifying these target distances using the scalar values, the expansion behaviour of the horizontal members could be driven by material-informed data rather than arbitrary geometric inputs.

This ensured that the final deformed state of the space frame was not merely a visual approximation, but a mathematically accurate representation of the timber's hygromorphic behaviour.

### 4.2.5 Validating the Grasshopper script

Once the parameters for fibre orientation, structural stability, and material-informed deformation were integrated into the global script, the form-finding script was validated for accuracy.

A comparative table was constructed between the radius of curvature derived from the original Timoshenko equation, and the final radius of curvature of the space frame after it deformed. Results were collected for two distinct bilayer combinations: beech (active) with pine (passive), and oak (active) with spruce (passive). A minimum thickness ratio of 4:1 between the active and passive layers was ensured, as Wood et al. (2018) identify this benchmark in their research for avoiding anticlastic curvature in bilayers with low aspect ratios (shapes approximating a square).

The distribution of results can be seen in figure 42 on the next page, which demonstrated an average inaccuracy of approximately 10.35%, where the simulated radius of curvature was consistently larger than the Timoshenko prediction. Notably, the average inaccuracy for the oak-spruce bilayer was slightly higher at 11.21%, compared to the beech-pine combination at 9.5%. Accuracy improved for both sets of bilayers as the overall thickness increased, reaching a minimum recorded error of 6.03%.

A potential reasoning to the disparity in results was the addition of bracing elements that spanned between the grid lines of the lattice frame. A consistent issue in the simulations for fibre orientations other than 0° or 90° was the vertical deviation of the expanding lines. Rather than experiencing torsional deformation, they would shift upwards relative to the magnitude of curvature, creating "bumps" across the surface, as seen below in figure 43. To mitigate this, a network of slightly stiffened bracing lines was introduced to help maintain linearity across the surface of the bilayer (see figure 44). However, these braces slightly resist

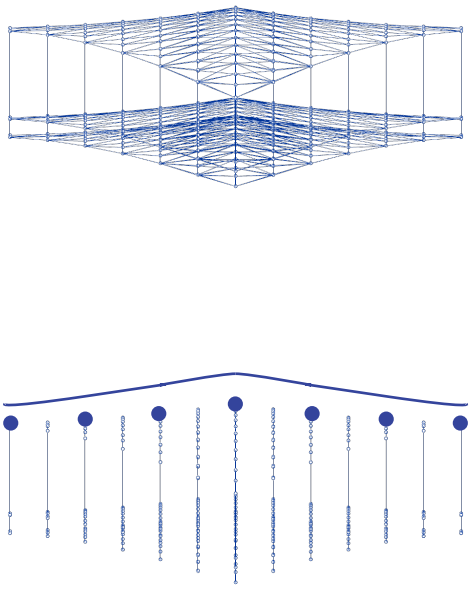

***figure 43:*** *vertical shifting of expansion lines leading to surface deformation*

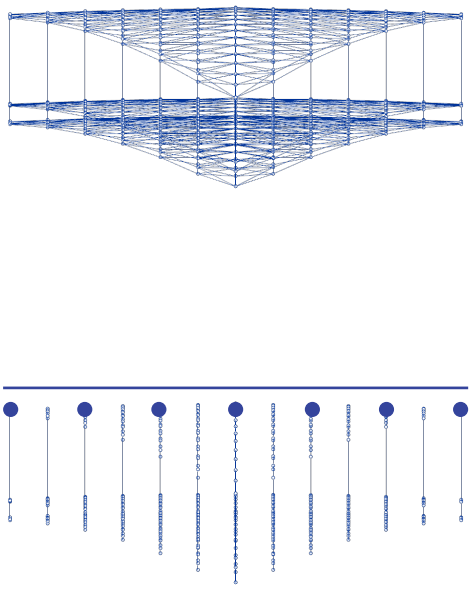

***figure 44:*** *lateral restrictions between the expansion lines to restrict vertical shifting*

**Inaccuracy:**
*the percentage difference between space frame curvature radius, and Timoshenko curvature radius*



*space frame curvature*



*Timoshenko curvature*

*active layer:* BEECH
*passive layer:* PINE

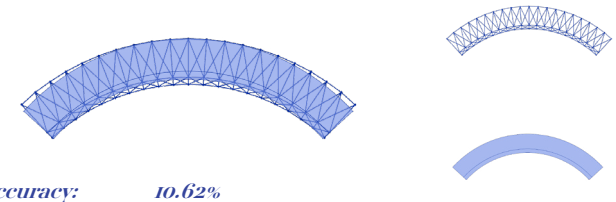

*inaccuracy:* 10.62%
active: 2mm passive: 0.5mm

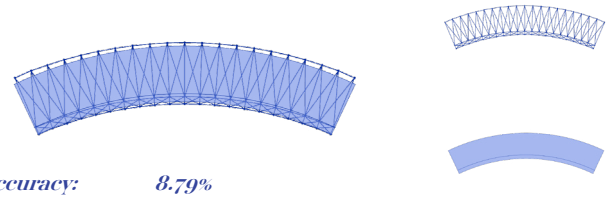

*inaccuracy:* 8.79%
active: 3mm passive: 0.5mm

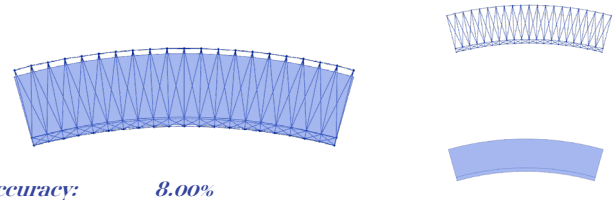

*inaccuracy:* 8.00%
active: 4mm passive: 0.5mm

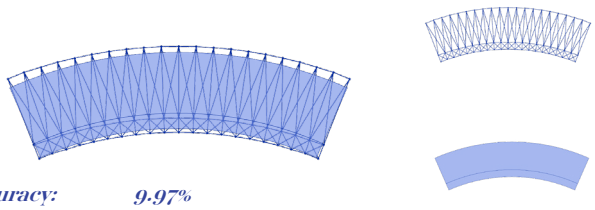

*inaccuracy:* 9.97%
active: 4mm passive: 1mm

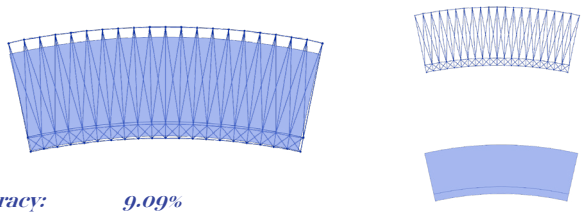

*inaccuracy:* 9.09%
active: 6mm passive: 1mm

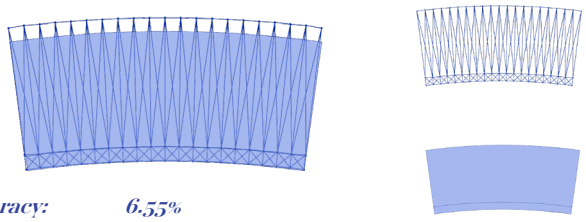

*inaccuracy:* 6.55%
active: 8mm passive: 1mm

*active layer:* OAK
*passive layer:* SPRUCE

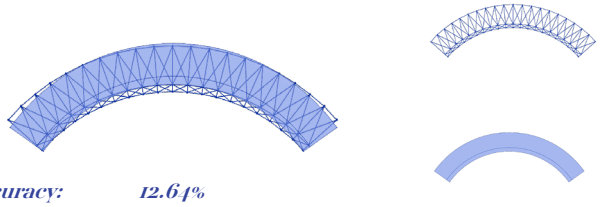

*inaccuracy:* 12.64%
active: 2mm passive: 0.5mm

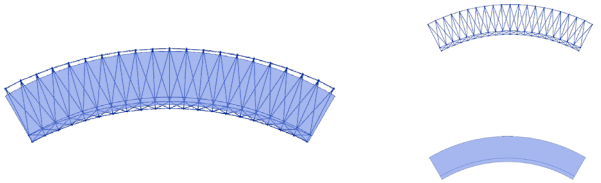

*inaccuracy:* 11.11%
active: 3mm passive: 0.5mm

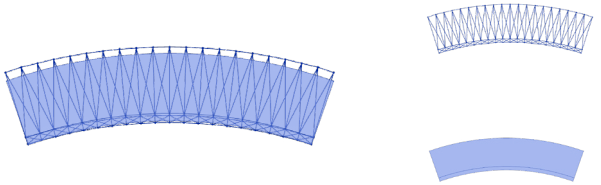

*inaccuracy:* 10.30%

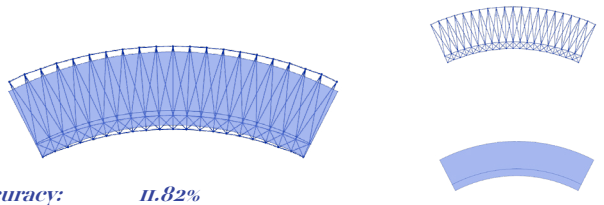

*inaccuracy:* 11.82%
active: 4mm passive: 1mm

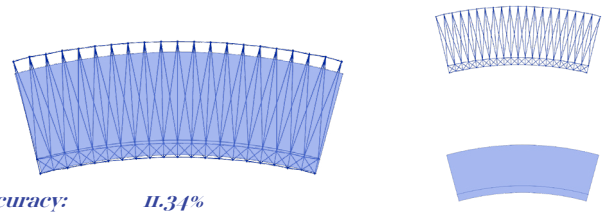

*inaccuracy:* 11.34%
active: 6mm passive: 1mm

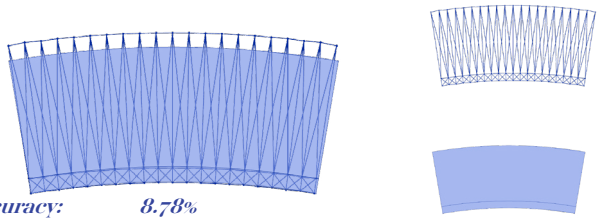

*inaccuracy:* 8.78%
active: 8mm passive: 1mm

**figure 42:** *selected results of Grasshopper script validity against Timoshenko curvature*

the expansion of the primary lines, resulting in the observed 10% deviation from the Timoshenko curvature.

### 4.2.6 Final simulation goals

To provide a clear overview of the final computational workflow, the following section categorises and discusses the applied forces and constraints for the completed simulation tool in predicting monoclastic curvature of bilayers. The final factors are organized into four distinct functional categories:

- Vertical member constraints
- Forced expansion
- Torsional restriction
- Material-informed hinging

#### Vertical Member Constraints

To maintain the integrity of the bilayer and promote predictable curved deformations, the normal axis where the two layers interface is constrained to maintain its length throughout the simulation. Additionally, the vertical columns between nodes and the internal bracing members are also restrained to ensure geometric continuity across the entire space frame (see figure 45).

#### Forced Expansion

The expansion factor derived from the Timoshenko formula is applied to all members parallel to the line of expansion, excluding the normal axis. The cross-bracing elements along this axis are also made to expand to ensure they do not over-constrain the deformation (see figure 46).

#### Torsional Restriction

To achieve the desired deformation, the expanding elements must remain parallel to one another and maintain a consistent offset distance while accommodating translation within their local horizontal planes. The points of the space frame are constrained to predefined geometric planes, establishing rigid two-dimensional boundaries for their movement (see figure 47).

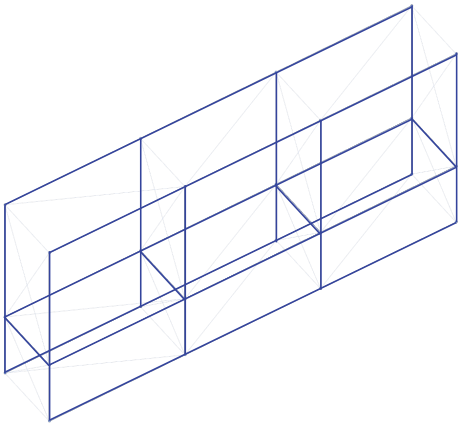

***figure 45:*** *All members whose lengths remain constrained during a simulation (source: own work)*

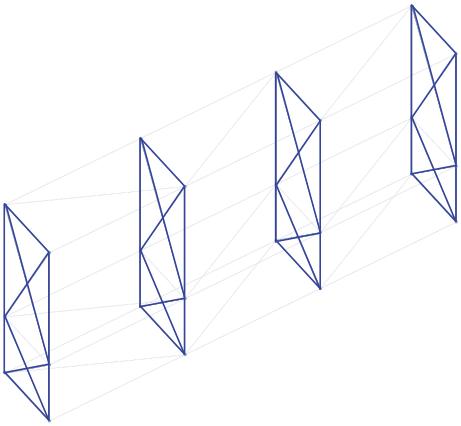

***figure 46:*** *All members whose lengths are expanded during the simulation (source: own work)*

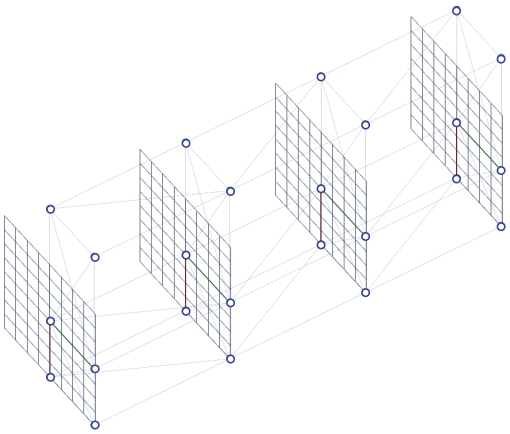

***figure 47:*** *Maintaining point positions along respective planes to prevent torsional deformation (source: own work)*

### Material-Informed Hinging

Material property parameters were included in the script to better emulate the curvature of specific timber species. By incorporating parameters for rotational stiffness at the hinges, the simulation outputs a more uniform and realistic curvature to reflects the material's mechanical resistance (see figure 48).

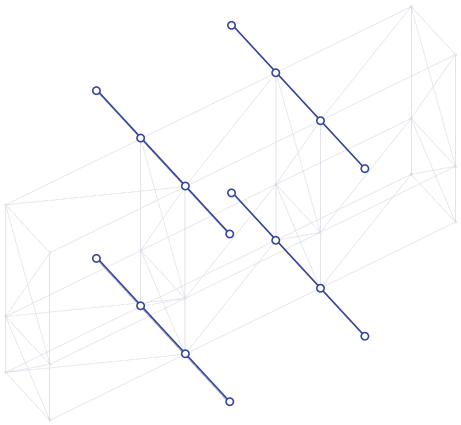

***figure 48:*** *Material data informs bending for polylines along the axis of expansion (source: own work)*

## 4.3 Multi-element assemblage

### 4.3.1 Principal curvature lines to inform fibre orientation

The primary objective for developing a script that simulates transformable fibre orientation is the synthesis of individual bilayers into a cohesive, multi-element system capable of complex structural deformation.

In their 2016 and 2018 papers, Wood et al. demonstrated that while a single hygromorphic bilayer is limited to either monoclastic curvature or anticlastic curvature, a strategically fabricated assemblage of elements with varied fibre orientations could successfully achieve dome-like, synclastic curvature (see figure 49). Notably, this precedent was also adapted by Kiesewetter et al. (2025) to achieve varied deformations for their furniture designs.

To successfully compute the specific fibre orientations required for global deformation, the surfaces of target shell geometries were analysed using a discrete vector field. The flow of expansion was dictated by the structural relationship between all the shell's supports, whereby the points - or areas - where the shell meets the ground served as attractors or force charges to simulate a vector flow across the undeployed surface of the mesh; mimicking the optimal expansion trajectories.

### 4.3.2 Simulation for synclastic curvature

The translation of the continuous vector field to the individual bilayer elements involved a discretisation process that averaged the vector results within each discretised face

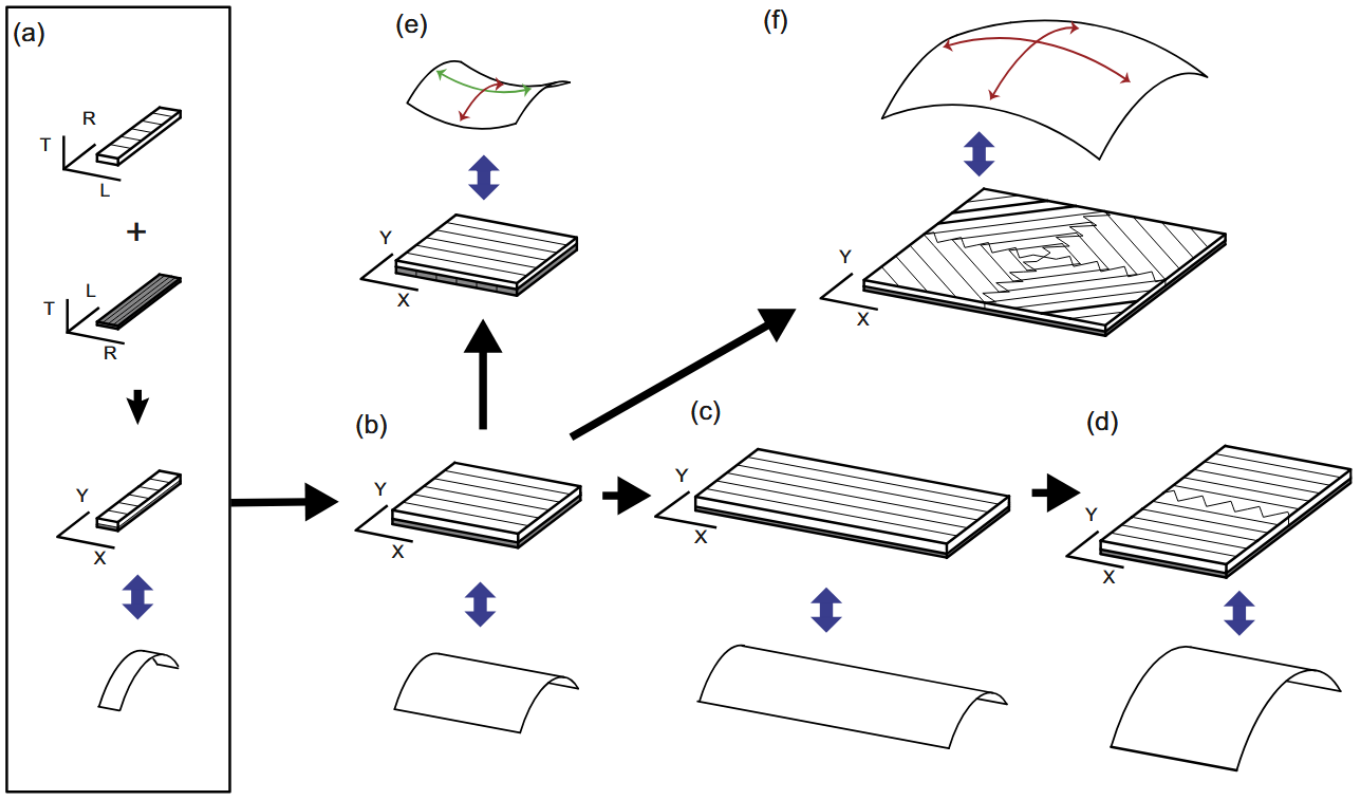


***figure 49:*** *achieving monoclastic, anticlastic, and synclastic curvature with single bilayers, or multi-element systems (source: Wood et al., 2018)*

extent.

The base mesh was subdivided into a set of individual panels that represented the required number of bilayers, and all the vectors contained within the extents of each panel were processed through a vector averaging component. This yielded a single, optimised orientation vector for each panel, effectively indicating the necessary direction of expansion of each element for the global requirements of the shell's curvature (see figure 50).

To verify the accuracy of the integrated script and its various parameters, a synclastic dome served as the primary validation model. Because this specific morphology is a foundational example of multi-element deformation in literature, it serves as a rigorous test for the material-informed logic of the algorithm.

Existing literature provided a comprehensive set of data for the necessary bilayer thickness, fibre orientations, Timoshenko curvature, and a visual assessment of the final executed geometry.

By synthesising the scalar expansion ratios with the required fibre orientations, the simulation was able to approximate the target synclastic geometry (see figure 51).

### 4.3.3 Reflection on multi-element simulations

The final form presented from the simulation failed to present a perfectly smooth, uniform synclastic curve. While the entire system successfully behaved as a unified structure, the centre appeared too flat and unproportional. While not entirely clear, this is likely due to the complexity of all the numerous competing parameters that activate and constrain each bilayer panel and which restrict movement between the neighbouring panels. Simulating the curvature was also computationally heavy and extremely slow, making the process inefficient for large-scale applications.

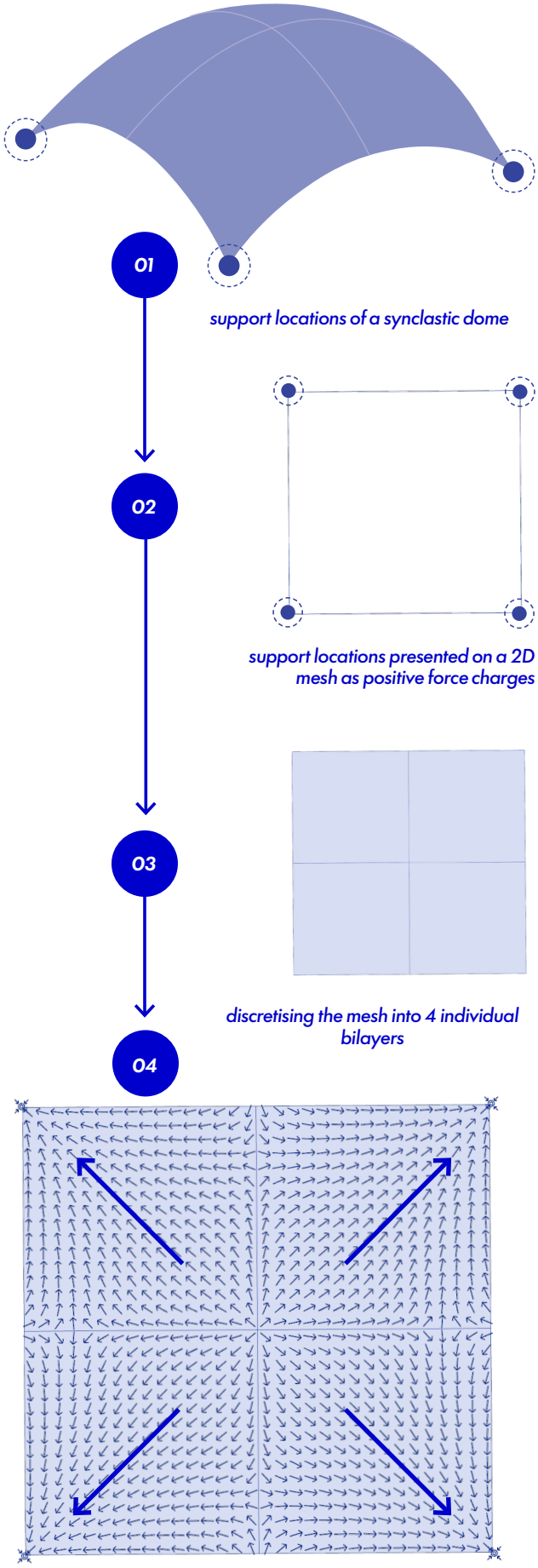


**figure 50:** *Vector field generated for synclastic curvature (source: own work)*

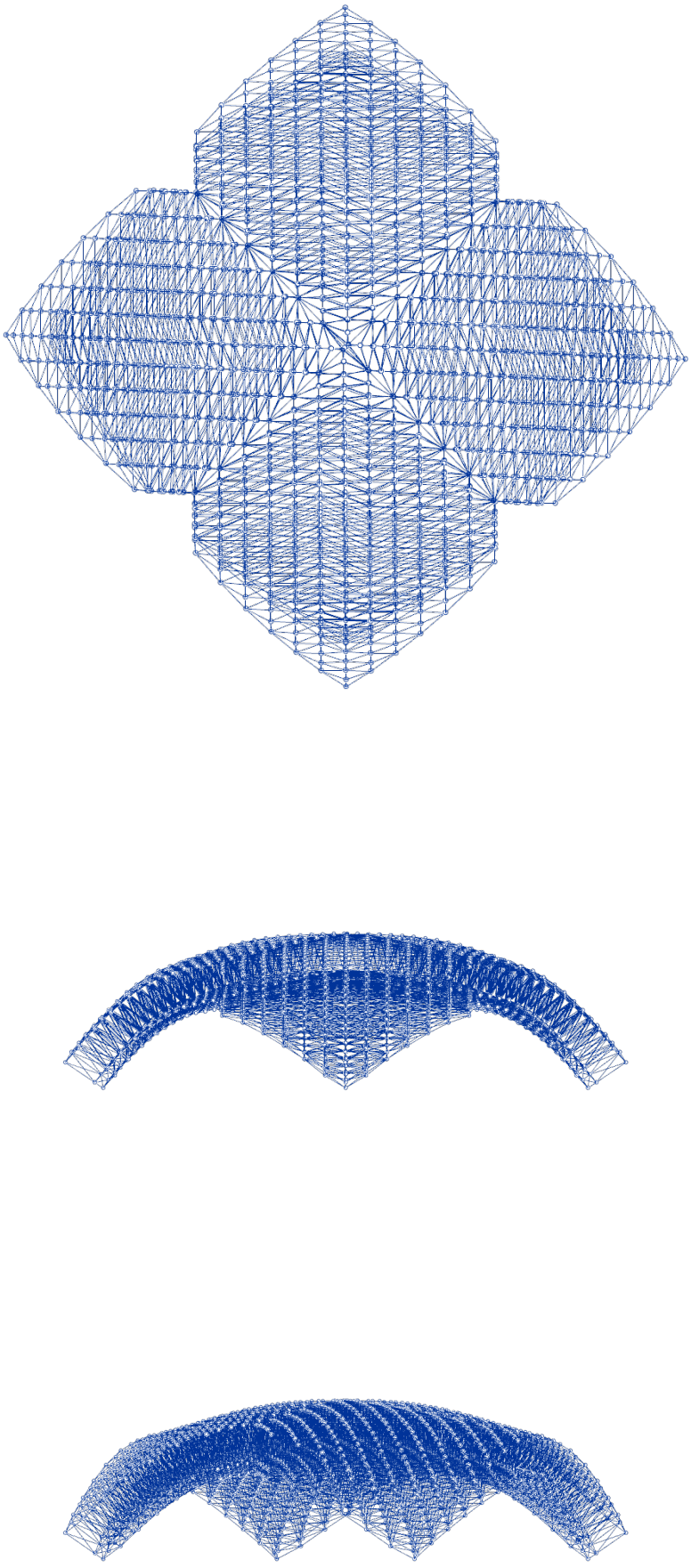

***figure 51:*** *Synclastic curvature [top-view & side-views] (source: own work)*

## 4.4 Flowchart of simulative tool for monoclastic curvature (see Appendix 5 [A.5] for Grasshopper script)

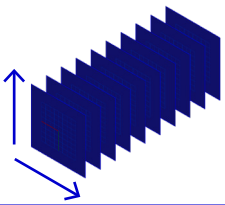

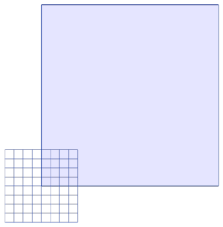

BILAYER EXTENTS

CONSTRCTING LATTICE GRID

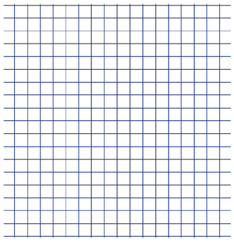

INTERSECTION BETWEEN ONE VERTICAL LINE AND ALL HORIZONTAL

DERIVE POINTS

GENERATE NORMAL PLANES AT POINTS

geometric intersection

VERTICAL LINES

HORIZONTAL LINES

geometric intersection

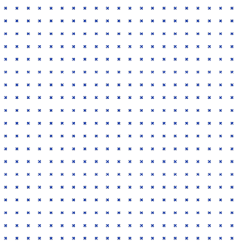

POINT GRID

VERTICAL OFFSET OF POINTS FOR LAYER THICKNESS

DIVIDE LINES INTO POINTS

thickness

TIMBER LENGTH

TIMBER WIDTH

ACTIVE LAYER PROPERTIES

YOUNG'S MODULUS

SWELLING COEFFICIENT

THICKNESS

PASSIVE LAYER PROPERTIES

YOUNG'S MODULUS

SWELLING COEFFICIENT

THICKNESS

MOISTURE CONTENT

width

length

TIMOSHENKO EQUATION

CIRCLE DERIVED FROM CURVATURE

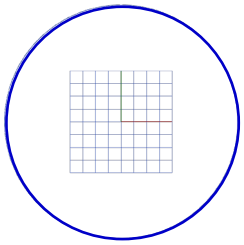

ARC DERIVED FROM BILAYER LENGTH

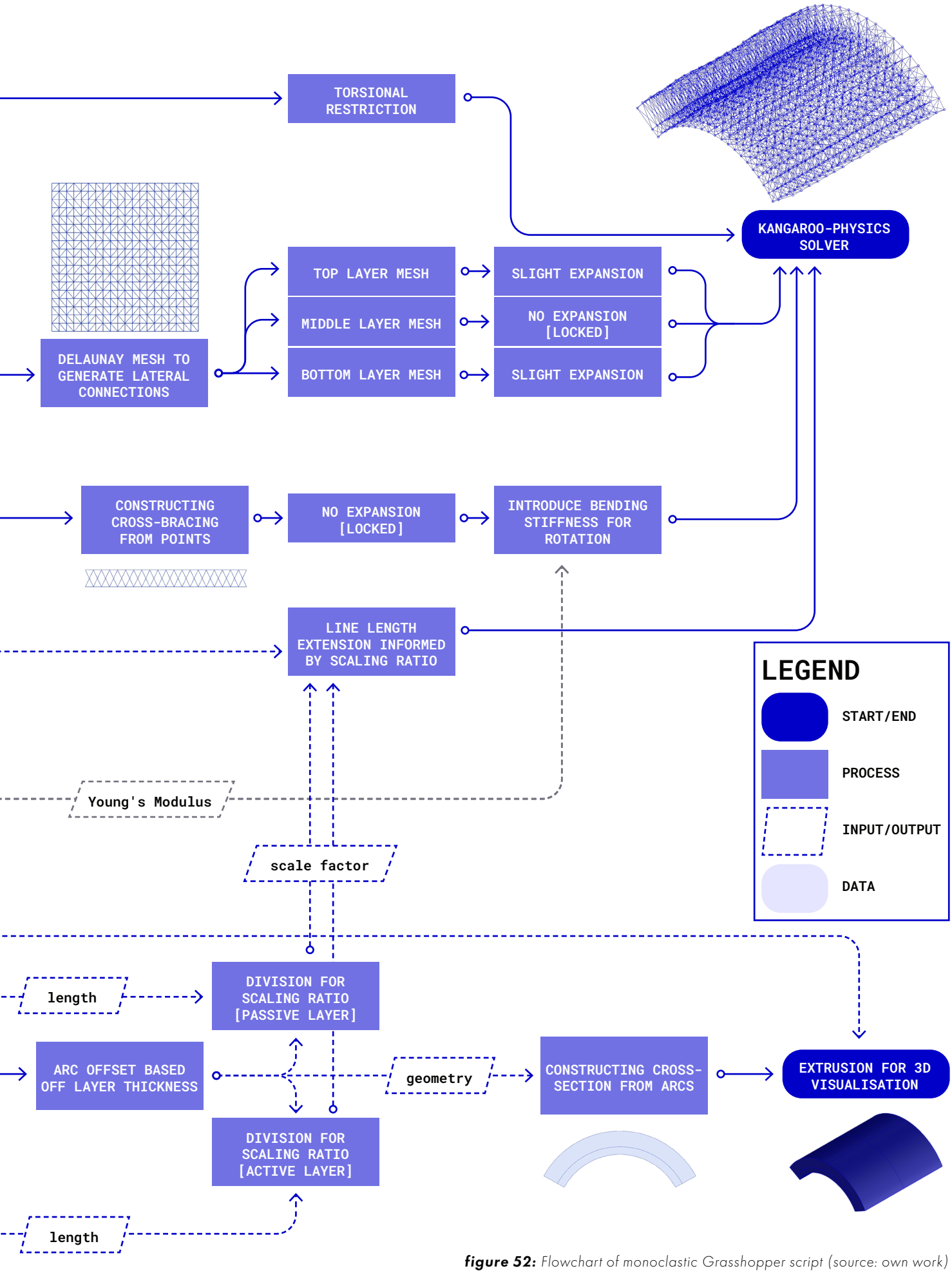


***figure 52:*** *Flowchart of monoclastic Grasshopper script (source: own work)*

# SIMULATING ANTICLASTIC CURVATURE

# 005

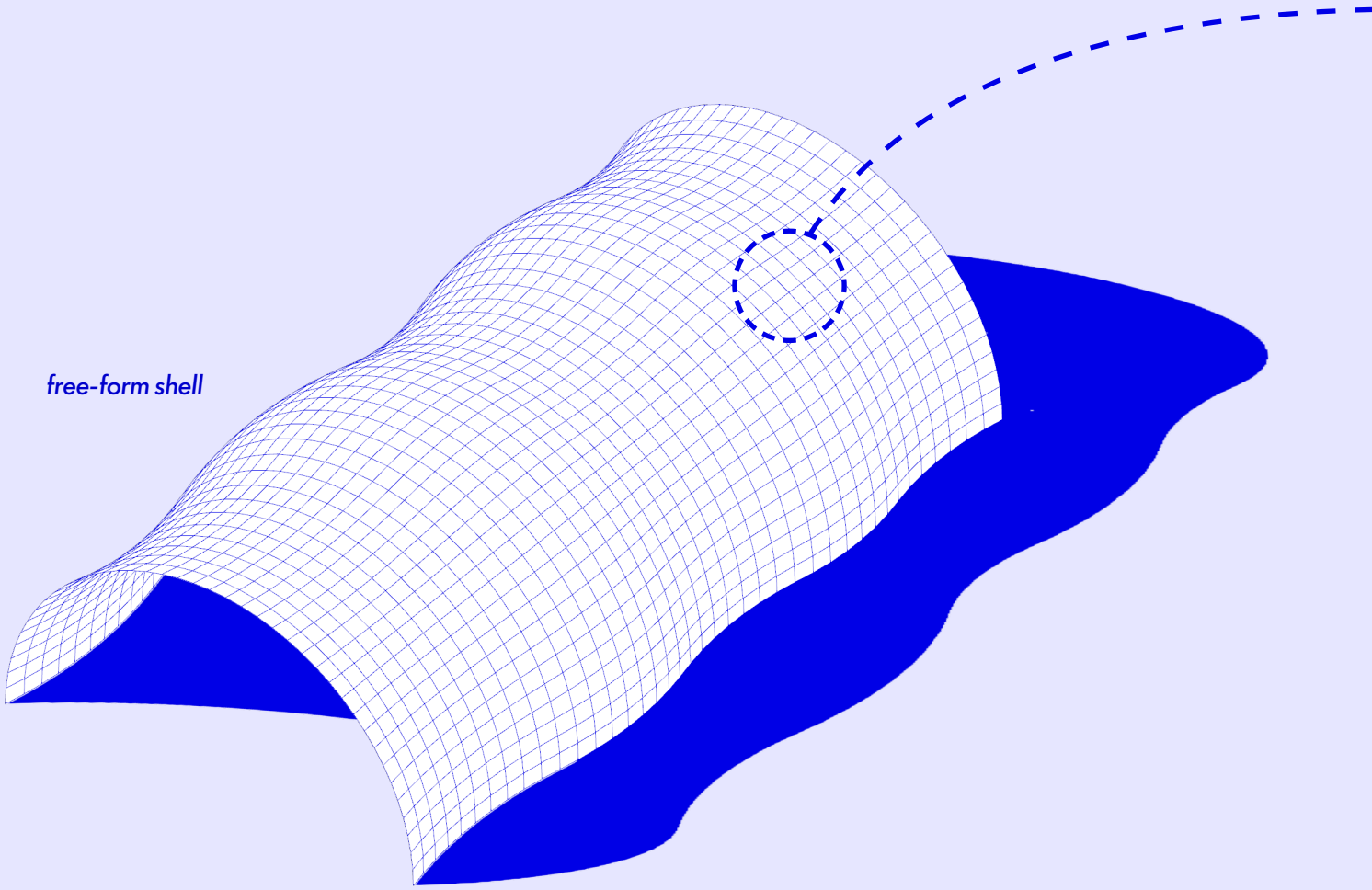


***figure 53:*** *Free-form shell with anticlastic element (source: own work)*

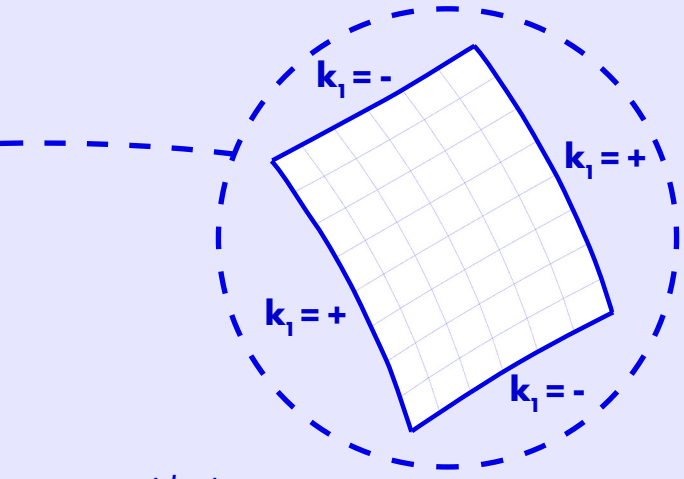


*anticlastic curvature exhibited by a panel*

## 5.1 Predicting anticlastic curvature

When considering the primary categories of shell surface curvature, the design of complex free-form structures that display varied and alternating curvature orientations requires a combination of bilayers exhibiting monoclastic and anticlastic curvature (with synclastic curvature being achieved through the interaction of 4 or more monoclastic panels).

The completed simulative tool for displaying bilayer curvature offers numerous transformable parameters for exploring a vast range of different bilayer configurations. Elements like timber species, bilayer thickness, width and length, and fibre orientation, can be re-adjusted smoothly to assess differing degrees of curvature.

Despite the range of possibilities, the tool was limited solely to monoclastic curvature. While this could accommodate deployed structures that mimicked monoclastic or synclastic shells, it limited the potential for designing free-form structures that curved in multiple directions (see figure 53).

To expand the applications of hygromorphic bilayers and breach the gap in literature, it was important to expand the predictive tool to also simulate anticlastic curvature.

### 5.1.1 Introducing multi-directional orthogonal expansion

Wood et al. state in their 2018 paper, that anticlastic curvature emerges in bilayers with low aspect ratios (approximating a square) when the thickness ratio between the active and passive layers falls below 4:1, respectively. Under these conditions, the increased thickness of the passive layer introduces a competing perpendicular influence against the primary direction of expansion of the active layer. As the bilayer absorbs or releases moisture, this interaction between the two layers generates deformations in opposing directions, resulting in anticlastic curvature.

Following this logic, it was necessary for the computational model to exhibit expansion in a secondary orthogonal direction. The process initially failed when the expansion parameters were introduced to the base model as they caused the lattice frame to behave independently along each axis. Rather than generating a unified anticlastic deformation, the system produced two separate monoclastic curvatures that only intersected at the centre of the bilayer.

Figure 54 illustrates the result of the final simulation for a fibre orientation of 45° across three different views, revealing the independent bending along the edges where the two layers detached from one another.

Further analysis of the script identified errors in the construction logic that limited the interaction between the particles and structural connections of the original space frame. As the digital model had initially been built from two independent groups of intersecting parallel lines, the expansion behaviour was applied separately to each set, rather than collectively as a cohesive system. To resolve this issue, it was necessary to re-construct the modelling logic of the space frame around the particles rather than the springs. This would allow the points at each intersection of the grid to merge into one unified system rather than two overlapping, but disconnected, systems.

### 5.1.2 Rebuilding the space frame

#### Particle data organisation

Originally, the computational modelling relied on the native Grasshopper component, "Contour", that could quickly construct a grid of lines within the boundaries of a pre-defined quadrilateral. External input parameters provided the freedom to easily rotate and re-define the distribution of grid lines to create denser or more minimal space frame structures.

Although it was possible to display the points of

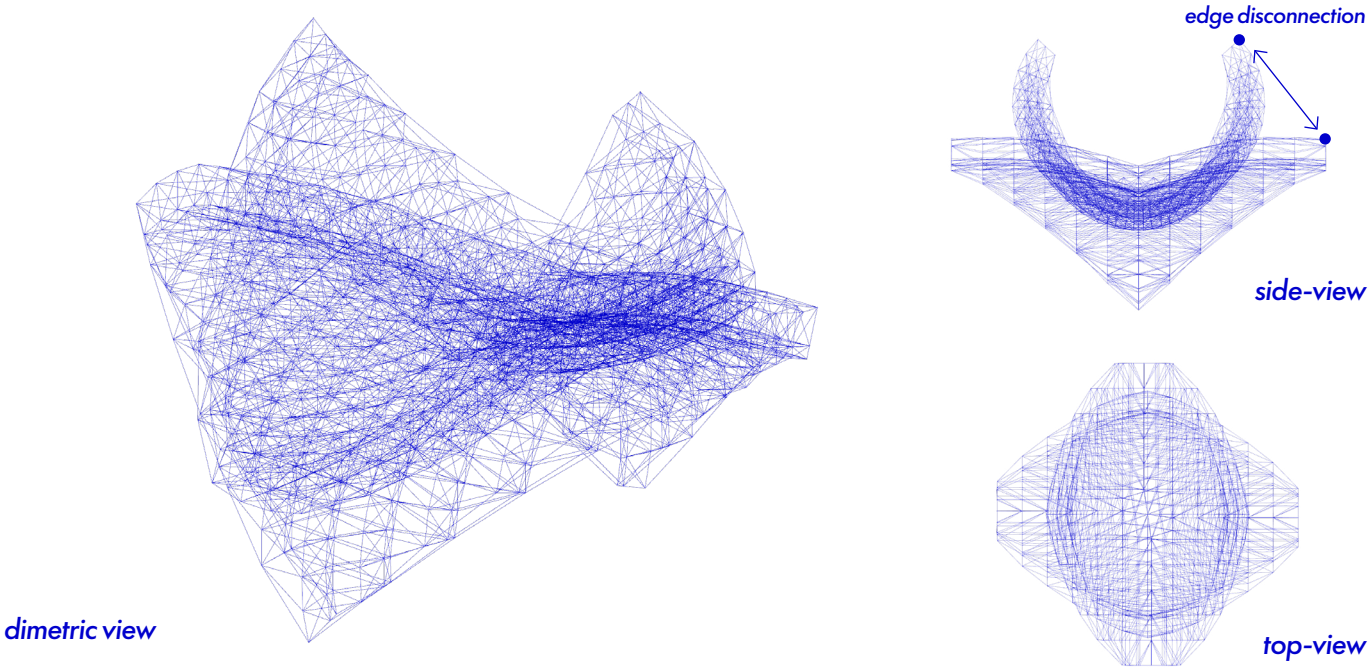


***figure 54:*** *Initial exploration of anticlastic curvature (source: own work)*

intersection between the two sets of grid lines as particles, the extracted data structure was too disorganised and random to effectively work with. This meant that the line-like spring elements for the lattice grid could not be re-introduced as they relied on adjacent points in an organised data structure, rather than random pairs of particles .

Within Grasshopper, data structures - commonly referred to as Data Trees - are incredibly important for maintaining scripting logic, and defining which particles should interact with specific springs. A Data Tree is a hierarchical organisation of data, made up of branches, list, and items (see figure 55). The smallest denomination is an item, which represents a single unit of data (e.g. a point, curve, surface, etc.). A list is a numerically ordered collection of items, with each item position being referred to as a "list index". Finally, the greatest denomination is a branch, which holds a list of items. This can range from a single branch containing a list in a Data Tree to an incredibly large number of branches containing lists, depending on the complexity of the data being handled. At its simplest, when handling interactions between two Data Trees with numerous branches,

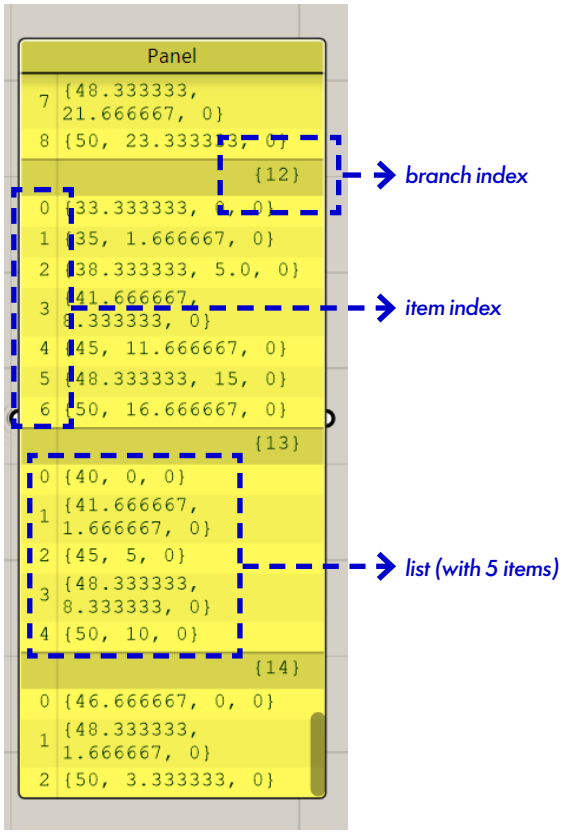


***figure 55:*** *A Data Tree with {14} branches and varied list lengths (source: own work)*

interactions will generally occur between corresponding list or branch indexes.

In the context of the modelling logic for the tool, each individual spring had to be constructed from the two adjacent particles along its axis of expansion. Achieving the necessary data structure required rebuilding the grid with manually scripted rotational parameters and boundary conditions that re-defined the grid extents, and later mapping the data structure of all the grid particles to each axis of expansion.

Figure 56 presents a grid of points for a fibre orientation of 0° where each list of points is grouped depending on its expansion in the x-direction (blue), or in the y-direction (red).

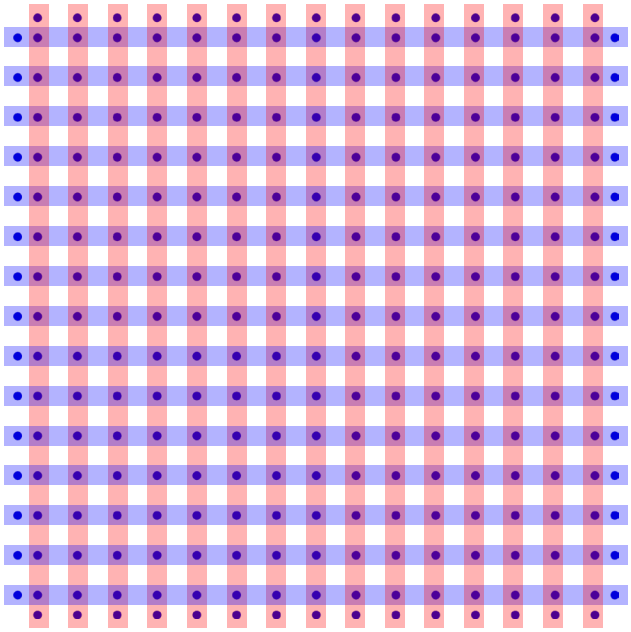

***figure 56:*** *Organising grid particles along the axis of expansion (source: own work)*

### Curvature simulation with the new system

The reconstructed bilayer model represented a much more cohesive and unified system where expansion forces in both directions would be exerted on each point. The deformation relied on the same principles of scaling ratios derived from the Timoshenko formula and the geometric modelling of the curvature, as was used in the predictive tool for monoclastic curvature.

While the values derived are appropriate for monoclastic curvature - given that the formula only calculates

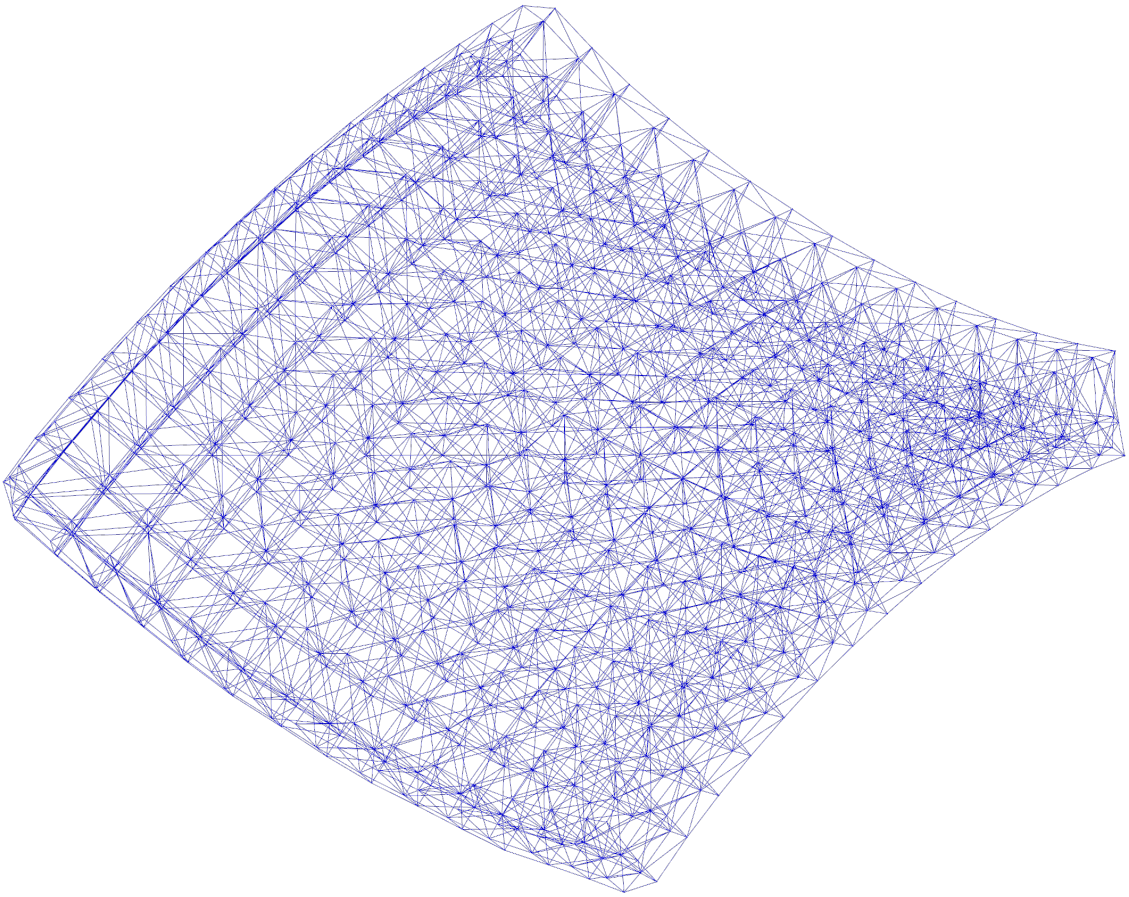

***figure 57:*** *Digital model exhibiting anticlastic curvature (source: own work)*

curvature for a single, uni-directional curve - the more complex interaction between two competing expansion criteria, in anticlastic curvature, is not so easily justified.

When a simulation was executed for an oak active layer and spruce passive layer, the bilayer model successfully exhibited anticlastic curvature. While this could be confirmed visually (see figure 57), this was not sufficient for justifying the final degrees of curvature for both orthogonal directions. In order to validate the digital model appropriately, physical data had to be prepared and collected for physical samples to validate the digital model.

***figure 58:*** *Deconstructed frame for anticlastic curvature (source: own work)*

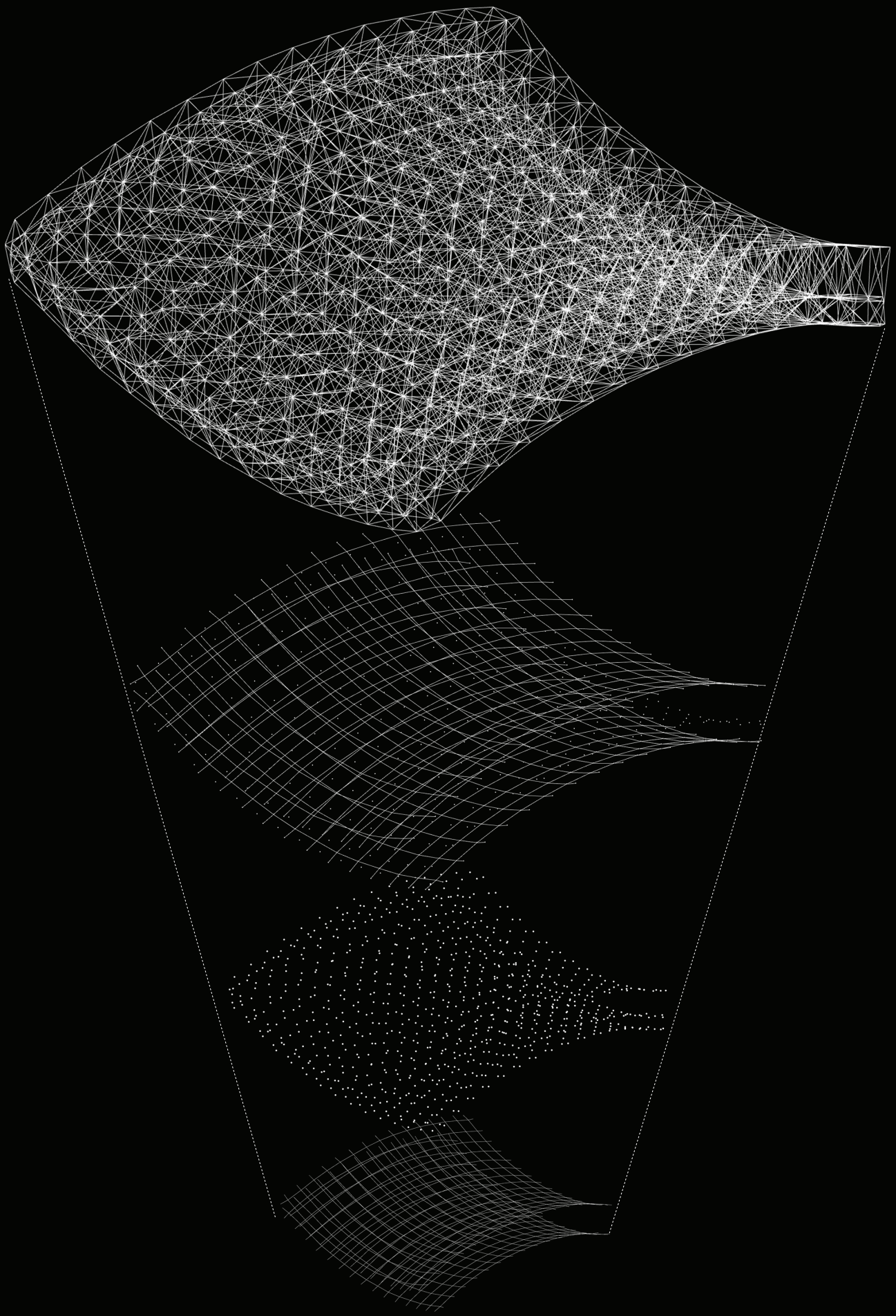

## 5.2 Developing the bilayer samples

### 5.2.1 Equipment and materials

Manufacturing a hygromorphic bilayer requires equipment for material sizing and trimming, appropriate conditioning, lamination of the individual layers, and testing at different relative humidities.

At Delft University of Technology, the Faculty of Architecture and the Built Environment - where this thesis is being conducted - offers lab and workshop spaces to assist in the construction of different samples. The laboratory includes equipment and chemical solutions for achieving and maintaining different relative humidity levels in insulated chambers, and the woodworking space is equipped with machinery for trimming down timber planks and re-sizing them to desirable aspect ratios. The university does not supply a large range of timber planks, so collecting materials required contact with external suppliers.

#### Heritage and Technology Lab

The basement of the Faculty of Architecture and the Built Environment is home to numerous labs and storage areas, including the Heritage and Technology Lab (H&T Lab). The main purpose of the space is for ". . . the development and assessment of solutions for the conservation of historic buildings" (TU Delft, 2026). The lab houses salt solutions that can lower or raise the dew point to control the amount of water vapour in the air, resulting in drier or over-saturated conditions. Moisture-reading devices are also available to assess the moisture content of samples that have been conditioned in climatic chambers.

When reaching out to prepare samples, the lab was already in-use by numerous PhD researchers who required access to the more high-powered conditioning chambers. A reliable alternative was a disconnected refrigerator that could serve as an insulated chamber to set a constant relative humidity. The internal dimensions of the refrigerator, where the samples could be stored, was around 410mm x 380mm x 530mm (see figure 59), making it small enough to quickly set the indoor climate while being spacious enough to accommodate numerous samples.




***figure 59:*** *internal dimensions of the refrigerator serving as the climatic chamber*

An uncovered plastic box (dimensions: 280mm x 185mm x 180mm) contained the salt solution for setting the relative humidity. Magnesium Nitrate Hexahydrate, Extra Pure, was used for setting a relative humidity of around 55%, at an average temperature range of 24-26°C. Two other salt solutions comprised of Potassium Chloride and Potassium Nitrate, condition the refrigerator to 85% and 95% relative

humidity, respectively.

Inside the refrigerator, a small ventilator fan is mounted on the top door shelf and angled towards the salt solution box at the bottom to improve the rate of evaporation and ensure the water vapour is dispersed evenly.

### Setting up the climatic chamber

To measure the changes in relative humidity, and ensure a constant state, humidity and temperature sensors were acquired to gather the appropriate data. The Environmental Research in Climate Lab (ERiC Lab) provided two separate sensors to allow for comparison and data consistency, and to ensure neither sensor was displaying unreliable or outlying results.

For the initial moisture conditioning, the container with the Magnesium Nitrate Hexahydrate, Extra Pure, was filled with deionised water and placed in the bottom of the refrigerator. Each sensor was placed towards the back, on different shelves above the container, to monitor whether their data would be matching to ensure the interior space was in equilibrium. Once the ventilator was powered on, constant monitoring was not necessary as the process was passive and self-regulating.

It is important to note that a state of equilibrium will only be achieved when the quantity of water is sufficient in saturating the chamber at the reduced dew point, but is not excessive enough to completely dissolve all the salt; resulting in an unsaturated solution. The water and salt mixture should mimic the consistency of wet sand, whereby the salt crystals are still visible, allowing them to absorb excess water from the air.

Determining the ideal water content required a small amount of trial and error, with initial climate settings displaying uncharacteristically high levels of relative humidity. The final ratio that achieved a constant relative humidity of 55% was approximately 3:1, with 318.98g of Magnesium Nitrate Hexahydrate, and 101.32g of deionised water.

### Acquiring timber samples

Acquiring the timber samples necessitated reaching out to external suppliers. This leads to certain financial limitations as timber - especially hardwoods - can be considerably expensive. Additionally, companies did not generally supply smaller samples as most distributors catered to construction companies with larger projects, such as flooring, or structural systems. Ultimately, the most accessible and affordable panels were acquired from the warehouse-style retailer chain, Hornbach, which supplied planks of untreated spruce wood (softwood) and oak wood (hardwood).

To achieve as much consistency as possible in the sample selection and uniformity of bilayer expansion, timber planks exhibiting minimal knots and cracking were carefully selected. This process is not entirely perfect as timber is an organic material. Therefore, during the fabrication process, cutting the planks into smaller bilayer samples involved working around any remaining deformations or irregularities still present where possible (see figure 60).

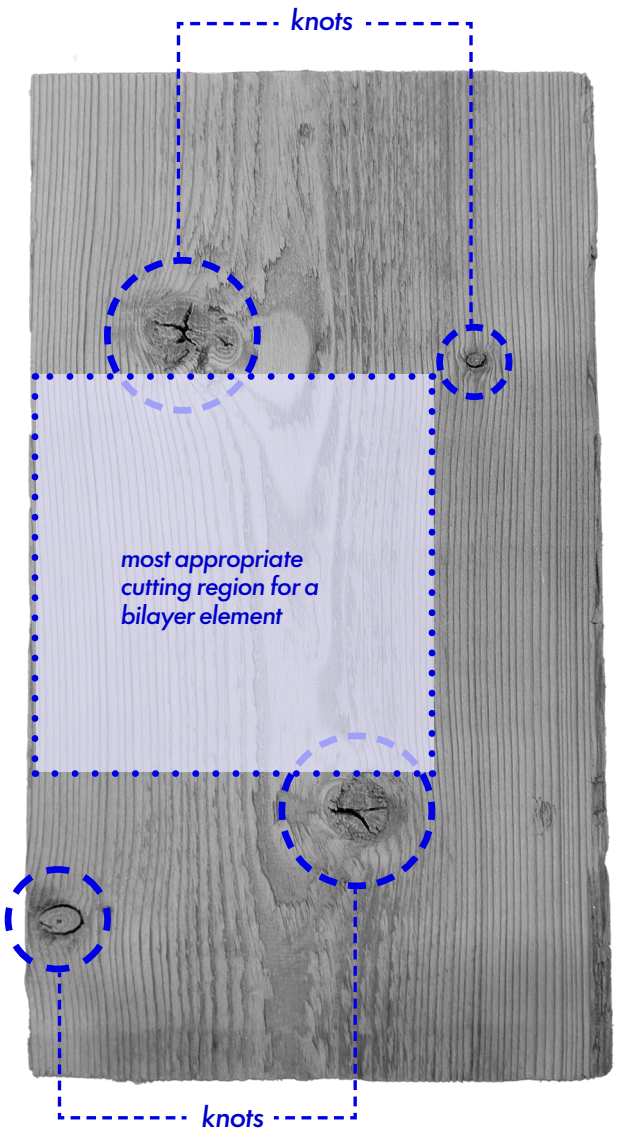


***figure 60:*** *Spruce plank with multiple knots (source: own work)*

## 5.2.2 Cutting the timber

### Formulating testing parameters and variables

When developing the sample range for any kind of laboratory testing, it is important to define the controlled, independent and dependent variables to ensure the results are organised, and can be compared against each other through shared factors to determine any trends.

To ensure the computational tool was validated extensively, the sample scope for the bilayer compositions had to vary across multiple factors. A range of different thicknesses and active-to-passive-layer ratios were explored, with controlled interval differences that made it easier to derive trends between samples.

As mentioned in prior sections, anticlastic curvature is achieved more reliably for samples with a low aspect ratio (Wood et al., 2018), therefore, as the first controlled variable, every hardwood and softwood panel was cut to the dimension of:

- 160mm x 160mm [length x width] (see figure 61)

This made the samples small enough to fit within the refrigerator for conditioning, but large enough to exhibit visible curving.

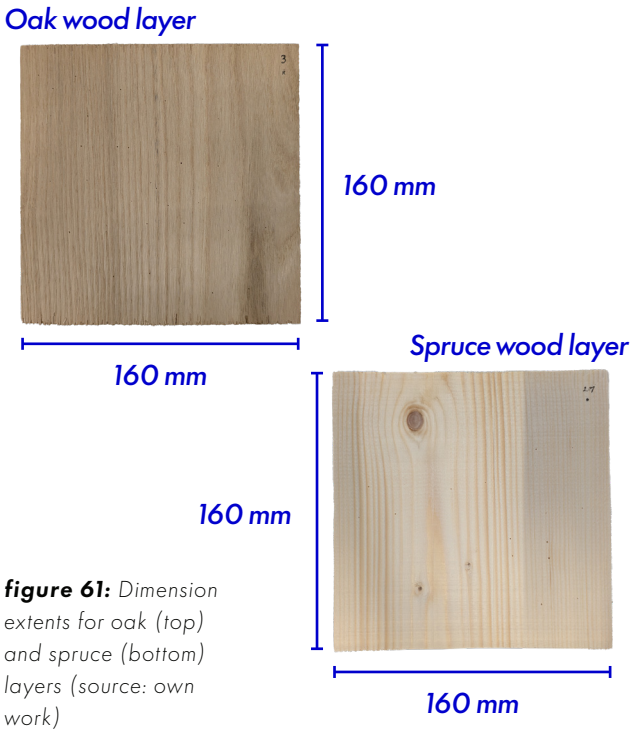


***figure 61:*** *Dimension extents for oak (top) and spruce (bottom) layers (source: own work)*

To achieve comparative results, three overall bilayer thicknesses were selected, ranging across:

- 6mm
- 8mm
- 10mm

It was important to maintain a consistent increase in overall thickness to ensure the difference between the lowest and highest values was linear. A secondary factor that influences anticlastic curvature is difference in thickness between the passive and active layer. A ratio greater than 1:4 (passive-to-active) should be avoided to achieve anticlastic curvature. Therefore, to explore how different bilayers behave, the following range of thickness ratios were constructed for the passive versus active layers:

- 1:1
- 1:2
- 1:3

The final sample distribution is displayed in the table below with associated layer thicknesses for each ratio:

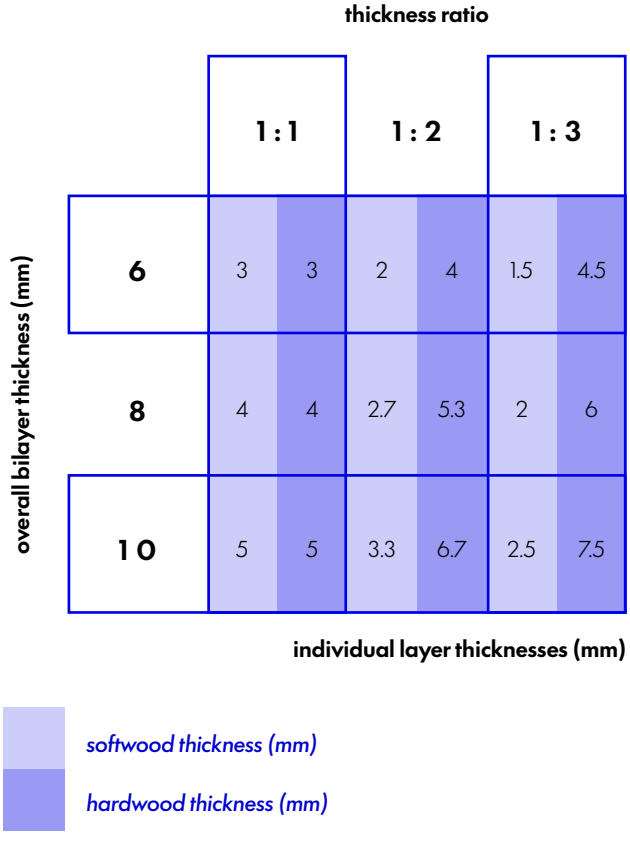


***figure 62:*** *Bilayer dimensions for sample range (source: own work)*

To allow for comparison, two groups of the entire sample distribution were constructed. A comparison across 3 groups would have been more ideal, but unfortunately due to the time constraints, available space within the refrigerator for conditioning, and the capabilities of the equipment for woodworking, only 2 sample groups could be realistically achieved.

**Trimming and sizing samples**

The initial dimensions of the oak planks were 195mm x 19mm x 2500mm (width x depth x length), while the spruce planks were 196mm x 18mm x 2100mm (width x depth x length).

To assist with achieving the smaller samples and thinning them down, the wood workshop at the architecture faculty (see figure 63) offers a range of machinery, including;

- Wood planer and joiner
- CNC-milling machines
- Circular saws
- Jigsaws
- Vertical band saws
- Disk sanders
- Belt sander
- Drum sanders
- Wet disk sander
- Polishing machine
- Standing drill presses
- Vacuum shaper
- Wood lathe (TU Delft, 2026)

Given the very specific range of layer thicknesses required for the oak and spruce wood, the planer was effective as an initial step to thin down the larger planks, before cutting each layer to the desired sample size with the vertical band saw. In the final stage, an electric belt sander was used to sand down each layer to their required thickness.

### 5.2.3 Conditioning the individual timber layers

**Assessing conditioning timeframe**

After completing the sizing, it was necessary for all the individual samples to reach a unified equilibrium moisture content as an initial starting point before corresponding panels could be laminated together into bilayers and re-conditioned.

Within current literature, there is a limited amount of research that clearly quantifies the amount of time



***figure 63:*** *Interior photograph of the wood workshop at the Faculty of Architecture and the Built Environment (source: own work)*

required for hardwood and softwood timber samples of different thicknesses to reach equilibrium moisture content under varying relative humidity conditions. A 2015 paper by Albrektas & Ukvalbergiene investigated how the absorption properties of six wood species were influenced by dimensions, cellular composition, and temperature. Part of their research compared the absorption time for samples with a thickness of 7, 12, 25 and 30mm. Across all four thicknesses, the relationship between moisture content and time followed an exponential trend: approximately 80% of moisture absorption occurred rapidly within the first two weeks, while the final stages of absorption for moisture content equilibrium required considerably more time. It is important to note that the thinner the sample, the shorter the period of time for initial moisture uptake, as can be seen below in figure 64 where the 7mm sample achieves moisture equilibrium earlier than its thicker counterparts.

Similarly, a 2024 paper by Tian et al. also examined how the dimensional thickness influenced moisture absorption rates. Laminated components with thicknesses of 6.35, 12.7, 63.5 and 200mm were analysed under conditions ranging from 0% to 18% equilibrium moisture content (see figure 65). The study found that it took, respectively, 3.9 days, 35 days, over 800 days, and an estimated "thousands of days", for each sample to achieve 95% equilibrium moisture content.

Although the exact values reported across studies are not fully consistent when compared against each other, the literature indicates that thicker timber samples require exponentially longer periods of time to reach equilibrium moisture content compared to thinner samples.

Given that the thickest oak panel conditioned in this study was 7.5 mm, based off the findings from the literature, it is estimated that more than 85% of the target moisture content will have been absorbed within 14 days. Under ideal conditions, the conditioning period would have extended beyond one month to ensure complete and uniform moisture equilibrium throughout the material. However, given the limited timeframe available for the research, a two-week conditioning period was adopted as a practical benchmark. This duration would still lead the oak layer to achieve the majority of its expansion in the bilayer system, while the remaining 15% of moisture absorption would likely have had only a minor influence on the final curvature.

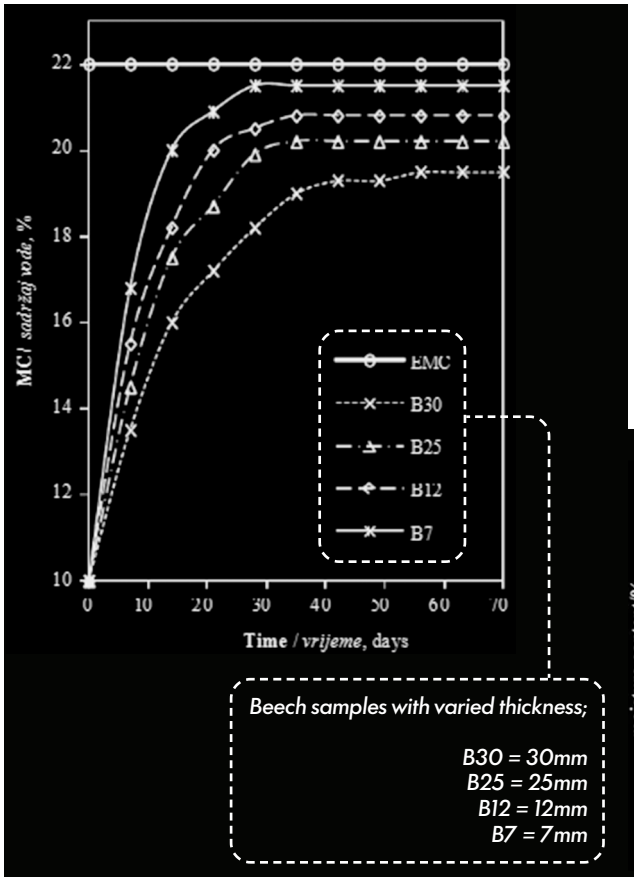


**figure 64:** *Changes in wood moisture content during the moistening process (source: Albrektas & Ukvalbergiene, 2015)*

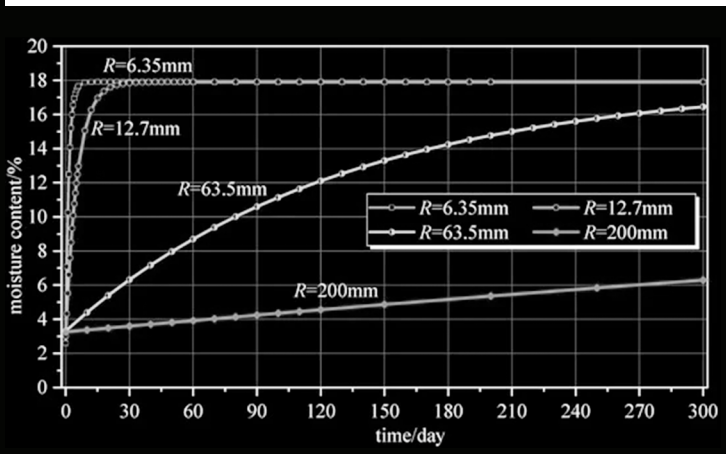


**figure 65:** *Influence of sample dimensions on average moisture content (source: Tian et al., 2024)*

## Determining initial data from samples

Collecting base-state data from the samples is important as a means for comparison throughout the absorption and lamination processes. To determine the initial

water moisture content, the Heritage and Technology Lab had a Bosch Universal Humid Meter available. The device is comprised of a small screen that presents the moisture content and two pins that extrude from the top. To measure data, the pins are inserted into the timber so that the distance between both pins is perpendicular to the grain orientation (see figure 66). Different timber groups can be selected for analysing softwoods versus hardwoods, although this process is manual and demands a certain degree of awareness when gathering data on the two different sides of the bilayer. For consideration - according to the Bosch website - results are displayed to an accuracy of 1% (Bosch, 2026). The weight of each sample was also recorded prior to the first stage of conditioning with the assistance of a METTLER Toledo scale that provided accurate data to two decimal places.

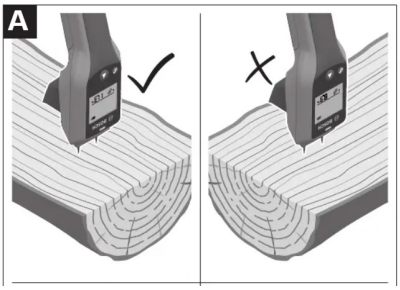


***figure 66:*** *How to measure moisture content with Bosch Universal Humid Meter (source: Bosch, 2026)*

### Setting up the samples

A total of 36 individual panels were cut for the purpose of the experiment. However, the refrigerator had limited capacity, consisting of only two small shelves near the top. As it was important for both sides of each panel to remain as exposed as possible to ensure even moisture absorption, stacking the panels directly on top of one another was not suitable.

To accommodate all the samples, while maximising uniform water absorption, the panels were arranged on small movable racks across the two shelves (see figure 67).




***figure 67:*** *Organising the refrigerator for moisture conditioning (source: own work)*

During the two week period, across which the samples remained in the refrigerator, the data from the humidity and temperature sensors was read out on multiple occasions to ensure the relative humidity was consistent.

Despite research indicating that the salt solution would achieve a relative humidity of approximately 55%, the climate inside the refrigerator stabilised at a slightly lower range of 51-54%, which nevertheless remained suitable for the experiment. During the first five days of conditioning, an irregularity in the process was observed when the relative humidity unexpectedly dropped from 56% to 41%. As a result, the climate within the refrigerator had to re-stabilise over a period of around two days, introducing a minor inconsistency in the conditioning process. A graph of the climatic conditions of the refrigerator are presented in figure 68, indicating relative humidity and internal temperature.

## 5.2.4 Laminating the panels

### Assessing moisture content post-conditioning

Once the two-week period had elapsed, each sample was re-weighed and the moisture content was measured again. It was important that all paired softwood and hardwood layers possessed near-identical moisture levels to ensure both layers absorbed equal amounts of moisture throughout the post-lamination conditioning process and to avoid any imbalances in expansion.

When collecting data with the Bosch Universal Humid Meter, minor inconsistencies within a decimal range were observed, as moisture levels were not entirely uniform across the surfaces of the panels. In order to improve the reliability of the measurements, multiple readings were taken across the surface (see figure 69 on next page) and on both sides of each sample, before being averaged. A maximum variation of 1% between the highest and lowest readings was considered acceptable to ensure no excessive deviations were present.

The averaged values were then compared with those of the corresponding paired panel within each bilayer. It was found that variations in the results for each individual panel, and between paired panels, all remained within the range of 1%. This indicated that all samples remained below the threshold in reaching moisture equilibrium, and that the

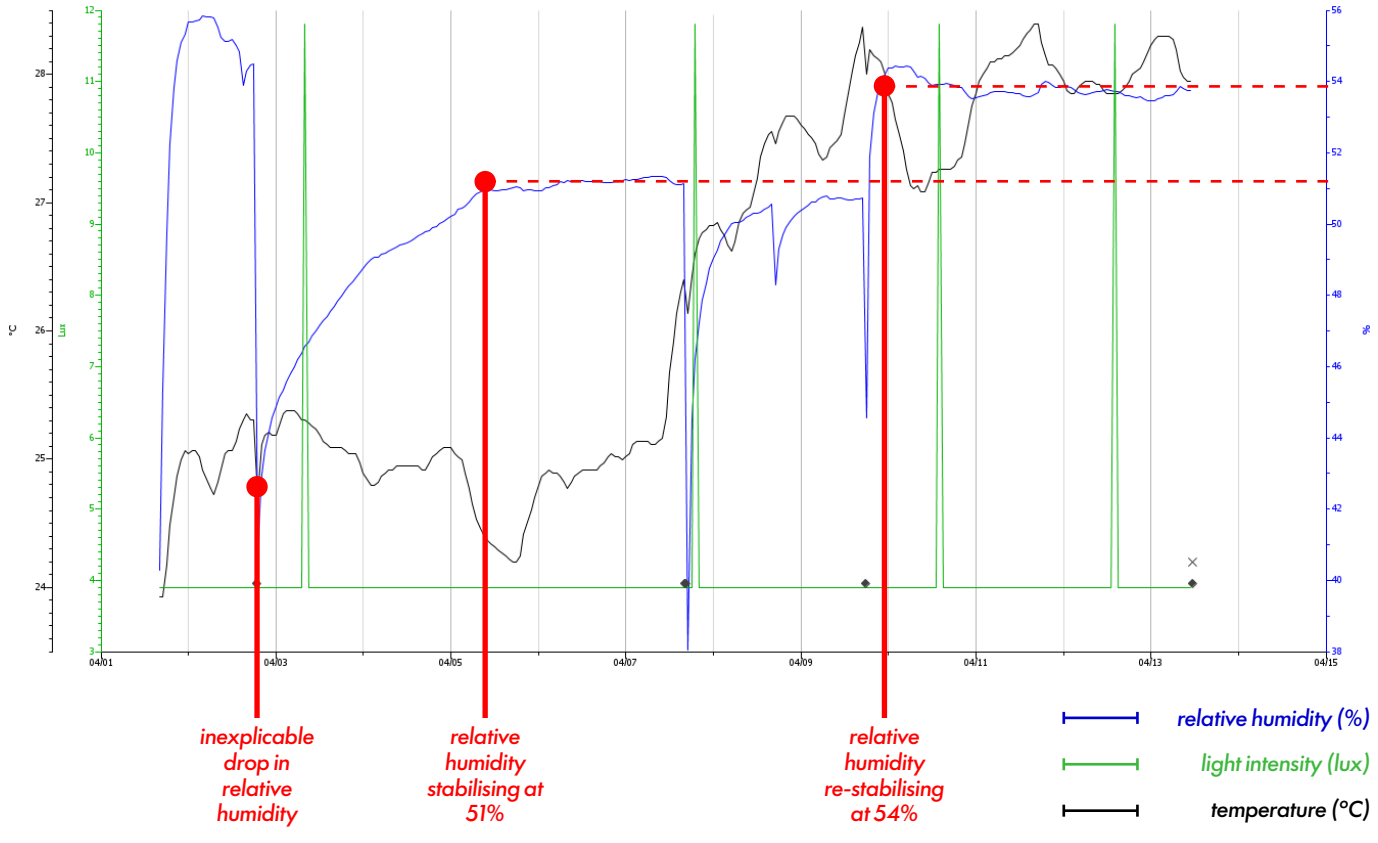


***figure 68:*** *Climatic data within the refrigerator across a period of 14 days (source: own work)*

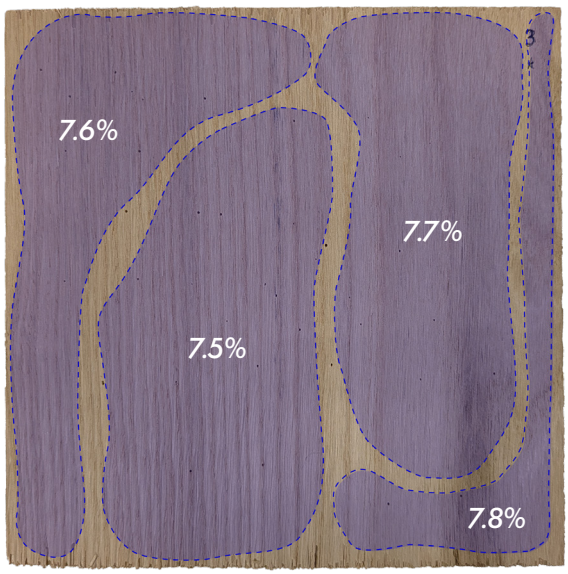


***figure 69:*** *Varied moisture content results from the Bosch Universal Humid Meter across the surface of an oak sample (source: own work)*

full sample set maintained a consistent moisture level of approximately 7–8%.

### Laminating the panels into bilayers

To laminate the panels, machinery for either a hot or cold press was not readily available. As a substitute, wood glue was used as the adhesive bonding agent, while the panels were firmly clamped together for a period of two days to allow the glue to cure. Due to the confined space within the refrigerator and the size of the clamps,the bilayers had to be constructed across two separate groups and stacked on top one another in an effort to minimise the number of clamps required (see figure 70).

This raised some concerns for the effectiveness of the lamination process, as well as the possibility of adjacent bilayers bonding together at the edges. While some unintended bonding did occur, the issue was easily resolved by separating the attached bilayers with a utility knife.

The final results were successful, although small amounts of excessive adhesive overflow were present on some samples. These were subsequently trimmed away to ensure smooth and even edges.

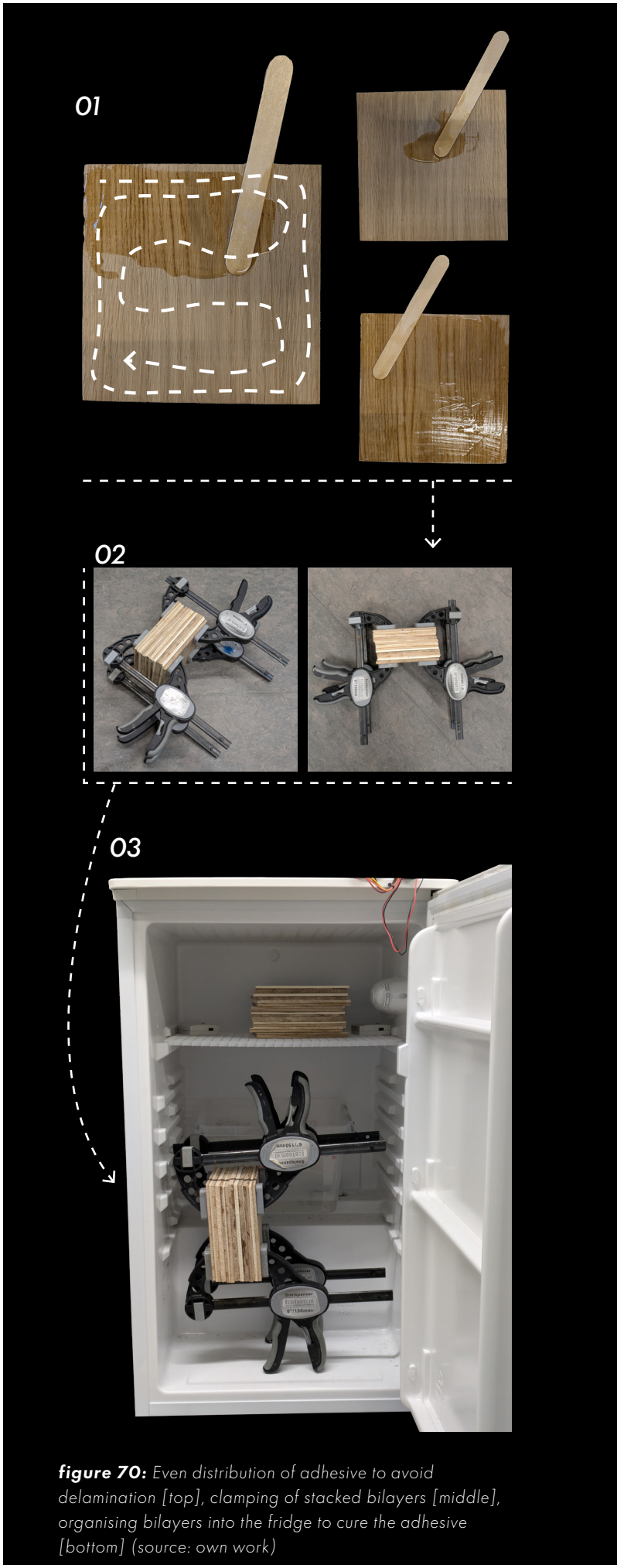


***figure 70:*** *Even distribution of adhesive to avoid delamination [top], clamping of stacked bilayers [middle], organising bilayers into the fridge to cure the adhesive [bottom] (source: own work)*

## 5.2.5 Raising the moisture content of the bilayers

### Achieving the target relative humidity

Similar to the conditioning process, raising the moisture content of the bilayers requires a stable climatic environment. Thankfully, the Heritage and Technology Lab offers salt compounds that can achieve stable climates of 85% and 95% relative humidity.

To achieve the greatest amount of moisture absorption - and therefore by extension, the greatest degree of expansion - the salt compound of Potassium Nitrate was used to create a controlled relative humidity of 95%.

Due to the slightly lower relative humidity achieved for the initial conditioning process, rather than use a mixture of 1:3 for water-to-salt, an approximate 1:1 mixture was used instead. Around 498.5g of salt was mixed with 450.98g of water to replace the Magnesium Nitrate Hexahydrate, Extra Pure, solution.

The bilayers were re-organised onto the shelves using the racks, and monitored using the sensors. The climatic data was read out approximately every two to three days to ensure the relative humidity was climbing steadily and a stable environment was being achieved (see figure 71).

Throughout the process, more water had to be added as the quantity in the container had dropped (due to the absorption from the panels) and the relative humidity wasn't climbing high enough. An additional amount of 150.56g was added in the first week, and 136.98g was added in the second week (see appendix 6 for all moisture graphs)

### Moisture content of bilayers post-humidification

Following the two weeks of humidification, the bilayers were removed from the refrigerator and their moisture contents were analysed again. From the assessments, bilayers with a moisture content disparity greater than 1% between the hardwood layer and the softwood layer were determined. From group one, the bilayer configurations with thickness 8mm and ratio 3:1, and thickness 10mm and ratio 1:1 fell outside the margin, and from group two, the bilayer configurations with thickness 6mm and ratio 1:1, thickness 8mm and ratio 2:1, and thickness 8mm and ratio 3:1 fell outside the margin. In all five cases, the greatest moisture content disparity was a difference of 1.5%. It was decided that the disparity wasn't enormous, and curvature results from these bilayers was still included (see appendix 7 for tables of moisture data).

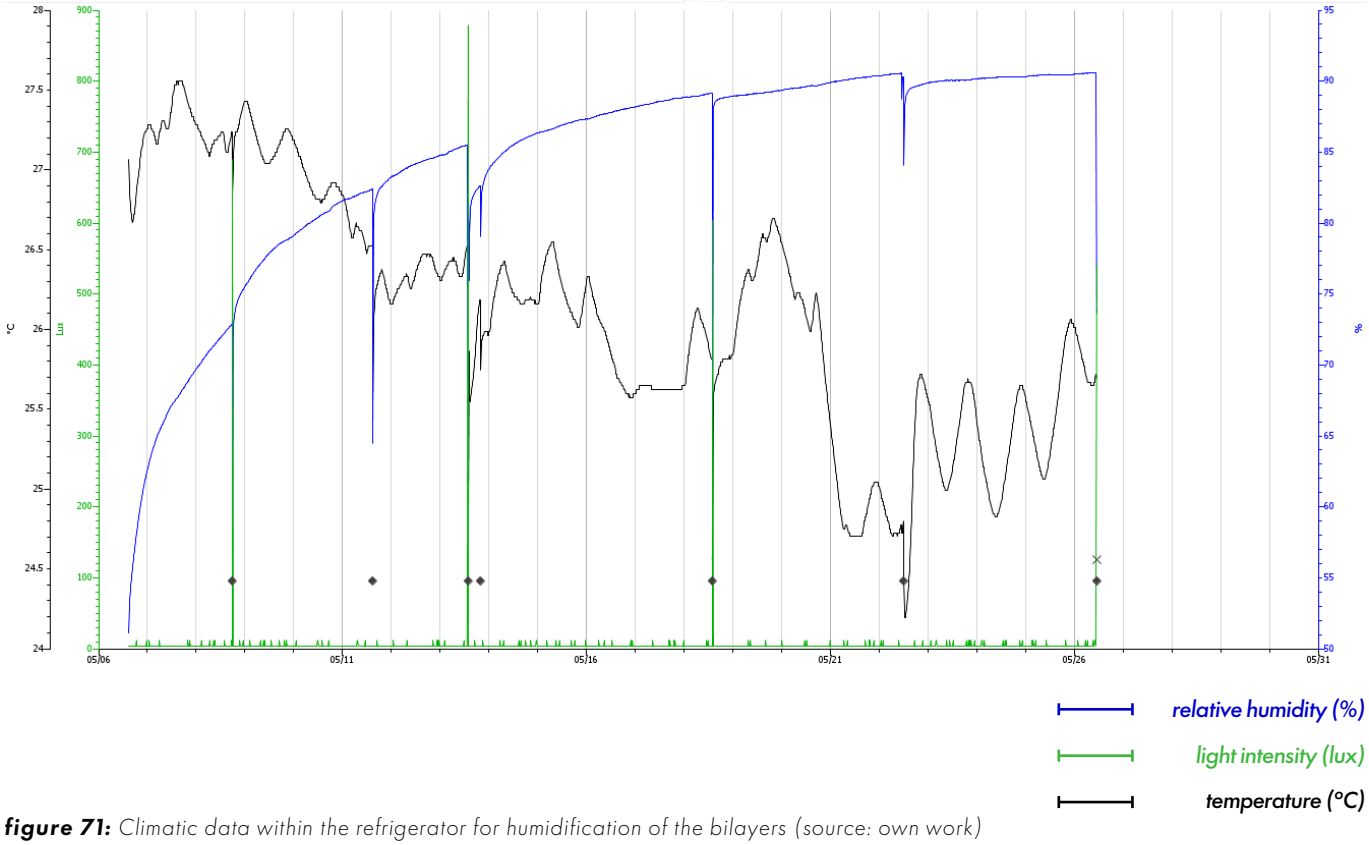


***figure 71:*** *Climatic data within the refrigerator for humidification of the bilayers (source: own work)*

## 5.3 Informing the anticlastic simulative tool

### 5.3.1 Deriving curvature from samples

The 2018 paper, "Hygroscopically actuated wood elements for weather responsive and self-forming building parts", by Wood et al., employs 3D scans of deformed bilayer samples to assess their curvature. Due to the high accuracy of modern 3D scanning software, a similar procedure is also carried out in this paper to gather data on the degree of curvature along both perpendicular directions of expansion.

#### DINED research space

In the faculty of Industrial Design Engineering, the DINED project, initiated by the Applied Ergonomics and Design Section of the Human-Centred Design Department, carries out research on the application of 3D scanning in anthropometry (Delft University of Technology, 2026). As a result, their lab is equipped with a range of high-powered 3D scanners. Given the dimensions of the timber samples, a full-body scanner is not necessary, and the handheld Artec Spider II scanner was used instead. Despite its smaller size, the Artec Spider II scanner is an extremely accurate 3D scanner, advertised to achieve a resolution of 0.05mm with an accuracy 0.05mm (Artec 3D, 2026).

#### Scanning the bilayers

At the DINED lab, each individual bilayer was setup on a rotating stool and elevated slightly atop a small cup to help leave the edges unobstructed (see figure 72). Scans were taken on one side of the bilayer before flipping and creating separate scans on the opposite side. To combine both scans into one 3D mesh geometry, post-processing was done within the Artec Studio software (see figure 73). The application offered a range of tools for mesh editing, refinement and exporting. including "Registration", "Outlier Removal", "Align" and "Fusion". Each scan was simplified with "Registration" and "Outlier Removal" to remove mesh faces that were introduced unnecessarily, before being rotated

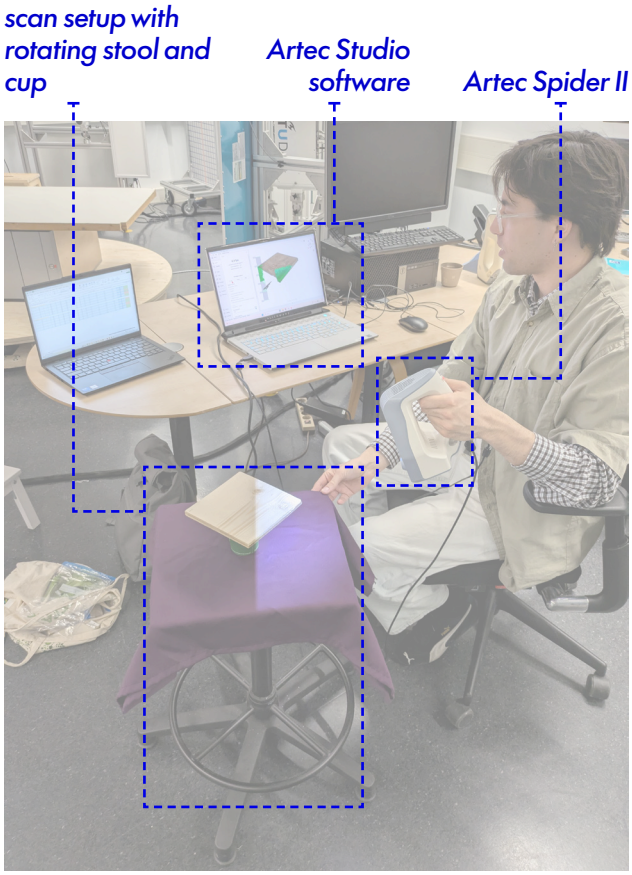


***figure 72:*** *Scanning setup (source: own work)*

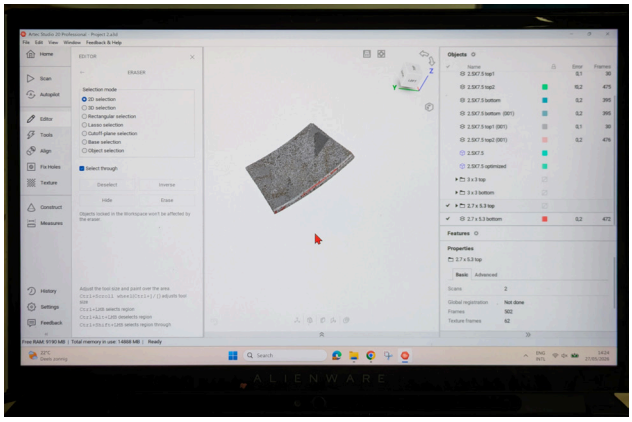

***figure 73:*** *Artec Studio software interface for mesh editing and optimisation (source: own work)*

and aligned automatically. The Studio software is capable of effectively analysing both mesh scans for matching images and organising alignment based on correlating photos. In the final step, both scans were fused together to create a single, digital geometry of the bilayer panel, which was compared to the real-world sample to ensure accuracy of the final model.

## Evaluating edge curvature

The degree of curvature for the scanned bilayers was evaluated geometrically in the 3D modeling software Rhinoceros3D as it presented the easiest method for deconstructing and analysing the 3D scans. To consider anticlastic deformation, curvature results were derived in both the direction of expansion of the hardwood (x-direction), and the direction of expansion of the softwood (y-direction).

Final curvature was evaluated by determining the opposing extremities of each edge as two points, before geometrically evaluating the intersecting centre as the third point (see figure 74). An arc was constructed through the three points and then re-positioned with Grasshopper components to ensure each point lay along the same planar axis. The final curvature was derived from the radius of the arc.

For each digital model, the uppermost and lowermost arc was evaluated along the two principal directions to determine limits and an average range; resulting in a total of four arcs.

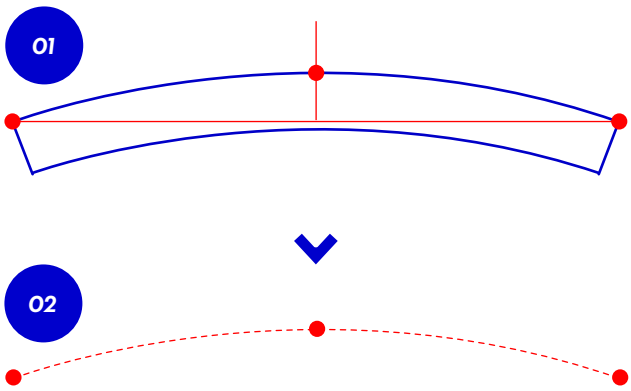


***figure 74:*** *Deriving curvature from the 3D scans by re-constructing an arc through the extremities and the central point (source: own work)*

## Analysing results

An overall analysis of the final curvature results displayed numerous trends that correlated appropriately with the expected behaviour. From an understanding of monoclastic curvature, as the ratio between both layers increases (i.e. the active layer becomes thicker than the passive layer), a greater degree of curvature should be exhibited. Additionally, a thicker passive layer will result in greater bending stiffness which will limit curvature for the hardwood but result in greater curvature from the softwood.

When deriving the results from the digital models, a greater degree of curvature along the direction of expansion of the spruce wood (y-direction) was most noticeable in bilayer samples with a thickness ratio of 1:1, as predicted, and especially for thinner samples. Taking curvature in the y-direction as negative, for group one, the bilayer configuration with layer thicknesses of 3mm x 3mm showed a curvature of $-0.148 \times 10^{-3}$ mm$^{-1}$. Whereas, for the bilayer configuration with 4mm x 4mm thick layers, the curvature was $-0.1455 \times 10^{-3}$ mm$^{-1}$, and for a configuration of 5mm x 5mm, the curvature was $-0.2745 \times 10^{-3}$ mm$^{-1}$. In a similar fashion, curvature along the direction of expansion of the hardwood (x-direction) was also greater for thinner samples with a ratio of 1:1.

This trend is also visible for samples with a thickness ratio of 2:1. For group two, the bilayer configuration with layer thicknesses of 4mm x 2mm showed a curvature of $2.361 \times 10^{-3}$ mm$^{-1}$. Whereas, the curvature for the bilayer with 5.3mm x 2.7mm was smaller, at $1.917 \times 10^{-3}$ mm$^{-1}$, and for the configuration of 6.7mm x 3.3mm, the curvature was $0.7245 \times 10^{-3}$ mm$^{-1}$.

For all samples with a thickness ratio of 3:1, curvature tended towards a monoclastic shape, indicating that the difference in the degree of curvature in the x-direction versus the y-direction was quite large. For both groups, the bilayer configuration with thickness 2.5mm x 7.5mm exhibited significantly greater curvature in the x-direction. For the sample in group 1, the curvature in the x-direction was $1.623 \times 10^{-3}$ mm$^{-1}$, and $-0.0675 \times 10^{-3}$ mm$^{-1}$ in the y-direction. The sample in group 2 displayed a curvature of $1.797 \times 10^{-3}$ mm$^{-1}$ in the x-direction, and $-0.0355 \times 10^{-3}$ mm$^{-1}$ in the y-direction. This indicates a significant disparity in the degree of curvature

in the x-direction compared to the y-direction.

As mentioned, these behavioural trends are not entirely unfamiliar, and build upon established literature concerning the behaviour of timber and monoclastic bilayer curvature. Although anticlastic and monoclastic curvature indicate different geometric types of deformation, the anticlastic curvature results exhibited a similar relationship regarding overall bilayer thickness, active-to-passive layer ratios. The consistency of these trends suggests that the observed anticlastic behaviour is not irregular or isolated, but rather it is grounded in the same underlying material and mechanical principles established in existing hygromorphic research. The translation of validated monoclastic deformation behaviours to anticlastic curvature provides greater confidence in the validity of the final physical findings presented in this study.

### 5.3.2 Informing the computational tool

#### Timoshenko-based scaling

Once curvature data for all 18 samples had been derived, the degree of curvature in the x-direction (where the expansion of the hardwood dominated) was compared against results from the Timoshenko formula. Considerable disparities between the sample data and mathematical results indicated critical limitations and drawbacks for the application of Timoshenko in anticlastic curvature

Curvature values for all bilayer configurations were calculated with Timoshenko, based on the moisture content of each physical sample. As predicted, the trends in results demonstrated an increasing radius for configurations were the passive layer became increasingly thinner than the active layer. A decrease in radius can also be noted where the overall thickness of the bilayers decreased (i.e. they became thinner). As mentioned previously, these trends are not unfamiliar and can be understood by the dominating behaviour of the active layer over the passive layer (see appendix 7 for all curvature results).

But when the values for curvature are analysed more closely, the Timoshenko results for the configurations with a layer ratio of 1:1 are disproportionately larger than those from the physical samples. This means that the radius of curvature predicted by Timoshenko is extremely small, whereas the physical samples present vastly greater radii. For the 3mm x 3mm configuration in group 2, the radius of curvature in the x-direction was 990mm, compared to 475mm from Timoshenko. Similarly, for the configuration of 4mm x 4mm, the radius of curvature was 1 937mm, while Timoshenko indicated a radius of 635mm. Finally, for the 5mm x 5mm configuration, the radius was recorded at 2 273mm, versus 769mm from Timoshenko. An important distinction to note, is that as the active layer became thicker, the results from the formula became more accurate.

This analysis demonstrates that while the Timoshenko formula can be relatively accurate for bilayers with dominating active layer behaviour, it is extremely inaccurate for configurations approximating anticlastic curvature. Timoshenko exclusively considers the longitudinal cross-section of a bilayer when deriving curvature, and therefore only a single direction of expansion is considered. Any influence on overall curvature from the passive layer's expansion in the perpendicular direction is completely disregarded. As the results indicate, the passive layer behaviour cannot be ignored as it restricts the active layer's curvature significantly.

#### From physical sampling to digital simulation

Informing the digital simulation for anticlastic forms with material data derived from formulae presents a significantly large research gap. Although Timoshenko works effectively for monoclastic simulations, where the active layer is (minimum) four times thicker than the passive layer, it is not applicable for anticlastic simulations. Deriving reliable calculations that can predict multi-directional curvature will demand considerably more research. Thankfully, both simulative tools are specifically constructed to receive numerical data from curvature, and adapt it quickly to form-finding. For the anticlastic simulation, this makes implementing the data gathered in physical samples extremely easy.

From the samples, the scaling ratio employed for monoclastic curvature can be calculated from the average curvature in both the x- and y-direction. This presents two scaling ratios that inform the simulative tool separately but

achieve a unified deformation.

To ensure consistency in the simulated behaviour of the final model, the curvatures along the x- and y-direction were re-calculated and then compared again to the original curvatures from the samples. The results presented a very disproportionate range of accuracy. For directions of expansion in which the degree of curvature was greater (largely exhibited by the hardwood layer), the simulation presented a very high accuracy of 94-98%. Whereas in cases where the degree of curvature was exceedingly small (largely exhibited by the softwood layer), the accuracy of the simulation was proportionally lower, ranging from 12-55%. The data on the following page provides an overview of compared results for group 1. For values of curvature greater than 0.00065, the accuracy remains above 95%. For curvatures below 0.00015, the accuracy got progressively worse in stages. The greatest range of accuracy was 44-55% for 0.00015 curvature, before dropping to around 21-36% for curvatures within 0.00010 - 0.00011. The lowest accuracy range of 12-15% was present for curvature between 0.00006-0.00009.

**Implications of results**

As determined from results, there is an exponential decrease in accuracy for the simulation as the degree of curvature becomes smaller. A significant reason for this is the margin of error is the disproportionate precision demanded between finitely small curvatures versus larger curvatures.

When the tool carries out its form-finding for extremely small curvatures, any minor deviations in vertical amplitude of the final curve can produce disproportionately large differences in the resulting curvature radius. Conversely, for higher degrees of curvature, the radius is far smaller and therefore similar deviations represent a much more minor influence on the overall geometric scale. For example, we can consider a width of 100mm, and amplitude ranges of 1mm versus 2mm, and 40mm versus 41mm. At an amplitude of 1mm, the radius is 1250.5mm, and at 2mm it is 626mm, indicating a difference of 624.5. In comparison, at an amplitude of 40mm, the radius is 51.25mm, and 51mm for an amplitude of 41mm, with a difference of 0.25mm. If we assume the same margin of error of 1mm for both cases, the difference in results between 1mm and 40mm amplitude is disproportionate.

As a result, although the simulative tool works to accurately approximate curvature through geometric expansion, it is severely limited for highly precise curvature demands. Back-calculating from the final results, the simulative tool appears to exhibit a margin of error for amplitude of +/- 1mm, which is considerably precise.

**Group 1**
3mm x 3mm

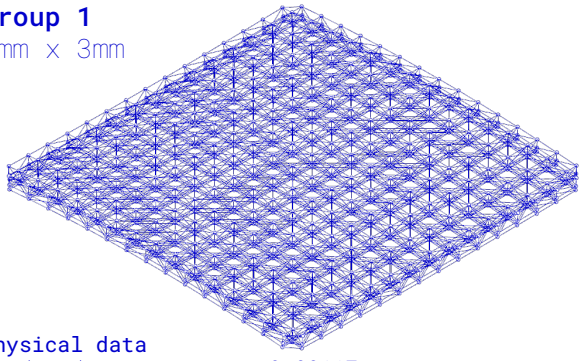

**Physical data**
hardwood curvature: 0.00117
softwood curvature: 0.00015

**Simulation results**
hardwood curvature: 0.00115 [accuracy; 98%]
softwood curvature: 0.00034 [accuracy; 44%]

**Group 1**
4mm x 2mm

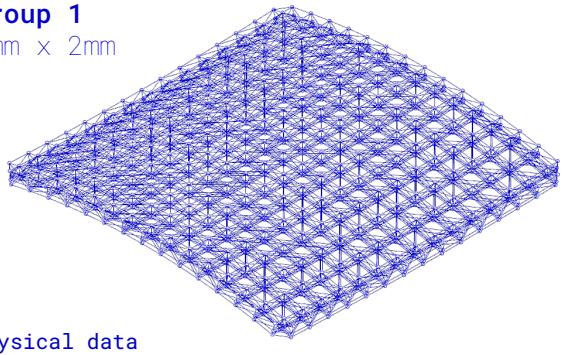

**Physical data**
hardwood curvature: 0.00299
softwood curvature: 0.00011

**Simulation results**
hardwood curvature: 0.00282 [accuracy; 94%]
softwood curvature: 0.00052 [accuracy; 21%]

**Group 1**
4.5mm x 1.5mm

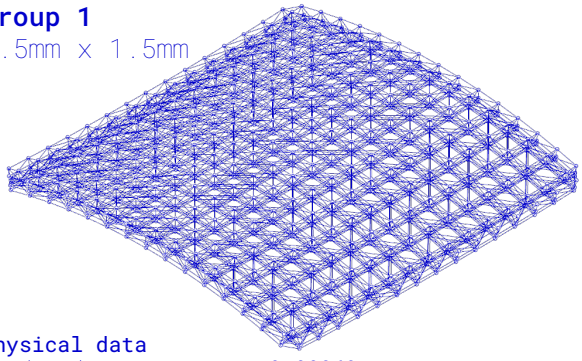

**Physical data**
hardwood curvature: 0.00362
softwood curvature: 0.00009

**Simulation results**
hardwood curvature: 0.00339 [accuracy; 94%]
softwood curvature: 0.00061 [accuracy; 15%]

## Group 1
4mm x 4mm

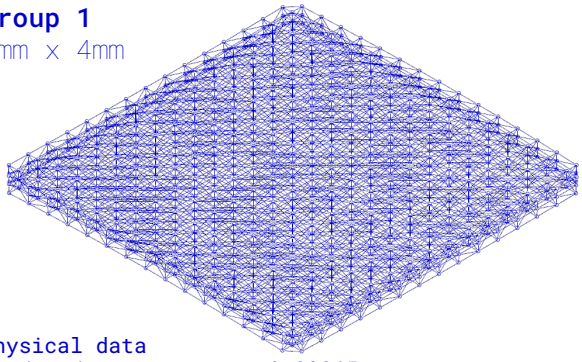

**Physical data**
hardwood curvature: 0.00065
softwood curvature: 0.00015

**Simulation results**
hardwood curvature: 0.00064 [accuracy; 98%]
softwood curvature: 0.00027 [accuracy; 55%]

## Group 1
5mm x 5mm

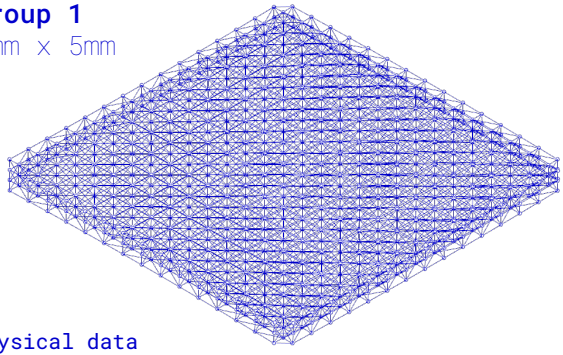

**Physical data**
hardwood curvature: 0.00033
softwood curvature: 0.00027

**Simulation results**
hardwood curvature: 0.00038 [accuracy; 87%]
softwood curvature: 0.00034 [accuracy; 79%]

## Group 1
5.3mm x 2.7mm

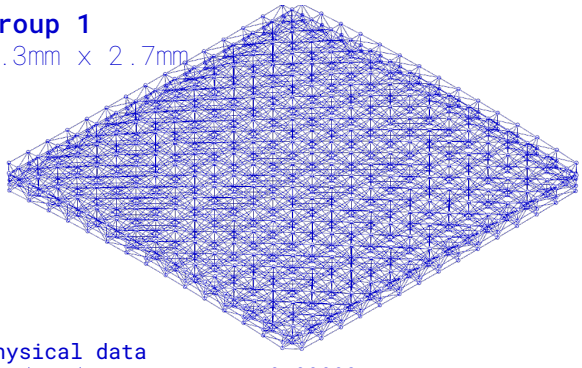

**Physical data**
hardwood curvature: 0.00093
softwood curvature: 0.00010

**Simulation results**
hardwood curvature: 0.00092 [accuracy; 99%]
softwood curvature: 0.00027 [accuracy; 36%]

## Group 1
6.7mm x 3.3mm

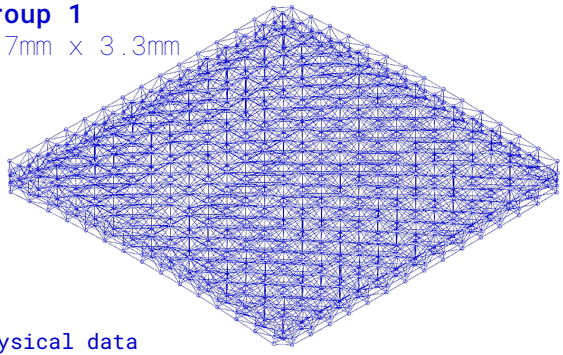

**Physical data**
hardwood curvature: 0.00105
softwood curvature: 0.00015

**Simulation results**
hardwood curvature: 0.00104 [accuracy; 99%]
softwood curvature: 0.00036 [accuracy; 42%]

## Group 1
6mm x 2mm

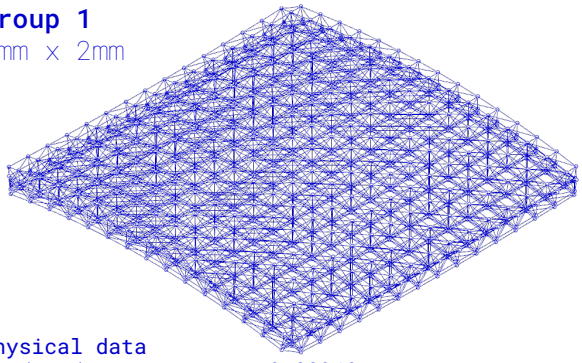

**Physical data**
hardwood curvature: 0.00240
softwood curvature: 0.00006

**Simulation results**
hardwood curvature: 0.00229 [accuracy; 95%]
softwood curvature: 0.00049 [accuracy; 12%]

## Group 1
7.5mm x 2.5mm

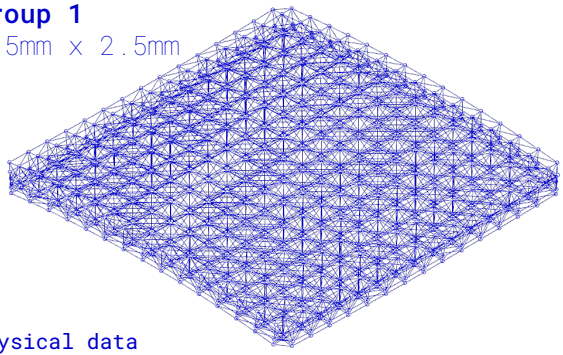

**Physical data**
hardwood curvature: 0.00162
softwood curvature: 0.00007

**Simulation results**
hardwood curvature: 0.00156 [accuracy; 96%]
softwood curvature: 0.00039 [accuracy; 17%]

## 5.4 Flowchart of simulative tool for anticlastic curvature (see appendix 8 for Grasshopper script)

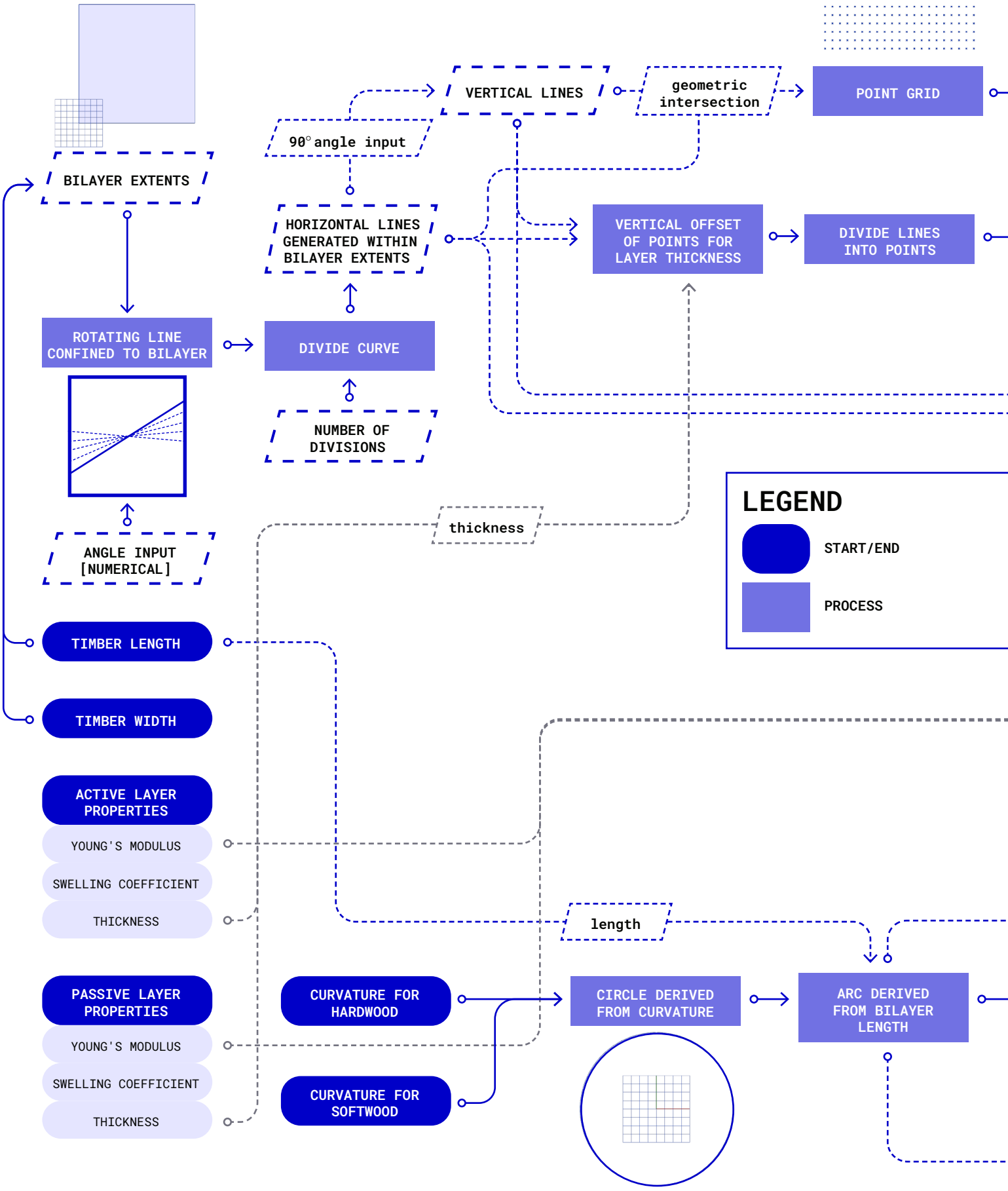

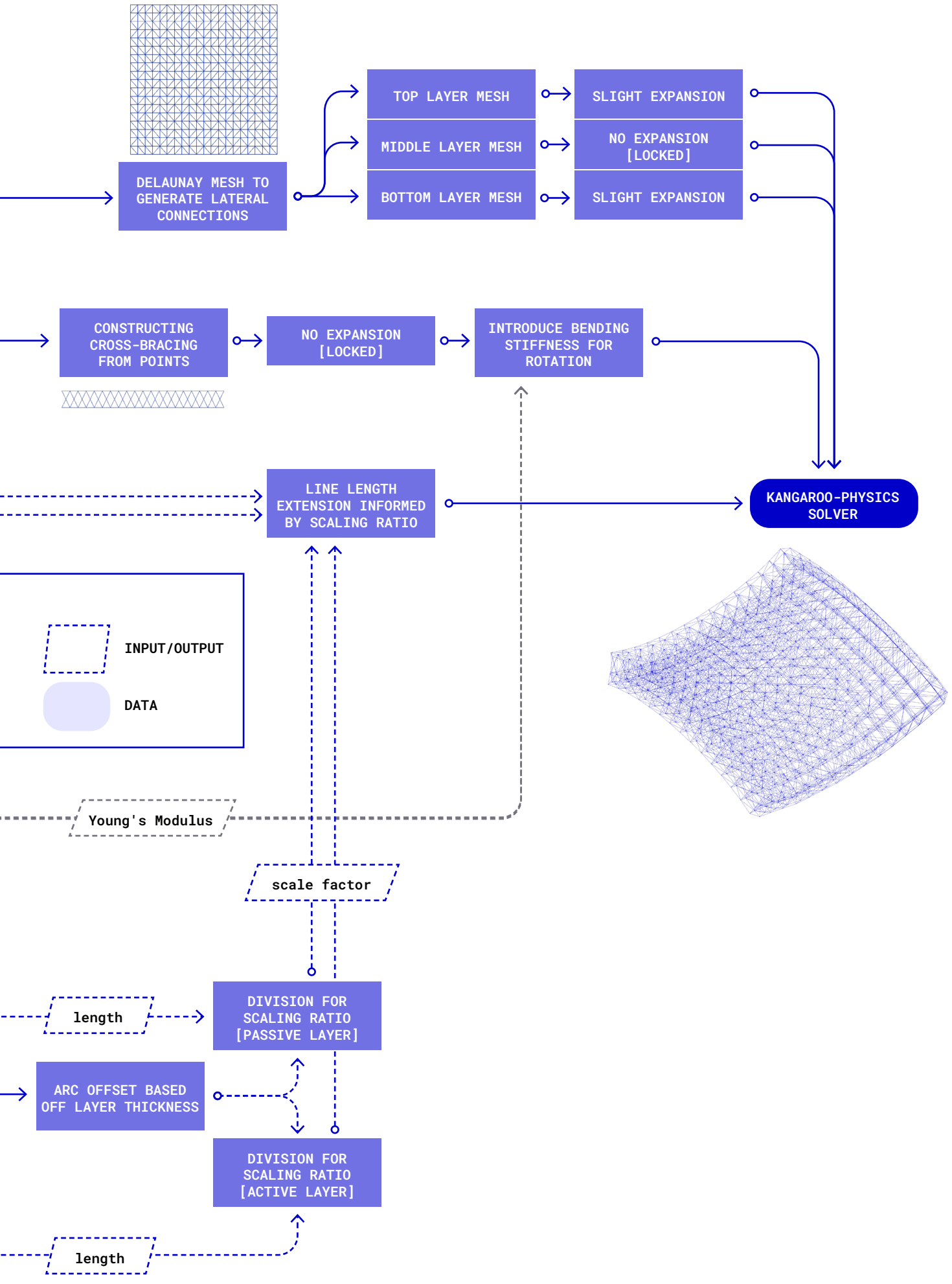


***figure 75:*** *Flowchart of anticlastic Grasshopper script (source: own work)*

# REVERSIBLE LOCKING SYSTEM

# 006



***figure 76:*** *Photograph of physical prototype for curve-line locking of monoclastic curve (source: own work)*

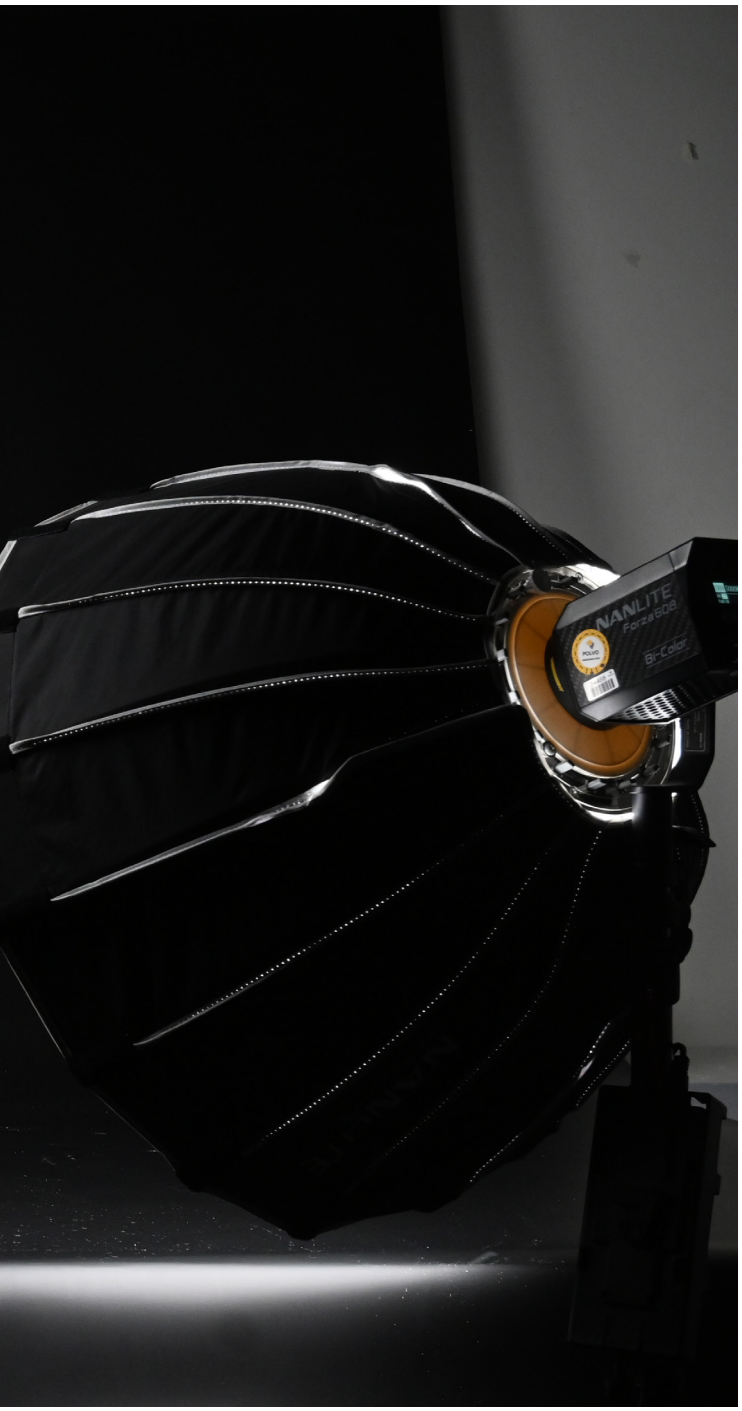


## 6.1 Introduction

The curvature achieved with bilayers reverses naturally when the relative humidity in an environment fluctuates and the timber panels lose or gain moisture to maintain equilibrium.

This process can be desirable in specific contexts, such as where passively-responsive external facade shades are installed to respond to changes in solar intensity throughout the day (Zhan et al., 2023, Cheng et al., 2024). But for the purpose of a deployable structure, serving as a temporary shelter, it is necessary for the system to maintain a deployed form for a prolonged period of time.

The challenge lies in developing a kinematic system that can activate alongside the bilayers as they undergo their transformation, and only locks once the desired curvature has been achieved. While this may sound like a highly specific system, the activation theory behind curve-line folding elements follows a very similar kinematic logic to the behaviour of hygromorphic bilayers.

Curve-line elements are able to induce rotational movement between two faces on either side of a curved crease by taking advantage of moment-inducing forces that generates curvature across one of the two faces. When bound to the surface of a hygromorphic bilayer, the curvature induced by the panel will slowly begin to match the shape of the crease along the curve-line element, leading one of the faces to rotate into a vertical position.

Given that the dimensions of a small sheltering structure appropriate for an average human individual, with a maximum curvature height of around 2000mm, a width

of 2000mm, and assuming monoclastic curvature, would still require a minimum of around 12.5m$^2$ of bilayer material, the time and resources required to achieve such a structure would be too ambitious for the timeframe of this thesis.

In order to still demonstrate the validity of the kinematic system with research grounded in physical validation, small scale models and prototypes are assessed instead. While this cannot be taken as a full indication of the behaviour for a large-scale structure, it demonstrates early validity of a design, and helps support future upscaling.

## 6.2 Early-stage exploration

### 6.2.1 Behaviour of curve-line elements for varied degrees of curvature

To better understand the effect of curve-line folding across different dimensional parameters, a series of simple physical models were constructed using paper. These models analysed the relationship between how varying the magnitude of curvature for the crease would influence the force required to achieve a full vertical deformation of the opposing face (i.e. a full rotation of 90° from flat to vertical).

Six models were developed with varying radii of curvature (see figure 77). Rather than etching the curved crease into a single strip of paper, each model was constructed from two separate components joined together with tape. It had become clear, early into the modeling phase, that working with two separate components ensured the curved element could be cut with greater accuracy by using scissors. This method was more reliable than manually creating a crease in the paper, which was a highly particular and delicate process, especially with models at a small scale. One of the two components had an arc cut out on one end to the intended radius (see figure 78), allowing the desired curvature and rotational behavior to emerge once the two pieces were connected.

Additionally, in their 2024 paper on "Self-locking and stiffening deployable tubular structures", Lee et al. highlight the importance of "pre-curving" the hinging element ( see figure 79) due to the risk that a flat component will fail

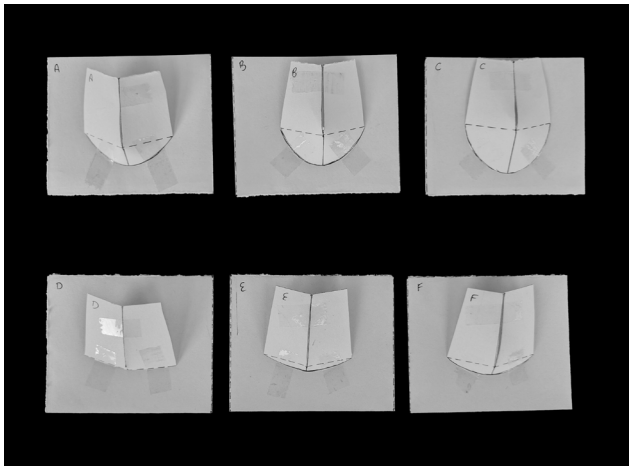

***figure 77:*** *Six models exploring different degrees of curvature (source: own work)*

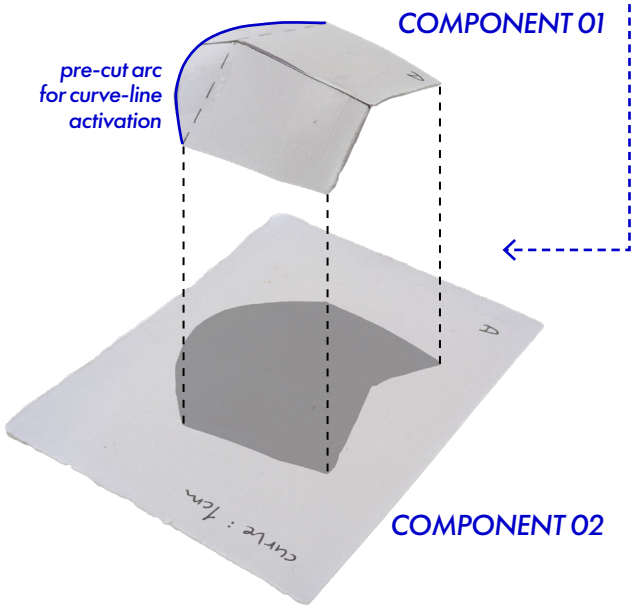


***figure 78:*** *Two-component curve-line exploration (source: own work)*

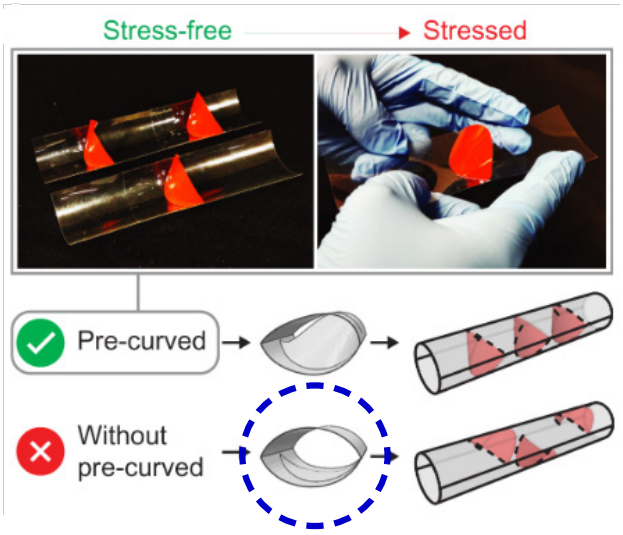


***figure 79:*** *Comparison of pre-curved and non pre-curved elements on successful deployment (source: Lee et al., 2024)*

to deploy as it could bend into the shell's curvature rather than away from it. Therefore, a narrow triangular cut was made on the opposing side of the curve to pull in the sides and pre-curve each element.

A varied range of curvatures were selected for testing, with the understanding that an arc with a smaller amplitude would demand less curving of one of the faces to activate when compared to an arc with a greater amplitude of curvature. The final values were 0mm (only pre-curved), 2.5mm, 5mm, 10mm, 15mm, and 20mm (see figure 80).

Upon testing the final models, it became apparent that the link between amplitude of curvature for the arc, and the required degree of curvature for activation were indeed correlated. Additionally, activation occurred very smoothly and both components worked efficiently as one unified system.

## 6.2.2 Curvature locking through alternating curve-line activation

### Designing the system

Although individual curve-line folding elements presented a very cohesive and responsive mechanism of activation with hygromorphic deformation, an individual element was insufficient to create a reliable reversible locking system. It was necessary to design and develop a more complex, multi-element system that could activate effectively

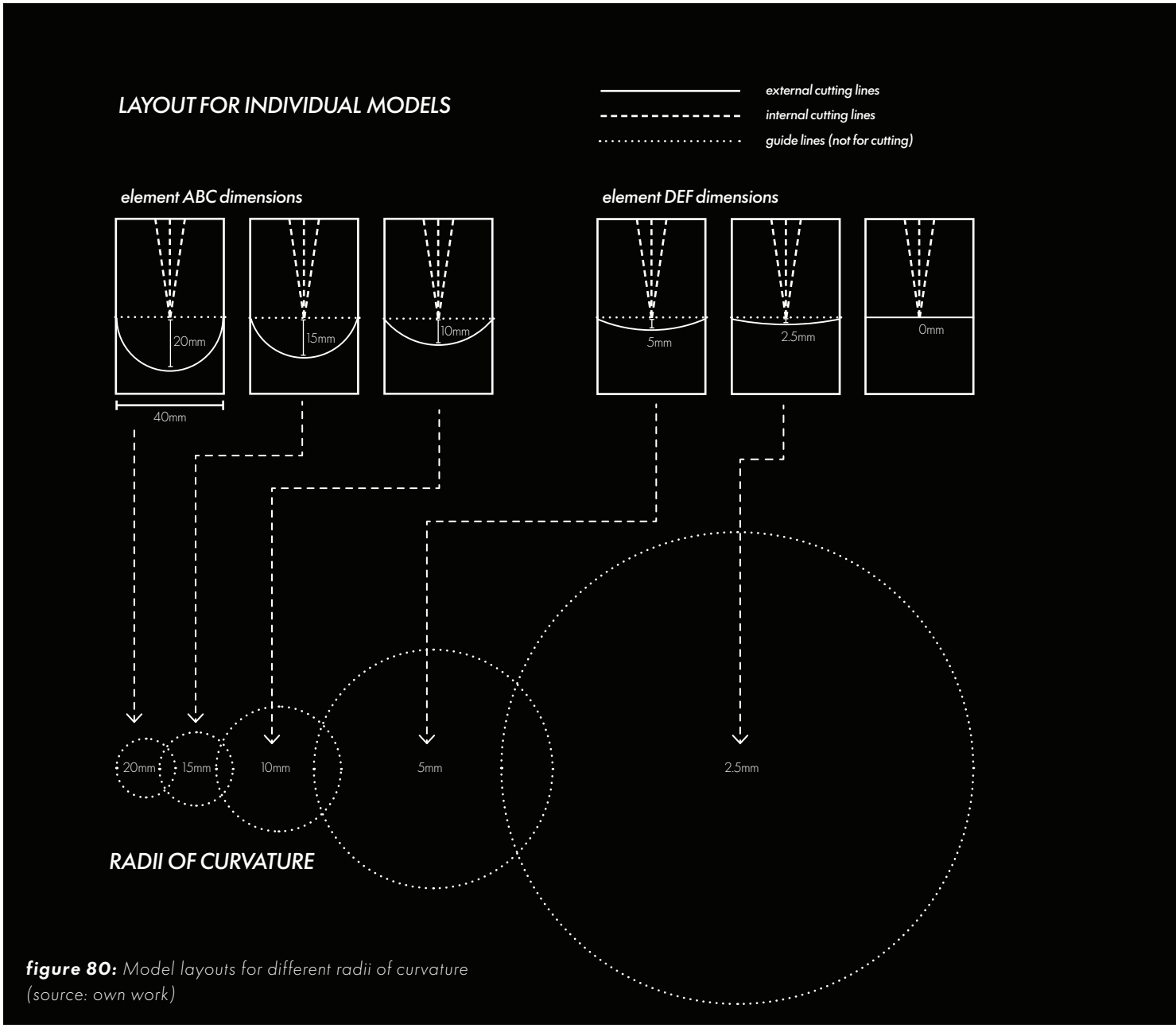


**figure 80:** *Model layouts for different radii of curvature (source: own work)*

across numerous bilayer panels and behave as a cohesive design to bind and stabilise the final deployed form.

As outlined in literature (Grönquist et al., 2020; Wood et al., 2020), a common method for locking hygromorphic bilayer panels into their deformed state is the addition of a third laminated layer that approximates the final curvature. This additional layer is usually a softwood panel which has been steam- or cold-bent to elastically achieve the desired curvature, before being bonded to the bilayer. Once laminated, the pre-curved layer works as a geometric stabiliser that restricts the bilayer's tendency to re-flatten as the relative humidity changes.

The design logic behind the approach is what informed the design of the locking system explored in this chapter of the paper. Rather than introducing a continuous third laminated surface which would result in permanent curvature, the principle of geometric stabilisation is considered through a system of adjacent curve-line elements instead. Curve-line elements are bonded to bilayer panels (see figure 81), before being upscaled into a larger, multi-element system through finger-joint connections (see figure 82). As hygromorphic deformation occurs it induces rotational hinging in the curve-line elements from a flat state to a full vertical position at the final curved state (see figure 83 on next page). Once deployed, adjacent curve-line elements will overlap and can be mechanically secured to one another, resulting in a locking condition that stabilises the shell geometry. To avoid adjacent edge collisions, each alternating element activates from the opposite direction before meeting and sliding across each other.

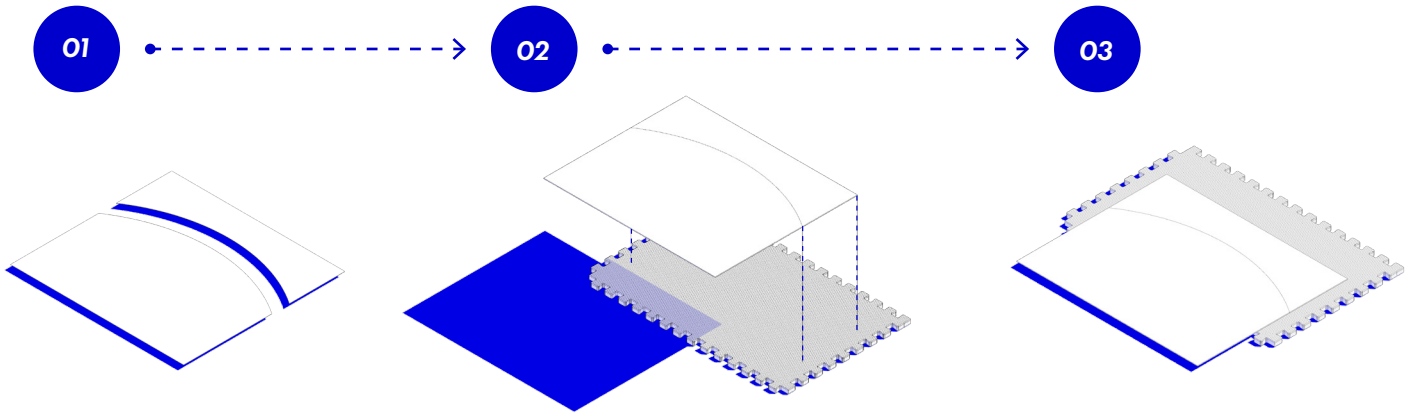


***figure 81:*** *Curve-line element laminated to hygromorphic bilayer (source: own work)*

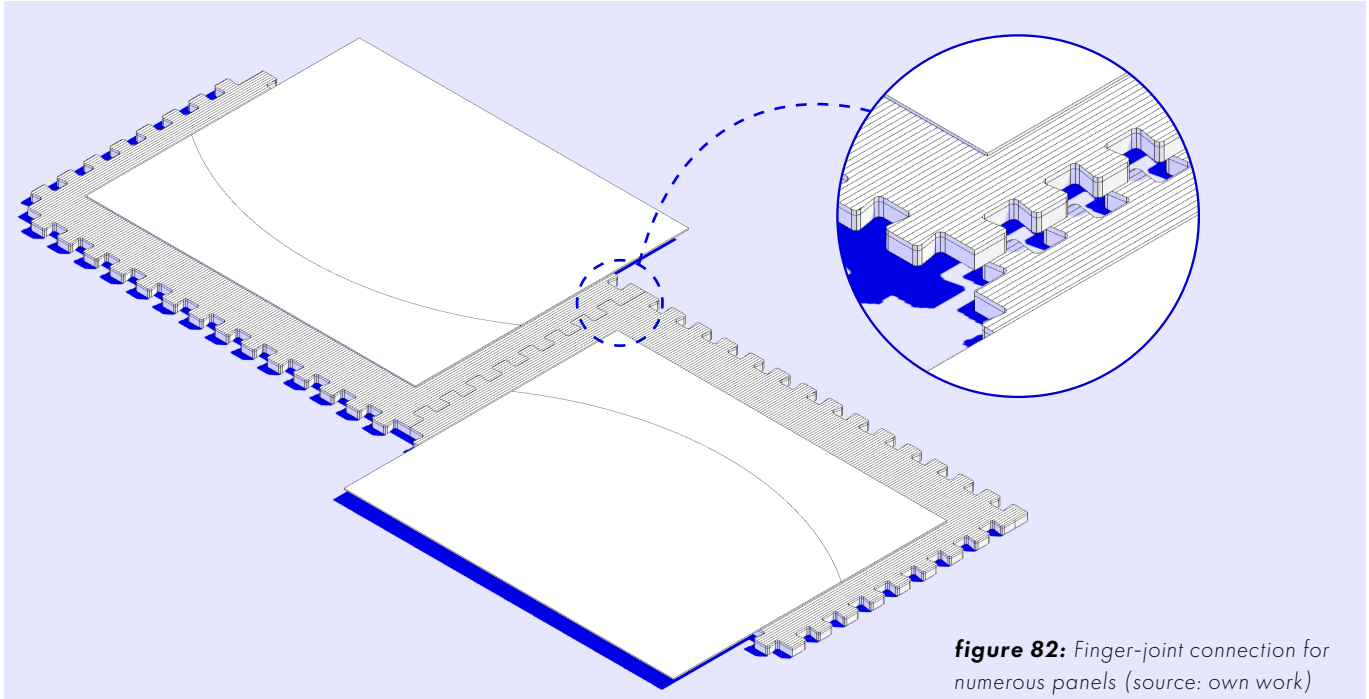

***figure 82:*** *Finger-joint connection for numerous panels (source: own work)*

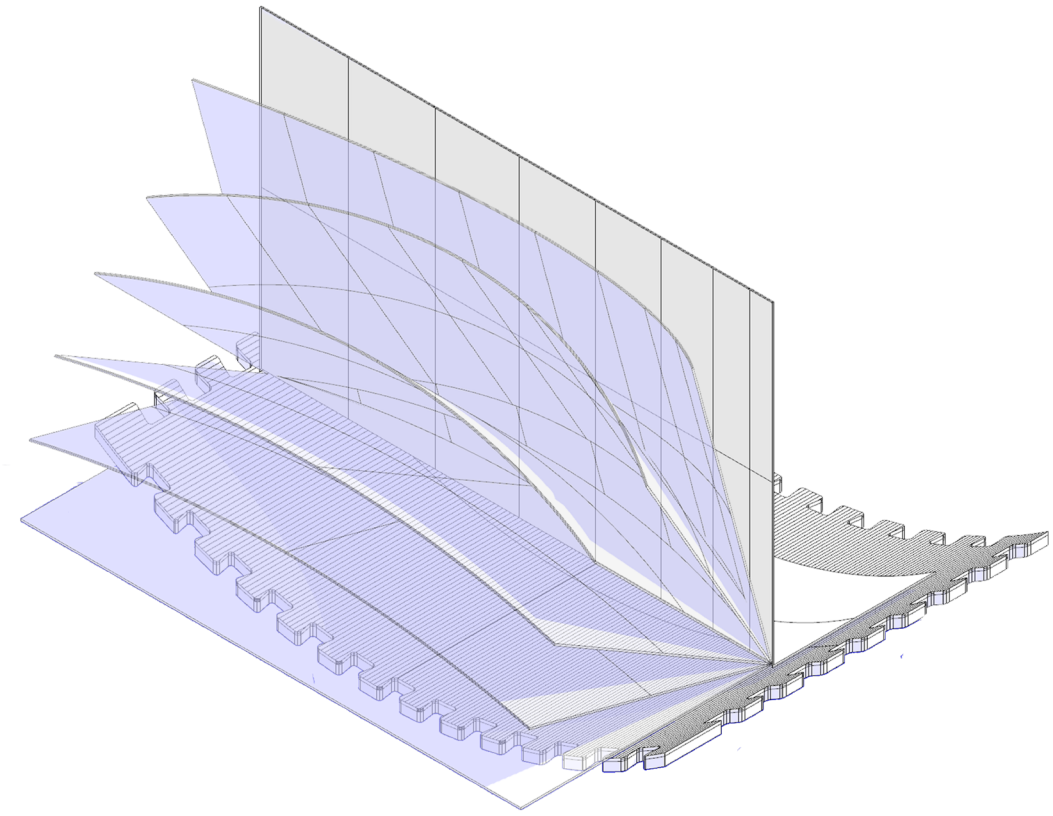

***figure 83:*** *Curve-line activation with hygromorphic deformation (source: own work)*

Through this process, the activated curve-line system performs a similar role as the third pre-curved laminated layer. Both strategies rely on introducing an additional geometric curve that reinforces and maintains the final deployed curvature/ This study explores a deployable locking system that achieves form stability for a monoclastic shell by securing the position of adjacent curve-line elements at the final curved shape.

## Collision and energy-barrier locking

Initial exploration of the locking system was based around a self-locking principle - rather than a reversible one - from Lee et al.'s 2024 paper on "Self-locking and stiffening deployable tubular structures", which took advantage of two common design strategies for self-locking;

1. Collision method
2. Energy-barrier method

The collision method involves the physical interaction of separate components to block extended motion beyond a specific point. This allows a system to be stable; limiting it to a desired deployment goal, while accommodating straightforward collapsibility when the deployment direction is reversed.

The energy-barrier method facilitates a transitional "snap-through" phase that facilitates deformation between two stable states. This is generally achieved by inducing excessive deformations in an element to overcome an energy threshold. Once the secondary stable state has been achieved, the energy-barrier method resists collapsibility in the deployment direction to help maintain structural rigidity under deformations.

In their paper, Lee et al. present a system comprised of two conjoined arcs that can transition from a cylindrical form to a flattened state, and vice versa, through hinging at the edges of contact. Multiple curve-line elements are contained internally, and activate as the system transitions from a flat form to a circular one. In their methodology, structural stiffness is achieved as the curve-line element collides with the roof of the cylindrical shell and undergoes elastic shell buckling to snap-through into an over-activated vertical position. In this process, the collision and energy-barrier methods are combined to achieve structural stiffness when the structure

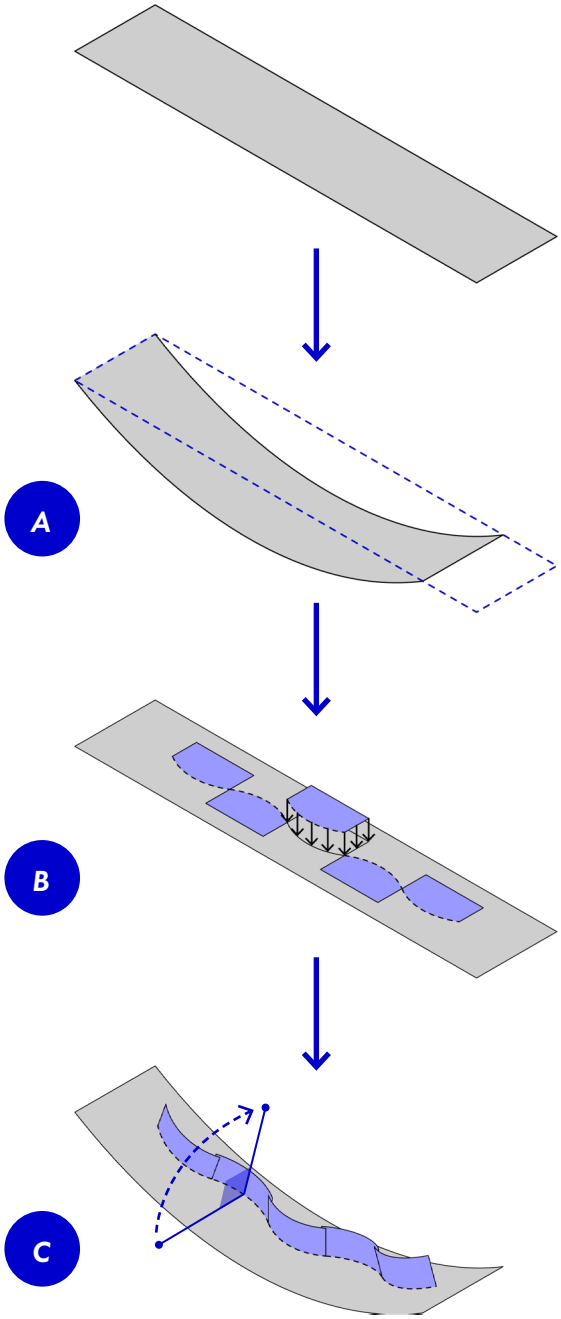


***figure 84:*** *Alternating curve-line activation set-up (source: own work)*

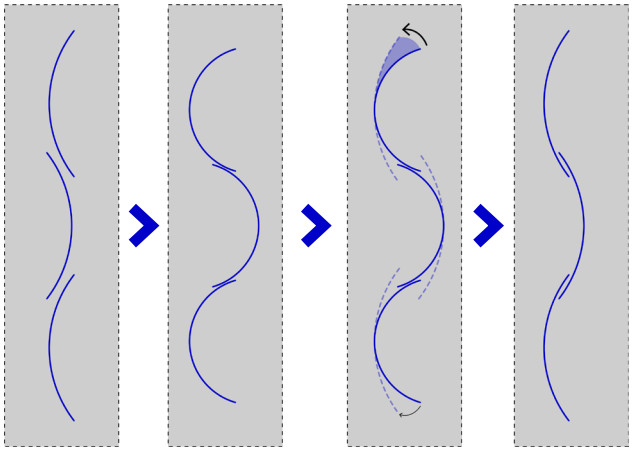

***figure 85:*** *Snap-through collision process (source: own work)*

undergoes compression (Lee et al., 2024).

The system explored in this paper attempted to adapt the collision and energy-barrier methods through the loaded interactions between adjacent, alternating curved-line elements. The base component undergoes elastic shell bending when the boundaries are compressed unidirectionally (see figure 84A). Curve-line elements are connected to the base to form the compliant mechanism (see figure 84B). Motion is triggered as the base curves, and each curve-line element rotates around the hinge line while angling towards each other (see figure 84C).

As adjacent curve-line elements deploy from alternating directions, they come into contact during rotation. This collision acts as a geometric constraint, where continued rotation builds a strain between neighbouring elements to induce elastic buckling (see figure 85). Upon undergoing the snap-through transition, the curve-line elements re-stabilise to prevent reverse rotation and re-flattening. The forces exerted for flattening are resisted by both the physical obstruction between adjacent curve-line elements and the energy-barrier associated with reversing the snap-through deformation.

## Exploring pseudo-deformation for activation

An extensive amount of time is required to construct, condition and deform a hygromorphic bilayer. As an alternate method to validate passive, self-locking activation, a pseudo-deformation process for monoclastic curvature was explored with shrink film and shrink plastic. The experiments successfully demonstrated that curvature could be induced in both paper and carboard plates that were bonded with shrink film or plastic under controlled conditions. Through iterative testing carried out, it was observed that the behaviour of deformation relied heavily on the orientation, aspect ratio, and distribution of the shrinking elements, with multiple thin strips producing greater and more controlled curvature than continuous surfaces (see appendix 9).

While the pseudo-deformation studies carried out were able to successfully replicate certain aspects of curvature-driven activation, both shrink film and shrink plastic proved insufficient for exploring a full locking system activation. The degree of force, stability, and consistency

in tested samples was unreliable, but nevertheless, these outcomes provided important methodological insights into the relationship between curvature progression and curve-line activation.

Ultimately, as the primary objective of the physical prototyping was to evaluate the kinematic behaviour of the locking mechanism itself, it was concluded that applying an external mechanical. A more detailed account of the pseudo-deformation experiments is provided in the appendix.

## Mechanically assessing the collision and energy-barrier self-locking system

Following the exploration of different passive curving models, the self-locking system relying on the collision and energy-barrier methods was built from carefully cut cardboard sheets and crease curve-line paper elements (see figure 85 and figure 86). The amplitude selected for the curve-line elements was considerably small (see figure 87) in order to achieve vertical activation without requiring excessive deformation of the cardboard strip.

As the cardboard strip underwent lateral compression and deformed into an arc, the curve-line elements activated successfully. Although alternating strips collided as expected, the rotational force generated by the activating curve-line elements proved insufficient to overcome the energy-barrier, even when additional force was applied to further increase the curvature of the cardboard strip.

The primary limitation to the system arises from the lateral movement of the curve-line elements as the cardboard bends. The greater the curvature exhibited by the strip, the more the colliding curve-line elements slide over each other (see figure 88). This interaction generates a greater

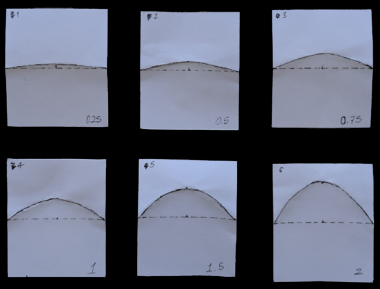

***figure 85:*** *Exploring different amplitudes of curve creases [0.25, 0.5, 0.75, 1, 1.5, & 2mm] (source: own work)*

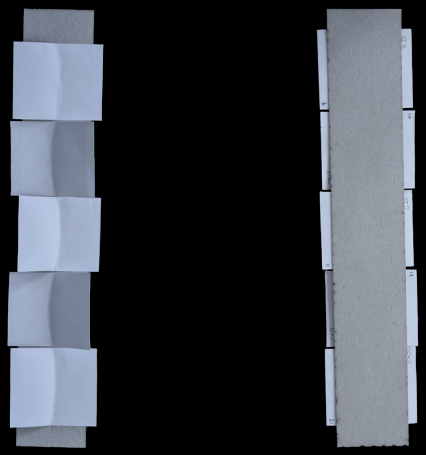

***figure 86:*** *Exploring different amplitudes of curve creases [0.25, 0.5, 0.75, 1, 1.5, & 2mm] (source: own work)*

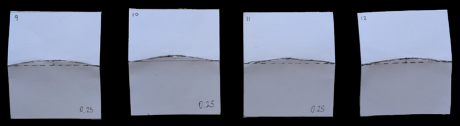

***figure 87:*** *Amplitude of 0.25mm used to test the collision and energy-barrier system (source: own work)*

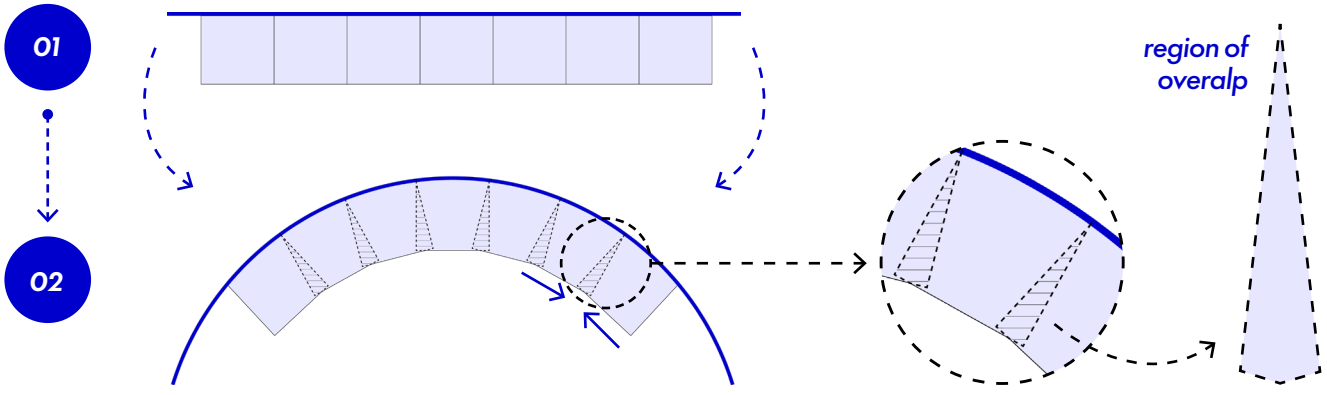


***figure 88:*** *Comparing the vertical activation of the curve-line elements to the degree of overlap caused by cardboard strip curving (source: own work)*

resistance to elastic bending, requiring significantly more force to overcome the energy-barrier. Ultimately, overcoming the energy-barrier required external interference which was not ideal for the intended system.

**Conclusions on the self-locking system**

When assessing the collision geometrically, it becomes apparent that conically narrowing the activating face of the curve-line element would help decrease the range of the overlapping region. Models were constructed to explore this behaviour, and although there were instances where the curve-line elements could overcome the energy-barrier, they lacked the structural integrity to prevent themselves from re-flattening. Designing an integrated self-locking system that relied exclusively on the collision and energy-barrier methods was ultimately inconclusive for the scope of this paper.

Although the trials were ultimately considered unsuccessful, the testing process was constrained by both limited time and the availability of suitable materials. While the development of a fully self-locking system may not have been feasible under these conditions, the experiments still revealed significant potential for further exploration of curve-line locking, particularly given the mechanism's effective performance under hygromorphic activation. Consequently, the following stage focused on the development of a reversible locking system instead, which continued to exploit the principles of alternating curve-line activation.

## 6.3 Designing a reversible locking system

### 6.3.1 Material selection

In prior trials, although print paper and cardboard exhibited elastic properties, they lacked rigidity and a resistance to larger forces. This would commonly lead to plastic deformation as they were bent into curves, especially at critical points in the curvature when the curve-line elements were approaching vertical activation. As an alternative, multiple papers exploring curve-line activation used polypropylene to design and cut folding systems instead (Brancart et al., 2015; Vergauwen et al., 2017; Reaisi & Ghiyasi, 2026).

Polypropylene is a heat-resistant and flexible thermoplastic polymer. As one of the most widely produced plastics, it is used for packaging, textiles and automotive parts, and comes in both standard and fibre-reinforced variants (Reaisi & Ghiyasi, 2026). Furthermore, polypropylene has a high resistance to fatigue, allowing it to endure repetitive folding and bending without undergoing permanent plastic deformation (Brancart et al., 2015).

To create the desired elements, the literature outlines the use of laser cutters for producing the desired patterns and engraving the curve-line folds into the polypropylene sheets. Thicknesses ranging from 0.5mm to 2mm were cut and engraved to create the desired curvature for the curve-line activation (Brancart et al., 2015; Reaisi & Ghiyasi, 2026).

Validity of the production process was presented in structurally successful models, ranging from small-scale samples (about a hands-width) to large-scale pavilions, such as the Undulatus Pavilion seen below in figure 89 (Brancart et al., 2015).



***figure 89:*** *The Undulatus pavilion suspended at the "Muziekgebouw aan't IJ" in Amsterdam (source: Brancart et la., 2015)*

## 6.3.2 Detailing of curve-line elements with polypropylene

All prototype models were cut from thin, white polypropylene sheets with a material thickness of only 0.8mm by using a CNC laser cutter for digital fabrication and precision. Due to their toughness, polypropylene sheets have a high resistance to tearing, which allowed surface engravings to serve as fold lines that acted as elastic hinges for repeated folding and folding for the curve-line bending.

Perfecting the curve-engraving required demanded multiple iterations and improvements. Engravings created by laser cutters are generally quantified by ablation depth, and refer to the quantity of material removed from a material by a laser without achieving complete penetration (i.e. without creating a cut) (Dobrev et al., 2006). The ablation depth is impacted by the interaction between the laser's energy density and the physical properties of the material being cut, such as laser power, density, and thermal conductivity (Dobrev et al., 2006).

The laser cutter employed for fabrication was contracted by an external company to the TU Delft, making the engraving process unfamiliar. Multiple samples and iterations were carried out to determine the most effective process for engraving curves onto the polypropylene that could induce appropriate hinging along the desired edge.

### Trial Test One

Similar to the first round of paper models that were made to explore curve-line activation at the beginning of this chapter, a set of 8 strips with varying degrees of amplitude were cut to determine the behavior of 0.8mm polypropylene.

The trial samples ranged from an amplitude of 2.5mm to 20mm, with a consecutive increase of 2.5mm (see figure 90), which were engraved onto strips of dimensions 60mm x 40mm.

The final results failed to exhibit any curvature as the ablation depth of the engraving was far too shallow. The insufficient depth meant the polypropylene couldn't be bent into a flexible hinge, and it didn't behave as was expected (see figure 91).

### Trial Test Two

In the following set of samples, rather than relying exclusively on engravings to outline the curve for activation, alternating incisions were included between engravings.

The pattern followed dividing a curve-line into an odd number of segments with all even segments marked as

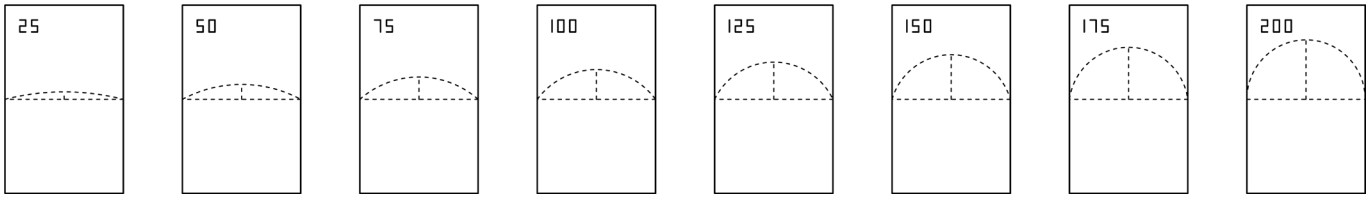


***figure 90:*** *Amplitude range for trial one samples (source: own work)*

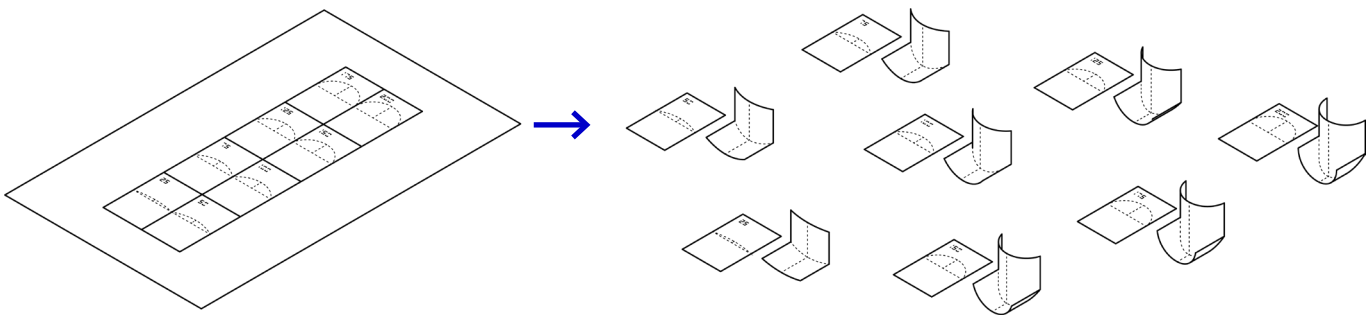

***figure 91:*** *Two-step production to engrave trial one samples with expected vertical activation (source: own work)*

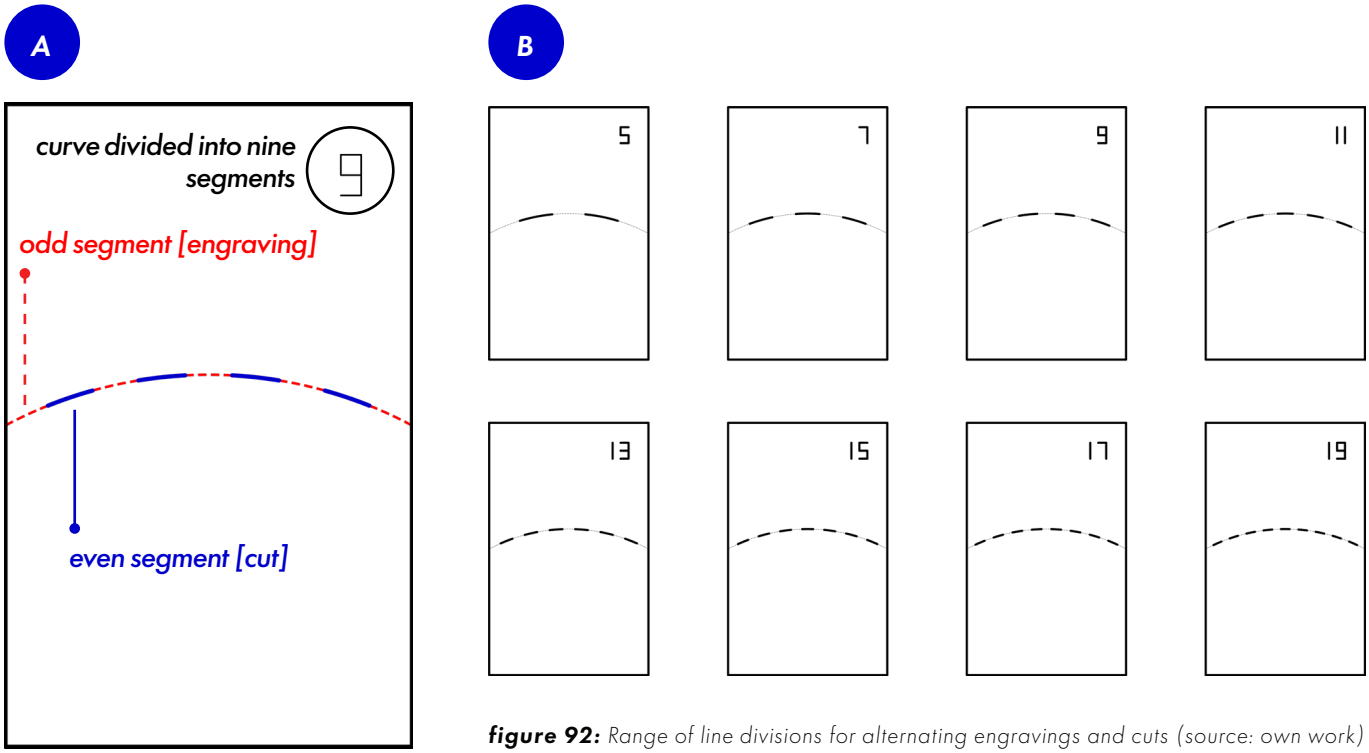


***figure 92:*** *Range of line divisions for alternating engravings and cuts (source: own work)*

cuts, and all odd segments marked for engraving (see figure 92A). A range of line divisions was tested to determine the number, and length, of cuts required to induce appropriate flexible hinging, from 5 segments (longest lines) to 19 segments (shortest lines) (see figure 92B).

These samples were far more successful, and activation could be induced when the elements were curved. The cuts made it easier to stretch the engravings and induce a slight degree of plastic deformation to achieve greater flexibility in the hinge. Additionally, samples with a greater number of divisions (above 13) achieved smoother activation. The samples with less divisions were not as reliable when activating as the polypropylene would frequently buckle into a monoclastic shell when compressed, rather than achieving rotational hinging.

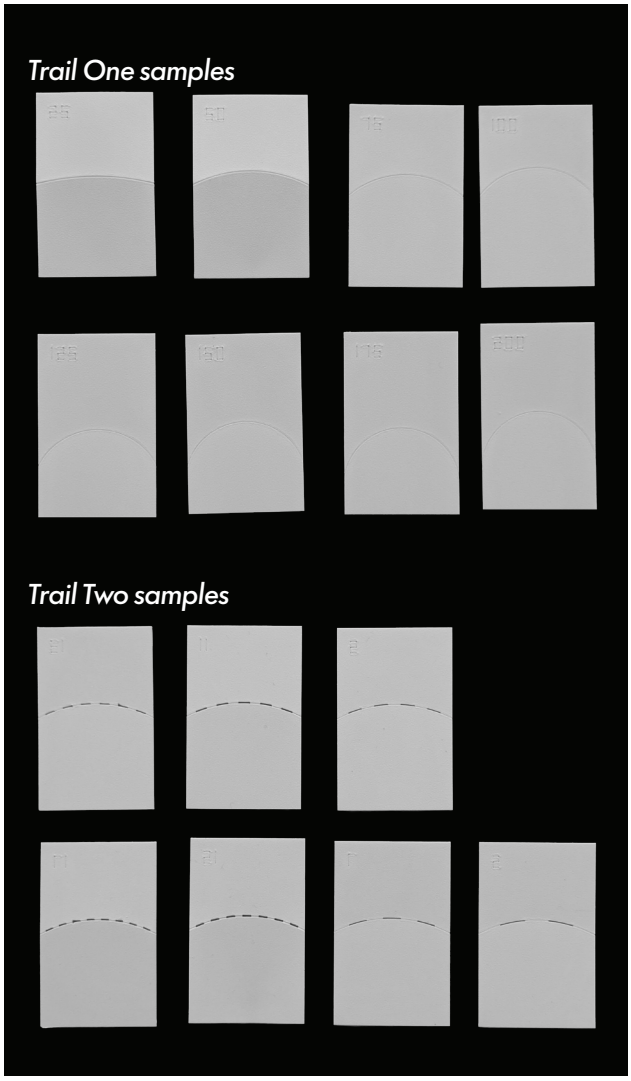


***figure 93:*** *Physical polypropylene samples with trial one [top] including only engravings, and trial two [bottom] with both engravings and cuts (source: own work)*

## 6.3.3 Digital fabrication and construction of a reversible locking system

The design for a reversible locking system builds on the limitations presented for the self-locking concept, whereby the region of overlap created by the activating curve-line elements acts as a point of tension to potentially bolt adjacent elements together.

### Region of intersection

The parameters that influence the total area across which adjacent elements overlap are the degree of curvature induced by the curve-line, the length of the hinging face, and the distance between adjacent curve-line elements. A greater degree of curvature leads to more overlap, and similarly, longer hinging faces that are closer together lead to greater overlap as well (see figure 94).

To secure adjacent elements when the desired curvature is achieved, it is important to ensure the curvature of the curve-line matches the final deployed form as this will allow them to exhibit full vertical activation, and that the hinging face is dimensioned appropriately to achieve sufficient overlap.

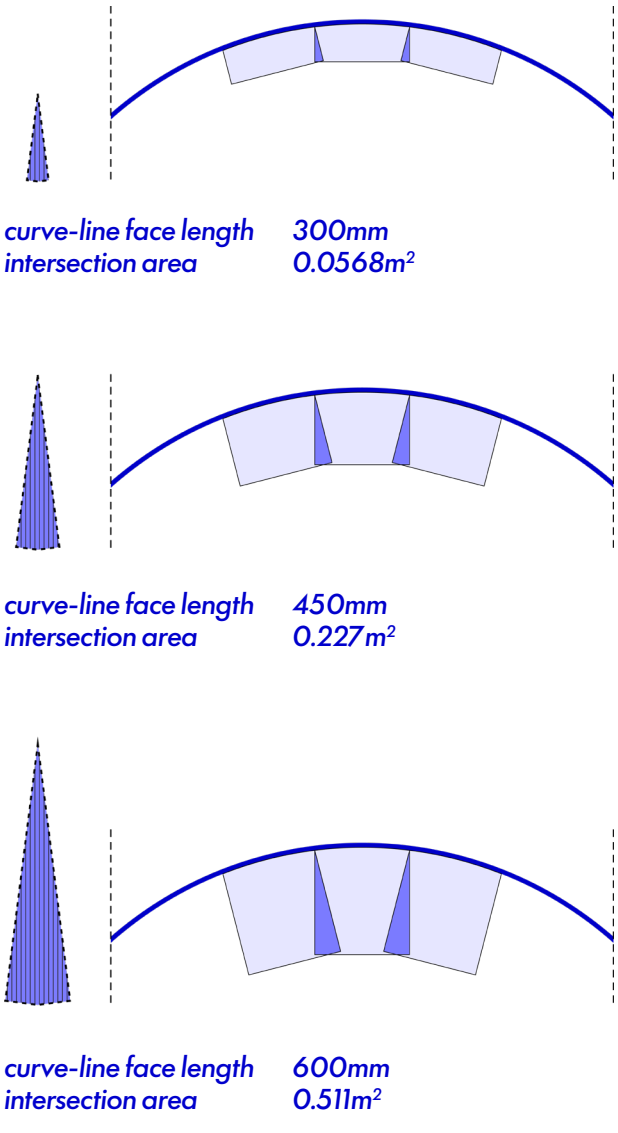


***figure 94:*** *Varying the length of hinging elements increases the area of overlap (source: own work)*

### Keyed alignment

Interconnection between panels is achieved through coincident openings on either curve-line face that enable a custom bolted connection when the panels align. The openings are positioned along the central line in the intersecting region (see figure 95) as this indicates the point of alignment.

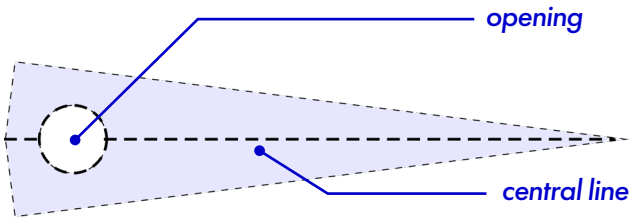


***figure 95:*** *Positioning openings for bolted connections within the overlapping area of adjacent curve-line elements (source: own work)*

### Custom bolt connection

Once adjacent panels overlap and are locked together, they constrain each others movement through tension. This mutual restraint prevents the curve-line elements from reversing their rotation and achieves structural rigidity in the deployed shell. To ensure the system remained as minimal as possible, it was necessary to design and construct a bolting element that could be inserted and locked into the opening with as little parts as possible.

Early iterations of the design were inspired by "S-hooks", which are heavy-duty stainless steel hooks that are deformed into a planar S-shaped curve with two inflection points. The geometry of the hook plays a crucial role in its performance when placed under tension. Because of the inflection points at both ends, connected components are prevented from slipping free as they cannot easily overcome the geometric transitions occurring at the extremities. In this way, a single S-hook is sufficient for reliably linking two separate elements while maintaining a stable locking connection under load.

The first design for a bolt simplified the continuous curved geometry of the S-hook into a vertical spine with two opposing horizontal extensions emerging on either end (see

figure 96). The bolt is inserted through a 45° rotation that reduces its vertical displacement, allowing it fit through the tightened opening before reverting to its original position (see figure 97A).

In following adaptions, materiality and structural integrity are maximised by reducing the displacement of the vertical member (see figure 97B). This decreases the displacement of the element when rotated and helps ensure the interlocking curve-line elements are kept closer together.

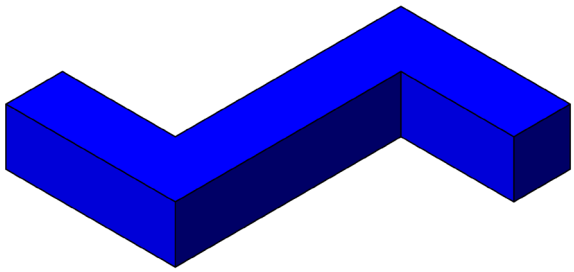

***figure 96:*** *S-hook inspired locking bolt (source: own work)*

**Accounting for weak points**

Although simplifying the S-hook geometry into vertical and horizontal elements preserved the fundamental principle of a continuous, interlocking connection, it introduced structural weaknesses at the junctions where the horizontal and vertical elements meet ( see figure 98).

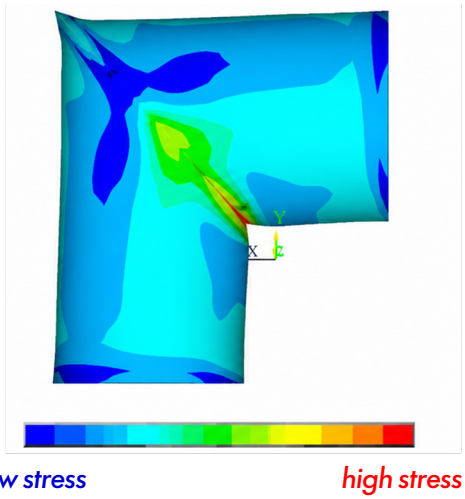


***figure 98:*** *Finite-element model of the stress concentration factor for a pressurised mitred pipe with 90° bend (source: Chang & Redekop, 2008)*

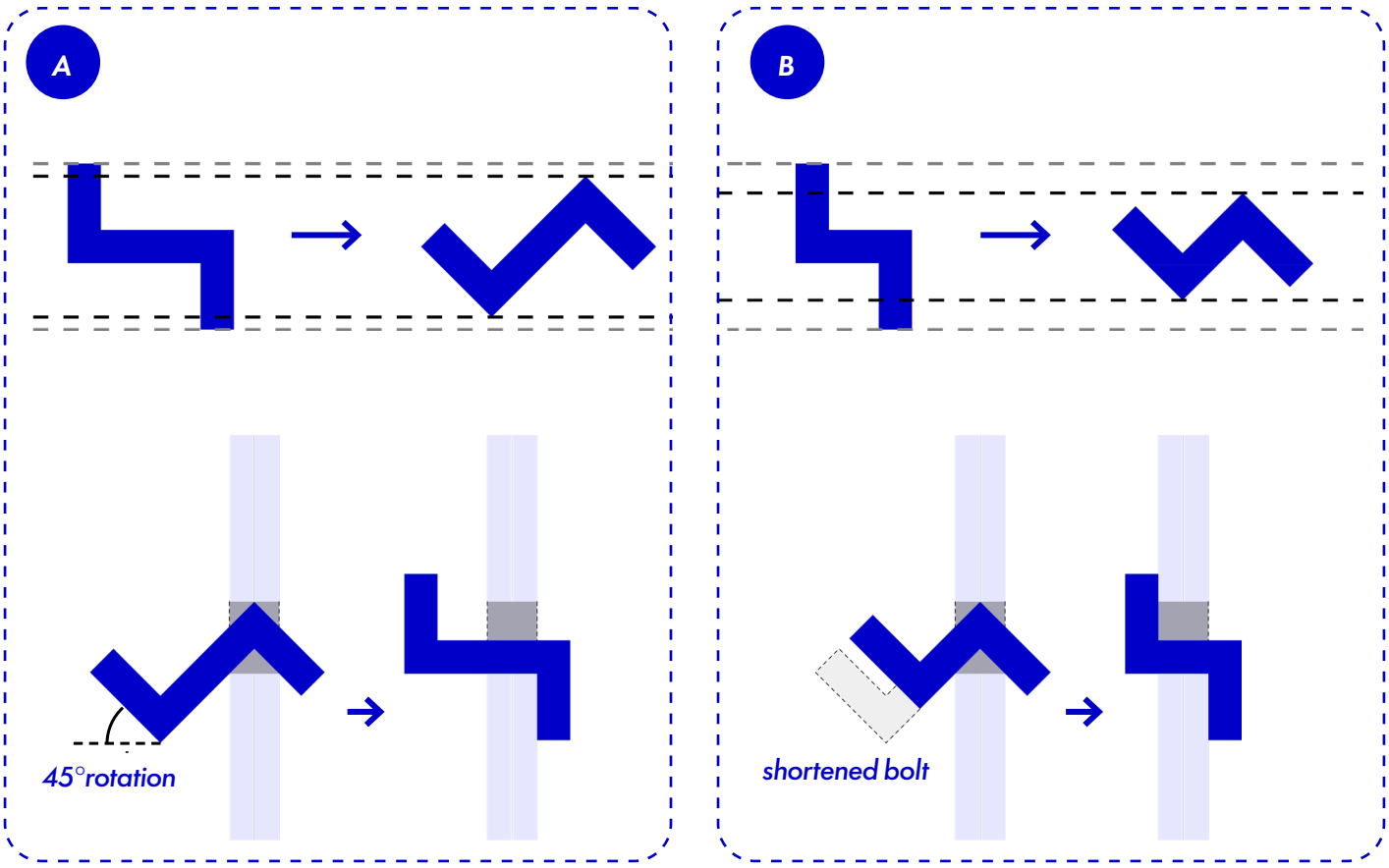


***figure 97:*** *Reduced vertical displacement when rotated 45°* with insertion process. Initial design [left], maximised design [right] *(source: own work)*

These transition points become regions of concentrated critical shear stress when they are subjected to axial and bending loads (Molski et al., 2020). When a rotational moment force is applied to the horizontal members on either side, as a result of the curve-line elements attempting to separate and move apart from each other, they transfer forces into the central vertical member, generating significant shear stresses at the intersections. Given that the horizontal and vertical members intersect at a 90° angle, the geometry changes abruptly at the corners, rather than distributing the forces smoothly along a continuous curve; as was the case in the design of the original S-hook. This leads the forces to accumulate locally at the inner corners, and creates vulnerable points where deformation, cracking, and material failure become more likely to occur (Molski et al., 2020).

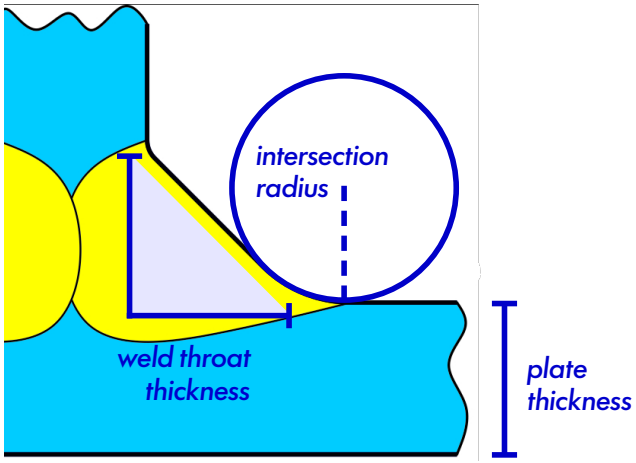


***figure 99:*** *Graphical abstraction of a welded T-joint with 45° fillet weld (source: Molski & Tarasiuk, 2021)*

The most important geometric parameters affecting stress concentration factors are the intersection radius, weld throat thickness, and plate thickness (Molksi & Tarasiuk, 2021; see figure 99). In the case of intersection radii approaching zero (i.e. a corner), the stress concentration factor increases exponentially, whereas an increasing magnitude of radii exponentially decreases the stress concentration factor (Molski et al., 2020; see figure 100).

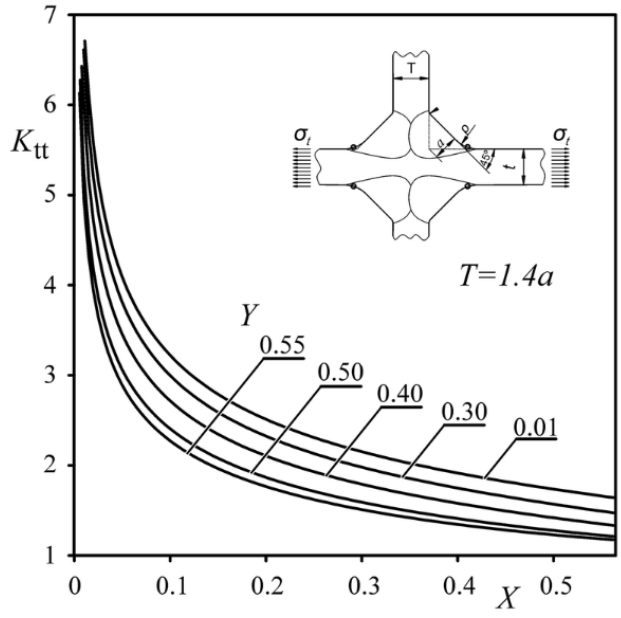


***figure 100:*** *Influence of intersection radius (X) on stress concentration factor ($K_{tt}$) (source: Molski et al., 2020)*

Building on these parameters and based on the stress concentration factor results in literature, the abstracted S-hook was re-designed with a angled flange connections between the horizontal and vertical members and filleted intersection transitions (see figure 101).

## Validation of "Z-hook" element

To validate the "Z-hook", physical models were constructed with polypropylene curve-line elements and locked into monoclastic arches.

Two initial variations were tested for the Z-hook

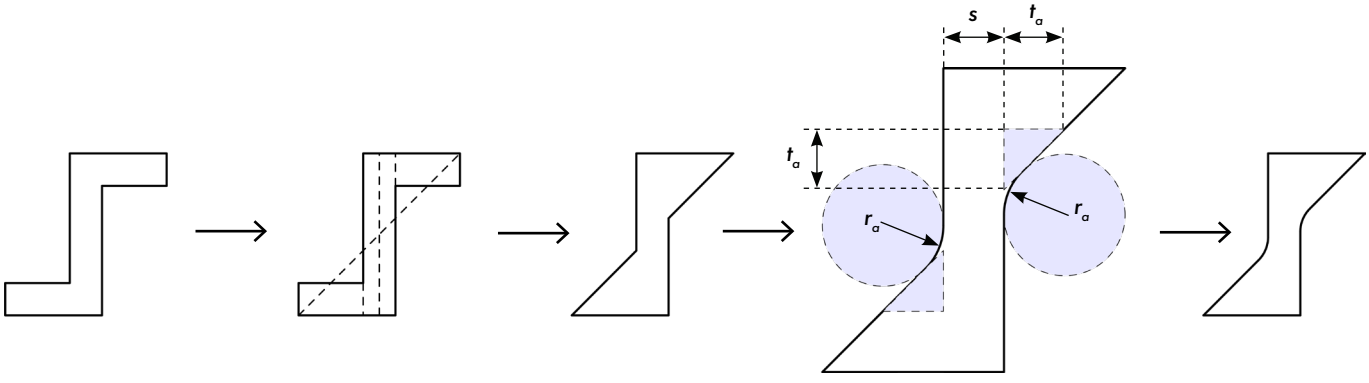


***figure 101:*** *Graphical presentation of S-hook re-design with angled flange connections and filleted intersections (source: own work)*

with varied degrees of vertical displacement (see figure 102). Much like the S-hook, the narrower element worked more efficiently and could help maintain proximity between adjacent curve-line elements.

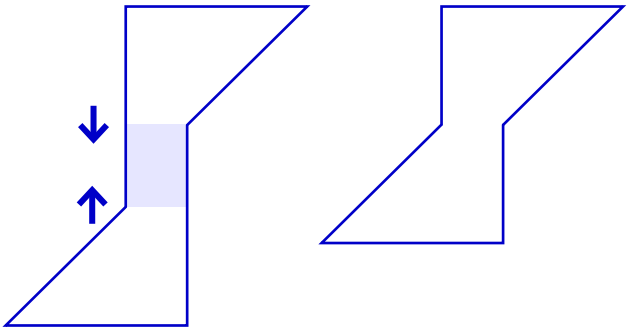

***figure 102:*** *Variations in initial Z-hook test models (source: own work)*

When engaging the Z-hook through the coincident openings, it is highly effective at resisting the rotational forces exerted onto it by the adjacent curve-line elements which seek to flatten themselves in opposing directions. A very important distinction presented through the models is the orientation of the opposing flanges of the Z-hook. To prevent structural instability and failure, the external tips of both flanges must always be pointed in the direction of movement that each curve-line element is exerting onto the hook as it attempts to re-flatten itself (see figure 103). This force tensions the hook into position, and prevents it from loosening itself.

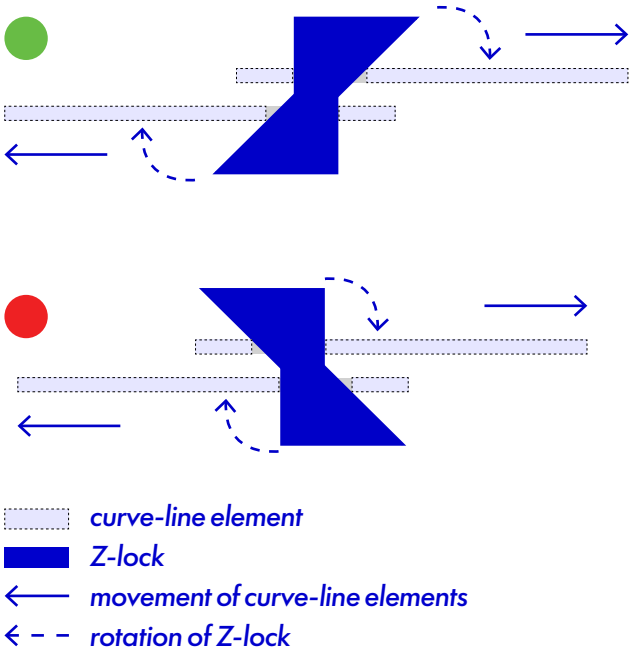


***figure 103:*** *Correct [top] and incorrect [bottom] Z-hook orientation (source: own work)*

Due to limitations on timeframe, the extents of the design validation did not involve any structural assessments or digital explorations. The small-scale models presented a proof-of-concept to bring the system from a theoretical concept into an early-stage exploration of the kinematic logic on whether a baseline-level of structural equilibrium could be achieved (see images on next page).

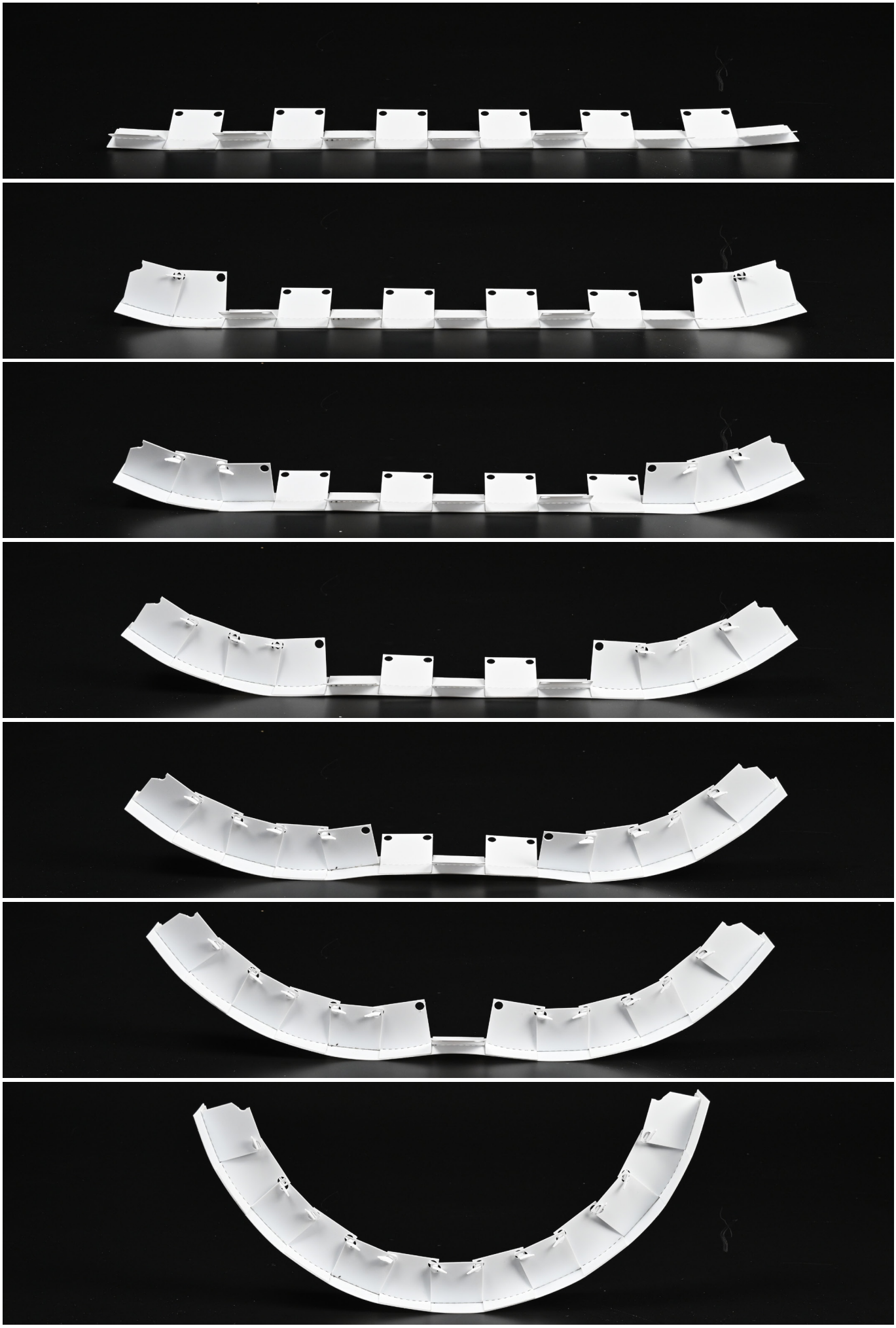

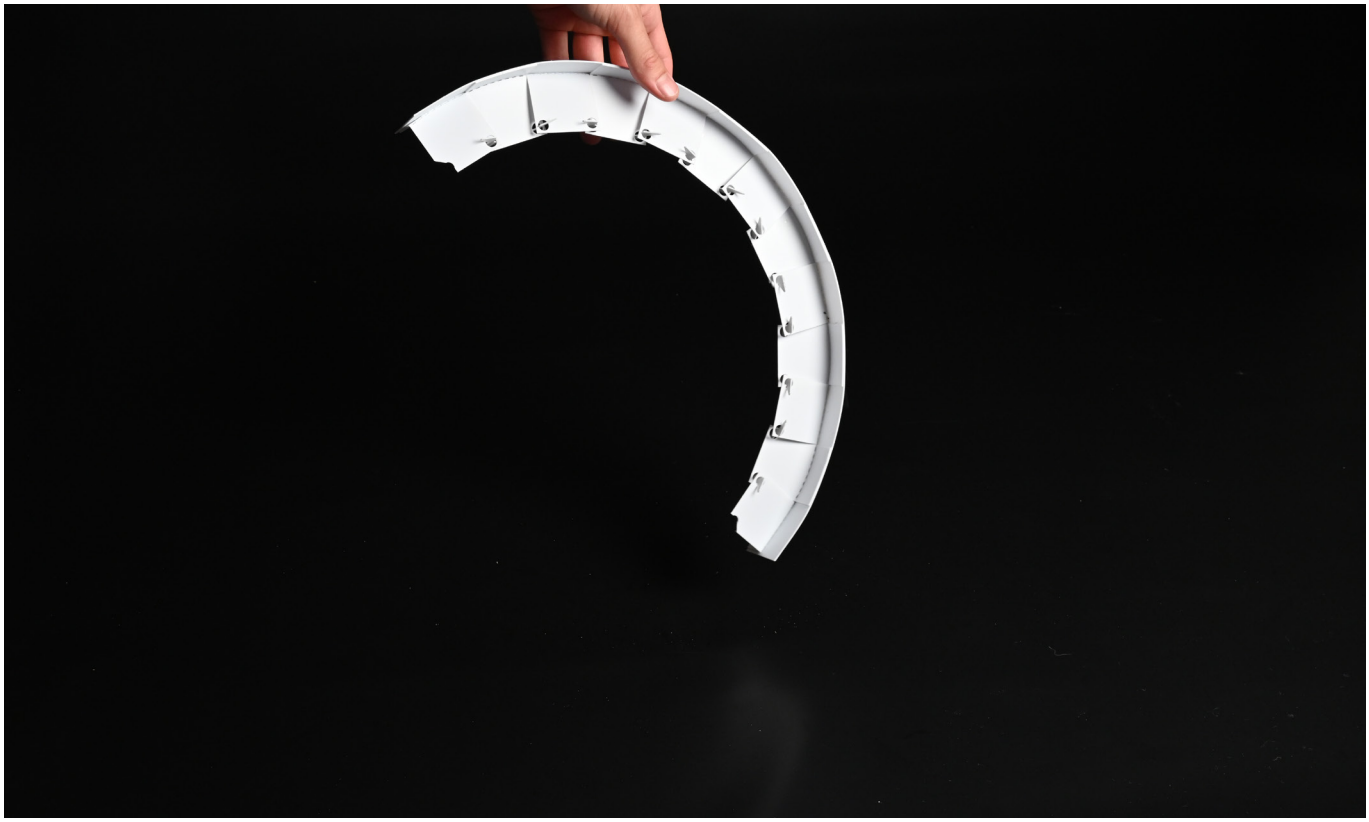







# SCALING-UP FOR REAL-WORLD APPLICATION

# 007



***figure 104:*** *Concept render of deployed structure in urban landscape, generated with Gemini [image sourcing include model image (source: own work), and photograph of Place de la Republique (source: The Parisian Guide, 2026)]*



## 7.1 Construction process

The research established in this paper serves as foundational steps for the future development of large-scale, free-form deployable structures. By deriving required material data from the simulative tools for monoclastic and anticlastic curvature, and building on the kinematic exploration of the reversible locking system, individual panels can be combined to achieve desired forms.

This section explores a theoretical procedure for design, commencing with shell exploration at a digital scale, to material selection and manufacturing, followed by modular packaging and shipping, and concluding with construction, deployment, and locking.

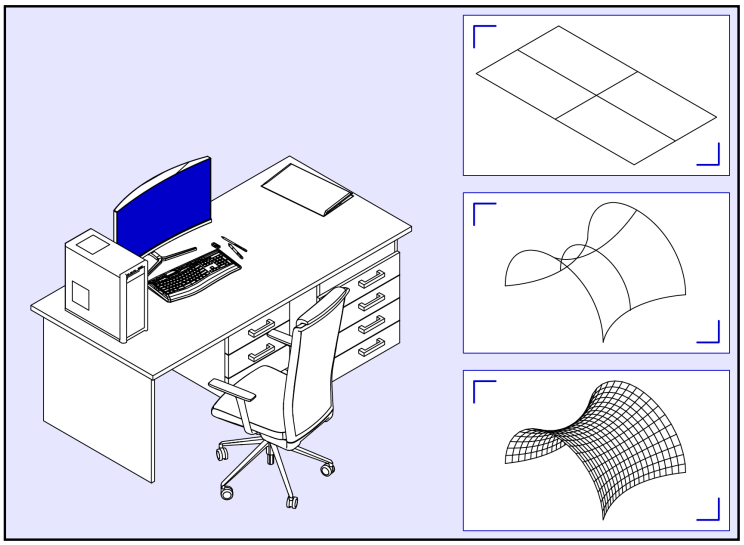

## Digital design exploration

Exploring shell structures through digital means is a crucial primary step in the construction process as it allows designers and engineers to investigate a wide range of geometries rapidly and efficiently. Numerous computational modeling and parametric design tools exist to assist with visualising concepts and assessing structural viability. This is comparatively more efficient than traditional physical prototyping.

The final result is a design that balances structural integrity, potential manufacturability, and aesthetic preference before fabrication even starts, minimising the need for cost adjustments during construction.

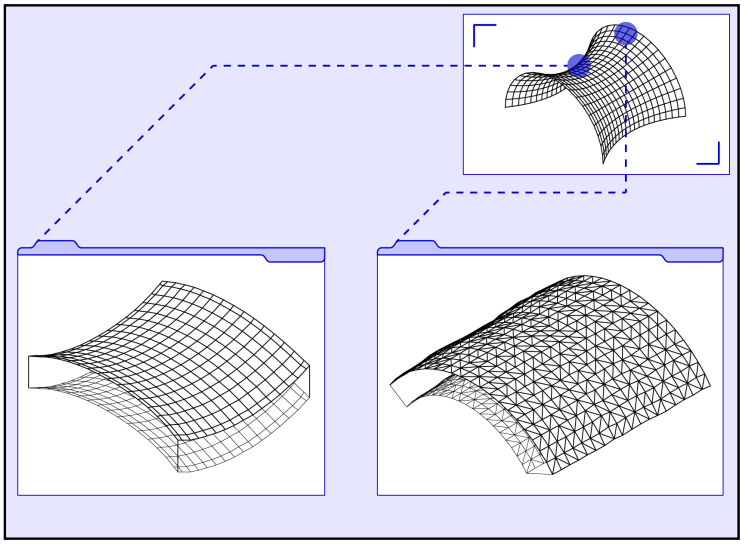

## Extracting the required curvature

Once the final form has been derived, the shell is discretised into the desired number of bilayer panels. Each element possesses individualised curvature that needs to be reproduced with the selected timber species.

The optimal scenario involves the use of locally produced timber panels. In the case of the Netherlands, neighbouring countries like Germany provide large quantities of exported timber, including spruce and beech wood which serve as ideal species of softwood and hardwood for bilayer construction. Once materiality has been determined, curvature can be simulated to determine the ideal dimensions for bilayer thickness, width and length.

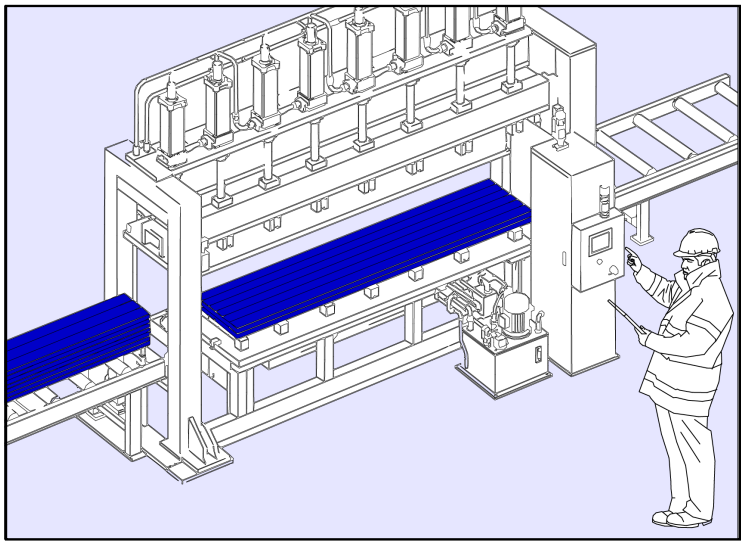

## Laminating hygromorphic bilayers

This stage of production demands a lot of high-powered machinery for sizing, conditioning, lamination and storage.

Early conditioning of timber samples can involve lowering the moisture content through kiln-drying, or raising the moisture content with large moisture chambers. When comparing energy cost, relying on moisture chambers for conditioning is considerably more efficient than kiln-drying. Both require an insulated space to maintain a stable temperature, but the moisture chamber only needs to rely on the passive hygroscopy of the salt compound. The moisture chamber can also be re-purposed later for the controlled storage of completed panels once they have been laminated.

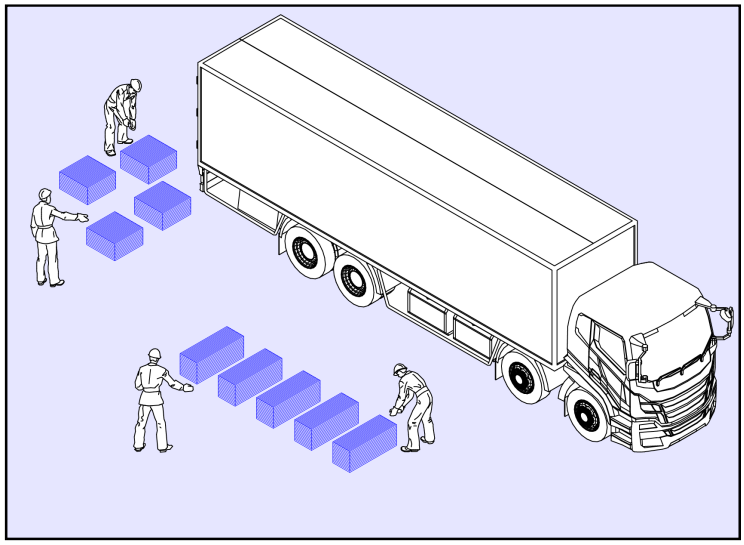

## Transporting hygromorphic bilayers

A key benefit of the discretisation process is supporting the transportability of the hygromorphic bilayers. Not only is it necessary to simplify large, free-form structures into smaller panels to ensure the desired curvature can be achieved, but it also results in a modular construction system.

This means individual panels can be stacked and sorted neatly to minimise space, rather than having to be transported as one entire structure.

A considerable risk is the potential for the bilayers to deform prematurely as they are being transported. To mitigate this issue, climate-controlled trucks or freight trains, which are commonly used to transport food, for example, can be employed to move the panels to site

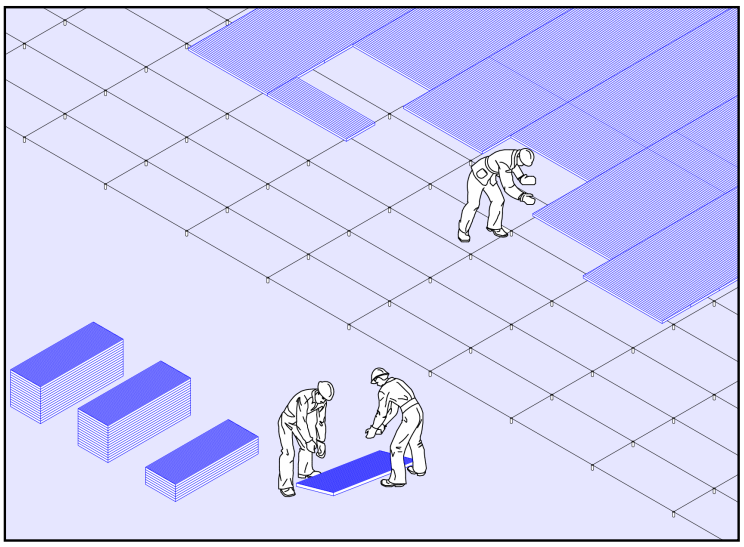

## Constructing the bilayer grid on-site

Prior to assembly, the site would be prepared with reference grid lines to ensure each element is positioned accurately in relation to the larger structure. The construction team would lay out the bilayer elements sequentially, beginning from an edge or central spine, and progressing outward in a controlled manner.

Finger joint connections ensure a simple and straightforward joinery process, with temporary clamps being employed along the edges to help maintain the form.

Depending on the site's elevation, a platform might need to be constructed to provide a smooth, flat region for the structure to deploy. An overly-irregular terrain may inhibit the deployment process.

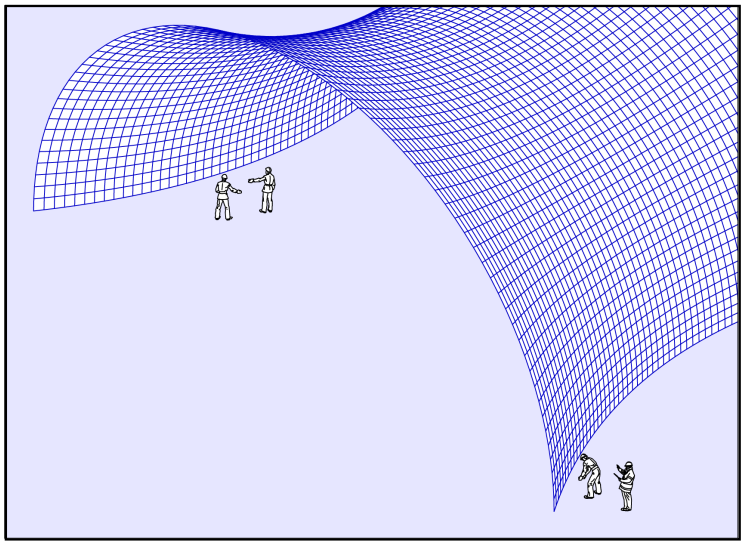

## Final deployment and locking

In an outdoor environment, the relative humidity can fluctuate frequently throughout a single day. By collecting seasonal, monthly, and weekly climatic data, the bilayers can be manufactured to activate within a specific period of time.

Due to the collision nature of the locking system, if the bilayers begin to over-bend they will not affect the interlocking curve-line elements as they will have already overlapped. For this reason, it is more effective to aim for a target moisture content that is slightly lower than the expected average to ensure the locking system will always fully activate.

# DISCUSSION & CONCLUSIONS 008



***figure 105:*** *Photograph of physical anticlastic samples (source: own work)*

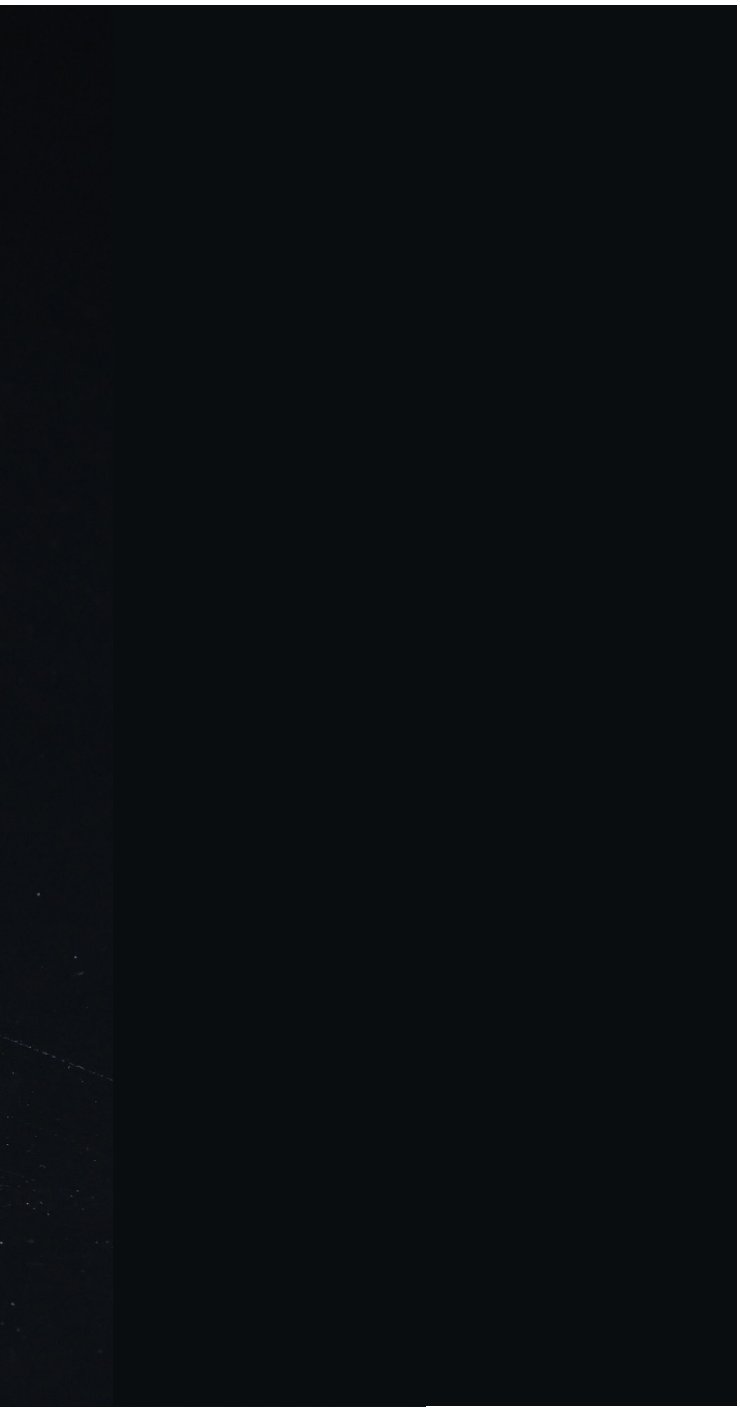

## 8.1 Introduction

The following chapter discusses and reflects on the insights gained from the research conducted in this paper. It elaborates on how the final results contribute to the existing literature, what the results imply for future developments and real-world applications, and reflects on the overall graduation process.

The main objective of this paper was to design, develop and validate a computational tool that could simulate the final curvature of individual hygromorphic timber bilayers for uni-directional and multi-direction curvature. The secondary objective was the kinematic exploration of a reversible locking system that could activate effectively under hygromorphic deformation.

## 8.2 Discussion of main findings

The literature explored for this paper highlights the potential of hygromorphic bilayer deformation to act as an inter-connected system for the deployment of more complicated curved forms. However, given the overall lack of existing and transparent research, numerous limitations were revealed regarding predictive modeling tools for bilayers, form exploration of anticlastic curvature, and transformable locking mechanisms. These were all addressed and explored in the paper, providing relevant contributions to the research gaps.

### 8.2.1 Simulating hygromorphic deformation

Digital simulations of curvature were carried out through the computational program Grasshopper. A particle-spring simulation model, constructed from transformable elements, was informed by mathematical curvature calculations to mimic bilayer deformation across different timber species.

To adapt the organic, anisotropic deformation of bilayer elements into a simplified and accurate computational model, a multi-level lattice frame structure was designed. Adaptive parameters were introduced to the spring elements of the structure to easily and efficiently manage varying dimensions across all three main Cartesian co-ordinate axes. The deformations were guided by curvature results derived from an adapted version of Timoshenko's formula for bi-metal bending, providing relevant data for timber bending instead.

Validation testing for the tool simulating monoclastic curvature was carried out for beech (hardwood) and pine (softwood) bilayers, and oak (hardwood) and spruce (softwood) bilayers. The results displayed an average curvature inaccuracy range of approximately 11% (11.05%) above the curvature results derived from the Timoshenko formula. This indicates that the simulations presented a slightly larger radii of curvature than mathematically predicted.

The computational tool was expanded to provide curvature simulations for varied fibre orientations within the full range of 0° to 180° (rotations within the range of 180° to 360° were excluded from the transformation range as they simply present mirrored reflections of the 0° to 180° orientations, and therefore do not produce unique curvature results). The lattice displayed appropriate structural integrity when subjected to simulations at 20°, 25°, 30°, 45°, 60°, 70°, and 75°. Deformation for unorthodox orientations were also assessed, including 17.2°, 29.7°, 41.3°, 64.4°, and 77.7°. Although it would be impossible to assess all possible orientations, the results presented allow us to derive the conclusion that the simulation is able to function effectively for an infinite degree of fibre orientations within 0° to 180°.

The maximum degree of curvature for the 45° simulations was extracted from the deformed results and compared to the Timshoenko formula as well. Similarily, a curvature innaccuracy of approximately 9% (9.59%) was derived for the beech and pine bilayer, and the oak and spruce.

The slight deviations in accuracy are a result of conflicting parameters in the simulation. To maintain structural integrity and uniform bending, it was necessary to integrate numerous limiters and parameters, including torsional restrictions, lateral bracing, and length constraints.

### 8.2.2 Anticlastic curvature

Following the curvature validation for the monoclastic simulations, the tool's methodological process was re-constructed to present multi-direction curvature in the shape of anticlastic deformation. An adapted particle-spring

model, based around the same multi-level lattice frame structure, was constructed for these simulations. Adaptive parameters were maintained to allow for the re-sizing of the bilayer's width, thickness and length in a similar fashion to the first tool.

Although data for the degree of curvature could be derived from Timoshenko's formula, the results only present curvature in a single (monoclastic) direction, and fail to consider multi-directional influence. To inform and validate the digital tool appropriately, physical samples were developed to asses their real-world curvature.

According to literature, bilayer deformation transitions from monoclastic to anticlastic curvature when samples approximate squares (low aspect ratio), and the difference in thickness between the hardwood (active) layer and the softwood (passive) layer is less than 4 times greater. Based on this data, independent variables for total bilayer thickness, and thickness ratio between the hardwood vs the softwood were introduced. A sample range of 6mm, 8mm, and 10mm was taken for overall bilayer thickness, with ratios of 1:1, 2:1, and 3:1 taken as the difference in thickness between the hardwood and the softwood. The final distribution for 6mm included:

- 3mm + 3mm,
- 4mm + 2mm,
- 4.5mm + 1.5mm;

for 8mm it included:

- 4mm + 4mm,
- 5.3mm + 2.7mm,
- 6mm + 2mm;

for 10mm it included:

- 5mm + 5mm,
- 6.7mm + 3.3mm,
- 7.5mm + 2.5mm.

The linear step-up in controlled variables was necessary to provide comparative data to determine trends across dimensional scaling.

The final sample range involved a total of 18 bilayer samples (two groups of 9) constructed using oak (hardwood) and spruce (softwood) panels. A width and length of 160mm x 160mm was taken as the controlled dimensional variable for all samples, along with a relative humidity of 55% for pre-lamination, and 95% for post-lamination. Following conditioning, valid samples were selected based on the moisture content disparity between the oak and spruce wood that remained within 1% to ensure moisture content uniformity across the bilayer.

3D scans were carried out for all valid samples to assess the final curvature across the direction of expansion of the hardwood (taken as the x-direction), and the direction of expansion of the softwood (taken as the y-direction) using the digital modeling software Rhinoceros 3D. Anticlastic curvature was most noticeable in bilayer configurations with a thickness ratio of 1:1, and narrower overall thicknesses. Whereby curvature in the x-direction is presented as positive, the bilayer configuration with thickness 6mm and ratio 1:1 exhibited curvature of $1.04 \times 10^{-3}\,mm^{-1}$ to $0.98 \times 10^{-3}\,mm^{-1}$ in the x-direction, and $-0.384 \times 10^{-3}\,mm^{-1}$ to $-0.307 \times 10^{-3}\,mm^{-1}$ in the y-direction. Alternatively, for all samples with a thickness ratio of 3:1, monoclastic curvature tended to dominate the deformation. The bilayer configuration with thickness 6mm and ratio 3:1 exhibited a curvature of $2.43 \times 10^{-3}\,mm^{-1}$ to $2.30 \times 10^{-3}\,mm^{-1}$ in the x-direction, which was considerably greater than the 1:1 ratio, but displayed a negligible curvature range of $-0.05 \times 10^{-3}\,mm^{-1}$ to $-0.01 \times 10^{-3}\,mm^{-1}$ in the y-direction.

Due to the dimensions of the samples, for bilayers with an overall thickness of 10mm, curvature in both directions was considerably less than when compared to the thinner samples. For a thickness of 10mm and ratio 1:1, almost no curvature was visible in both directions, resulting in nearly flat sample, although the configuration with thickness 10mm and ratio 3:1 exhibited a curvature of $1.67 \times 10^{-3}\,mm^{-1}$ to $1.57 \times 10^{-3}\,mm^{-1}$ in the x-direction.

As the simulative tool relies on numerical inputs for curvature, the integration of physical data into the digital workflow was extremely easy. To ensure consistency, a validation was carried comparing the geometry of the form-finding for anticlastic curvature and the original data. The results indicated a very large disparity in accuracy. For samples with a greater degree of curvature, above 0.00065, the accuracy remains above 94%. Conversely, as the degree of curvature decreases, the accuracy drops exponentially. The highest range of calculated accuracy was 44-55% for 0.00015 curvature, before dropping to around 21-36% for

curvatures within 0.00010 - 0.00011. The lowest accuracy range of 12-15% was present for curvature below 0.00009.

A significant reason for this is the margin of error is the disproportion in precision demanded between finitely small curvatures versus larger curvatures. When the tool carries out its form-finding for extremely small curvatures, any minor deviations in vertical amplitude of the final curve can produce disproportionately large differences in the resulting curvature radius. Conversely, for higher degrees of curvature, the radius is far smaller and therefore similar deviations represent a much more minor influence on the overall geometric scale. Back-calculations of the final results revealed that the simulative tool exhibits a margins of error for amplitude of +/- 1mm. Naturally, for very small radii, this level of error is less influential, but for radii multiple magnitudes larger, this presents an enormous imprecision.

### 8.2.3 Reversible locking

Kinematic exploration of a reversible locking system for multi-element hygromorphic bilayer arrangements was carried out with physical prototyping. Curve-line activation was explored using hinging paper models with varied degrees of curvature that helped determine the influence of induced deformation on vertical activation. 6 different samples were explored with collective curvature widths of 40mm, and varying amplitudes of 2.5mm, 5mm, 7.5mm, 10mm, 15mm, and 20mm. For samples with lower amplitudes of curvature, full vertical activation was achieved with minimal deformation, whereas samples with greater amplitude required a greater degree of deformation to activate successfully.

Development of polypropylene samples introduced greater material rigidity. Rather than employing hinges, curve-lines were cut using an incision and engraving pattern. 8 sample curvatures with a width 40mm and an amplitude of 5mm were assessed across curve divisions of 5, 7, 9, 11, 13, 15, 17, and 19. Samples with a greater number of divisions achieved smoother activation than samples with less divisions.

13 curve-line elements with a division of 19 were laser cut to assess the structural equilibrium of a reversible "Z-hook" for monoclastic curvature. Based off an S-hook with two inflection points, the Z-hook achieved structural equilibrium by locking adjacent curve-line elements under tension, introducing a restrain that successfully prevented re-flattening. The planar orientation of the Z-hook flanges is a critical component to its success, wherein both flanges must be pointed in the direction of movement of its corresponding curve-line element as it attempts to re-flatten.

The final prototype presents a successful proof-of-concept of the kinematic mechanisms of the locking system for structural equilibrium under a controlled environment.

### 8.2.4 Further research suggestions

As the research presented in this paper covers a more foundational scope, with the development of digital tools and a locking system to facilitate upscaling, ample opportunity exists for further research to explore human-scale applications.

**Free-form shells at human-scale**

There is currently very little empirical research that explores how a deployable structure comprised of hygromorphic bilayers would behave in fluctuating humidity conditions at a human scale.

Building on the tools presented in this paper, further research could explore the practical process of designing individual bilayers, connecting them as one system, and determining how they interact throughout the process of deployment. Real-world validation is extremely important for assessing the minute complexities of multi-element systems, especially were bilayers are all exhibiting slightly different curvature. Questions arise on whether activation will be smooth, whether adjacent elements will disengage from each other and lead to collapse, whether the target form can be achieved successfully from computational data or whether the physical prototype deviates from predictions.

Kiesewetter et al. (2025) explored multi-element systems at a smaller scale as furniture. In their paper only uni-direction designs were explored, but their process provides an ideal precedent for adaption into multi-direction, free-

form structures. Given that indoor climates in modern buildings tend to be much more stable than outdoor environments, they present a less unpredictable environment to test long-term activation.

**Reversible locking system**

Continuing this scope of research, the integration of the reversible locking system into a complete structure will provide practical data on its behaviour, success and viability.

While the physical prototypes presented in this paper have successfully validated the kinematic mechanism, extensive research is still necessary to create a working prototype. This includes exploration on the potential materiality of the curve-line elements, and the lamination process to bond them to individual bilayers. The interaction between both parts is also a critical consideration. Notably, the curvature of the bilayer is the most critical influence to the smoothness of activation, and vice versa, the curve-line element may resist expansion and limit the hygromorphic deformation as the timber expands.

**Environmental assessment**

Research in a controlled indoor environment can assist in perfecting a system and ensuring it functions successfully. To fully validate a deployed system, further research must be carried out in external environments. This provides insight on the structure's resilience and the effectiveness of the locking mechanism.

Constant fluctuations in relative humidity are one of the most critical considerations for achieving a successful deployment. A complete analysis of 2D construction to 3D deployment for different seasons, bilayer thicknesses and structural dimensions need to be carried out in order to determine necessary tolerances and adjustments for future designs. Research on the influence of weather conditions is also extremely important, as sunlight or rain may lead to less or greater moisture absorption than predicted. Therefore, the impact of treating timber bilayers on their curvature should also be explored in an attempt to make them more resilient.

## 8.3 Conclusions

Through computational exploration, mathematical derivation, physical prototyping, and material exploration, this paper successfully presented validated results and tools for the main research question;

**How can a computational design workflow be developed for simulating hygromorphic bilayer deformation to support the design of deployable free-form structures?**

Exploration of the literature presented the potential for hygromorphic bilayers to act as a multi-element system for deployable structures; activating from flat, 2D configurations to 3D domes as a result of changes in moisture content. However, to achieve upscaling for large curved forms, the relevant literature displayed a lack of available predictive modeling tools to simulate hygromorphic curvature.

The results of this paper demonstrate that both the uni-directional, and multi-directional curvature possible with bilayers can indeed be successfully translated into a physics-based particle-spring model. Upon qualitative analysis, both computational workflows achieve monoclastic and anticlastic curvature across a full range of fibre orientations (0° - 180°), and bilayer dimensions, without exhibiting structural failure or unpredictable deformations. For monoclastic simulations, the final curvature is presented with an accuracy of 90%, based on validations from mathematical formula. In the case of anticlastic curvature, mathematical formulas are not appropriately developed to handle multi-directional curvature derivations, demanding validation with physical samples. The process of transferring physical, numerical data into the digital form-finding proved successful, with qualitative analysis of the final simulations indicating appropriate anticlastic curvature. A lengthier validation process, comparing concrete values of curvature, raised concerns for the accuracy of the tool at extremely small degrees of curvature. The tool can handle a margin of error of +/- 1mm in amplitude for all curvatures, and while this is precise at a larger scale, for finitely small degrees of curvature (around 0.00009) accuracy drops to 12%.

While further research and validation is necessary for large-scale architectural implementation, the conclusions presented in this research can support manufacturing at the scale of single elements. The design and fabrication of individual bilayers can be accelerated through computational exploration that doesn't demand time and financial resources to explore varied bilayer configuration.

### 8.3.1 Sub-research questions

**To what extent can the computational workflow be adapted to generate different target geometries?**

The workflows developed in this paper successfully employ particle-spring simulations to translate data on spring expansion into curvature. Variables such as spring length, grid structure, torsional rigidity, lateral reinforcement, and dimensional adaptability all impose an important influence on the final simulation.

To achieve anticlastic over monoclastic curvature, the computational workflow indicates that the interaction between the expanding springs in a primary direction versus the perpendicular direction, needs to be unified as one complete system with competing force parameters. By re-constructing the simulation model around a single group of points, the behaviour of the spring is concentrated at the intersecting nodes. As presented in the paper, failing to unify the system will result in two separate, perpendicular monoclastic shells.

For both workflows, qualitative data is gathered through personal observation to determine if the curvature

presented in the simulations is indeed approximating monoclastic or anticlastic curvature.

The final validation for the monoclastic tool presents quantitative data indicating an accuracy of around 90%. Computational simulations tend to exhibit a radius of curvature that is 10% larger than mathematically derived. To match the digital simulation to real-world behaviour, quantitative data is extracted from the geometric properties of physical anticlastic samples. Measuring the actual curvature of these samples provides the necessary numerical parameters to inform the simulation, ensuring it closely approximates physical behavior.

**How can material data be effectively integrated into a digital simulation of hygromorphic behaviour?**

As derived from literature, the adapted version of Timoshenko's bi-metal curvature formula can accurately calculate the degree of curvature of a timber bilayer configuration. The formula considers moisture content, differential swelling coefficients, moduli of elasticity, and layer thickness, allowing material properties from different timber species to be implemented into the equation.

Although the formula doesn't present information on expansion, a scaling ratio was successfully derived from geometric exploration that provided numerical information on the degree of expansion across the bilayer's cross-section. The final simulations were validated against the formula's curvature to determine accuracy.

A key limitation is that the formula predicts curvature under idealised conditions. As timber is an organic material, slight inconsistencies will arise between panels of the same species and dimensions. Additionally, the process of moisture conditioning and lamination can be imperfect, resulting in minor irregularities. Therefore, the curvature presented in the computational workflows serves as a guide, and manufactured bilayers may not necessarily match with 100% accuracy.

**To what extent can varied bilayer configurations generate anticlastic curvature behaviour?**

To generate anticlastic behaviour, it is necessary for the passive layer to exhibit a greater influence on the overall bilayer system as moisture is absorbed.

For the physical tests, configurations with a thickness ratio of 1:1 displayed greater degrees of curvature along the passive direction of expansion. This occurs as a result the passive layer's increased bending stiffness and greater directional strain as it expands. Anticlastic curvature begins to fail where the passive layer is thinner. For example in thickness ratios of 3:1, the active layer begins to dominate and overpowers the passive layer as hardwoods exhibit greater expansion and bending stiffness due to their cellular structure.

Varying the overall thickness of the system also decreases or increases the degree of curvature in both directions. Where samples are thicker, they curve less due to an increased stiffness, whereas thinner samples display more curvature.

**How can hygromorphic deformation facilitate kinematic activation for an integrated locking system?**

Bilayer expansion results in a very unique deformation, which demands a locking system that is not rigid and can activate effectively from a flat state to a curved 3D form. Curve-line activation was explored in this paper as a reliably applicable system for varied bilayer curvature.

Physical prototyping demonstrated activation across a range of different curvatures, indicating that curve-line elements can perform effectively for varied bilayer curvatures. Samples were explored with constrained width but varied degrees of amplitude, and findings determined that a greater amplitude (and naturally a greater curvature) demands more bending to achieve full vertical activation. Given that bilayers can exhibit a near infinite range of curvature depending on thickness, material selection and planar dimensions, curve-line elements can be adapted easily for different configurations.

By considering the collision locking method, a configuration of alternating curve-line elements were organised along a rectangular strip with a high aspect ratio. Upon inducing curvature in the thin rectangular strip, the curve-line elements activated to a vertical position and

simultaneously overlapped with adjacent elements. This collision-based overlap creates a self-aligning overlap that presents the opportunity for rigidisation in the deployed state.

The physical prototypes indicate that hygromorphic deformation can effectively facilitate passive kinematic activation by transforming local curvature into controlled geometric engagement.

**How can a joinery system be designed to achieve both structural equilibrium and reversibility for curved forms?**

To build upon the system of curve-line activation, a reversible lock with dry connection based on a "Z-hook" was explored.

Due to the curve-line elements' tendency to re-flatten and move away from each other as the curvature of the bilayers is reversed, they induce tension in the Z-hook as it restricts their movement. This rigidises the hooking mechanism and helps maintain the deployed curvature. Based on literature, an angled flange profile provides greater structural reinforcement. It reduces the possibility of shearing between the vertical and horizontal elements in the hook. Additionally, as derived from the physical prototyping, the planar orientation of the hook is an essential factor that locks the element or allows it to be easily and smoothly disengaged from between the curve-line elements. This makes it easy to both lock the entire system and also release it for deconstruction and removal when necessary.

Once the hook element was designed, it was applied to a physical model after bending from a flat state into a curved geometry. The final shape was maintained without separation for over 24 hours as the hooks resisted tension in the system, indicating geometric stability.

## 8.3.2 Implications and recommendations

**To what extent are the results applicable in practice?**

The goal behind the research carried out in this paper was the possibility of upscaling hygromorphic bilayers into larger, more complicated systems of deployable structures. Currently, the field of material research on hygromorphic bilayers for such structures is still in its infancy and extremely narrow. While the results achieved in this paper provide a foundational step for potential upscaling, the current research gap is too vast to accommodate large-scale designs.

However, from a manufacturing standpoint, there is strong potential for employing the computational tools in this paper, and expanding upon them as they assist in the design and construction of individual panels. With a greater access to advanced cutting machinery, climatic chambers, and controlled timber samples, the accuracy for anticlastic deformation can also be vastly improved.

**To what extent has the projected innovation been achieved?**

The intended goals for the research were achieved largely with success. Bilayer curvature prediction for monoclastic shells across varied fibre orientations and thicknesses was achieved successfully, as well as the kinematic exploration of a reversible locking system. The tool simulating anticlastic curvature was constructed successfully, but the validation with physical samples was ultimately too small. In an ideal scenario, with a greater time frame, a larger collection of samples would have been constructed to gather a greater pool of data.

**Does the project contribute to sustainable development, and what is the impact of your project on sustainability (people, planet, profit/ prosperity)?**

Modern deployable structures are constructed largely from energy-intensive materials such as steel, glass, plastics, and even paper (on smaller scales), while also demanding high amounts of energy or labour for activation.

By presenting hygromorphic bilayers as an alternative element for deployable structures, the system incorporates an organic and naturally sustainable material while taking advantage of passive activation through moisture. In this way, energy demands for production are reduced as the timber can be maintained in its raw form and cut to size, as opposed to steel or glass which need to be heated and re-shaped. Additionally, samples can be conditioned after

they have been cut and planed to accelerate the process and reduce the need of high-powered kilns for drying. Rather than demanding a large labour force and additional energy to deploy, the blayers can be interlocked on-site before deforming passively.

A limitation to the sustainability of the project is the use of chemically-harmful adhesives to laminate bilayers. Not only is production of the adhesive environmentally unfriendly, as they rely on petrochemicals, they make wood products nearly impossible to recycle.

**What is the socio-cultural and ethical impact of the project?**

By presenting timber's tendency to deform under changing humidity conditions in a beneficial light, this paper helps to shift how manufacturers and architects consider the different properties of timber. Rather than discrediting timber bending as undesirable or something to be restricted in light of trying to achieve linear forms, it raises awareness on the possibilities of design applications.

The methodology carried out in this paper is clearly explained in the hopes that it can be employed and built upon to ease manufacturing and design, challenging the notion that timber deformations are unpredictable and difficult to work with.

**How does the project affect architecture or the built environment?**

Modern trends in architecture are slowly beginning to shift towards fluid, curved shapes, as can be seen in projects from firms such as Zaha Hadid Architects, MAD Architecuts, and UN Studio.

Creating curvature from inherently rigid materials such as steel, concrete and glass demands more energy, especially through heating which makes these materials more deformable. Hygromorphic bilayers are able to achieve this curvature passively, before being locked into their curved form permanently with a third lamination layer. This process can help support a more sustainable and ethical production of the curved forms that are becoming more and more desirable in modern architecture.

## 8.3.3 Reflection on considerations and limitations

**How is the graduation topic positioned within the context of the Building Technology studio?**

The Delft University of Technology describes the Building Technology track as a university program focused on sustainable design and innovative building elements. This graduation topic is positioned within the Design Informatics and Material Research studios in the Building Technology track. The design and development of the computational tools for simulating bilayer curvature fall under the category of Design Informatics as they encompass digital form exploration, scripting and simulation. Alternatively, research on hygromorphic deformation for anticlastic and monoclastic curvature embody material research as it expands knowledge on an organic, physical material.

**How did the research approach work out, and what are the strengths, weaknesses, opportunities and threats associated with the methodology?**

The research approach was largely successful, combining computational simulation, adaptive form-finding, material exploration, and deformation analysis to support and improve the tools and prototypes developed.

**Strengths:** Physics-based particle-spring modeling demonstrated a very effective method for translating physical real-world deformations of timber behaviour into an easily adaptive and explorative simulative tool. Based on qualitative analysis, the final simulation visually assumes an accurate monoclastic or anticlastic form in 3D, digital space. Quantitative data was derived from comparing the simulated curvature to the mathematical results with 90% accuracy, and analysing the xyz co-ordinates of the particles. Especially when considering vertical translation, each node shifted across the digital, 3D space, indicating deformation.

The computational workflows help support the production of predictable bilayer forms. It is not longer necessary to rely on the mass production of hundreds of different bilayers to gauge the desired deformation, as this

is extremely time-intensive, highly demanding of physical resources, and extremely costly. By employing computational tools, varied configurations and forms can be explored quickly and smoothly to assess the most effective dimensions.

Prototyping of the reversible locking system helped realise the system from a conceptual design to a practical system. Building upon literature, the design of the locking element is optimised to maintain structural deformation under tension while limiting shear. A qualitative observation of the system indicated the effectiveness of the Z-hook's orientation in either rigidising the structure or enabling smooth disengagement. Although there were limitations on timeframe, a quantitative analysis was conducted on geometric stabilisation across a 24 hour period. The system demonstrated structural resilience, indicating that future development and upscaling are highly plausible.

**Weaknesses:** Time constraints, financial costs, and the manufacturing tools available heavily limited the scope of physical sampling and computational exploration.

Acquiring timber for cutting became a considerably costly and complicated procedure. Hardwoods were especially inaccessible and very expensive to purchase. Additionally, requesting planks with specific sizing was not feasible for almost all manufacturers as they would either refuse completely or demand a greater financial contribution. Ultimately, the most accessible planks were collected from a local hardwood store. Unfortunately, in the case of the softwood planks, the drying process had resulted in slight cupping of all the planks along the short edge. This meant that samples were not completely flat, but rather exhibited bending prematurely. Where possible, the flattest planks were selected.

Additionally, due to costs, cutting and sizing of the samples was done manually. Although dimensions were achieved within a 2mm range for length and width, and a 0.5mm range for thickness, given the very specific dimensions of different bilayer configurations, this presented a slight inaccuracy range for the construction process.

For conditioning, only the disconnected refrigerator was available, which proved to present numerous difficulties for maintaining a stable relative humidity. The temperature inside the refrigerator fluctuated slightly, and the relative humidity rose very slowly before stabilising. Due to time constraints this was not ideal, and made conditioning the samples more difficult and time-consuming. The limited dimensions of the refrigerator also meant that the individual samples had to be smaller in order to fit, whereas bigger samples would have been more ideal for exploring curvature.

Given the lack of machinery, the lamination process involved manually clamping timber samples with wood glue. Although this was quite successful, and curvature was achieved without any significant delamination, there were still instances of very small separations along the edges of some bilayers.

**Opportunities:** There is a severe lack of available, empirical research on the topic of hygromorphic timber bilayers, especially for the design of long-term, multi-element system. Therefore, as a result, there is significant potential to build upon and expand the research field for more viable real-world applications.

A greater range of physical samples exploring anticlastic curvature can be constructed to develop a repository of data that can provide more information to the simulative tool. Not only can more configurations be explored but also other timber species.

For real-world validation an expanded system of interlocking bilayers can be constructed to assess dimensional scaling and applicability. There is currently no research on a deployable form that can shelter an average person. Critical research also needs to be carried out on the lifespan of bilayer elements in outdoor environments, especially as treated timber will exhibit very different moisture absorption capabilities.

The design and prototyping of a reversible locking mechanism presents a novel, and original contribution to hygromorphic bilayer deployment. For a human-scale design, the reversible locking system can be upscaled to a practical application to acquire quantitative data on structural rigidity and long-term deployment. The exploration of a system that has so much potential to work effectively with curved deformations presents a very promising research direction, and hopefully something to be built upon and improved in

future papers.

**Threats:** It is worth remembering that the manufacturing of timber bilayers can be slightly unpredictable due to the organic nature of the material. This means the cellular structure of every panel will be infinitely different, even for identical species, cuts, width and height, and thickness. Although this presents a more complex variable, significant values such as moduli of elasticity, and swelling coefficients will remain relatively stable, meaning that any deviations in curvature will generally be quite small.

Large-scale, real-world testing has still not been carried out rigorously for deployable structures with hygromorphic bilayers. Therefore, launching into construction is ill-advised and demands more years of research, and digital and material exploration. It is necessary to derive qualitative and quantitative data on environmental unpredictability and how the bilayers will behave with continuous humidity fluctuations as a unified system. Long-term data needs to be derived when timber is subjected to constant loads over an extended period of time. The bilayers will begin to deform permanently due to the load, which will heavily impact the angle of curvature and overall stability of the system. Under external environmental conditions there is also the risk of delamination and splitting, which poses a significant structural concern.

The reversible locking system has also not been validated for structural resilience in bilayer systems, and cannot be considered for application in its current state. Further research should begin by exploringe small, bilayer samples with the integrated locking elements to determine how the system behaves at a small scale. This is especially critical for assessing structural stability, load distribution, and the impact of laminated curve-line elements on the overall deformation of bilayers.

**What is the correlation between the methodological approach carried out by the student, and the approach prioritised by the department?**

In Building Technology, all thesis graduation topics encompass a minimum for two different topics, in fields such as Design Informatics, Material Research, Structural Design, etc. to present well-rounded and validated research. The final demands also include a design or product based on the research achieved throughout the graduation process.

The topic explored in this paper centres around both Design Informatics and Material Research. This ensures that the methodology for achieving the computational tool is continuously validated and re-informed by both literature, mathematical formula, and first-hand physical data. The goal for the tool development was the design of a free-form deployable shell, which presents a scenario for real-world application and grounds the research in a broader context, rather than presenting it as an individual, isolated topic.

**How does the research relate with the final design?**

The final design was a computational tool for predicting bilayer curvature for both monoclastic and anticlastic forms. The research carried out included adapting timber expansion to a particle-spring model and implementing a formula for curvature into the design before testing for validity with physical samples. In this way, the research supported the accuracy of the final design to help ensure it could be applied to practical manufacturing.

**Where there any moral or ethical issues or dilemmas encountered during the research process, and if so, how were they dealt with?**

No moral or ethical issues or dilemmas were encountered throughout the course of this research.

# LITERATURE + FIGURE REFERENCES

009





# LITERATURE


Abdelmohsen, S., Adriaenssens, S., El-Dabaa, R., Gabriele, S., Olivieri, L., & Teresi, L. (2019). A multi-physics approach for modeling hygroscopic behavior in wood low-tech architectural adaptive systems. Computer-Aided Design, 106, 43–53. https://doi.org/10.1016/j.cad.2018.07.005

Ağırbaş, A., Kutucu, S., Ağırbaş, A., & Kutucu, S. (2025). Computational Design and Optimization of Discrete Shell Structures Made of Equivalent Members. Buildings, 15(17). https://doi.org/10.3390/buildings15173070

Albrektas, D., & Ukvalbergiene (2026). Impact of Wood Species, Dimensions and Drying Temperature on Sorption Behaviour of Wood. ResearchGate. https://doi.org/10.5552/drind.2015.1369

Al-Najjar, A., & Dodoo, A. (2023). Modular multi-storey construction with cross-laminated timber: Life cycle environmental implications. Wood Material Science & Engineering, 18(2), 525–539. https://doi.org/10.1080/17480272.2022.2053204

Artec 3D. (2026). Artec Spider II: Ultra-high-resolution 3D scanner. https://www.artec3d.com/portable-3d-scanners/artec-spider

Averseng, J., & Dubé, J. F. (2012). Design, Analysis and Self Stress Setting of a Lightweight Deployable Tensegrity Modular Structure. Procedia Engineering, 40, 14–19. https://doi.org/10.1016/j.proeng.2012.07.048

Avramidis, S. (2004). Physical Properties of Wood. Elsevier Ltd, 1828–1835.

Bechert, S., Schlopschnat, C., Göbel, M., Aicher, S., Menges, A., & Knippers, J. (2025). livMatS biomimetic shell: Structural advancements of segmented timber shells towards permanent building constructions. Structures, 79, 109524. https://doi.org/10.1016/j.istruc.2025.109524

Block, P., & Ochsendorf, J. (2007). Thrust network analysis: A new methodology for three-dimensional equilibrium. Journal of the International Association for Shell and Spatial Structures, 48.

Brancart, S., Vergauwen, A., Roovers, K., Van Den Bremt, D., De Laet, L., & De Temmerman, N. (2015). UNDULATUS: design and fabrication of a self-interlocking modular shell structure based on curved-line folding. In Proceedings of the IASS 2015 Symposium "Future Visions"

Burgert, I., & Fratzl, P. (2009). Actuation systems in plants as prototypes for bioinspired devices. Philosophical Transactions of the Royal Society A: Mathematical, Physical and Engineering Sciences, 367(1893), 1541–1557. https://doi.org/10.1098/rsta.2009.0003

Caetano, I., Santos, L., & Leitão, A. (2020). Computational design in architecture: Defining parametric, generative, and algorithmic design. Frontiers of Architectural Research. https://doi.org/10.1016/j.foar.2019.12.008

Cassell, A., Hobbs, R., & Otter, J. (1966). Dynamic relaxation. Ice Proceedings, 35, 633–656. https://doi.org/10.1680/iicep.1966.8604

Harris, R. (2015). 8 – Cross laminated timber. Wood Composites, 141-167. https://doi.org/10.1016/B978-1-78242-454-3.00008-1

Chen, C., Li, B., Kanari, M., & Lu, D. (2019). Epoxy Adhesives. Adhesives and Adhesive Joints in Industry. https://doi.org/10.5772/intechopen.86387

Cheng, T., Tahouni, Y., Sahin, E. S., Ulrich, K., Lajewski, S., Bonten, C., Wood, D., Rühe, J., Speck, T., & Menges, A. (2024). Weather-responsive adaptive shading through biobased and bioinspired hygromorphic 4D-printing. Nature Communications, 15(1), 10366. https://doi.org/10.1038/s41467-024-54808-8

Delft University of Technology. (2026). About. DINED. https://dined.io.tudelft.nl/en/about

DeSimone, A., & Teresi, L. (2025). Mechanics of Curved Crease Origami: One-Degree-of-Freedom Mechanisms, Distributed Actuation by Spontaneous Curvature, and Cross-Talk Between Multiple Folds. Journal of Applied Mechanics, 92(8), 081005. https://doi.org/10.1115/1.4068453

Dobrev, T., Dimov, S., & Thomas, A. (2006). Laser milling: modelling crater and surface formation. Proceedings of The Institution of Mechanical Engineers, Part C: Journal of Mechanical Engineering Science, 220(11), 1685-1696. https://doi-org.tudelft.idm.oclc.org/10.1243/09544062JMES221

Doroftei, I., & Doroftei, I. A. (2014). Deployable Structures for Architectural Applications—A Short Review. Applied Mechanics and Materials, 658, 233–240. https://doi.org/10.4028/www.scientific.net/AMM.658.233

Dutta, G. S., Meiners, D., & Ziegmann, G. (2024). A Study of Deployable Structures Based on Nature Inspired Curved-Crease Folding. Polymers, 16(6), 766. https://doi.org/10.3390/polym16060766

El-Dabaa, R., & Abdelmohsen, S. (2023). Hygroscopy and adaptive architectural façades: An overview. Wood Science and Technology, 57(3), 557–582. https://doi.org/10.1007/s00226-023-01464-8

Fenci, G. E., & Currie, N. G. (2017). Deployable structures classification: A review. International Journal of Space Structures, 32(2), 112–130. https://doi.org/10.1177/0266351117711290

Gao, J., Chen, M., Wang, Y., Yang, Z., Tang, L., Xu, P., & Chen, W. (2025). Force density method's energy principle and application in membrane-cable-strut-beam hybrid structures. Journal of Building Engineering, 99, 111523. https://doi.org/10.1016/j.jobe.2024.111523

Grönquist, P., Panchadcharam, P., Wood, D., Menges, A., Rüggeberg, M., & Wittel, F. K. (2020). Computational analysis of hygromorphic self-shaping wood gridshell structures. Royal Society Open Science, 7(7), 192210. https://doi.org/10.1098/rsos.192210

Grönquist, P., Wood, D., Hassani, M. M., Wittel, F., Menges, A., & Rüggeberg, M. (2019). Analysis of hygroscopic self-shaping wood at large scale for curved mass timber structures. Science Advances, 5, eaax1311. https://doi.org/10.1126/sciadv.aax1311

Guha, S. (2025). 3DP Glass Assemblies: A novel Workflow for Circular Assembly using 3D-Printed Glass

Masonry Units with a Kirigami inspired interlayer. Delft University of Technology.

Hanaor, A., & Levy, R. (2001). Evaluation of Deployable Structures for Space Enclosures. International Journal of Space Structures, 16(4), 211–229. https://doi.org/10.1260/026635101760832172

Henriksson, V., & Hult, M. (2015). Rationalizing freeform architecture Surface discretization and multi-objective optimization. Chalmers University of Technology.

Herzog, A., Kerschbaumer, T., Schwarzenbrunner, R., Barbu, M.-C., Petutschnigg, A., Tudor, E. M., Herzog, A., Kerschbaumer, T., Schwarzenbrunner, R., Barbu, M.-C., Petutschnigg, A., & Tudor, E. M. (2021). Efficiency of High-Frequency Pressing of Spruce Laminated Timber Bonded with Casein Adhesives. Polymers, 13(23). https://doi.org/10.3390/polym13234237

Hou, L., & Jiao, R. J. (2020). Data-informed inverse design by product usage information: A review, framework and outlook. Journal of Intelligent Manufacturing, 31(3), 529–552. https://doi.org/10.1007/s10845-019-01463-2

Howell, L., Magleby, S., & Olsen, B. (2013). Handbook of compliant mechanisms. Chichester, West Sussex, United Kingdom: John Wiley & Sons. https://doi.org/10.1002/9781118516485.ch1

Iuorio, O., & Korkis, E. (2019). Design and fabrication of a tessellated shell. Proceedings of the International FIB Symposium on Conceptual Design of Structures, 361-368.

Joosten, S., Radaelli, G., & Vallery, H. (2021). Passive autonomy: Hygromorphic rotational actuators. Smart Materials and Structures, 30(2). https://doi.org/10.1088/1361-665x/abcf1e

Kiesewetter, L., Wood, D., Körner, A., Takahashi, K., Knippers, J., & Menges, A. (2023). HYGROSHELL – In Situ Self-shaping of Curved Timber Shells. ResearchGate. https://doi.org/10.1515/9783111162683-004

Kiesewetter, L., Wood, D., & Menges, A. (2025). HygroShape: Programming Flat-pack, Self-shaping Wood Furniture. Proceedings of the ACM Symposium on Computational Fabrication, 1–15. https://doi.org/10.1145/3745778.3766658

Körner, A., Mader, A., Saffarian, S., & Knippers, J. (2016). Bio-Inspired Kinetic Curved-Line Folding for Architectural Applications. ResearchGate, 36. https://doi.org/10.52842/conf.acadia.2016.270

Kuijvenhoven, M., & Hoogenboom, P. C. J. (2012). Particle-spring method for form finding grid shell structures consisting of flexible members. Electronic Proceedings in Theoretical Computer Science, 53.

Lee, M. (2024). Structural behaviour of concrete shells using brittle reinforcement materials: A case study on stay-in-place flexible formworks with integrated high-strength textiles. Proceedings of the IASS 2024 Symposium, 199-209.

Lee, T.-U., Lu, H., Ma, J., Ha, N. S., Gattas, J. M., & Xie, Y. M. (2024). Self-locking and stiffening deployable tubular structures. Proceedings of the National Academy of Sciences, 121(40), e2409062121. https://doi.org/10.1073/pnas.2409062121

Mahmood, A., & Khalil, A. (2023). Shell Foundation Configuration and Geotechnical Behavior (A Review). International Information and Engineering Technology Association, 18(4), 861-868. https://doi.org/10.18280/ijdne.180412

Martínez-Criado, C., Lara-Bocanegra, A. J., Roig, A., Martín-Pastor, A., & Majano-Majano, A. (2024). Parametric design and digital fabrication of disassemblable elastic timber gridshells with principal curvature lines network and carpentry joints. Proceedings of the IASS 2024 Symposium, 499-509.

Moisture-related wood movement. (n.d.). Swedish Wood. Retrieved January 14, 2026, from https://www.swedishwood.com/wood-facts/about-wood/wood-and-moisture/moisture-related-wood-movement/

Molski, K. L., & Tarasiuk, P. (2021). Stress Concentration Factors for Welded Plate T-Joints Subjected to Tensile, Bending and Shearing Loads. Materials, 14(3), 546. https://doi.org/10.3390/ma14030546

Molski, K. L., Tarasiuk, P., & Glinka, G. (2020). Stress concentration at cruciform welded joints under axial and bending loading modes. Welding in the World, 64(11), 1867–1876. https://doi.org/10.1007/s40194-020-00966-4

Museum of Hamburg History, Glass Roof—Projects—gmp Architekten. (n.d.). Retrieved January 14, 2026, from https://www.gmp.de/en/projects/410/museum-

of-hamburg-history-glass-roof

Naboni, R., Sartori, S., & Mirante, L. (2018). Adaptive-Curvature Structures with Auxetic Materials. Advanced Materials Research, 1149, 53–63. https://doi.org/10.4028/www.scientific.net/AMR.1149.53

Neugebauer, J., Wallner-Novak, M., Lehner, T., Wrulich, C., & Baumgartner, M. (2018). Movable Thin Glass Elements in Façades. Conference on Architectural and Structural Applications of Glass (6). https://doi.org/10.7480/cgc.6.2133

Panetta, J., Isvoranu, F., Chen, T., Siéfert, E., Roman, B., & Pauly, M. (2021). Computational inverse design of surface-based inflatables. ACM Transactions on Graphics, 40, 1–14. https://doi.org/10.1145/3476576.3476584

Patera, A., Derluyn, H., Derome, D., & Carmeliet, J. (2016). Influence of sorption hysteresis on moisture transport in wood. Wood Science and Technology, 50. https://doi.org/10.1007/s00226-015-0786-9

Pelliccia, G., Baldinelli, G., Bianconi, F., Filippucci, M., Fioravanti, M., Goli, G., Rotili, A., & Togni, M. (2020). Characterisation of wood hygromorphic panels for relative humidity passive control. Journal of Building Engineering, 32, 101829. https://doi.org/10.1016/j.jobe.2020.101829

Peng, H., Liu, Z., Zhu, J., Jiang, J., Lyu, J., & Zhan, T. (2023). Bending responses of self-shaping wood bilayers: Comparison between adsorption and desorption processes. Journal of Wood Science, 69(1), 29. https://doi.org/10.1186/s10086-023-02105-1

Piker, D. (2013). Kangaroo: Form Finding with Computational Physics. Architectural Design, 83(2), 136–137. https://doi.org/10.1002/ad.1569

Pone, S., Colabella, S., D'Amico, B., Fiore, A., Lancia, D., & Parenti, B. (2013). Timber post formed grid shell: Digital form finding / drawing and building tool. Proceedings of the International Association for Shell and Spatial Structures (IASS) Symposium 2013. https://doi.org/10.13140/2.1.1339.1686

Qatu, M. S., Sullivan, R. W., & Wang, W. (2010). Recent research advances on the dynamic analysis of composite shells: 2000–2009. Composite Structures, 93(1), 14–31. https://doi.org/10.1016/j.compstruct.2010.05.014

Rabinovich, M., Hoffmann, T., & Sorkine-Hornung, O. (2019). Modeling Curved Folding with Freeform Deformations. Association for Computing Machinery Transactions on Graphics, 38(6), 1-12. https://doi-org.tudelft.idm.oclc.org/10.1145/3355089.3356531

Reaisi, S., & Ghiyasi, T. (2026). Active Bending Curved-line Folding as Lightweight Structures Transforming Flat Sheets into Complex 3D Forms. ResearchGate. Architectural Research Centers Consortium (ARCC) 2025. https://www.researchgate.net/publication/404720170_ACTIVE_BENDING_CURVED-LINE_FOLDING_AS_LIGHTWEIGHT_STRUCTURES_TRANSFORMING_FLAT_SHEETS_INTO_COMPLEX_3D_FORMS

Reichert, S., Menges, A., & Correa, D. (2015). Meteorosensitive architecture: Biomimetic building skins based on materially embedded and hygroscopically enabled responsiveness. Computer-Aided Design, 60, 50–69. https://doi.org/10.1016/j.cad.2014.02.010

Rodrigo, M. & Gilfranco, A. (2017). Between Designer and Design: Parametric Design and Prototyping Considerations on Gaudí's Sagrada Familia. Periodica Polytechnica Architecture. 47. 89-93. https://doi.org/10.3311/PPar.10335

Rüggeberg, M., & Burgert, I. (2015). Bio-Inspired Wooden Actuators for Large Scale Applications. PLOS ONE, 10(4), e0120718. https://doi.org/10.1371/journal.pone.0120718

Salzberger, M. (2024). Shape-Changing Wood Joints in Crafts and Industry and Their Potential for Building Construction and Wood Culture. (2024). International Journal of Wood Culture, 4(1), 58–95. https://doi.org/10.1163/27723194-bja10031

Shams, S. (2025). A comparative analysis of building materials for sustainable construction with emphasis on CO2 reduction. https://www.academia.edu/3308515/A_comparative_analysis_of_building_materials_for_sustainable_construction_with_emphasis_on_CO2_reduction

Simón, C., Esteban, L. G., de Palacios, P., Fernández, F. G., & García-Iruela, A. (2016). Thermodynamic properties of the water sorption isotherms of wood of limba (Terminalia superba Engl. & Diels), obeche (Triplochiton scleroxylon K. Schum.), radiata pine (Pinus radiata D. Don) and chestnut (Castanea sativa Mill.). Industrial Crops and Products, 94,

122–131. https://doi.org/10.1016/j.indcrop.2016.08.008

Stagno, V., Ricci, S., Longo, S., Verticchio, E., Frasca, F., Siani, A., & Capuani, S. (2022). Discrimination between softwood and hardwood based on hemicellulose content obtained with portable nuclear magnetic resonance. Cellulose. https://doi.org/10.1007/s10570-022-04728-x

Tachi, T. (2009). One-DOF Cylindrical Deployable Structures with Rigid Quadrilateral Panels. Proceedings of the International Association for Shell and Spatial Structures (IASS) Symposium 2009.

Thybring, E., Fredriksson, M., Zelinka, S., & Glass, S. (2022). Water in Wood: A Review of Current Understanding and Knowledge Gaps. Forests, 13, 2051. https://doi.org/10.3390/f13122051

Tian, P., Han, J., Guo, S., Di, J., & Han, X. (2024). Prediction Distribution Model of Moisture Content in Laminated Wood Components. Polymers, 16(11). https://doi.org/10.3390/polym16111453

Timoshenko, S. (1925). Analysis of Bi-Metal Thermostats. (n.d.). Retrieved December 3, 2025, from https://opg-optica-org.tudelft.idm.oclc.org/josa/fulltext.cfm?uri=josa-11-3-233

Tran, A., Konnerth, J., & Gindl-Altmutter, W. (2024). Adhesive strength and micromechanics of wood bonded at different moisture contents. International Journal of Adhesion and Adhesives, 132, 103688. https://doi.org/10.1016/j.ijadhadh.2024.103688

Tupenaite, L., Kanapeckiene, L., Naimaviciene, J., Kaklauskas, A., Gecys, T., Tupenaite, L., Kanapeckiene, L., Naimaviciene, J., Kaklauskas, A., & Gecys, T. (2023). Timber Construction as a Solution to Climate Change: A Systematic Literature Review. Buildings, 13(4). https://doi.org/10.3390/buildings13040976

Vekariya, M., & Makwana, A. (2021). A Review on Thin-shell Structures: Advances and Trends. International Journal of Research Publication and Reviews, 2, 1593–1608.

Vergauwen, A., Laet, L. D., & Temmerman, N. D. (2017). Computational modelling methods for pliable structures based on curved-line folding. Computer-Aided Design, 83, 51–63. https://doi.org/10.1016/j.cad.2016.10.002

Wood, D. M., Correa, D., Krieg, O. D., & Menges, A. (2016). Material computation—4D timber construction: Towards building-scale hygroscopic actuated, self-constructing timber surfaces. International Journal of Architectural Computing, 14(1), 49–62. https://doi.org/10.1177/1478077115625522

Wood, D., Grönquist, P., Bechert, S., Scheder-Bieschin, L., Riggenbach, D., Lehmann, K., Rüggeberg, M., Burgert, I., Knippers, J., & Menges, A. (2020). From Machine Control to Material Programming: Self-Shaping Wood Manufacturing of a High Performance Curved CLT Structure – Urbach Tower. ResearchGate. https://doi.org/10.2307/j.ctv13xpsvw.11

Wood, D., Vailati, C., Menges, A., & Rüggeberg, M. (2018). Hygroscopically actuated wood elements for weather responsive and self-forming building parts – Facilitating upscaling and complex shape changes. Construction and Building Materials, 165, 782–791. https://doi.org/10.1016/j.conbuildmat.2017.12.134

Xhexhi, K., & Aliaj, B. (2025). Water Absorption, Moisture Content, and Capillarity Action in Wood: A Comparative Analysis of Fir, Pine, Beech, and Oak. Advanced Engineering Forum, 55, 1–16. https://doi.org/10.4028/p-ZYzbZ6

Yao, L., & Ishii, H. (2019). Hygromorphic living materials for shape changing. Robotic Systems and Autonomous Platforms (pp. 41–57). Woodhead Publishing. https://doi.org/10.1016/B978-0-08-102260-3.00003-2

Younis, A., & Dodoo, A. (2022). Cross-laminated timber for building construction: A life-cycle-assessment overview. Journal of Building Engineering, 52, 104482. https://doi.org/10.1016/j.jobe.2022.104482

Zhan, T., Li, R., Liu, Z., Peng, H., & Lyu, J. (2023). From adaptive plant materials toward hygro-actuated wooden building systems: A review. Construction and Building Materials, 369, 130479. https://doi.org/10.1016/j.conbuildmat.2023.130479

Zhang, L., Larsson, A., Moldin, A., & Edlund, U. (2022). Comparison of lignin distribution, structure, and morphology in wheat straw and wood. Industrial Crops and Products, 187, 115432. https://doi.org/10.1016/j.indcrop.2022.115432

Zhao, Z., & Yu, L. (2024). Geometric Design Methodology for Deployable Self-Locking Semicylindrical

Structures. Buildings, 14(6), 1690. https://doi.org/10.3390/buildings1406169

# FIGURES

Figure 1:

Institute for Computational Design and Construction (ICD), University of Stuttgart. (2019). Urbach Tower. https://www.itke.uni-stuttgart.de/research/built-projects/urbach-tower/

Figure 2:

Kim, H.-G., Kim, D.-G., Do, R.-H., Koo, K.-R., & Yu, Y.-J. (2024). Development of Deployable Reflector Antenna for the SAR-Satellite: Part 1. Design and Analysis of the Main Reflector Using Honeycomb Sandwich Composite Structure. Applied Sciences, 14(4), 1590. https://doi.org/10.3390/app14041590

Figure 3:

Holstov, A., Morris, P., Farmer, G., & Bridgens, B. (2015). Towards sustainable adaptive building skins with embedded hygromorphic responsiveness.

Figure 4:

Wood, D. M., Correa, D., Krieg, O. D., & Menges, A. (2016). Material computation—4D timber construction: Towards building-scale hygroscopic actuated, self-constructing timber surfaces. International Journal of Architectural Computing, 14(1), 49–62. https://doi.org/10.1177/1478077115625522

Figure 5:

Wood, D., Vailati, C., Menges, A., & Rüggeberg, M. (2018). Hygroscopically actuated wood elements for weather responsive and self-forming building parts – Facilitating upscaling and complex shape changes. *Construction and Building Materials*, *165*, 782–791. https://doi.org/10.1016/j.conbuildmat.2017.12.134

Figure 6:

Kiesewetter, L., Wood, D., & Menges, A. (2025). HygroShape: Programming Flat-pack, Self-shaping Wood Furniture. Proceedings of the ACM Symposium on Computational Fabrication, SCF '25, 1–15. https://doi.org/10.1145/3745778.3766658

Figure 7 & 8:

Institute for Computational Design and Construction (ICD), University of Stuttgart. (2019). Urbach Tower. https://www.itke.uni-stuttgart.de/research/built-projects/urbach-tower/

Figure 9:

Naboni, R., Sartori, S., & Mirante, L. (2018). Adaptive-Curvature Structures with Auxetic Materials. Advanced Materials Research, 1149, 53–63. https://doi-org.tudelft.idm.oclc.org/10.4028/www.scientific.net/amr.1149.53

Figure 10:
Own work

Figure 11:
Own work

Figure 12:
Own work

Figure 13:
Own work

Figure 14:

Institute for Computational Design and Construction (ICD), University of Stuttgart. (2019). Urbach Tower. https://www.itke.uni-stuttgart.de/research/built-projects/urbach-tower/

Figure 15:
Own work

Figure 16:

Jakes, J.E., Zelinka, S.L., Hunt, C.G., Ciesielski, P., Frihart, C.R., Yelle, D., Passarini, L., Gleber, S.C., Vine, D., & Vogt S. (2020). Measurement of moisture-dependent ion diffusion constants in wood cell wall layers using time-lapse micro X-ray fluorescence microscopy. Sci Rep 10, 9919. https://doi-org.tudelft.idm.oclc.org/10.1038/s41598-020-66916-8

Figure 17:

Thybring, E., Fredriksson, M., Zelinka, S., & Glass, S. (2022). Water in Wood: A Review of Current Understanding and Knowledge Gaps. Forests, 13, 2051. https://doi.org/10.3390/f13122051

Figure 18:
Own work

Figure 19:

Thybring, E., Fredriksson, M., Zelinka, S., & Glass, S. (2022). Water in Wood: A Review of Current Understanding and Knowledge Gaps. Forests, 13, 2051. https://doi.org/10.3390/f13122051

Figure 20:
Own work

Figure 21:

Rowell, R. (2012). 4 Moisture Properties. Handbook of Wood Chemistry and Wood Composites. https://doi.org/10.1201/b12487-7

Figure 22:

Ibitolu, J.B. (2018). DETERMINATION OF PROPERTIES OF SOME NIGERIAN TIMBERS FOR EN 338 STRUCTURAL SIZE SPECIMEN STRENGTH CLASSIFICATION. University of Ilorin, Nigeria. https://doi.org/10.13140/RG.2.2.24188.90248

Figure 23:

Todd, J. (2018). Veneer – The Background Basics. Florida School of Woodwork. https://schoolofwoodwork.com/veneer-the-background-basics/

Figure 24:
Own work

Figure 25:
Own work

Figure 26:

Seehanam, S., Chancharoen, W., & Promoppatum, P. (2023). Assessing the effect of manufacturing defects and non-Newtonian blood model on flow behaviors of additively manufactured Gyroid TPMS structures. Heliyon. 9. e15711. https://doi.org/10.1016/j.heliyon.2023.e15711

Figure 27:

Timoshenko, S. (1925). Analysis of Bi-Metal Thermostats. (n.d.). Retrieved December 3, 2025, from https://opg-optica-org.tudelft.idm.oclc.org/josa/fulltext.cfm?uri=josa-11-3-233

Figure 28:

Kiesewetter, L., Wood, D., & Menges, A. (2025). HygroShape: Programming Flat-pack, Self-shaping Wood Furniture. Proceedings of the ACM Symposium on Computational Fabrication, 1–15. https://doi.org/10.1145/3745778.3766658

Figure 29:

Shapeways. (2017). Tutorial Tuesday 18: Parametric Modeling With Grasshopper. https://www.shapeways.com/blog/tutorial-tuesday-18-parametric-modeling-grasshopper?srsltid=AfmBOoqOKI7VZkXX4j-eWMQlWVcTlfgCMbQrTZYSt_cd2jiEmm4TJPO

Figure 30:

Vergauwen, A., Laet, L. D., & Temmerman, N. D. (2017). Computational modelling methods for pliable structures based on curved-line folding. Computer-Aided Design, 83, 51–63. https://doi.org/10.1016/j.cad.2016.10.002

Figure 31:

Howell, L., Magleby, S., & Olsen, B. (2013). Handbook of compliant mechanisms. Chichester, West Sussex, United Kingdom: John Wiley & Sons. https://doi.org/10.1002/9781118516485.ch1

Figure 32:
Own work

Figure 33A & B:

Kiesewetter, L., Wood, D., & Menges, A. (2025). HygroShape: Programming Flat-pack, Self-shaping Wood Furniture. Proceedings of the ACM Symposium on Computational Fabrication, SCF '25, 1–15. https://doi.org/10.1145/3745778.3766658

Figure 34:
own work

Figure 35:
Own work

Figure 36:
Own work

Figure 37:
Own work

Figure 38:
Own work

Figure 39:
Own work

Figure 40:
Own work

Figure 41:
Own work

Figure 42:
Own work

Figure 43:
Own work

Figure 44:
Own work

Figure 45:
Own work

Figure 46:
Own work

Figure 47:
Own work

Figure 48:
Own work

Figure 49:

Wood, D., Vailati, C., Menges, A., & Rüggeberg, M. (2018). Hygroscopically actuated wood elements for weather responsive and self-forming building parts – Facilitating upscaling and complex shape changes. Construction and Building Materials, 165, 782–791. https://doi.org/10.1016/j.conbuildmat.2017.12.134

Figure 50:
Own work

Figure 51:
Own work

Figure 52:
Own work

Figure 53:
Own work

Figure 54:
Own work

Figure 55:
Own work

Figure 56:
Own work

Figure 57:
Own work

Figure 58:
Own work

Figure 59:
Own work

Figure 60:
Own work

Figure 61:
Own work

Figure 62:
Own work

Figure 63:
Own work

Figure 64:
Albrektas, D., & Ukvalbergiene (2026). Impact of Wood Species, Dimensions and Drying Temperature on Sorption Behaviour of Wood. ResearchGate. https://doi.org/10.5552/drind.2015.1369

Figure 65:
Tian, P., Han, J., Guo, S., Di, J., & Han, X. (2024). Prediction Distribution Model of Moisture Content in Laminated Wood Components. Polymers, 16(11). https://doi.org/10.3390/polym16111453

Figure 66:
Bosch Power Tools GmbH. (2026). Universal Humid Meter. Bosch DIY. https://www.bosch-diy.com/nl/nl/p/universalhumid-0603688001

Figure 67:
Own work

Figure 68:
Own work

Figure 69:
Own work

Figure 70:
Own work

Figure 71:
Own work

Figure 72:
Own work

Figure 73:
Own work

Figure 74:
Own work

Figure 75:
Own work

Figure 76:
Own work

Figure 77:
Own work

Figure 78:
Own work

Figure 79:
Lee, T.-U., Lu, H., Ma, J., Ha, N. S., Gattas, J. M., & Xie, Y. M. (2024). Self-locking and stiffening deployable tubular structures. Proceedings of the National Academy of

Sciences, 121(40), e2409062121. https://doi.org/10.1073/pnas.2409062121

Figure 80:
Own work

Figure 81:
Own work

Figure 82:
Own work

Figure 83:
Own work

Figure 84:
Own work

Figure 85:
Own work

Figure 86:
Own work

Figure 87:
Own work

Figure 88:
Own work

Figure 89:

Brancart, S., Vergauwen, A., Roovers, K., Van Den Bremt, D., De Laet, L., & De Temmerman, N. (2015). UNDULATUS: design and fabrication of a self-interlocking modular shell structure based on curved-line folding. In Proceedings of the IASS 2015 Symposium "Future Visions".

Figure 90:
Own work

Figure 91:
Own work

Figure 92:
Own work

Figure 93:
Own work

Figure 94:
Own work

Figure 95:
Own work

Figure 96:
Own work

Figure 97:
Own work

Figure 98:

Chang, D., & Redekop, D. (2008). Stress Analysis of Pressurized Multiple 90 Degree Mitred Pipe Bends. ResearchGate. The 4th International Conference on Advances in Structural Engineering and Mechanics (ASEM'08). https://www.researchgate.net/publication/260634481_Stress_Analysis_of_Pressurized_Multiple_90_Degree_Mitred_Pipe_Bends

Figure 99:

Molski, K. L., & Tarasiuk, P. (2021). Stress Concentration Factors for Welded Plate T-Joints Subjected to Tensile, Bending and Shearing Loads. Materials, 14(3), 546. https://doi.org/10.3390/ma14030546

Figure 100:

Molski, K. L., Tarasiuk, P., & Glinka, G. (2020). Stress concentration at cruciform welded joints under axial and bending loading modes. Welding in the World, 64(11), 1867–1876. https://doi.org/10.1007/s40194-020-00966-4

Figure 101:
Own work

Figure 102:
Own work

Figure 103:
Own work

Figure 104:
Place de la République. (2026). The Parisian Guide. https://www.theparisianguide.com/s/place-de-la-republique/; Google. (2026). Gemini (Advanced version) [Large language model]. https://gemini.google.com/

Figure 105:
Own work

# APPENDIX 010





# [APPENDIX 1]

# A.1

# A.1 Architecture of activation

## A.1.1 Deployable structures

The following section provides a condensed review and explanation on the types of deployable structures that exist for architectural applications in the modern day. These systems rely on geometric principles, material behaviour and kinematic mechanisms – including folding, hinging, bending, or elastic deformation – to transform from a compact form into an expanded configuration that serves as a shelter. As such, the type and range of deployable structures is extremely expansive and covers a wide breadth of activation systems and technologies to achieve controlled, predictable movement.

**A classification of deployable structures for architectural applications**

Given the vast range of existing deployable systems, numerous research papers and reviews have worked to simplify the classification into two major morphological structures; lattice or skeletal structures, and continuous or stressed-skin structures. While both spatial enclosures utilize a functional skin, they are distinguished by their primary load-path mechanisms. In lattice structures, structural integrity is maintained by an assembly of discrete, interconnected members, whereas, in continuous structures, the surface membrane itself serves as the principal load-bearing element (Hanaor & Levy, 2001).

Within these structural typologies, the method of deployment (i.e. how the transformation is carried out) is

categorised by the nature of the transformation; either as deployable or demountable. Deployable systems utilise kinematic mechanisms to transform from a condensed state to a fully functional, open form. The two major sub-categories for kinematic deployable systems include rigid links – such as bars or plates – and systems of deformable components, including fabrics or cables, which lack flexible stiffness (Hanaor & Levy, 2001). Alternatively, demountable systems are designed with modular, inter-locking components as a "kit-of-parts"; meant for iterative assembly, disassembly, and replacement (Fenci & Currie, 2017).

### Lattice bar structures (scissor and pantographic mechanisms)

One of the foundational classes of deployable systems is the lattice bar structure, involving rigid bar connections that are connected through hinges or revolute joints. They cover three major types: double-layer grids and single-layer grids for curvature, and linear grids for membrane or hybrid structures (Hanaor & Levy, 2001).

The basic component to these systems is the scissor-like element (SLE) (see figure 27), consisting of two intersecting bars that are connected to each other with a revolute joint, allowing them to rotate along a single shared axis. This mechanism can be inter-linked to create either a 3D prismatic unit (see figure 28), or a flat 2D connection depending on the desired final geometry. Once all SLE components have been linked together, the bundle can be expanded through tension to achieve forms like domes, shells, towers, and bridges, among other things (Doroftei & Doroftei, 2014).

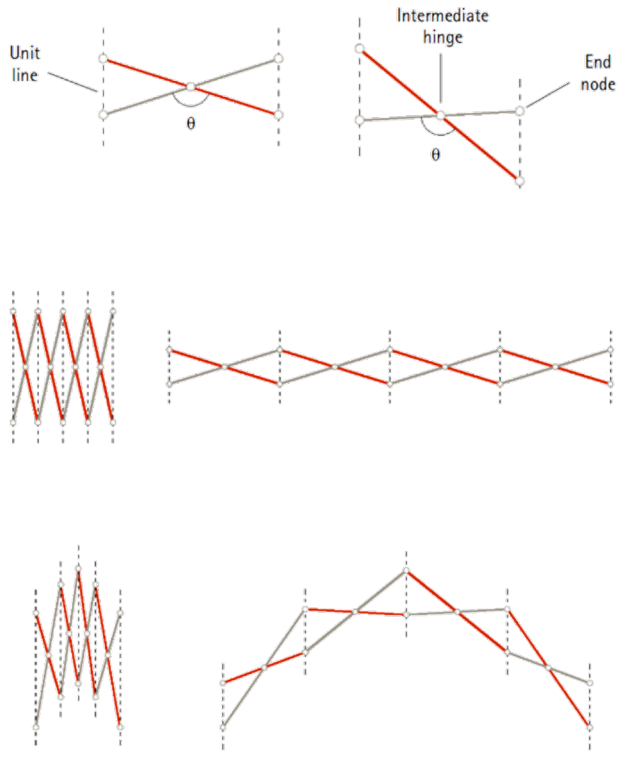


***figure 27:*** *Scissor-like element diagrams (source: Doroftei, I., & Doroftei, I. A., 2014)*

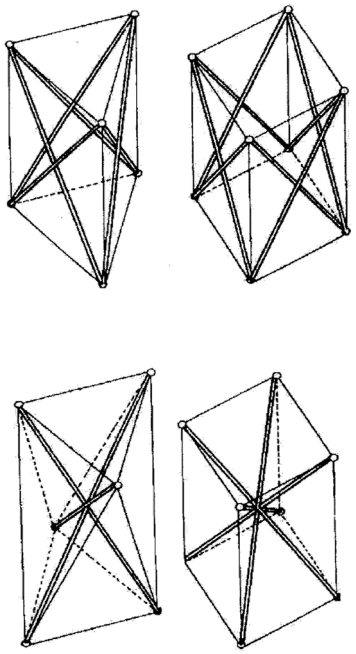

***figure 28:*** *Range of 3D prismatic units comprised of interlocking SLE elements and cables (source: Hanaor & Levy, 2001)*

### Foldable plate structures

Another category is foldable plate structures, which utilise rigid panels interconnected via rotational hinges or sliding joints. In this system, the geometric transition from a condensed state to an expanded configuration is achieved through the rotation, sliding, or overlapping of discrete plate elements. Two distinctions exist between planar elements which achieve deployment through the articulation of boundary hinges, whereas pre-curved surfaces are often categorised as demountable, and leverage their surface deformation to achieve the necessary structural depth (Hanaor & Levy, 2001).

Origami serves as a very common design precedent for the development of folding mechanisms that can be

upscaled for plate structures (Tachi, 2009) (see figure 29). These systems rely on rigid elements that simulate tessellated surfaces, often incorporating pantographic mechanisms or origami-inspired folding patterns to optimize both volumetric compactness and post-deployment stiffness. Despite these mechanical advantages, the structural efficiency of foldable plates is frequently offset by logistical complexities, including the requirement for extensive scaffolding, labour, and prolonged assembly timelines (Doroftei & Doroftei, 2014).

**Strut-cable (Tensegrity) structures**

Commonly referred to as tensegrity structures, this category of strut-cable structures blends elements resisting compression (struts) with tension elements (cables) to create a network of self-equilibrium (see figure 30). As all tension elements include cables, this results in a nearly-transparent structures with a very lightweight system and high strength-to-weight ratio (Averseng & Dubé, 2012).

As cables can be tensioned or relaxed, and struts can pivot around joints, tensegrity structures can shift smoothly between states without the need for heavy or rigid actuation mechanisms. Their applications stretch from architecture and civil engineering (as towers, and bridges), to robotics and aerospace (for antennas and space masts).

A shortfall to these type of system is the lack of structural efficiency. When compared to other double-layer grids constructed exclusively from bars, tensegrity structures exhibit relatively low structural efficiency as a result of the long unbraced bars (Hanaor & Levy, 2001).

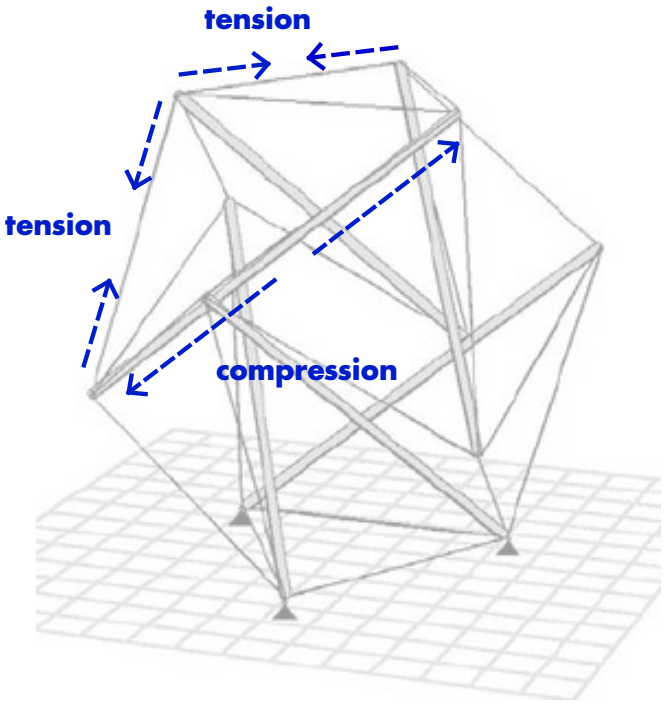


***figure 30:*** *Tensegrity model comprised of 24 tensioned cables and 6 struts in compression (source: Stamenovic et al., 2007)*

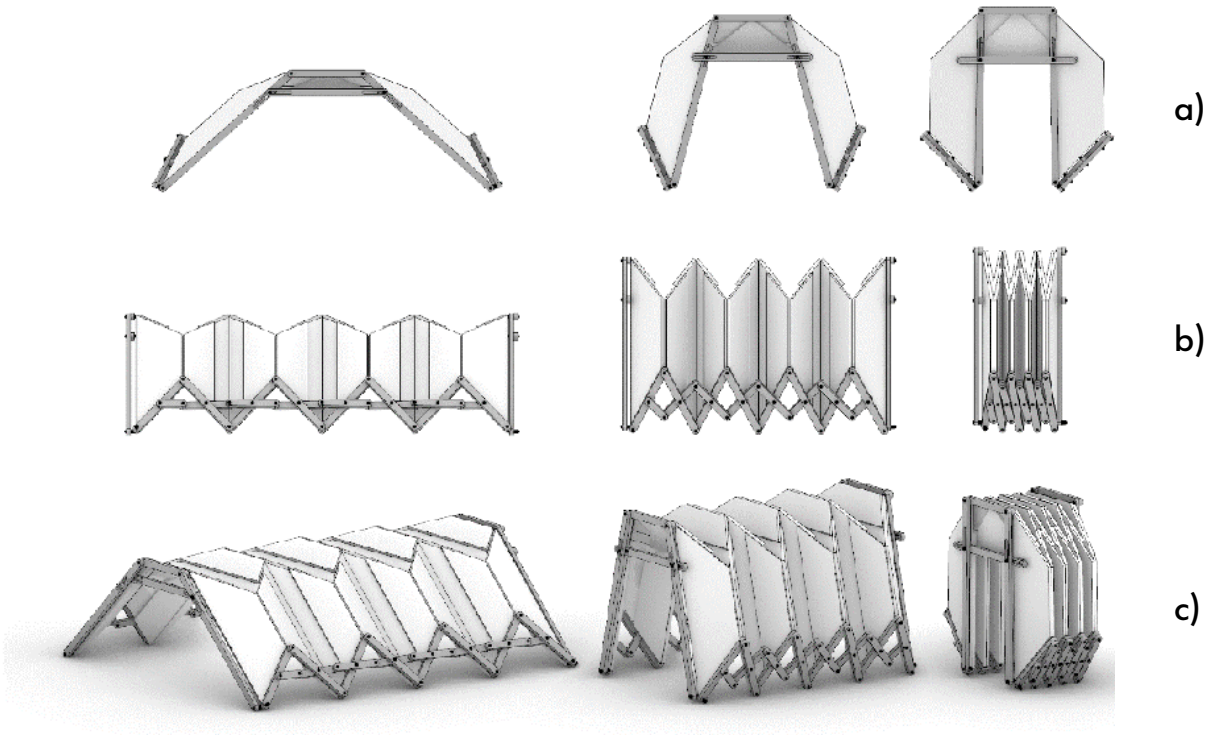


***figure 29:*** *Deployment sequence for a conceptual foldable plate structure (source: Vlachaki & Liapi,2024)*




***figure 31:*** *Ontario's Celebration Zone Pavilion (source: Hariri Pontarini Architects, 2015)*

**Membrane and surface deployable structures**

Membrane structures often rely on tensioned fabrics or thin films to support structural frames for stability and adequate stiffness. These include inflatable deployments, where air pressure helps to maintain the final form (see figure 31), and retractable membrane roofs that unfurl over public spaces. The membrane itself serves as the primary enclosing surface, with deployment being achieved through rollers, pneumatic systems, or sliding tracks (Hanaor & Levy, 2001).

These deployment systems excel for large-span, low-weight applications requiring rapid transformation, and are commonly used for pavilions, stadiums, and canopies. Given that the membrane serves as both the covering space and actuation element, membrane shelters can readily provide shading, rain protection, and enclosure (Hanaor & Levy, 2001).

**Smart-material deployable structures**

As research within field of material science advances and develops, the traditional distinction between rigid or flexible construction materials is slowly being redefined by the inclusion of a third classification: stimuli-responsive "smart" materials, which hygromorphic bilayers notably fall under. Unlike conventional mechanical systems, deployable structures within this category utilise materials that have been engineered to transfer movement through changes in their physical properties. These systems don't rely on traditional mechanical joints for actuation, and instead utilise elasticity, shape-memory effects, or smart actuation to drive structural activation (Fenci & Currie, 2017).

**Summary on the different deployable forms and systems**

Across the scopes of architecture and engineering, multiple forms of deployable structures have emerged. Lattice bar structures with SLE provide robust motion with high expansion rations, which can be scaled up for roofs or shelters. Foldable plate systems enable panels to slide and rotate into open configurations, while tensegrity systems create lightweight, stable frameworks. Membrane and surface deployable structures offer large-span, expansive covers, while more recently the application of smart materials allows for autonomous activation without traditional mechanical joints. Collectively, these typologies are applicable to a wide range of structures from temporary architecture to adaptive building skins and space structures (see figure 32).

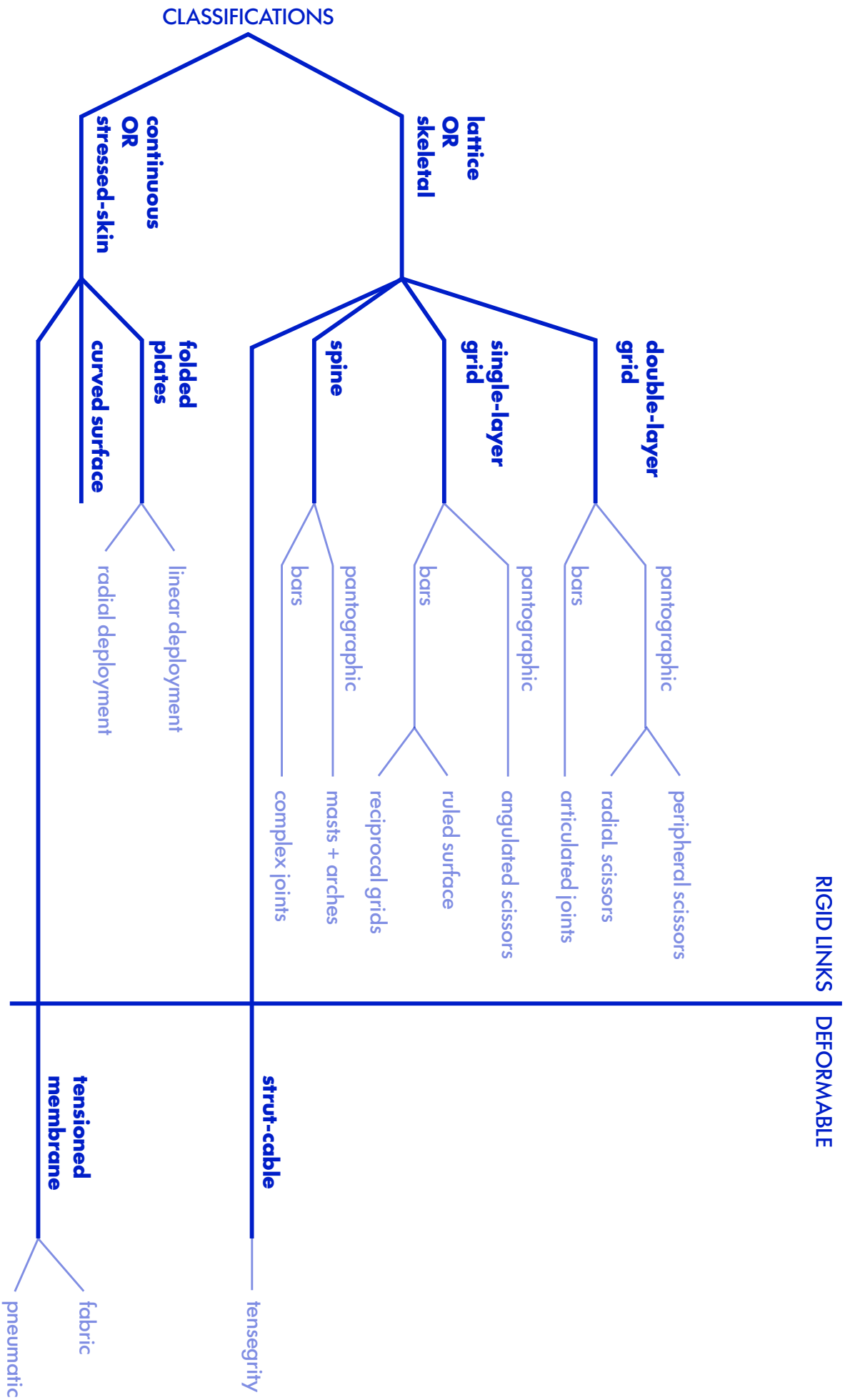


***figure 32:*** *Classification of deployable structures (source: adapted from Fenci & Currie, 2017)*

# [APPENDIX 2]

# A.2

## A.2 Computational methods

### A.2.1 Design methods

To evaluate the feasibility of a self-locking structure, derived from the complex curvatures of hygromorphic bilayer panels, a geometric workflow informed by mathematical equations is employed. This approach will facilitate an iterative feedback loop between the generated designs, and validation through mathematical formulae and dynamic physics-based simulations. The final result will be a well-informed visualisation tool that will support the design of larger, multi-element deployable systems.

When developing a concept, architectural workflows can follow a forward design process, where the initial, undeployed state serves as the baseline, and the deployed form is determined through computational simulations or the testing of physical prototypes (Hou & Jiao, 2020). This can be intuitive and suitable for exploratory form-driven projects, but it is often an inefficient system for more complex material-adaptive systems.

Conversely, the inverse design problem starts with a desired performance outcome – in this case, the final deployed form – and works backwards to determine the optimal undeployed configuration and material properties to achieve it (Hou & Jiao, 2020). This is more effective in designing with hygromorphic bilayers that need to be pre-programmed to achieve the desired curvature. For hygromorphic bilayers, this inverse approach is more effective as it allows the material to be pre-programmed during the manufacturing process, and ensures the transition from a planar state to a complex, self-locking configuration is both predictable and geometrically reconciled.

An example of the inverse design problem being applied to solving the design configuration for a deployable membrane structure is the 2021 paper by Panetta et al. on "Computational Inverse Design of Surface-Based Inflatables". Rather than beginning with a flat form and iteratively testing designs through forward simulations, the authors begun with the target design of a double-curved surface made from inextensible sheet material, and developed a workflow to compute the internal layout of air channels that would best approximate the given design when inflated. The workflow was based around a physics-based simulation of the inflation process, which was perfected with a machine-learning optimisation that continuously updated the network of air channels to minimise the difference between the simulated form and the target form (Panetta et al., 2021). The final design is ultimately validated with physical prototypes, demonstrating how an inverse process can help realise conceptual designs.

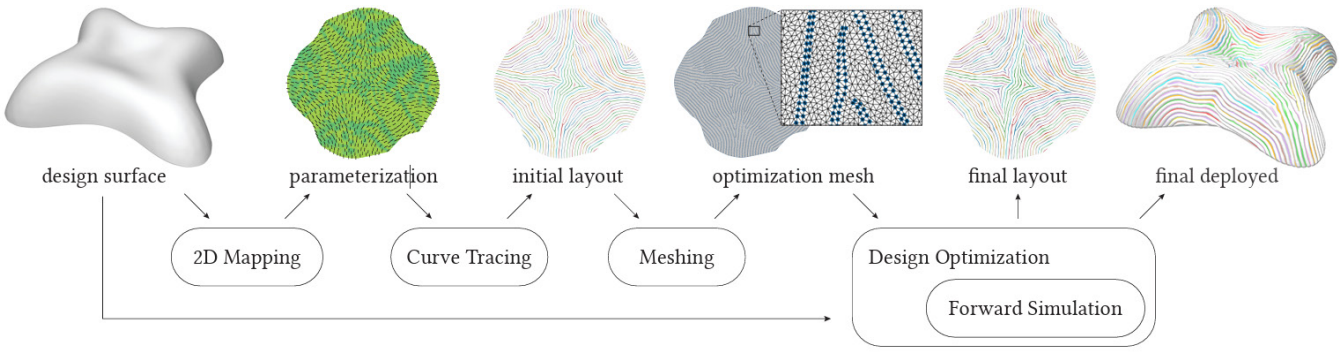


***figure 36:*** *Flowchart displaying computational workflow for a membrane surface deployable structure with optimised airflow channels (source: Panetta et al., 2021)*

The use of computational tools for design has become more prevalent in recent years, and both aforementioned iterative design processes are being continually supplemented and streamlined with modern technology.

Some key examples of computational processes include;

- parametric design
- generative design
- optimisation-based algorithms
- form-finding methods,
- and machine-learning approaches

Parametric design (see figure 37) operates through a set of geometric parameters and rules that help inform the final shape, including (but not limited to) elements such as height, width, curvature, openings, divisions, etc. By changing a single variable, the entire model can be cohesively and quickly updated.

Generative design (see figure 38) is an iterative process that leverages artificial intelligence and algorithms to create a large array of possible design solutions according to a set of requirements. This process is effective for diversity in the design process, but can lead to unconventional alternatives, especially if the requirements are not clearly and extensively outlined.

Optimisation-based algorithms (see figure 39) are mathematical methods for improving an existing design against a collection of requirements or factors, such as daylight accessibility, floor space, structural dimensions, etc. They are frequently used to build on and improve parametric or generative workflows (Caetano et al., 2020).

Form-finding methods (see figure 40) consider physics-based simulations, such as gravity, and tension or compression, to determine the shape of the structure at equilibrium. A famous example that follows the same logic (although not computational) are Antoni Gaudi's hanging chains for the structural design of the Sagrada Familia (Rodrigo & Gilfranco, 2017). More recently, machine-learning approaches have been used for design, but their scope will not be covered in this paper.

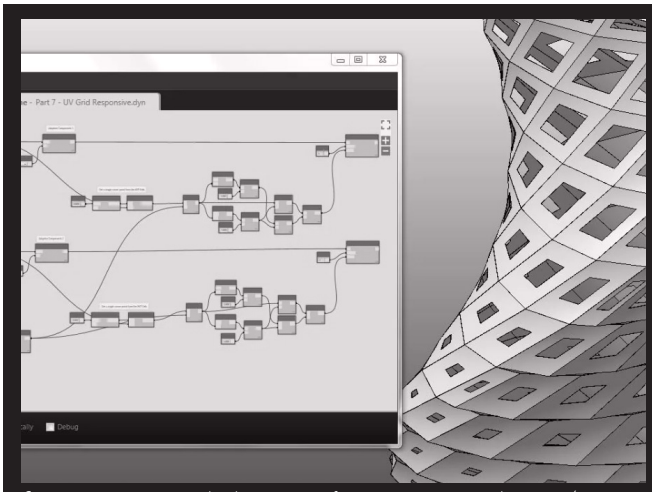

***figure 37:*** *Autodesk Vasari for parametric design (source: Autodesk, 2026)*

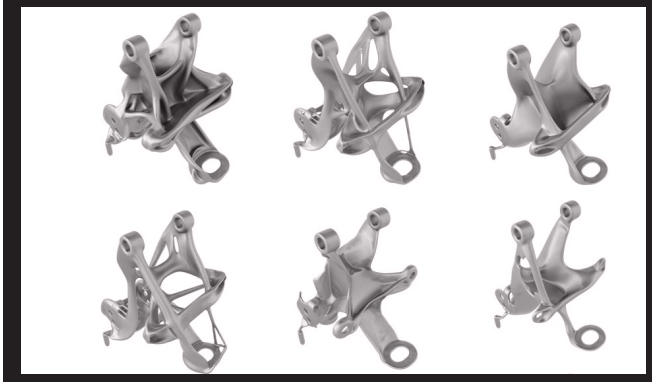

***figure 38:*** *Design iterations of a seat bracket using generative design (source: Danon, 2018)*

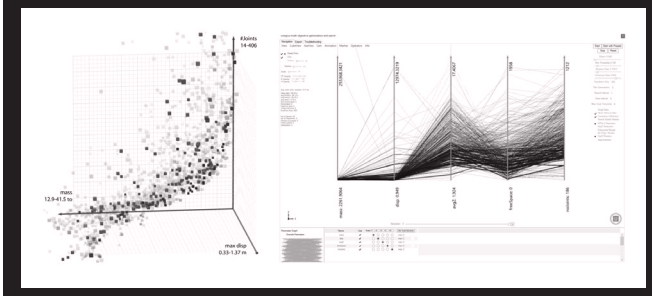

***figure 39:*** *Interface for Octopus; an optimisation plugin for Grasshopper in Rhino (source: Vierlinger, 2018)*

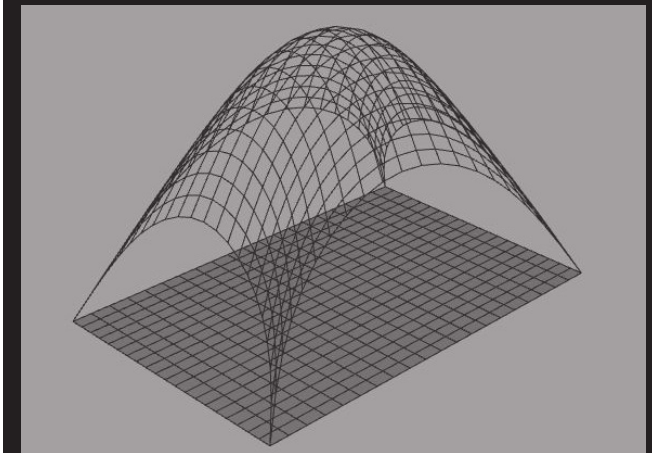

***figure 40:*** *Mesh relaxation for the form-finding of a funicular shell structure (source: Piker, 2017)*

Within this paper, the computational workflow that will be used most readily, and which will facilitate linking digital simulations to real-world processes are form-finding methods.

## A.2.2 Generating shell structures

The initial stage in developing the computational workflow involves the design of a discrete shell structure, mimicking the form and load-bearing properties of a continuous curved shell that has been constructed from a large number of inter-linked individual elements.

Shell structures have been used in architecture for many centuries as they provide a high weight-to-span ratio (i.e. they can span considerable distances while remaining lightweight) and structural effectiveness. While constructing curved surfaces can be quite challenging, digital design processes enable easier form exploration and development (Ağırbaş et al., 2025).

Several numerical form-finding methods exist to assist in determining the overall shape of the shell design. These include;

- Force Density Method
- Particle-spring Method
- Dynamic Relaxation Method
- Thrust Network Analysis.

The Force Density Method (see figure 41) is often used to design cable nets and tensile members by simplifying non-linear forms into linear problems through the ratio of force-to-length as a constant value for each cable (Gao et al., 2025).

The Particle-Spring Method (see figure 42) reconstructs a form as points connected by elastic springs to emulate simplified dynamic movement (Kuijvenhoven & Hogenboom, 2012).

Dynamic Relaxation (see figure 43) simulates a structures' movements under loads until it comes to a rest, demonstrating the final stable position at static equilibrium (Cassell et al., 1966).

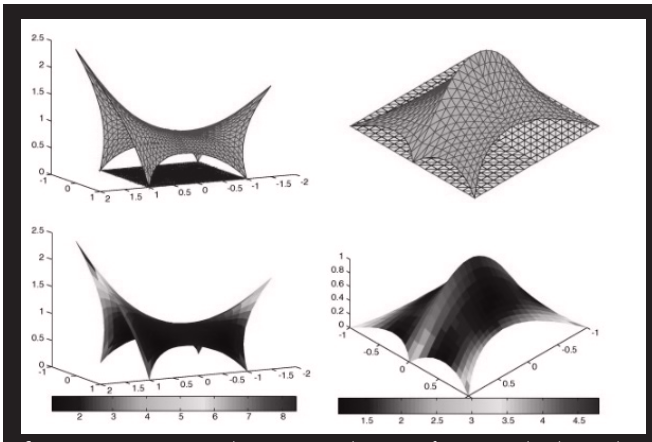

***figure 41:*** *Force density simulations for stretched meshes (source: Pauletti & Pimenta, 2008)*

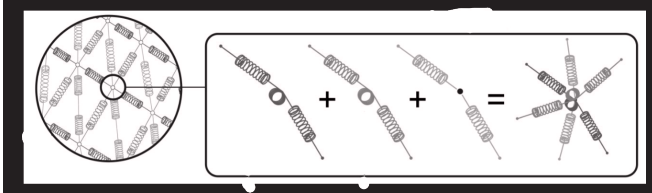

***figure 42:*** *Visualisation of particle-spring elements (source: Lee et al., 2024)*

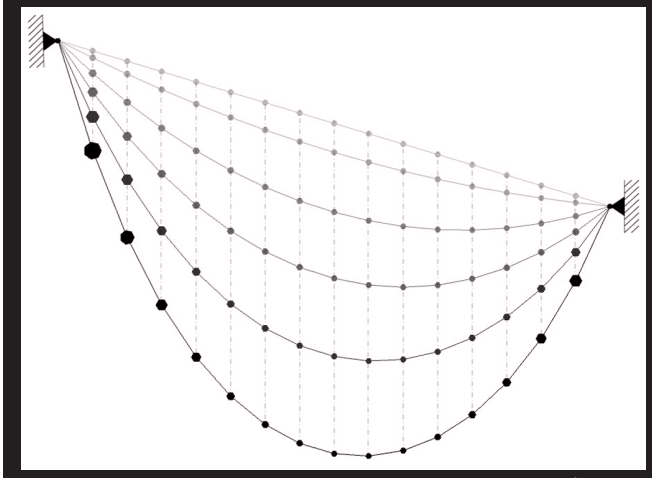

***figure 43:*** *Dynamic relaxation of a pinned cable (source: Harding & Shepherd, 2011)*

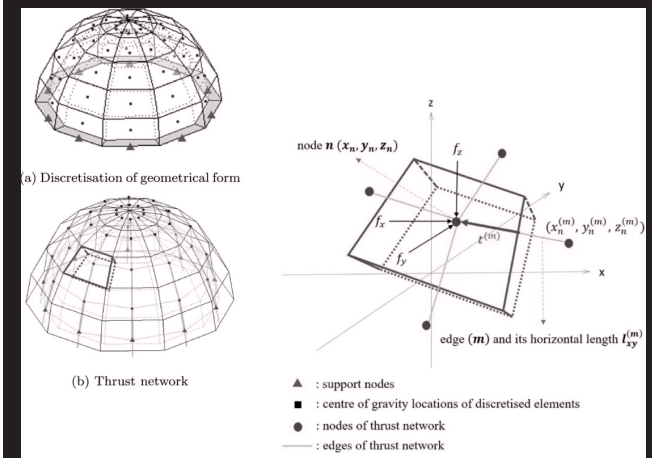


***figure 44:*** *Thrust network for a masonry vault (source: Lee et al., 2024)*

Finally, Thrust Network Analysis (see figure 44) is used for structures like masonry vaults to ensure internal forces remain compressive and structural stability occurs without tensile reinforcement (Block & Ochsendorf, 2007).

Based off the literature research (Ağırbaş et al., 2025; Guha, 2025; Naboni et al., 2018; Abdelmohsen et al., 2019), the computational workflow in this paper will use a combination of particle-spring method with relaxation-based form-finding to develop a shell from an initial two-dimensional surface. This process will also allow the topology to be discretised during its undeployed state, ensuring similarity-based quad face clustering to reduce geometric variety for constructing the hygromorphic bilayer panels.

The process of dynamic relaxation is effective for creating a straightforward design solution that is based on the assumption that once the form reaches a relaxed solution it is in equilibrium under the load of pre-specified forces (such as its self-load and gravity). A 2025 research paper by a previous Delft University of Technology (TU Delft) master graduate, Swornava Guha, on glass assembly for compression-only masonry vault structures, followed this similar process and elaborated on the use of the visual programming environment and parametric tool, Grasshopper 3D (commonly referred to as GH; see figure 45), to achieve doubly-curved vault shapes (Guha, 2025).



***figure 45:*** *Grasshopper 3D software icon (source: Rutten, 2026)*

To extend the functionality of Grasshopper's default toolset, a multitude of add-ons (referred to as "plug-ins") can be downloaded. They provide a range of specialised components for tasks such as environmental analysis, structural engineering, or design optimisation. For the simulation of dynamic relaxation, the plug-in "Kangaroo Physics" was chosen (Piker, 2013; see figure 46).

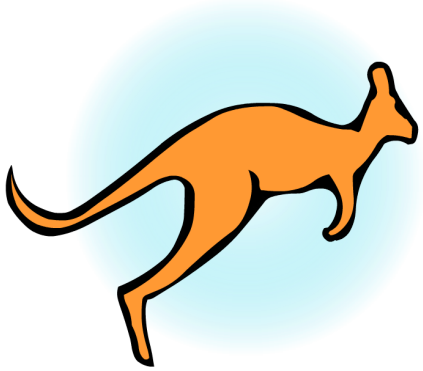

***figure 46:*** *Kangaroo Physics plugin icon (source: Piker, 2026)*

A simplified step-by-step process is outlined in Swornava's master paper and it includes inputting a base typology, defining the supports, anchors, and edges, before defining the elasticity factor and forces, and finally relaxing the mesh into a three-dimensional form (Guha, 2025). Another useful plugin is RhinoVAULT – based on Thrust Network Analysis, that helps design funicular (compression-only) structures by projecting form and force diagrams onto a flat surface (Guha, 2025).

## A.2.3 Discretising of 3D forms for panelisation

A common method for simplifying free-form surfaces is through discretisation; a process of converting continuous shapes or models (also applicable to data and functions) into individual separate and distinct elements. These methods vary in a number of different edge compositions, node complexities, face curvature, etc., so it is important to determine which method fits most closely to the desired manufacturing requirements.

Manufacturing unique curved elements is often impractical because each component requires its own custom mould. In many cases, the cost of creating these specialized moulds tends to exceed the cost of actual the

parts themselves. In contrast, producing planar elements is far more economical, as multiple components can be created from a single, standardized mould, meaning the production process becomes faster and significantly more cost-effective (Henriksson & Hult, 2015).

### Tessellation

A subcategory to discretisation is tessellation: the systematic subdivision of a form or surface into repeating geometric units (such as triangles or quadrilaterals), and highlighted by the need for non-overlapping, gap-free geometric shapes. The process can vary in regularity and complexity, either as regular tessellations that use congruent shapes, fitting together perfectly without gaps, or semi-regular and irregular tessellations that change in panel size, shape, or orientation to ensure smooth, gap-free discretisation (Iuorio & Korkis, 2019). In the modern world, tessellation often involves algorithmic design tools, like GH, that help determine panel distribution.

### Triangular meshes

The triangulation of meshes (see figure 47) is one of the most common ways to discretise a surface as it generates the greatest number of elements, allowing for improved structural optimisation. This can be an advantage, as many curved surfaces can be easily approximated with triangular panels, but also a disadvantage as it leads to greater production and node complexity (given that more edges meet at each node when compared to quadrilateral meshes).

Additionally, to achieve a structurally efficient design, the transfer of loads must occur through membrane forces with minimal bending. Triangular panels are particularly good in this aspect, as each element is stable for in-plane forces (Henriksson & Hult, 2015).

A possibly well-known example of a triangulated grid is the glass roof over the Great Court of the British Museum in London, comprised of around 3,312 panels of glass embedded into a steel grid (Williams & Shepherd, 2010).

### Quadrilateral meshes

A quadrilateral mesh (see figure 47) has a few advantages over a triangular mesh. Primarily, less elements are generated at the same fixed length, meaning less overall manufacturing time. They are also easier to manufacture as less mullions are required and fewer machining operations need to be carried out. The node complexity is also lower,

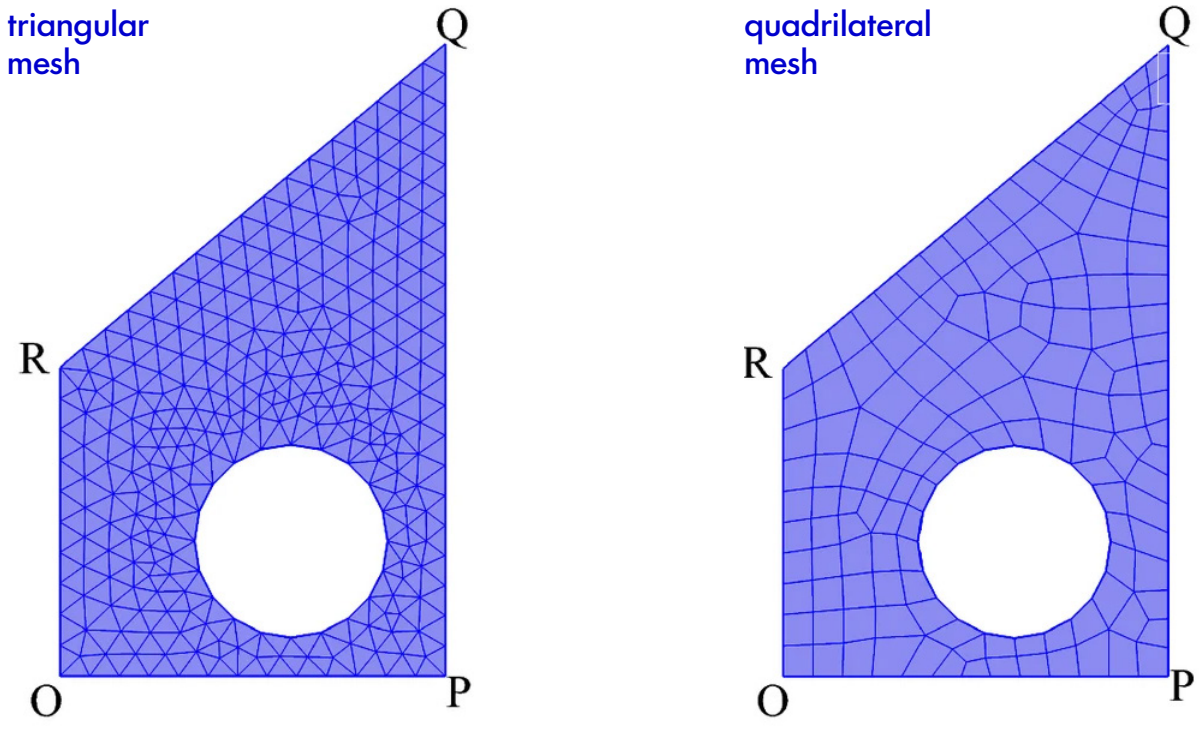


***figure 47:*** *Examples of triangular and quadrilateral discretisation (source: Dey & Idesman, 2020)*

and they have a higher structural transparency as a result of the lesser number of intersecting edges. A drawback is the accuracy of discretisation when compared to triangulation, as planar hinging of quadrilateral panels can only occur along two perpendicular directions rather than three (Henriksson & Hult, 2015). Quadrilateral mesh faces also tend to become more varied if the mesh surface is not a rectangle, leading to a greater number of distinct and varied elements.

An example of a quadrilateral mesh structure is the glass roof at the Museum of Hamburg History, consisting of numerous flat glass panels and a curved steel grid (GMP Architekten, 1990).

**Grasshopper software for tessellation**

Several GH plugins exist for discretisation, and they often involve converting continuous non-uniform rational B-spline (NURBS) geometries into meshes, voxels or panelised systems.

- Weaverbird
- LunchBox
- Mesh+ (MeshPlus)
- Starfish
- Python coding

***figure 35:*** *Shell structures with varied openings (source: own work)*

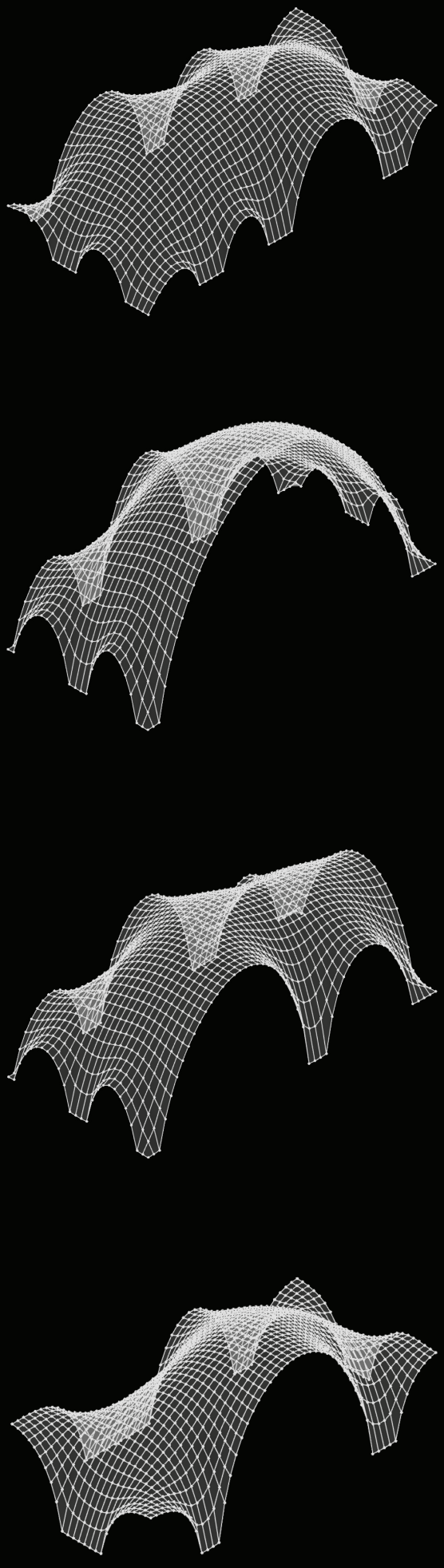

# [APPENDIX 3]

# A.3

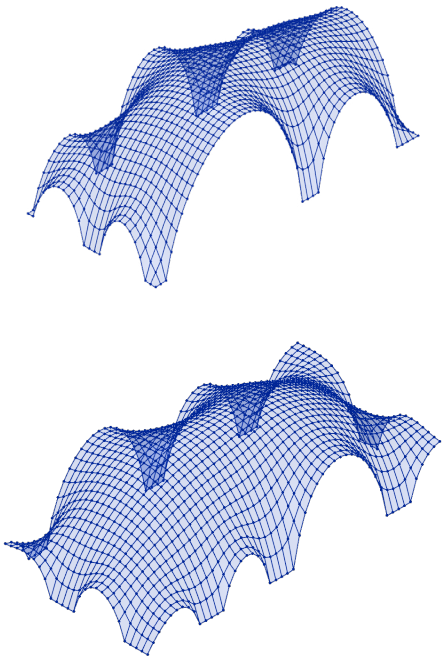

## A.3 Conceptual exploration of shell structures with bilayers

### A.3.1 Computational form-finding of shell geometries

Initial explorations for the shell structures were carried out using Grasshopper and components from the live physics simulation engine, Kangaroo Physics.

An initial script was developed to explore different shell shapes by relying on a simple, rectangular surface mesh and transformable control points along the edges that served as the anchor points to ground the final structure. A uniform, vertical force was applied across the mesh to pull it up from its flat state and into a 3D form.

When the simulation is executed, the interactions between the competing criteria of the anchor points and the vertical force are presented through a particle-spring system to emulate elastic tension across the mesh face.

Once equilibrium is achieved through dynamic relaxation, the most optimal, force-balanced shapes are presented as seen in figure 1.

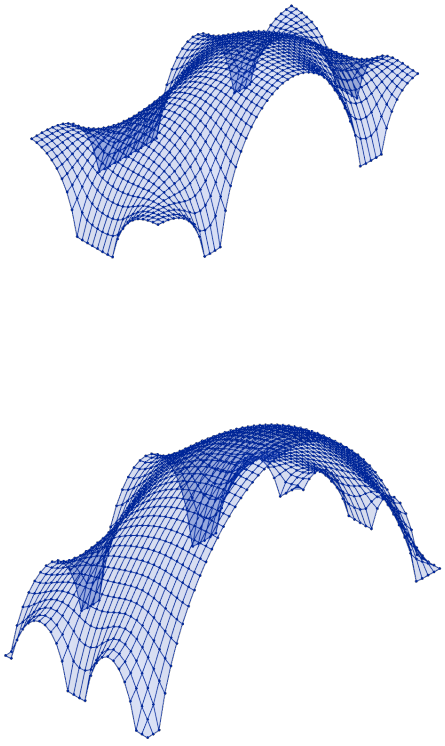

***figure 1:*** *Initial form exploration with varied foundational anchor points (source: own work)*

## Re-defining the forces

It was necessary that the form-finding process was underpinned by the idea that deployment should emulate a system of timber panels as closely as possible. This meant maintaining the dimensions of the discretised panels throughout the entire deployment process, and avoiding any warping or stretching of the shell surface.

The discretised panels from the mesh face in the initial exploration displayed this failure due to a lack of constraints and elastic deformation that resulted in irregular, non-orthogonal quadrilaterals, as seen below in figure 2.

To solve this issue, the workflow was re-built with defined geometric parameters to create rigid dimensional constraints, while also re-defining the behaviour of the anchor points.

The activation logic considered for the improved workflow involves the same processes wherein a flat piece of paper will undergo out-of-plane deformation when in-plane compressive forces are acted onto it from opposite edges. This causes the material to self-organize into a semi-cylindrical shell geometry as the opposite edges approach each other. This methodology more closely resembles the process of activation of a hygromorphic bilayer as it curls into shape through moisture absorption or expansion.

To replicate this, the anchor points were re-programmed to allow for horizontal translation in the x-direction, rather than fixing them to specific coordinates; which had been the case previously and had resulted in mesh face deformation. Limitations were still placed on translations in the y- and z-directions to prevent torsional bending and detachment from the base plane. In addition, new goals were defined for the edge lengths of each discretised face to ensure their original dimensions are maintained throughout the entire simulation. As was the case in the previous script; to activate the mesh from a flat state into a 3D form, a uniform vertical force was applied on the surface.

This decision ultimately proved unsuccessful as the transformation relied on a constant frictionless force that was exerted continuously on the surface. This would cause the deployed shell to narrow infinitely due to to a lack of horizontal restraints, as can seen in figure 3 below.

New manual restrictions were applied to the anchor

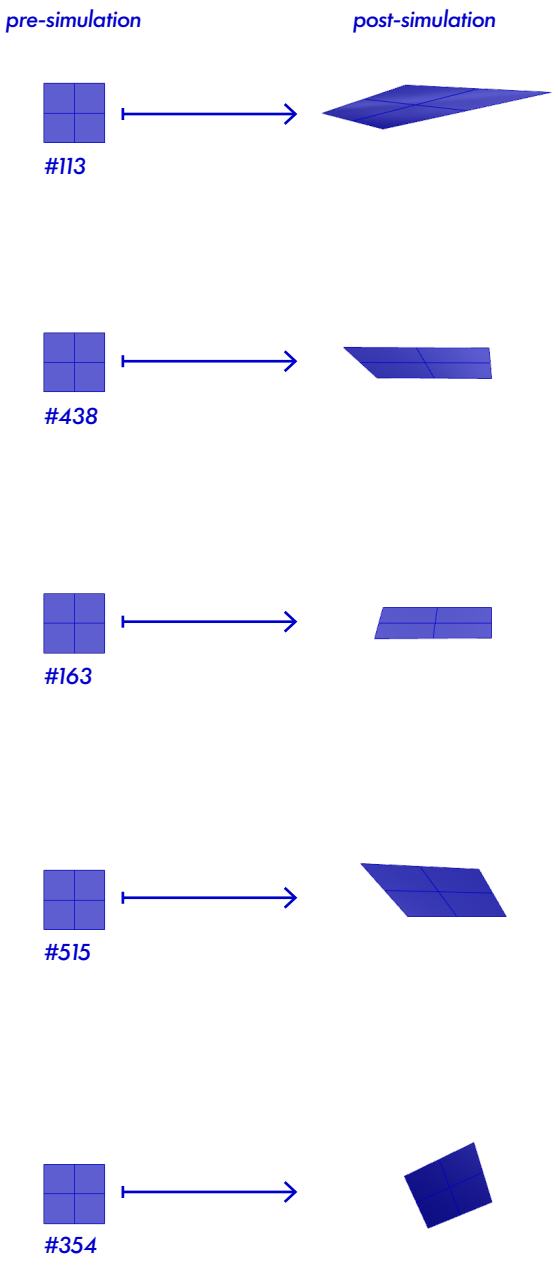


***figure 2:*** *Diagram of force distribution for a hanging catenary (left) and inverted catenary (right) (source: own work)*

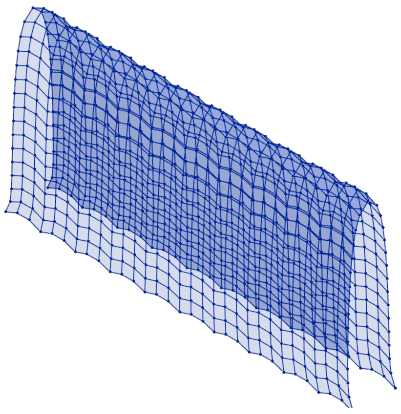

***figure 3:*** *Undesired narrowing of deployed shell (source: own work)*

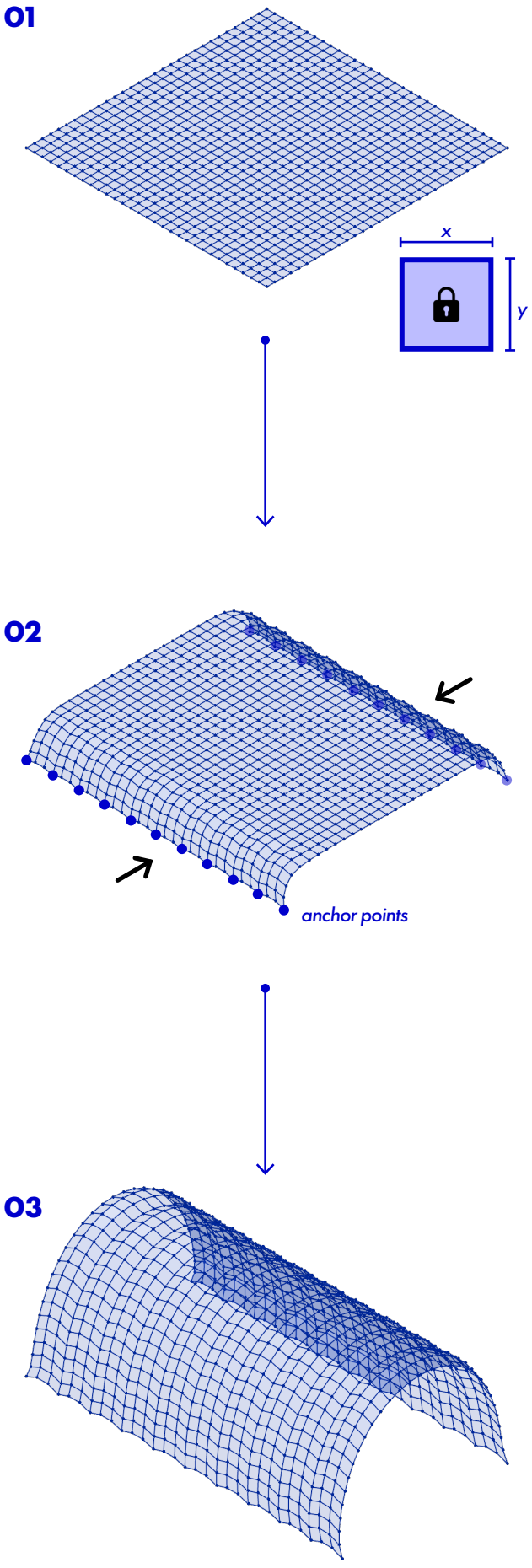


***figure 4:*** *Sequence figures displaying fixed mesh dimensions with manual anchor translation to achieverce monoclastic curvature (source: own work)*

points through the use of numerical sliders ranging from 0 to 100, representing the percentage of translational movement available to each opposing edge line from its initial position at the perimeter of the square toward the centre. A value of 0 maintains the edge at its original boundary position, while a value of 100 moves the edge fully to the centre point, where the opposing edges converge. This method successfully restricyed the geometry, and offered greater control over the final curvature. See figure 4 for a sequential display of shell deployment with lateral translation of the anchor points.

### Material-informed deformation

Given that the force goal behaves uniformly across the mesh surface - in much the same way gravity would behave on a suspended chain - the resulting shells tend to resemble the form-finding process for a catenary vault (see figure 5).

To achieve more uniform curvature, material

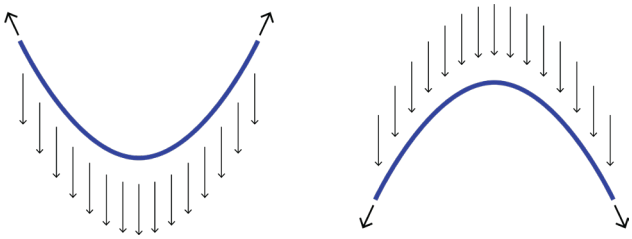

***figure 5:*** *Diagram of force distribution for a hanging catenary (left) and inverted catenary (right) (source: own work)*

property parameters were included in the updated script to better emulate the bending and deformation of the shell for different timber species.

This was carried out by including axial and bending strength data to inform the angle of curvature between neighbouring mesh faces. The axial strength is informed by the cross-sectional area of the bilayer and the Young's Modulus of the timber species, while the bending strength is determined by the product of the Young's Modulus and the Second Moment of Inertia of the bilayer cross-section.

The final simulation resulted in continuous curvature, which was more characteristic of a semi-circle, rather than

a catenary vault, and resembled the deformation expected from hygromorphic bilayers presented in literature (see figures 6 and 7).

Despite proper management of the goal

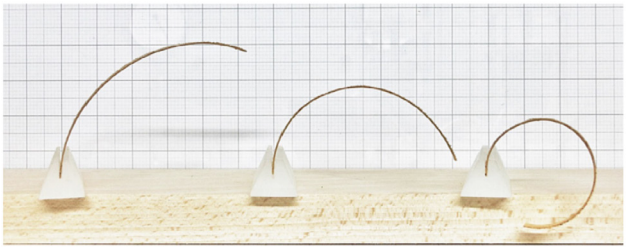

***figure 6:*** *Sequence for bilayer curvature (source: Zhan et al., 2017)*

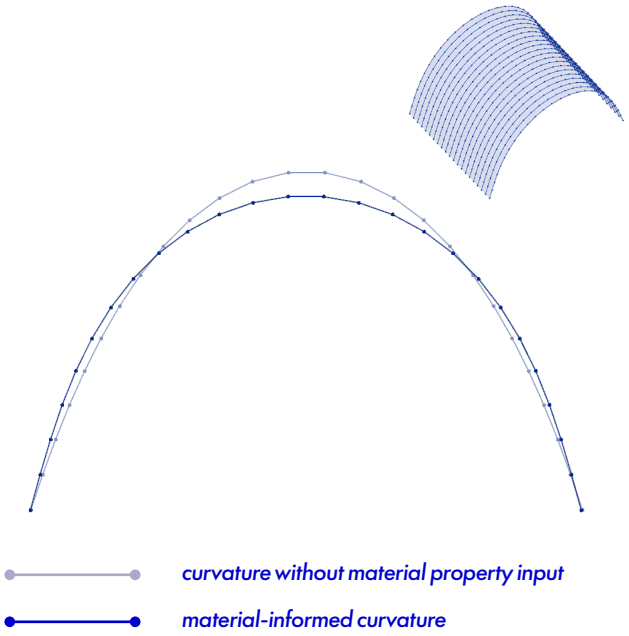


***figure 7:*** *Section comparison of deployed shell with and without material information (source: own work)*

components when organising the parameters for the Kangaroo simulations, during the process of deformation it is difficult to validate consistency in the dimensions of the discretised panels before and after the simulations. Manually measuring each panel in the output and comparing it to the flat state is extremely time-consuming, and implausible to carry out for numerous different shell geometries.

It became necessary to re-discretise the deployed surface with a custom-built Python component that would offer greater control over the discretisation dimensions.

```python
import rhinoscriptsyntax as rs
import ghpythonlib.treehelpers as th

# extract information about surface domain in U & V direction

srfDomainU = rs.SurfaceDomain(srf,0)
srfDomainV = rs.SurfaceDomain(srf,1)
pts = []

U_step = srfDomainU[1]/N
V_step = srfDomainV[1]/N

for i in range(N+1):
    col = []
    for j in range (N+1):
        srf_U = U_step*i
        srf_V = V_step*j
        srfPt = rs.EvaluateSurface(srf, srf_U, srf_V)
        col.append(srfPt)
    pts.append(col)

pts_T = th.list_to_tree(pts)

U_lines = []
for col in pts:
    U_lines.append(rs.AddPolyline(col))

V_points = []
for i in range(N+1):
    row = []
    for j in range(N+1):
        row.append(pts[j][i])
    V_points.append(row)

V_lines = []
for col in V_points:
    V_lines.append(rs.AddPolyline(col))

```

***figure 8:*** *Python script for discretisation component (source: own work)*

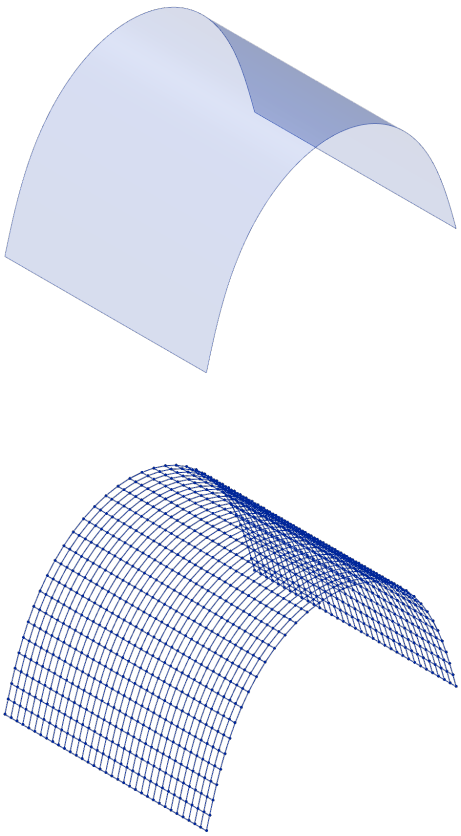

***figure 9:*** *Discretisation of shell surface, post-simulation (source: own work)*

## A.3.2
## Flowchart for computational workflow combining curvature prediction, shell generation, and discretisation

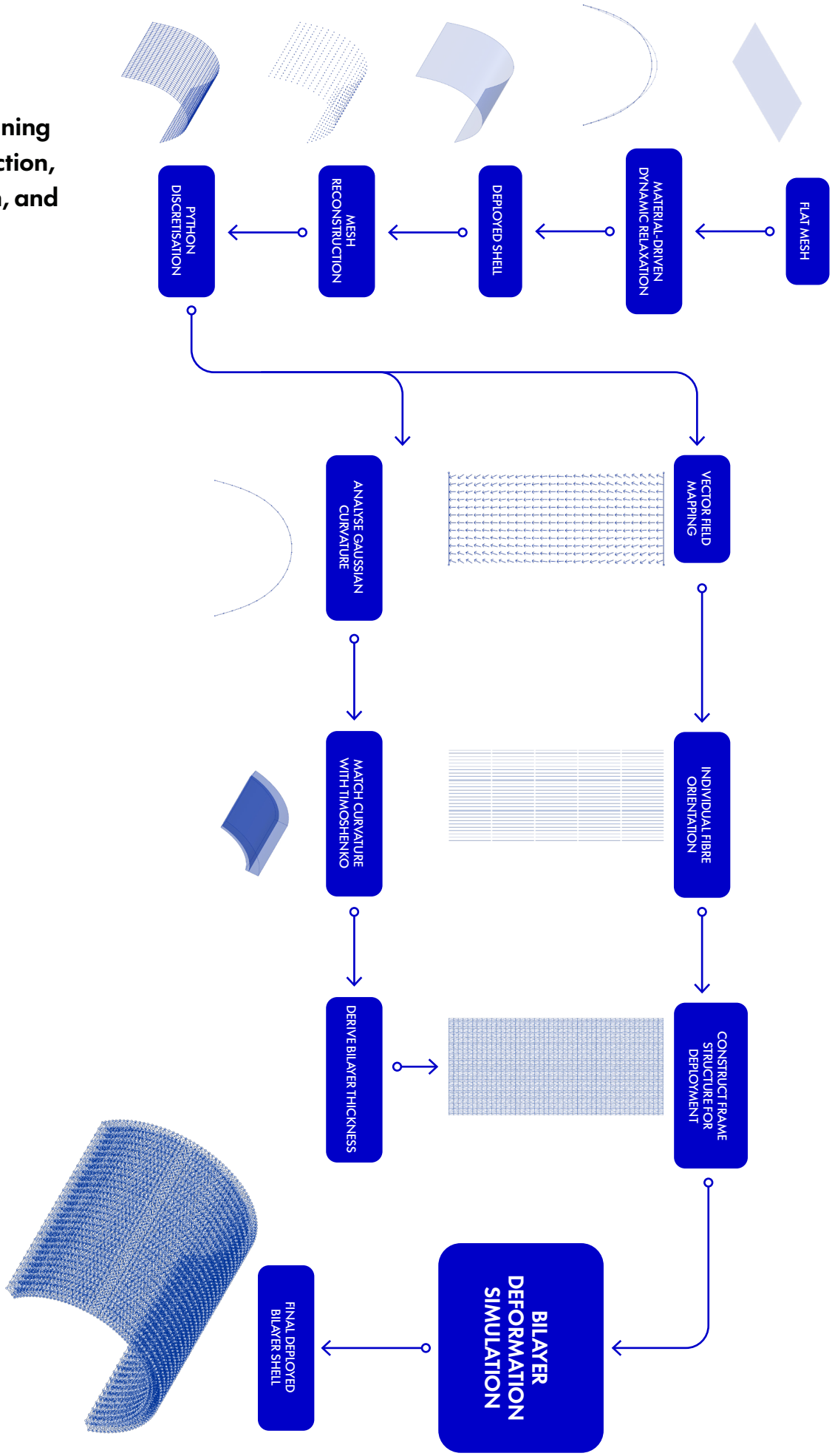


***figure 10:*** *computational workflow flowchart*

# [APPENDIX 4]

# A.4

## FINAL MONOCLASTIC SIMULATIONS FOR VARIED FIBRE ORIENTATIONS

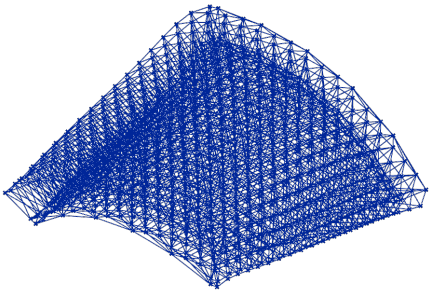

17.2° ROTATION

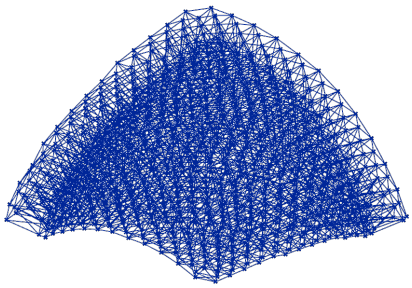

41.3° ROTATION

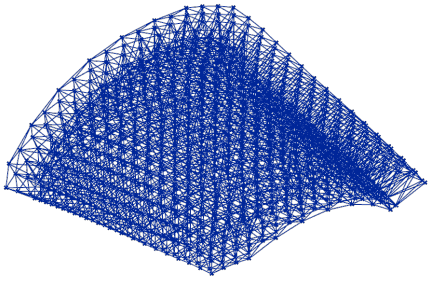

64.4° ROTATION

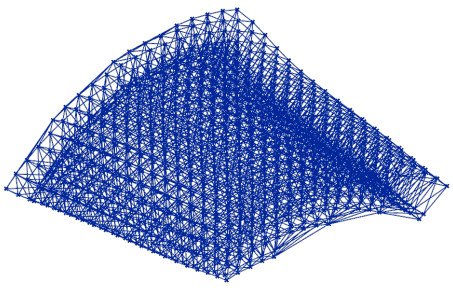

77.7° ROTATION

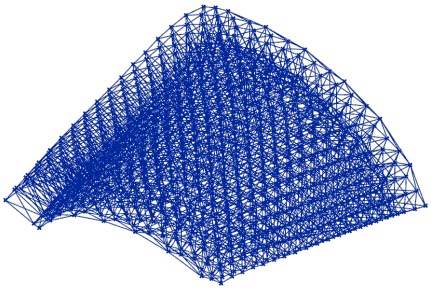

20° ROTATION

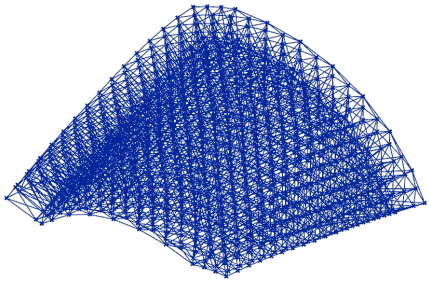

25° ROTATION

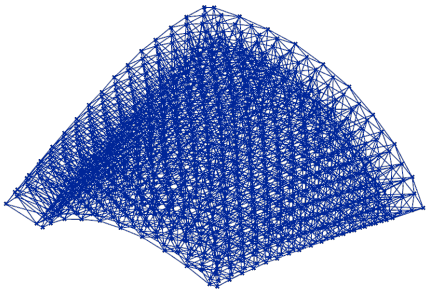

30° ROTATION

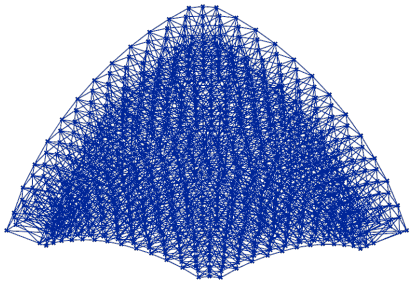

45° ROTATION

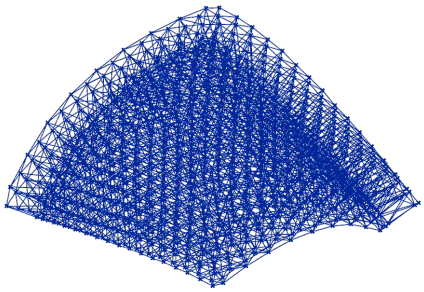

60° ROTATION

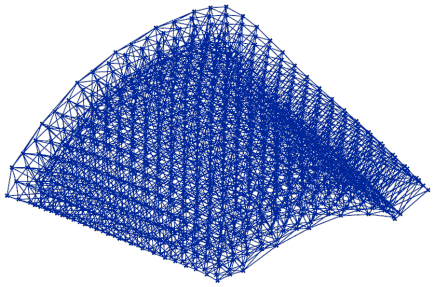

70° ROTATION

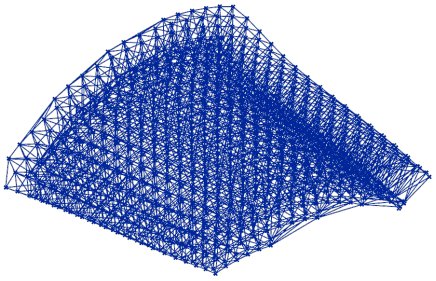

75° ROTATION

# [APPENDIX 5]

# A.5

DEVELOPING LATTICE GRID

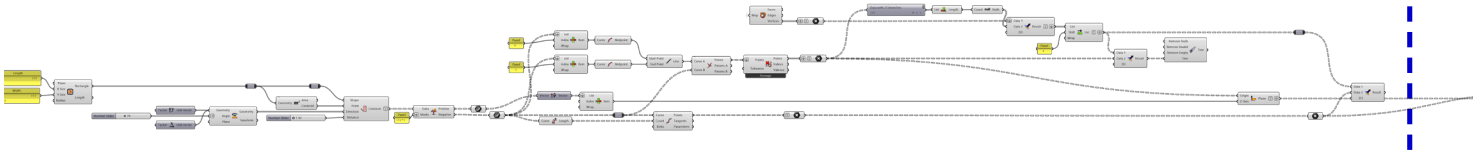

MATERIAL DATA

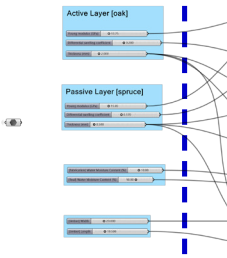


TIMOSHENKO FORMULA

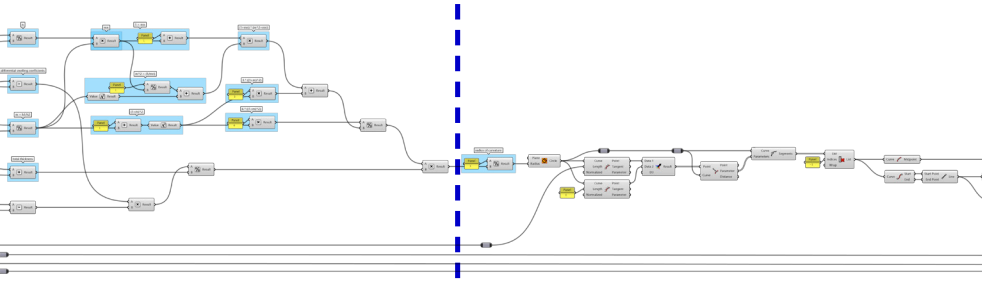

# GRASSHOPPER SCRIPT FOR MONOCLASTIC CURVATURE

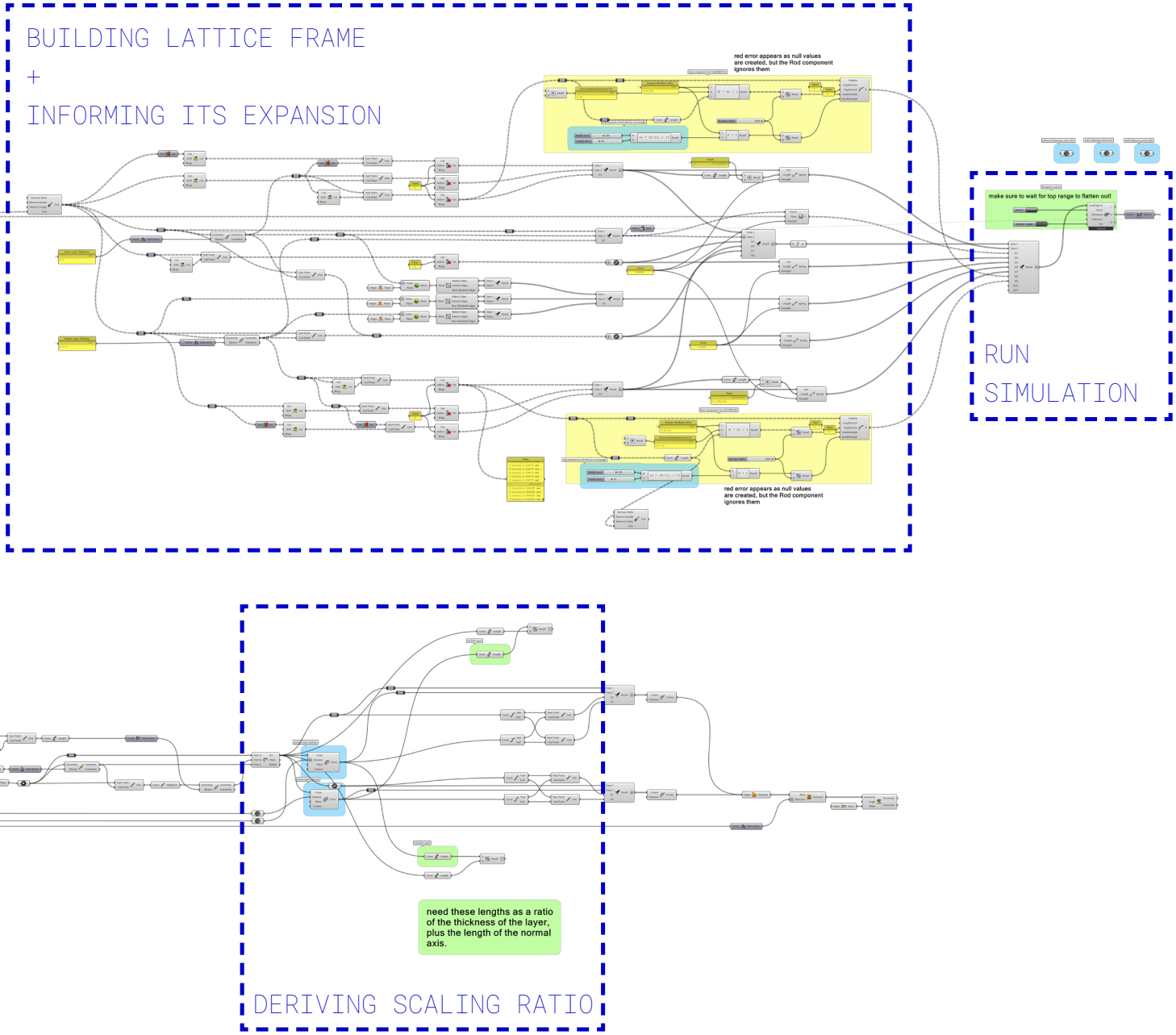

# [APPENDIX 6]

# A.6

## LEGEND

TEMPERATURE (°C)

RELATIVE HUMIDITY (%)

LIGHT INTENSITY (lux)

**SETTING RELATIVE HUMIDITY TO 55%;**

PRIOR TO CONDITIONING INDIVIDUAL TIMBER LAYERS

*(climatic sensor 1)*

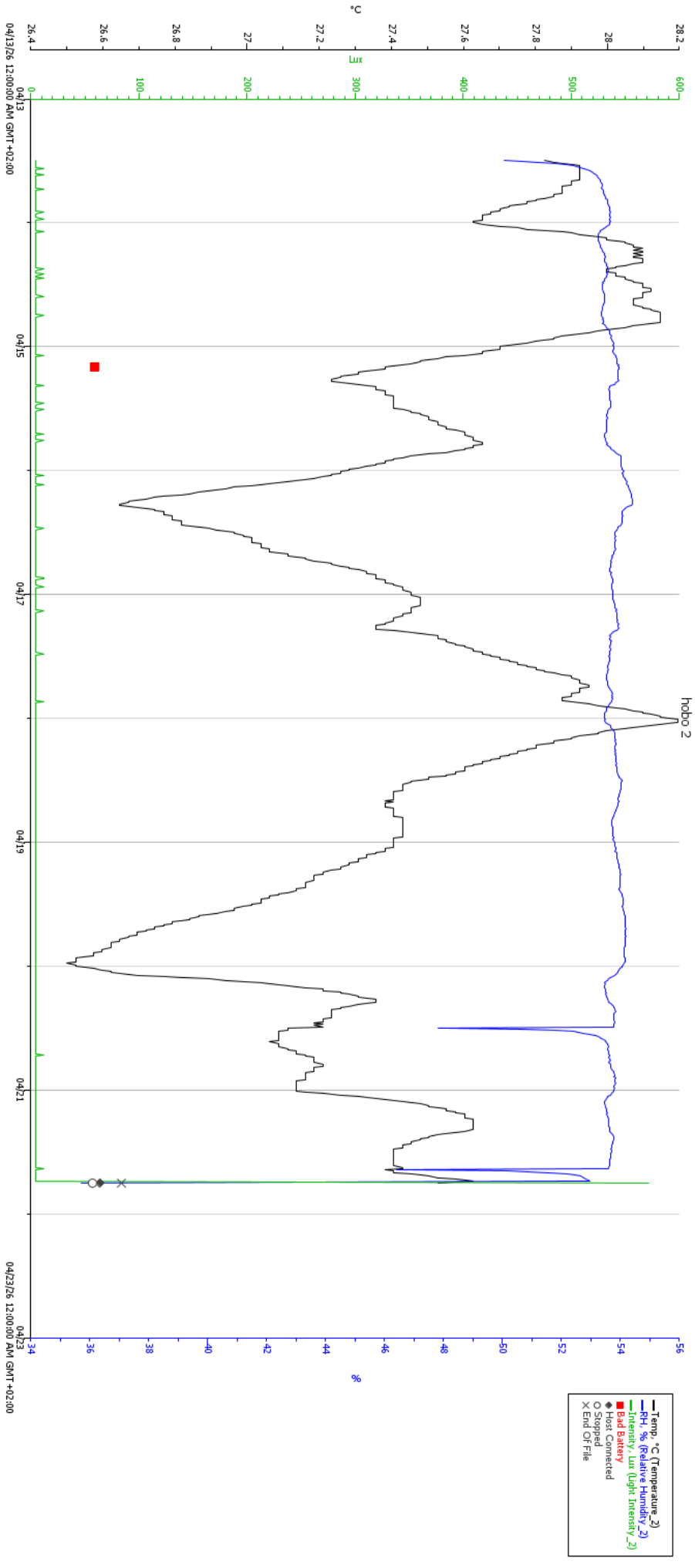

**SETTING RELATIVE HUMIDITY TO 55%;**

PRIOR TO CONDITIONING INDIVIDUAL TIMBER LAYERS

*(climatic sensor 2)*

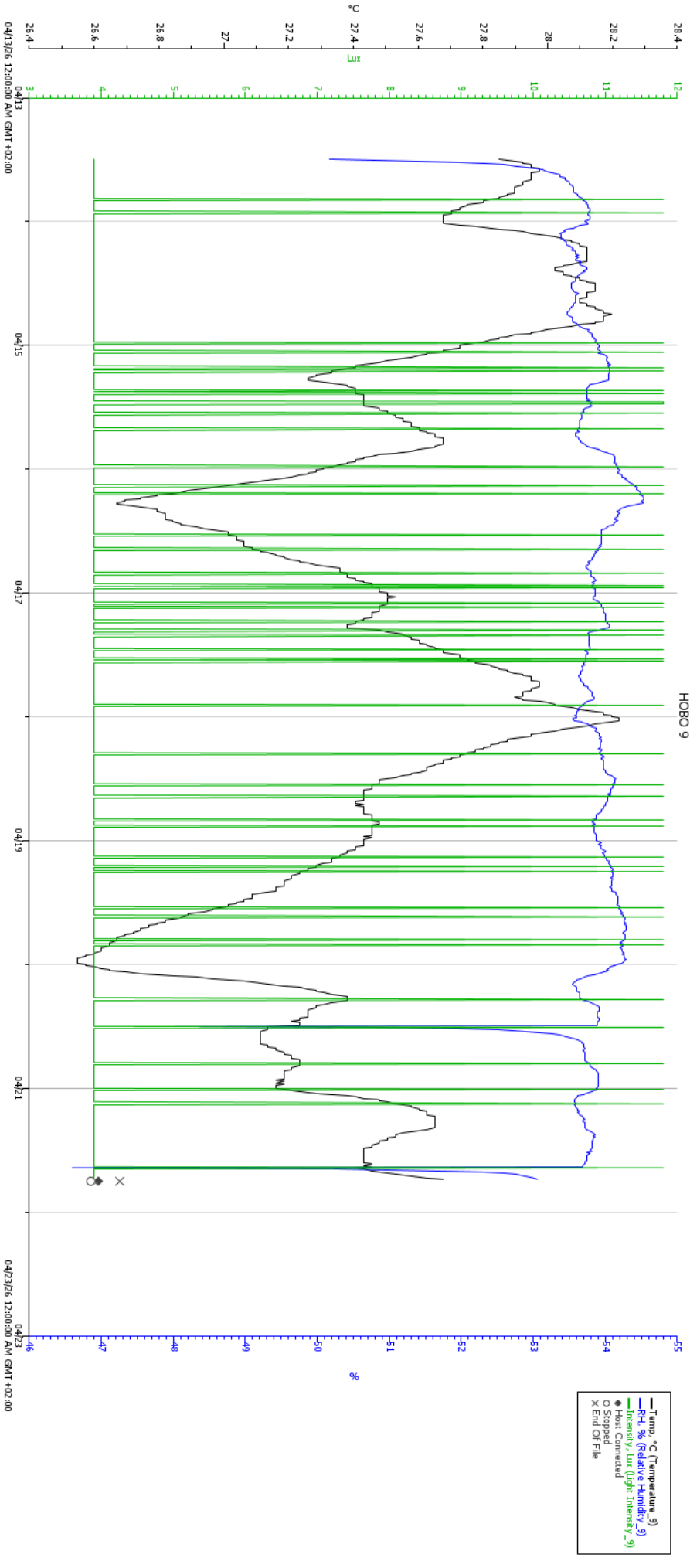

**MAINTAINING RELATIVE HUMIDITY AT 55%;**

INDIVIDUAL TIMBER LAYERS KEPT IN FRIDGE FOR CONDITIONING

*(climatic sensor 1)*

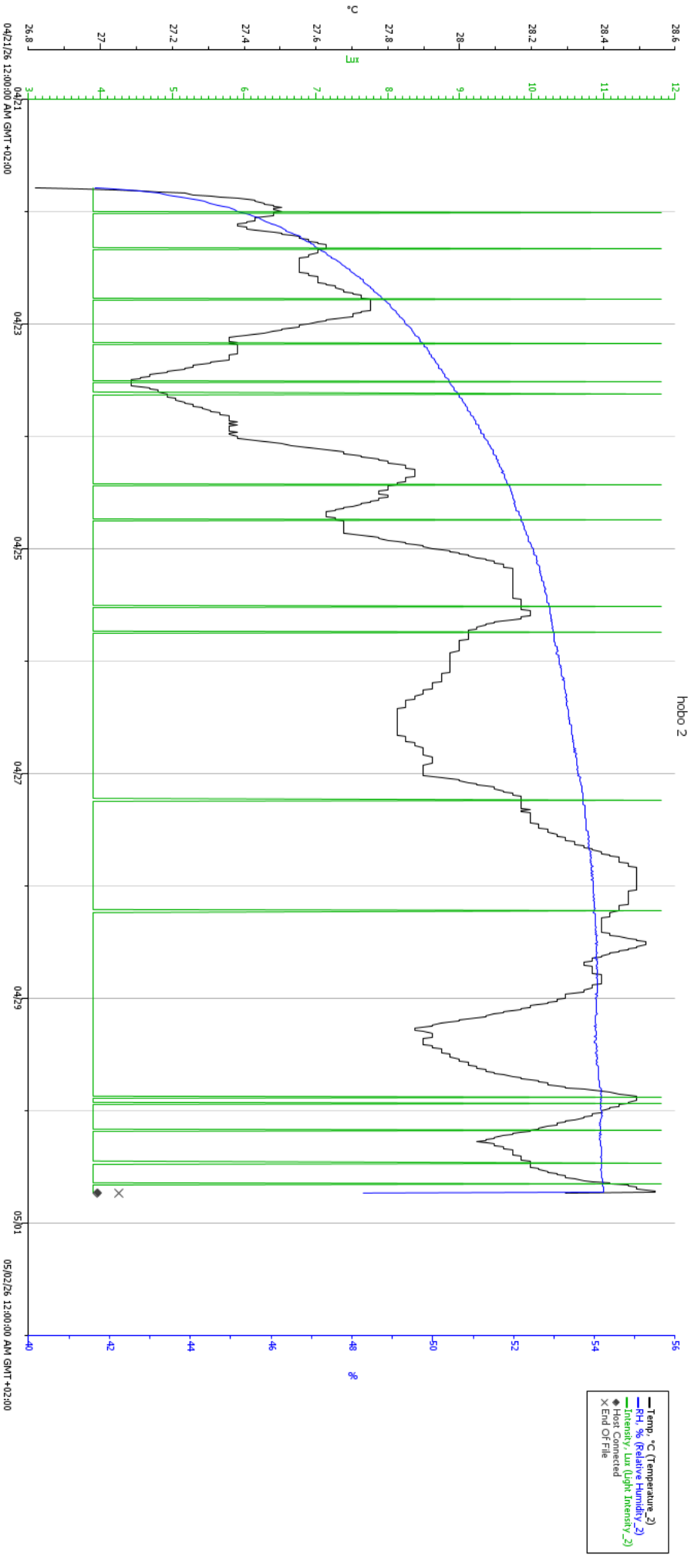

**MAINTAINING RELATIVE HUMIDITY AT 55%;**

INDIVIDUAL TIMBER LAYERS KEPT IN FRIDGE FOR CONDITIONING

*(climatic sensor 2)*

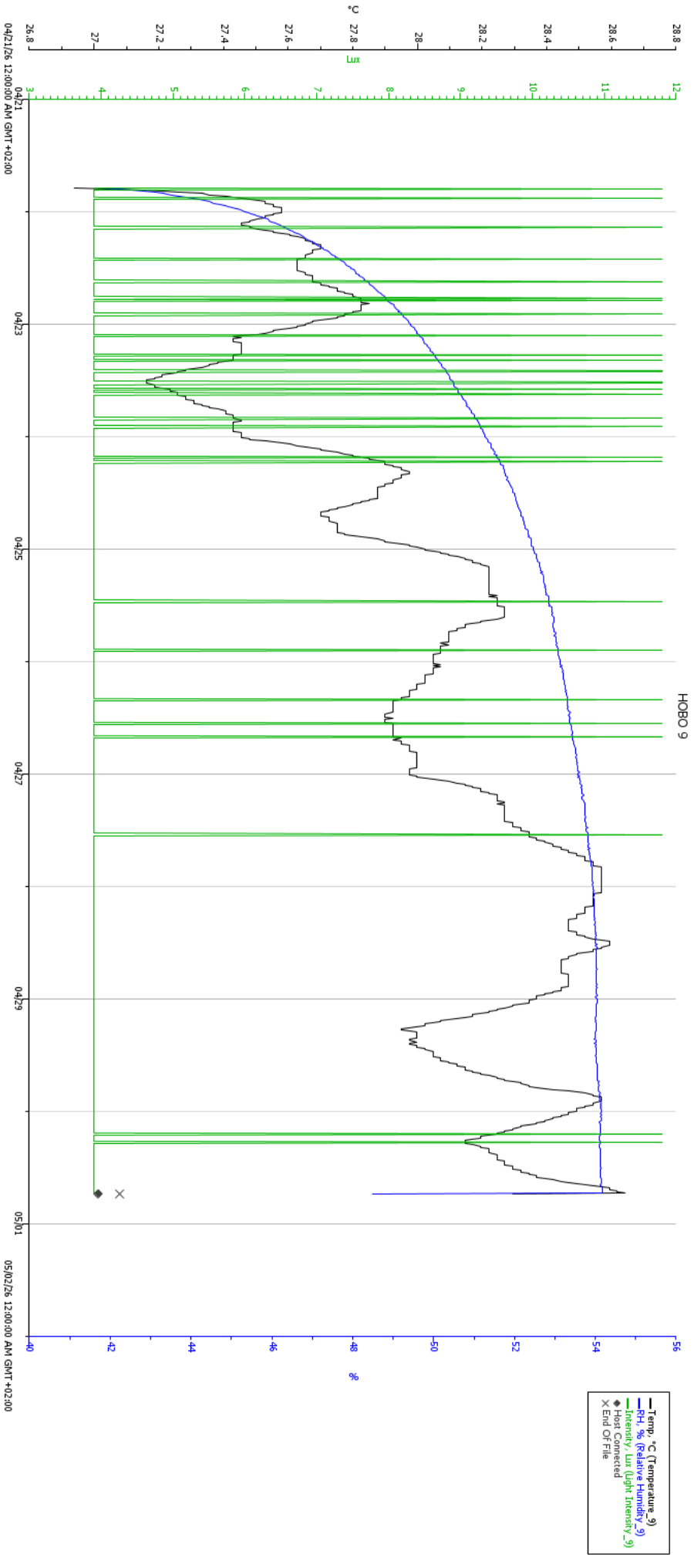

## LAMINATING BILAYERS AT 55% RELATIVE HUMIDITY;

BILAYER PANELS HAD TO BE CONDITIONED IN TWO GROUPS OVER A PERIOD OF 3 DAYS PER GROUP

*(climatic sensor 1)*

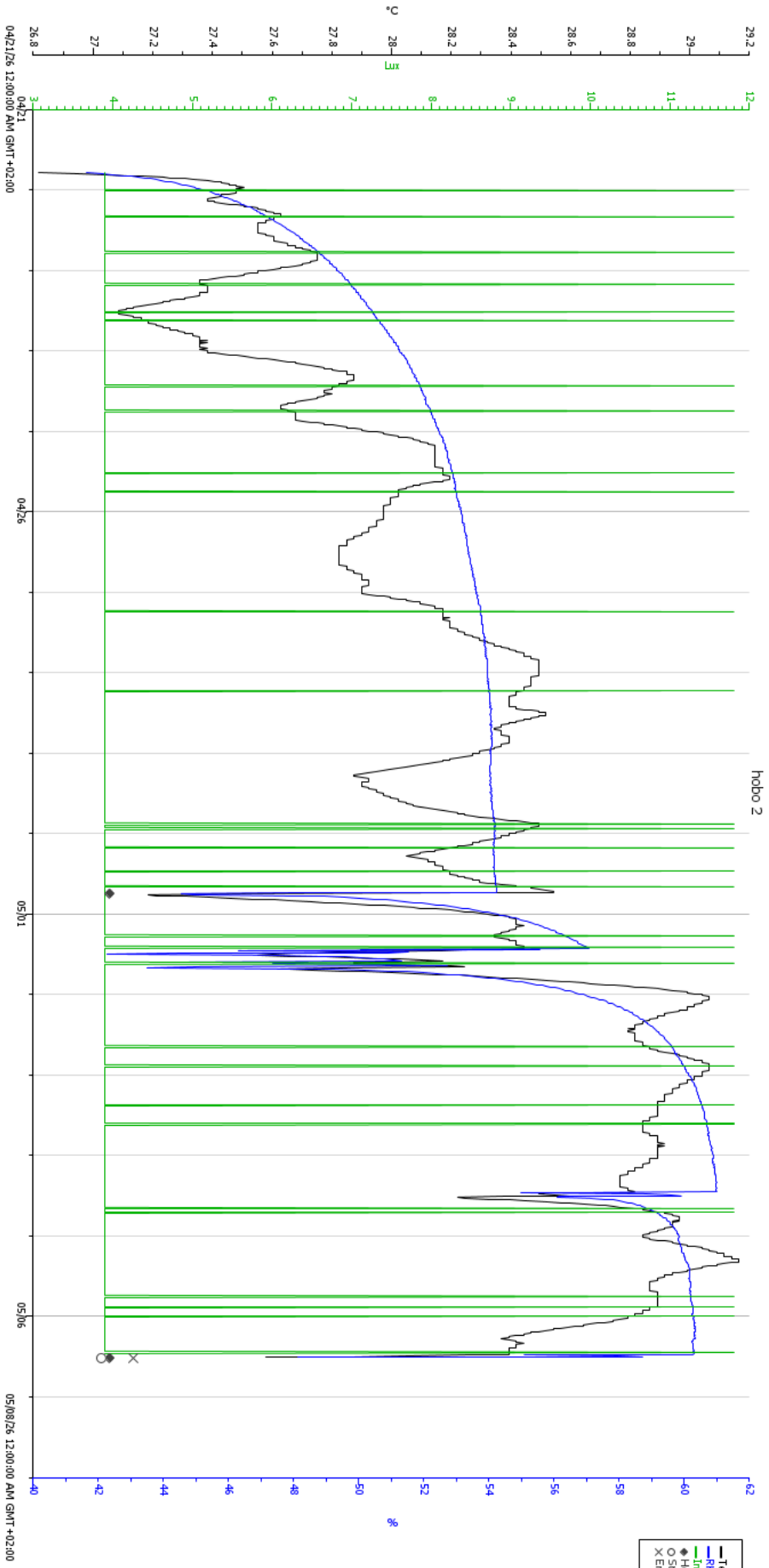

**LAMINATING BILAYERS AT 55% RELATIVE HUMIDITY;**

BILAYER PANELS HAD TO BE CONDITIONED IN TWO GROUPS OVER A PERIOD OF 3 DAYS PER GROUP

*(climatic sensor 2)*

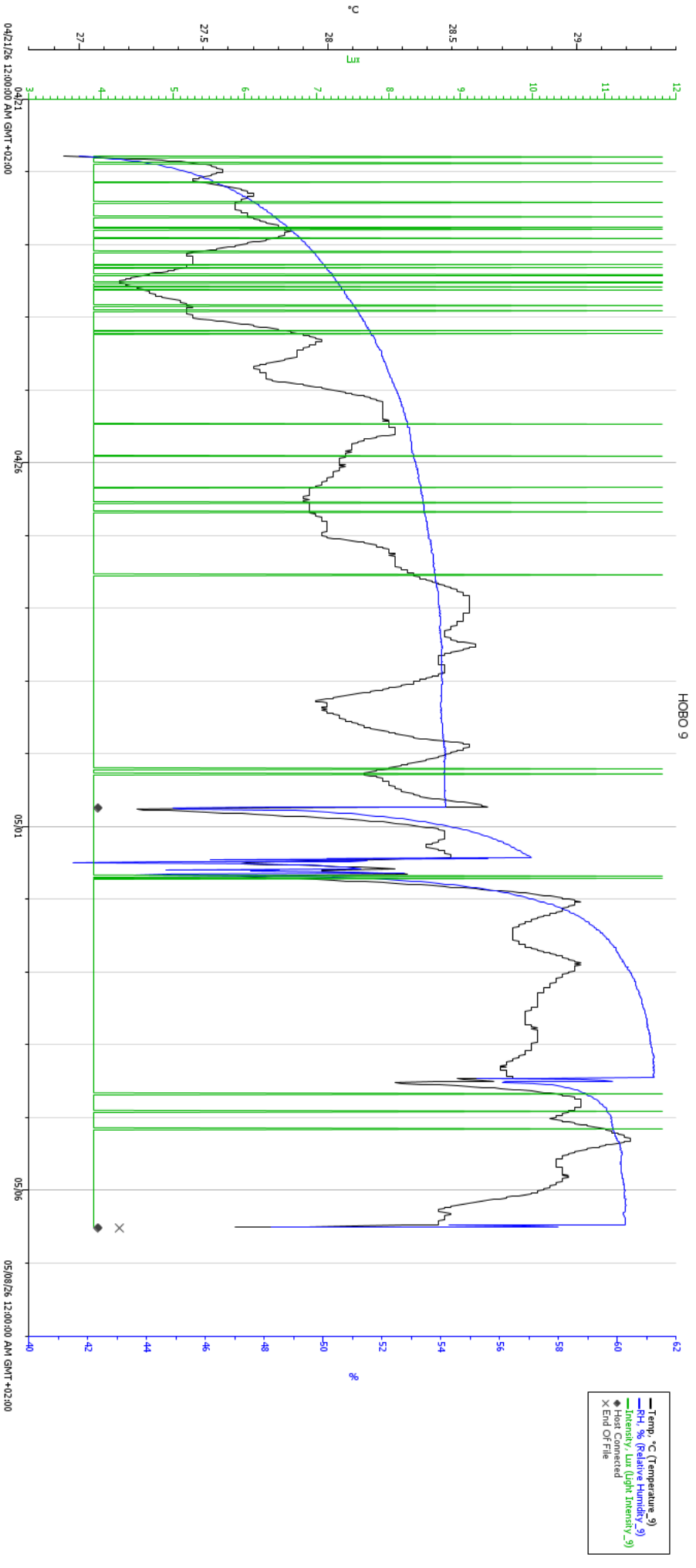

## HUMIDIFYING BILAYERS AT 95% RELATIVE HUMIDITY;

ONCE THE ADHESIVE HAD CURED, THE BILAYERS WERE HUMIDIFIED AT A HIGHER RELATIVE HUMIDITY

*(climatic sensor 1)*

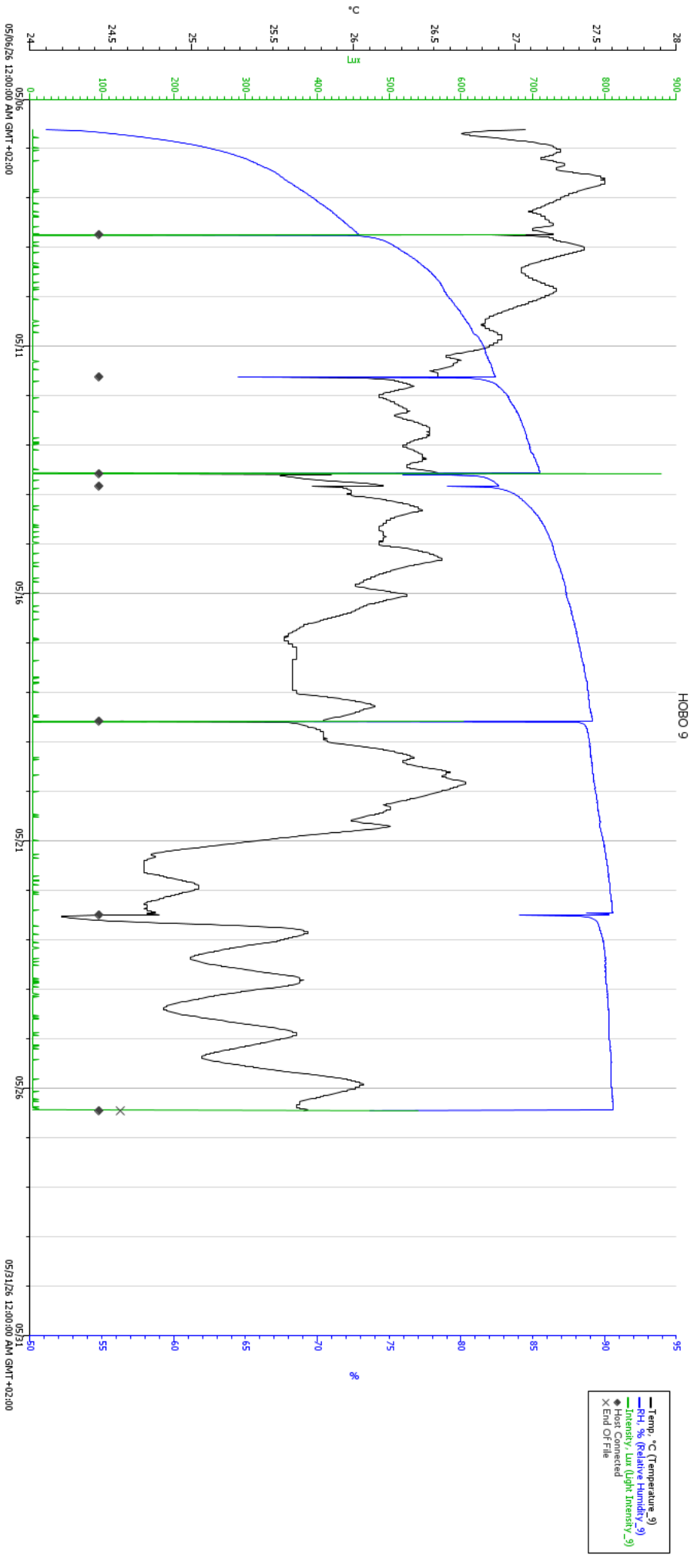

**HUMIDIFYING BILAYERS AT 95% RELATIVE HUMIDITY;**

ONCE THE ADHESIVE HAD CURED, THE BILAYERS WERE HUMIDIFIED AT A HIGHER RELATIVE HUMIDITY

*(climatic sensor 2)*

***The battery of the sensor had to be replaced in the middle. Therefore, two graphs are required to display the full timeframe (see next page)***

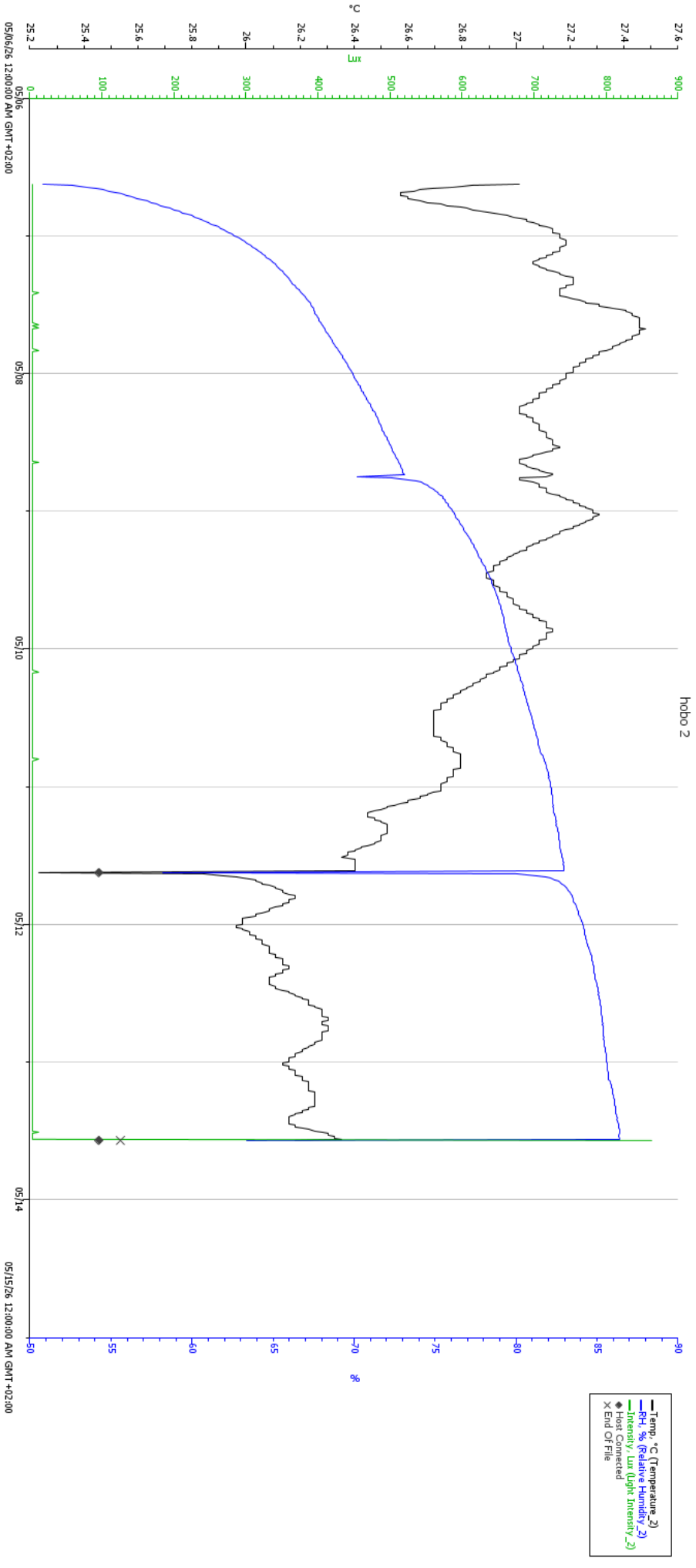

## HUMIDIFYING BILAYERS AT 95% RELATIVE HUMIDITY;

ONCE THE ADHESIVE HAD CURED, THE BILAYERS WERE HUMIDIFIED AT A HIGHER RELATIVE HUMIDITY

*(climatic sensor 2)*

***The battery of the sensor had to be replaced in the middle. Therefore, two graphs are required to display the full timeframe (see previous page)***

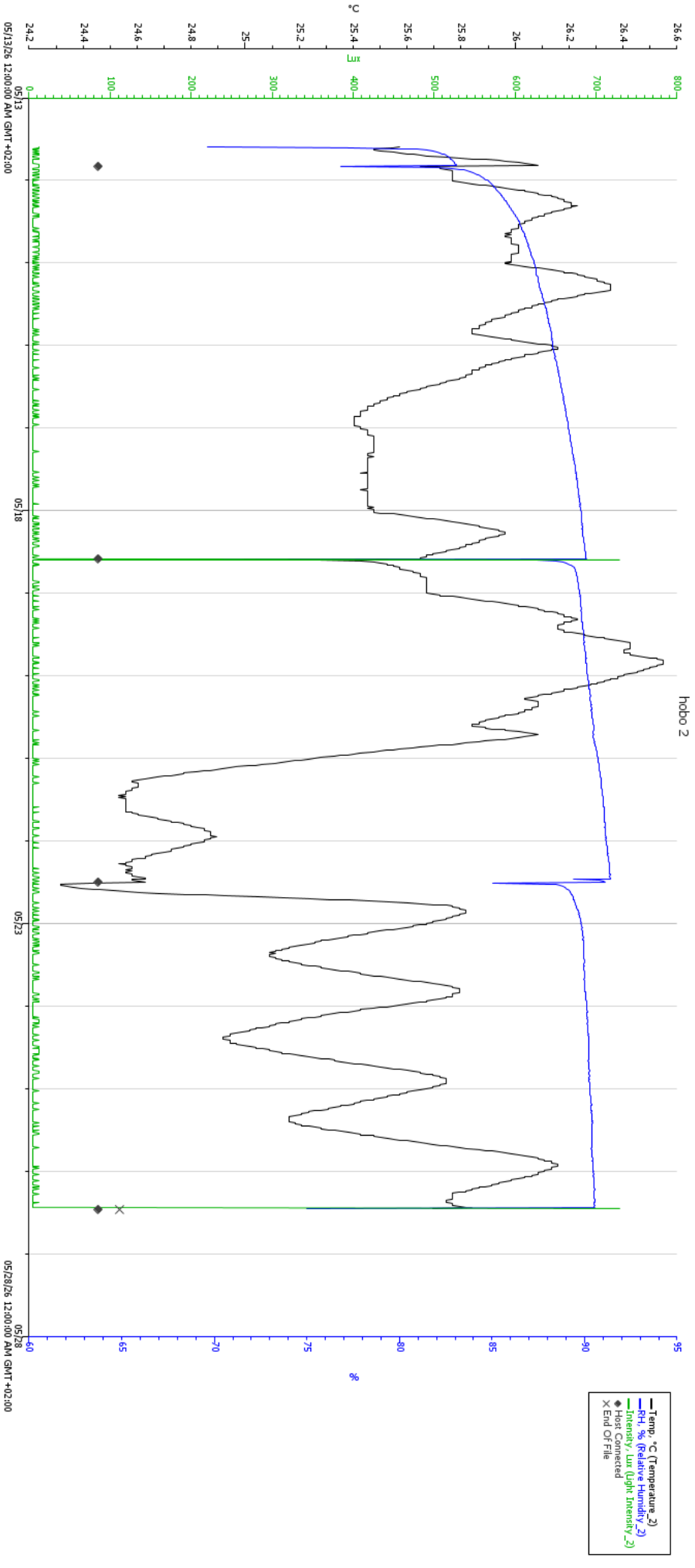

# [APPENDIX 7]

# A.7

## DATA OF ANTICLASTIC SAMPLES

(from conditioning to lamination)

| Timber Species | | Width x Length (mm) | Thickness (mm) | Combined Thickness (mm) | Ratio | Before Conditioning - 21/04/2026 | |
|---|---|---|---|---|---|---|---|
| | | | | | | Weight (g) | Wood Moisture Content (%) |
| GROUP 2 - circle | | | | | | | |
| oak | | 160 x 160 | 3 | 6 | 1:1 | 70.84 | 7.7 |
| | spruce | - | 3 | | | 36.63 | 7.1 |
| oak | | - | 4 (a) | 6 | 2:1 | 94.82 | 8.1 |
| | spruce | - | 2 (a) | | | 28.47 | 7.6 |
| oak | | - | 4.5 | 6 | 3:1 | 101.67 | 8.3 |
| | spruce | - | 1.5 | | | 23.71 | 7.2 |
| oak | | - | 4(b) | 8 | 1:1 | 99.03 | 8.3 |
| | spruce | - | 4 | | | 52.04 | 7.3 |
| oak | | - | 5.3 | 8 | 2:1 | 112.39 | 7.1 |
| | spruce | - | 2.7 | | | 28.71 | 7.8 |
| oak | | - | 6 | 8 | 3:1 | 124.91 | 7.7 |
| | spruce | - | 2 (b) | | | 28.49 | 7.6 |
| oak | | - | 5 | 10 | 1:1 | 104.72 | 8 |
| | spruce | - | 5 | | | 61.66 | 8.2 |
| oak | | - | 6.7 | 10 | 2:1 | 146.68 | 7.6 |
| | spruce | - | 3.3 | | | 48.73 | 8.1 |
| oak | | - | 7.5 | 10 | 3:1 | 169.37 | 7.9 |
| | spruce | - | 2.5 | | | 30.11 | 7.7 |
| GROUP 1 - star | | | | | | | |
| oak | | 160 x 160 | 3 | 6 | 1:1 | 57.32 | 6.4 |
| | spruce | - | 3 | | | 38.61 | 7.2 |
| oak | | - | 4 (a) | 6 | 2:1 | 72.91 | 7 |
| | spruce | - | 2 (a) | | | 18.77 | 7.1 |
| oak | | - | 4.5 | 6 | 3:1 | 81.75 | 6.4 |
| | spruce | - | 1.5 | | | 16.72 | n/a |
| oak | | - | 4 (b) | 8 | 1:1 | 83.59 | 6.5 |
| | spruce | - | 4 | | | 45.81 | 7.4 |
| oak | | - | 5.3 | 8 | 2:1 | 101.23 | 6.7 |
| | spruce | - | 2.7 | | | 41.78 | 7.6 |
| oak | | - | 6 | 8 | 3:1 | 94.28 | 6.5 |
| | spruce | - | 2 (b) | | | 17.97 | 7.1 |
| oak | | - | 5 | 10 | 1:1 | 91.95 | 6.4 |
| | spruce | - | 5 | | | 64.3 | 7.5 |
| oak | | - | 6.7 | 10 | 2:1 | 153.38 | 6.4 |
| | spruce | - | 3.3 | | | 44.71 | 7.6 |
| oak | | - | 7.5 | 10 | 3:1 | 167.45 | 7.4 |
| | spruce | - | 2.5 | | | 30.09 | 7.5 |

| After Conditioning - 01/05/2026 | | | | |
|---|---|---|---|---|
| Wood Moisture Content FRONT (%) | Average | Wood Moisture Content BACK (%) | Average | Weight (g) |
| 7.2-8 | 7.6 | 7.8-8.2 | 8 | 111.36 |
| 7.2-7.4 | 7.3 | 7.3-7.6 | 7.45 | |
| 7.3-8 | 7.65 | 7.3-8.1 | 7.7 | 126.31 |
| 7.2-7.4 | 7.3 | 7.2-7.5 | 7.35 | |
| 7.3-8.2 | 7.75 | 7.3-8.2 | 7.75 | 128.28 |
| 7.2-7.4 | 7.3 | 7.2-7.7 | 7.45 | |
| 7.1-7.8 | 7.45 | 7.2-8 | 7.5 | 154.26 |
| 7.8-7.9 | 7.85 | 7.7-7.9 | 7.8 | |
| 7.4-8.1 | 7.75 | 7.6-8.1 | 7.85 | 143.76 |
| 7.2-7.3 | 7.25 | 7.2-7.4 | 7.3 | |
| 7.2-7.9 | 7.55 | 7.1-7.8 | 7.45 | 156.28 |
| 7.2-7.6 | 7.4 | 7.3 | 7.3 | |
| 7.8-8.3 | 8.05 | 7.8-8.3 | 8.05 | 169.62 |
| 7.2-7.6 | 7.4 | 7.3-7.6 | 7.45 | |
| 7.3-8 | 7.65 | 7.2-7.6 | 7.4 | 198.83 |
| 7.2-7.6 | 7.4 | 7.4-7.8 | 7.6 | |
| 7.5-8.1 | 7.8 | 7.4-8.4 | 7.9 | 202.99 |
| 7.1-7.7 | 7.4 | 7.2 | 7.2 | |
| 6.5-7.1 | 6.8 | 6.5-6.9 | 6.7 | 99.25 |
| 7.4-7.6 | 7.5 | 7.3-7.5 | 7.4 | |
| 6.8-7.5 | 7.15 | 6.6-7.3 | 6.95 | 95.88 |
| 7.1 | 7.1 | 7.1 | 7.1 | |
| 6.6-7.1 | 6.85 | 6.6-7.3 | 6.95 | 101.76 |
| 7.1-7.3 | 7.2 | 7.1-7.2 | 7.15 | |
| 6.5-7 | 6.75 | 6.5-7.2 | 6.85 | 133.14 |
| 7.5-8 | 7.75 | 7.7-7.9 | 7.8 | |
| 6.7-7.4 | 7.05 | 6.7-7.5 | 7.1 | 146.95 |
| 7.7-8.2 | 7.95 | 7.2-7.8 | 7.5 | |
| 6.6-7.2 | 6.9 | 6.6-7.2 | 6.9 | 115.73 |
| 7.2-7.4 | 7.3 | 7.1-7.3 | 7.2 | |
| 6.5-7.5 | 7 | 6.8-7.3 | 7.05 | 160.66 |
| 7.3-7.9 | 7.6 | 7.3-7.8 | 7.55 | |
| 6.6-7.3 | 6.95 | 7.4-7.6 | 7.5 | 201.73 |
| 7.4-7.9 | 7.65 | 7.4-8 | 7.6 | |
| 7.5-7.9 | 7.7 | 8-8.5 | 8.25 | 201.49 |
| 7.8-8 | 7.9 | 7.5-8.1 | 7.8 | |

HARDWOOD SPECIES

SOFTWOOD SPECIES

LENGTH X WIDTH (mm)

INDIVIDUAL LAYER THICKNESS

OVERALL THICKNESS

THICKNESS RATIO

WEIGHT (g) [before conditioning]

MOISTURE CONTENT (%) [before conditioning]

MOISTURE ON FRONT (%) [after conditioning]

MOISTURE AVERAGE (%) [after conditioning]

MOISTURE ON BACK (%) [after conditioning]

MOISTURE AVERAGE (%) [after conditioning]

WEIGHT (g) [after conditioning]

MOISTURE CONTENT(%)
[after bonding layers]

MOISTURE CONTENT(%)
[after bonding layers]

MOISTURE CONTENT(%)
[after humidifying]

MOISTURE CONTENT(%)
[after humidifying]

AVERAGE MOISTURE (%)
[after humidifying]

| Laminated Stage 1 - 06/05/2026 | | Laminated Post-conditioning - 25/05/2026 | | |
|---|---|---|---|---|
| Wood Moisture Content HARDWOOD (%) | Wood Moisture Content SOFTWOOD (%) | Wood Moisture Content HARDWOOD (%) | Wood Moisture Content SOFTWOOD (%) | Average of HARDWOOD and SOFTWOOD |
| 7.7-8.2 | 7.8-8.0 | 12.9-14 | 14.2-14.6 | 13.45 |
| 8.2-8.9 | 8.0-8.2 | 13.7-14.2 | 14.5-15.2 | 14.4 |
| 7.9-8.6 | 7.8-8.4 | 13-13.4 | 13.3-13.6 | 14.95 |
| 8.2-8.7 | 8.2-8.4 | 13.1-13.6 | 14.2-14.5 | 13.2 |
| 7.9-8.6 | 7.8-8.2 | 13.5-14.1 | 14.4-14.9 | 14.85 |
| 7.6-8.1 | 7.9-8.3 | 12.9-13.8 | 14.5-14.9 | 13.45 |
| 8.2-8.9 | 8-8.6 | 13.2-13.8 | 14.6-15.3 | 13.35 |
| 7.7-8.3 | 7.3-7.6 | 13.4-14.1 | 14.2-14.9 | 14.35 |
| 8.0-8.7 | 7.9-8.2 | 13.2-13.9 | 13.7-14.1 | 13.5 |
| | | | | 14.95 |
| | | | | 13.75 |
| | | | | 14.55 |
| | | | | 13.55 |
| | | | | 13.9 |
| 6.9-7.2 | 7.5-7.7 | 13.3-13.5 | 14.1-14.9 | 13.4 |
| 7.1-7.7 | 7.1-7.6 | 12.7-13.3 | 13.2-14 | 14.5 |
| 7.0-7.5 | 7.2-7.5 | 12.7-13.3 | 12.9-13.1 | 13 |
| 7.2-7.4 | 7.9-8.3 | 12.8-13.1 | 13.4-14 | 13.6 |
| 7.3-7.8 | 7.9-8.2 | 12.6-13 | 14-14.4 | 13 |
| 7.1-7.6 | 7.4-7.8 | 12.7-12.9 | 13.8-14.4 | 12.95 |
| 7-7.5 | 7.7-8.2 | 12.7-13.3 | 13.3-13.6 | 13.7 |
| 7.8-8.3 | 8.0-8.6 | 13-13.7 | 13.9-14.2 | 12.8 |
| 8.5-8.9 | 8.1-8.6 | 12.2-12.7 | 11.9-12.4 | 14.2 |
| | | | | 12.8 |
| | | | | 14.1 |
| | | | | 13 |
| | | | | 13.45 |
| | | | | 13.35 |
| | | | | 14.05 |
| | | | | 12.45 |
| | | | | 12.15 |

# DATA OF ANTICLASTIC CURVATURE

RADIUS (mm)

RADIUS (mm)

DEGREE OF CURVATURE

## [GROUP 1]

| GROUP 1 - STAR | | Positive Curvature (hardwood dominates) | | Negative Curvature (softwood dominates) | | Average | | |
|---|---|---|---|---|---|---|---|---|
| Thickness (mm) | Layer Thickness (mm) | Hardwood | Softwood | Hardwood | Softwood | Hardwood dominates | Softwood dominates | Timoshenko Results |
| 6 | 3×3 | 0.001509 | 0.000839 | 0.000148 | 0.000148 | 0.001174 | 0.000148 | 0.002338 |
| | | 662.69 | 1,191.90 | 6,756.76 | 6,756.76 | 927.29 | 6,756.76 | 427.72 |
| 6 | 2×4 | 0.002996 | 0.002984 | 0.000061 | 0.000263 | 0.00299 | 0.000162 | 0.002786 |
| | | 333.78 | 335.12 | 16,393.44 | 3,802.28 | 334.45 | 10,097.86 | 358.94 |
| 6 | 1.5×4.5 | 0.003903 | 0.003343 | 0.000085 | 0.000096 | 0.003623 | 0.0009905 | 0.002828 |
| | | 256.21 | 299.13 | 11,764.71 | 10,416.67 | 277.67 | 11,090.69 | 353.61 |
| 8 | 4×4 | 0.000687 | 0.000609 | 0.000071 | 0.00022 | 0.000648 | 0.0001455 | 0.001538 |
| | | 1,455.60 | 1,642.04 | 14,084.51 | 4,545.45 | 1,548.82 | 9,314.98 | 650.20 |
| 8 | 2.7×5.3 | 0.000975 | 0.00088 | 0.000075 | 0.000133 | 0.0009275 | 0.000104 | 0.002048 |
| | | 1,025.64 | 1,136.36 | 13,333.33 | 7,518.80 | 1,081.00 | 10,426.07 | 488.28 |
| 8 | 2×6 | 0.003099 | 0.001705 | 0.000027 | 0.000102 | 0.002402 | 0.0000645 | 0.002154 |
| | | 322.68 | 586.51 | 37,037.04 | 9,803.92 | 454.60 | 23,420.48 | 464.25 |
| 10 | 5×5 | 0.000351 | 0.0003 | 0.0002 | 0.000349 | 0.0003255 | 0.0002745 | 0.00121 |
| | | 2,849.00 | 3,333.33 | 5,000.00 | 2,865.33 | 3,091.17 | 3,932.66 | 826.45 |
| 10 | 3.3×6.7 | 0.001132 | 0.00097 | 0.000056 | 0.000235 | 0.001051 | 0.0001455 | 0.001633 |
| | | 883.39 | 1,030.93 | 17,857.14 | 4,255.32 | 957.16 | 11,056.23 | 612.37 |
| 10 | 2.5×7.5 | 0.001674 | 0.001572 | 0.000039 | 0.000096 | 0.001623 | 0.0000675 | 0.001656 |
| | | 597.37 | 636.13 | 25,641.03 | 10,416.67 | 616.75 | 18,028.85 | 603.86 |

## [GROUP 2]

| GROUP 2 - CIRCLE | | Positive Curvature (hardwood dominates) | | Negative Curvature (softwood dominates) | | Average | | |
|---|---|---|---|---|---|---|---|---|
| Thickness (mm) | Layer Thickness (mm) | Hardwood | Softwood | Hardwood | Softwood | Hardwood dominates | Softwood dominates | Timoshenko Results |
| 6 | 3×3 | 0.001038 | 0.000984 | 0.000307 | 0.000384 | 0.001011 | 0.0003455 | 0.002101 |
| | | 963.39 | 1,016.26 | 3,257.33 | 2,604.17 | 989.83 | 2,930.75 | 475.96 |
| 6 | 2×4 | 0.002426 | 0.002295 | 0.0001 | 0.000144 | 0.0023605 | 0.000122 | 0.003246 |
| | | 412.20 | 435.73 | 10,000.00 | 6,944.44 | 423.97 | 8,472.22 | 308.07 |
| 6 | 1.5×4.5 | 0.002761 | 0.00273 | 0.000097 | 0.000124 | 0.0027455 | 0.0001105 | 0.003299 |
| | | 362.19 | 366.30 | 10,309.28 | 8,064.52 | 364.24 | 9,186.90 | 303.12 |
| 8 | 4×4 | 0.00059 | 0.000459 | 0.000087 | 0.000442 | 0.0005245 | 0.0002645 | 0.001576 |
| | | 1,694.92 | 2,178.65 | 11,494.25 | 2,262.44 | 1,936.78 | 6,878.35 | 634.52 |
| 8 | 2.7×5.3 | 0.001995 | 0.001839 | 0.000064 | 0.000221 | 0.001917 | 0.0001425 | 0.00219 |
| | | 501.25 | 543.77 | 15,625.00 | 4,524.89 | 522.51 | 10,074.94 | 456.62 |
| 8 | 2×6 | 0.003009 | 0.002957 | 0.000054 | 0.000132 | 0.002983 | 0.000093 | 0.002239 |
| | | 332.34 | 338.18 | 18,518.52 | 7,575.76 | 335.26 | 13,047.14 | 446.63 |
| 10 | 5×5 | 0.000506 | 0.000389 | 0.000085 | 0.000354 | 0.0004475 | 0.0002195 | 0.001301 |
| | | 1,976.28 | 2,570.69 | 11,764.71 | 2,824.86 | 2,273.49 | 7,294.78 | 768.64 |
| 10 | 3.3×6.7 | 0.000797 | 0.000652 | 0.000039 | 0.000161 | 0.0007245 | 0.0001 | 0.001646 |
| | | 1,254.71 | 1,533.74 | 25,641.03 | 6,211.18 | 1,394.22 | 15,926.10 | 607.53 |
| 10 | 2.5×7.5 | 0.001823 | 0.00177 | 0.000026 | 0.000045 | 0.0017965 | 0.0000355 | 0.00167 |
| | | 548.55 | 564.97 | 38,461.54 | 22,222.22 | 556.76 | 30,341.88 | 598.80 |

# [APPENDIX 8]

# A.8

DEVELOPING LATTICE GRID

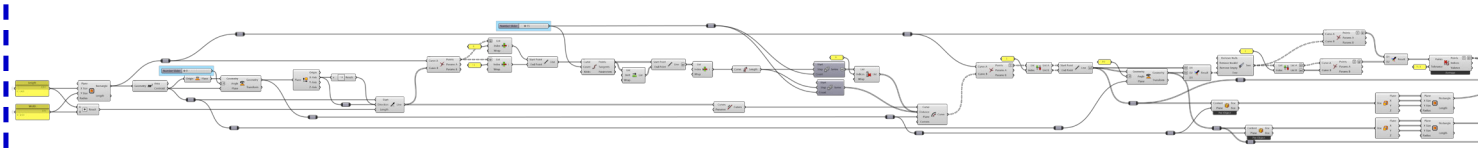

PHYSICAL SAMPLE DATA

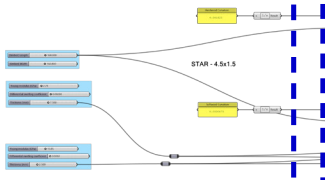


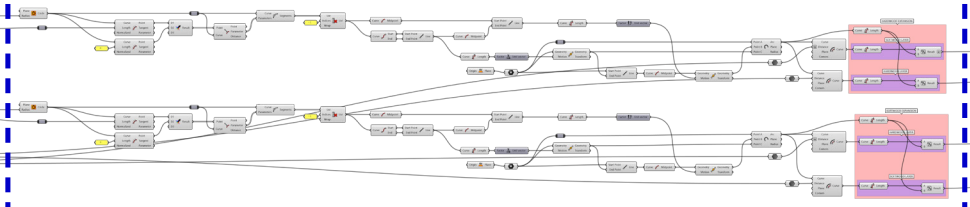

DERIVING SCALING RATIO

# GRASSHOPPER SCRIPT FOR ANTICLASTIC CURVATURE

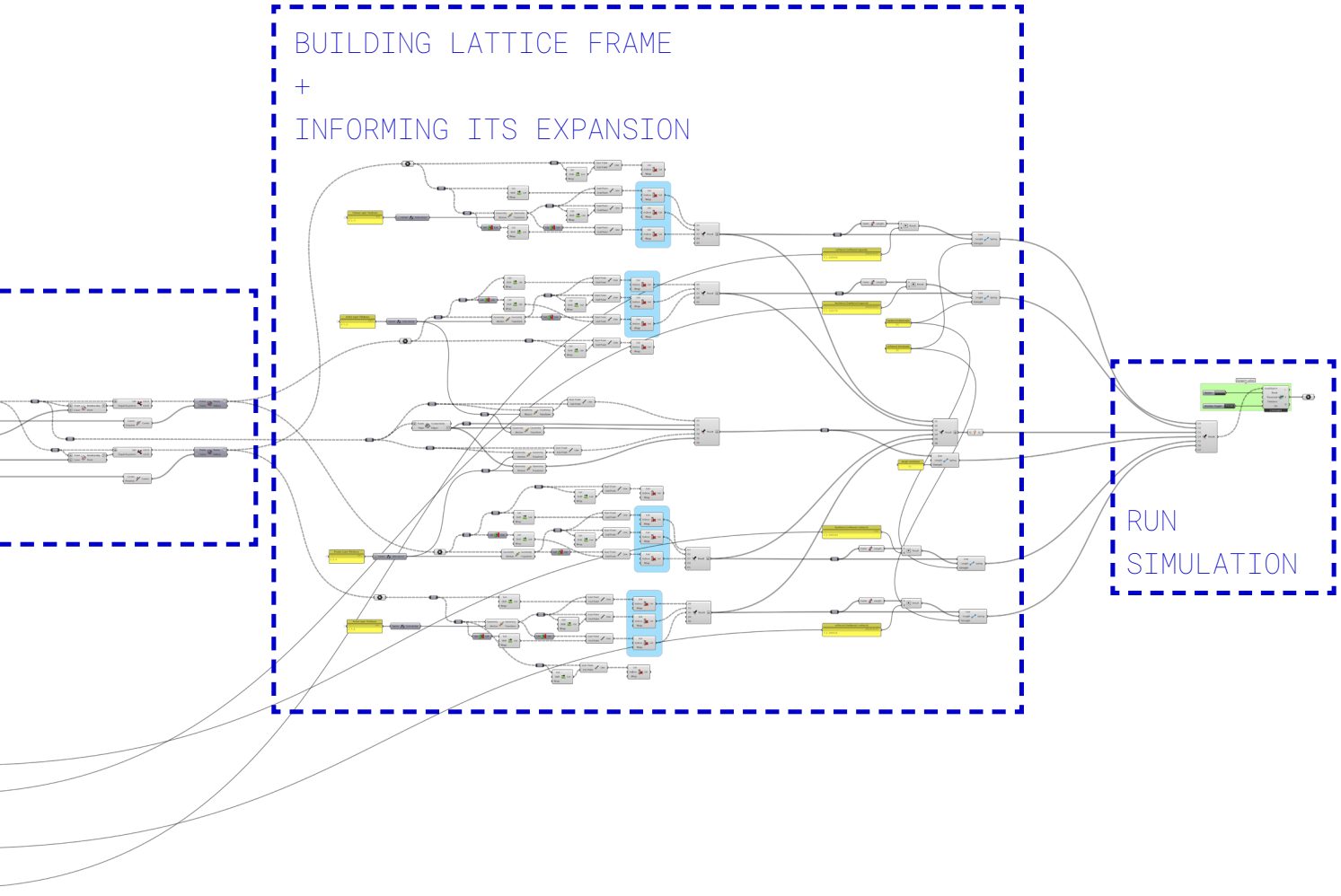

# [APPENDIX 9]

# A.9

## A.9.1 Exploring pseudo-deformation for activation

### Shrink film and shrink plastic

Exploration of the collision and energy-barrier locking system was achieved with paper and cardboard models. Both materials exhibit elastic behaviour under moderate, low-strain forces and can be easily cut into the desired shapes for curve-line activation. Due to the extensive amount of time required to construct, condition and deform

a hygromorphic bilayer, a pseudo-deformation process for monoclastic curvature was explored with shrink film and shrink plastic.

Shrink film is a thin plastic polymer, commonly made from low-density polyethylene that shrinks when subjected to heat. It is generally used for packaging to seal and tighten products for delivery and shipment. Experiments were carried out using thin sheets of shrink film glued onto paper strips to assess the types of curvature and deformations achieved as the plastic shrunk.

Room temperature cure epoxy glue was used as a bonding agent given its chemical and heat-resistant properties to temperatures below 120°C. The glue is supplied and prepared in two-component packaging comprised of an epoxy resin and a curing agent. When the two compounds are mixed together, the epoxy resin will react with the curing agent to form the final adhesive (Chen et al., 2019).

In the first set of samples, narrow strips of dimension 80mm x 200mm (width x length) were cut from 80gsm (grams per square metre) print paper. Sheets of shrink film were cut to the same dimensions and glued down across the entire strip (see figure 11A). A hairdryer was used to heat and shrink the entire surface of film as evenly as possible. Deformation was almost immediate and the paper strip curved into a monoclastic shell along the shorter edge (see figure 11B). This final state was not desirable, given that monoclastic curvature had to be achieved along the long edge.

This behaviour is attributed to the differential distribution of lateral compressive forces along the short edges versus the longer edges. As the shrink film contracts into itself, it exerts a uniform force across the surface of the paper, where a greater amount of lateral compression is induced along the longer edge due to its length (see figure 12). Additionally, a greater amount of force is necessary to curve the paper along the longer edge rather than the short side. Ultimately, the stress induced across the paper strip is resolved through out-of-plan bending along the short axis.

To achieve the appropriate monoclastic curvature, it was necessary to minimise the amount of lateral force exerted along the long edge, and maximise the lateral force exerted along the short edge. Rather than using an entire sheet, a

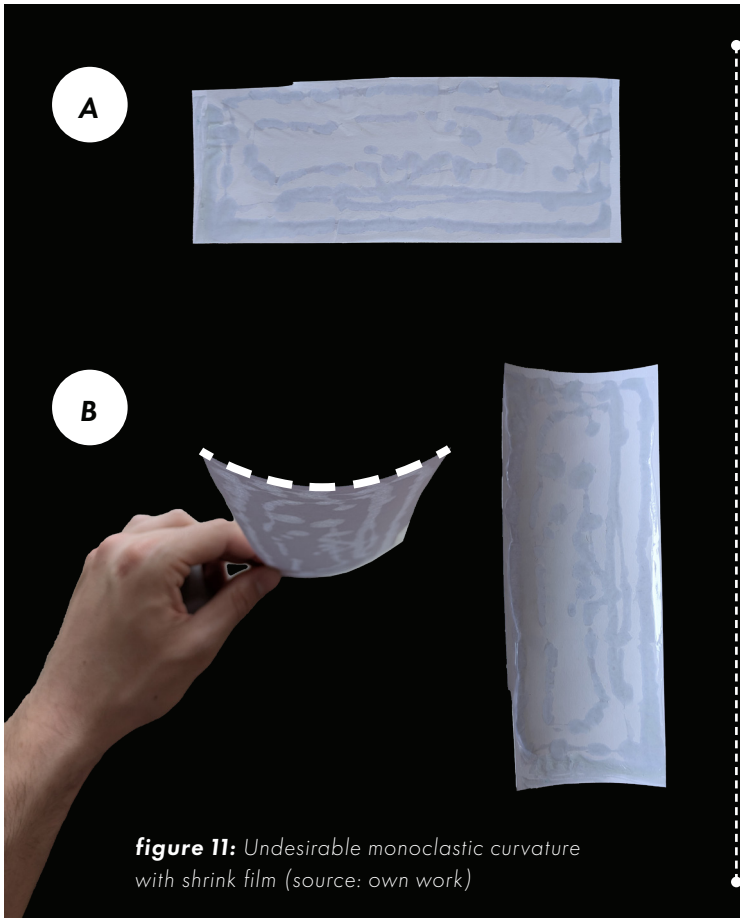


**figure 11:** *Undesirable monoclastic curvature with shrink film (source: own work)*

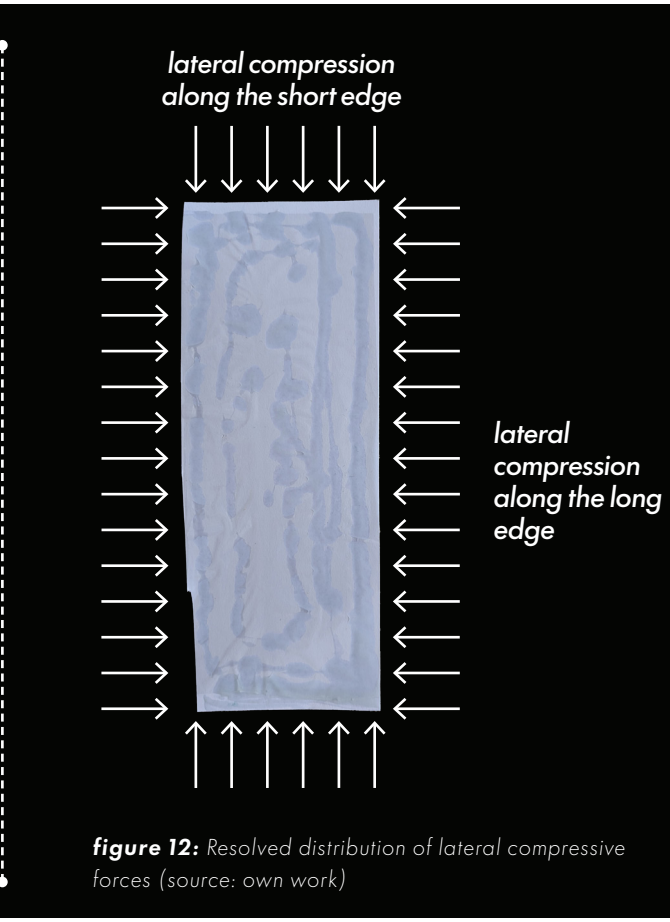


**figure 12:** *Resolved distribution of lateral compressive forces (source: own work)*

thinner strip was cut from the shrink film instead to create a strip with an extremely high aspect ratio.

Figure 13A below presents the final layout for the second round of trials. When subjected to heat, the deformation exhibited was far more successful, with monoclastic curvature occurring along the long edge as anticipated (see figure 13B).

For the third round of trials, to improve the degree of curvature and build on the behaviour established in the previous test, multiple thin strips were bonded to the paper strip instead (see figure 14). When comparing the degree of curvature between the second and third round of trials, the models with numerous thin strips of shrink film displayed greater curvature (see figure 15).

Although the final results were successful, the strength of the shrink film was considerably low, which limited the amount of curvature that could be achieved. An alternative was to employ shrink plastic to induce deformation. Shrink plastic is a craft material made from polystyrene, that shrinks as it is heated - usually in an oven. Similar to shrink film, the sheets can be cut to size easily with household scissors, and after heating they shrink to 40% to 30% their original size, and becoming around nine times thicker (see figure xx). The result is a considerably rigid, flat form that is far less elastic and deformable than the original sheet.

Shrink plastic needs to be heated to around 150°C to 180°C in the oven for 5 minutes to properly re-size. Given that epoxy glue can generally only handle temperatures of 120°C for a short period of time, the shrink plastic was tested to determine its behaviour at a lower temperature. The plastic successfully shrunk to the right size when compared to the 150°C sample, although it failed to flatten completely (see figure 16). While this presents a slightly less-than-perfect outcome, the shrink plastic still exhibited the desired degree

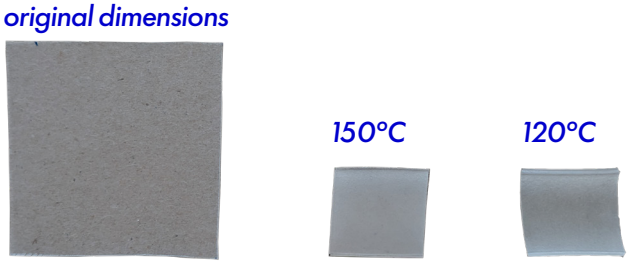


***figure 16:*** *Shrink plastic behaviour at 150°C [middle] and 120°C [right] displaying slight curvature (source: own work)*

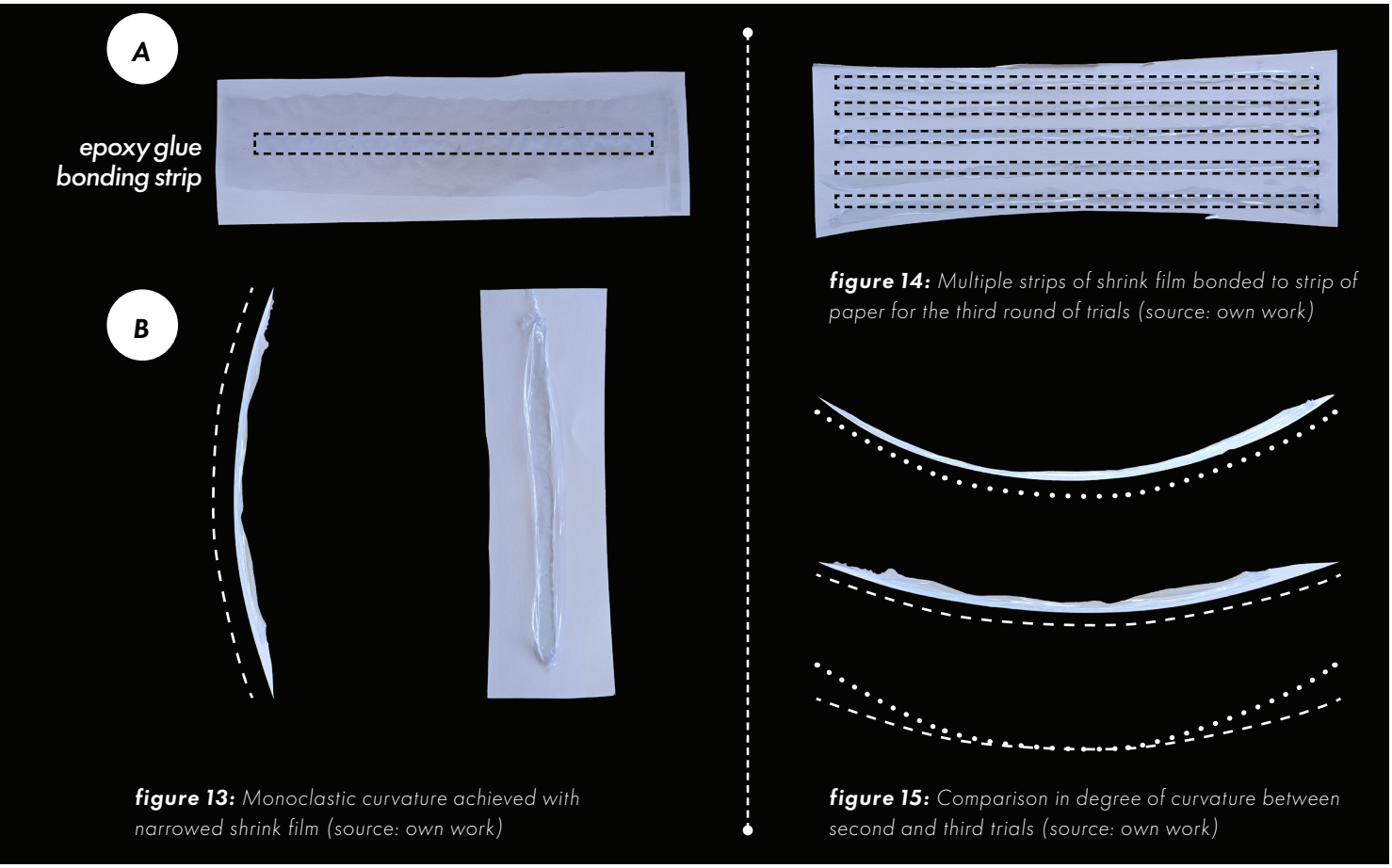


***figure 13:*** *Monoclastic curvature achieved with narrowed shrink film (source: own work)*



***figure 14:*** *Multiple strips of shrink film bonded to strip of paper for the third round of trials (source: own work)*



***figure 15:*** *Comparison in degree of curvature between second and third trials (source: own work)*

of shrinkage, which is the main driving force to achieve monoclastic curvature.

0.5mm thick cardboard sheets were used rather than the 8gsm print paper as it could pose a fire hazard in the oven. In a similar fashion to the third trials with paper and shrink film, a row of thin strips of the shrink plastic were glued to the cardboard sheet (see figure 17). Due to the degree of heat required to re-shape the plastic, the epoxy glue had to be allowed to cure for two hours prior to having the test models placed in the oven.

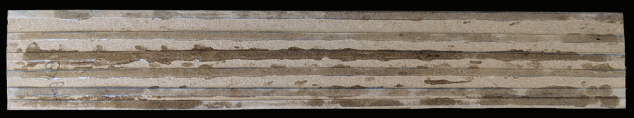

***figure 17:*** *Composition of shrink plastic and cardboard strip to achieve monoclastic curvature (source: own work)*



***figure 18:*** *Re-flattened cardboard strip after 5 minutes (source: own work)*

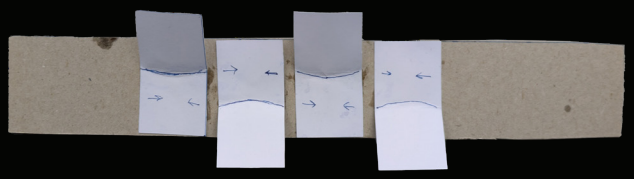

***figure 19:*** *Creased curve-line elements bonded to the cardboard with epoxy glue (source: own work)*

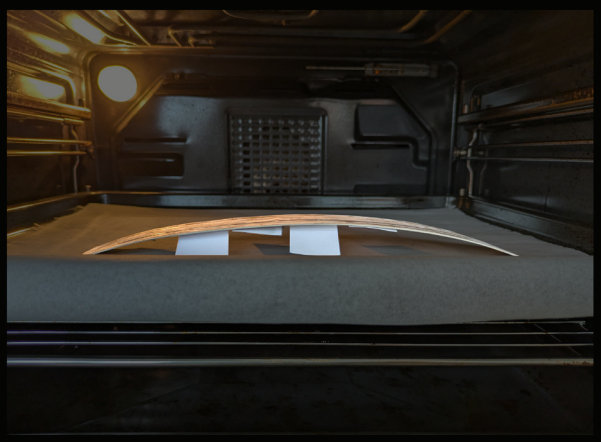

***figure 20:*** *Maximum amplitude achieved in the oven with curve-line elements (source: own work)*

For the first round of tests, the oven was set to 120°C and the cardboard sheet begun bending within five seconds. Maximum curvature was reached at one minute, with an amplitude of around 75mm. After another minute, the cardboard sheet started lowering again and re-flattened at three minutes (see figure 18). Prior to this, at 2.20 minutes, some of the shrink plastic elements separated from the cardboard, although most remained attached. A very unexpected outcome was that curvature occurred on the opposite side than predicted from the paper and shrink film tests. Rather than curving into the side where the shrink plastic had been glued, curvature occurred away from the plastic. While the re-flattening of the cardboard sheet and the curvature occurring in the opposite direction than initially expected might seem like drawbacks, they presented an ideal situation for testing the locking system.

Curve-line elements were bonded to the cardboard sheet to evaluate whether they could be fully activated to achieve locking behaviour to prevent or limit the re-flattening (see figure 19). In the second round of tests, the cardboard strip only begun curving at 1.26 minutes. A maximum amplitude of only around 20mm was reached at 2.05 minutes (see figure 20). The curve-line elements did not activate as intended, before the cardboard flattened again at 4.45.

### Takeaways from exploring pseudo-deformation

Ultimately, the behavior of the tested models demonstrated that shrink film and shrink plastic were insufficient for effectively achieving curve-line activation, or properly testing the locking mechanisms. Since the kinematic behaviour of the locking mechanism was identified as the most critical aspect to validate, it was concluded that applying an external mechanical force would provide the simplest and most effective method for further exploration of the system.



